IMPERIAL COLLEGE LONDON

Faculty of Engineering

Department of Civil and Environmental Engineering

Seismic Retrofitting of Substandard Frame Buildings Using Steel Shear Walls

Xi Chen

Submitted in fulfilment of the requirements for the degree of Doctor of Philosophy in the Department of Civil and Environmental Engineering of Imperial College London and the Diploma of Imperial College London

April 2022

Statement of Originality

I herewith certify that the work presented in this thesis is my own work. All material in this thesis which is not my own work has been properly acknowledged.

Copyright Declaration

Abstract

The use of steel shear panels represents an effective strategy to enhance the seismic performance of substandard framed buildings not designed to resist earthquakes. The seismic response of framed structures equipped with steel walls can be predicted using finite element models with accurate shell elements for representing the steel panels. However, such a detailed numerical description requires significant computational resources, especially for nonlinear dynamic analysis of large retrofitted buildings with steel infill plates. Besides, the design of steel shear walls for seismic retrofitting has been addressed mainly by trial-and-error methods in previous research and practical applications. Therefore, there is a clear need for more simplified and efficient numerical models for accurate simulations of steel shear walls under earthquake loading and enhanced seismic retrofitting design procedures with automatic selection of the retrofitting components.

In this research, an 8-noded macroelement formulation is first proposed incorporating six nonlinear springs with asymmetric constitutive relationships. To improve the macroelement performance, material parameters are calibrated via genetic algorithms (GAs) based on the numerical results from validated shell element models. Subsequently, simple functions for macroelement material parameters in terms of steel plate geometrical properties are determined using multiple linear regressions. Applications to numerical examples have confirmed the accuracy and computational efficiency of the proposed macroelement with calibrated material properties.

An improved optimal seismic retrofitting design procedure utilising steel shear wall macroelements is developed based on the capacity spectrum method. The proposed approach regards the selection and design of infill plates as a multi-objective optimisation problem with constraints solved by GA procedures. Nonlinear regression for equivalent viscous damping of steel shear walls is also carried out to determine the hysteretic damping ratio as a function of plate dimensions and drift demand. Afterwards, the proposed optimal design strategy is applied to the seismic retrofitting of a deficient 4-storey RC frame building. Seismic assessment is finally conducted for the retrofitted structure, where a significant enhancement of the seismic performance is observed.

Acknowledgements

Pursuing a PhD is like an itinerary with thousands of failures and only several successful milestones, and the traveller's heart fills with diligence and endeavour, stress and anxiety, sadness and tiredness on the way, but happiness when reaching the milestones. I would have never reached the end of this itinerary without the generous help and kind encouragement I have received over these years.

First of all, I'd like to express my sincere gratitude to my supervisors, Dr Lorenzo Macorini and Prof Bassam Izzuddin, for guiding me through the whole journey toward my PhD destination. Their ideas, suggestions and encouragement have made priceless contributions to my research and have inspired me to go for new topics. I would like to sincerely thank Dr Macorini for his valuable time and endless support in discussing this work with me every week and modifying the full draft. I also wish to express my heartfelt thanks to Prof Izzuddin for his excellent allocation of resources, his wealth of experience and his constructive feedback on my research, without which this work would not have been accomplished.

The financial support provided by the Skempton Scholarship of Imperial College and the Scholarship of the China Scholarship Council (CSC) is thankfully acknowledged. I want to appreciate all my colleagues in the Computational Structural Mechanics (CSM) group in 317A for providing me with helpful comments and being my lunch mates before the COVID-19 pandemic. I sincerely wish everyone in the CSM group could conquer all the convergence problems and have a bright future. I am also very grateful to all the teachers and staff I have met in Imperial College to give me sincere and generous help.

I would like to thank my family and friends most, especially my parents Ms Peng Duan and Mr Mingwen Chen, my grandparents Ms Daizhu Guan and Mr Qilu Duan, my besties Dr Yuting Liu and Dr Yuxin Zhang, for their selfless love and care during my whole lifetime. They have been talking with me overseas anytime I need encouragement and provided me with valuable emotions that support my mind and keep me sane throughout my graduate studies.

I must appreciate my cutest kitties, Taro and Rice, for being my 'colleagues' during the two working-from-home years since 2020. They have kept me company 24 hours seven days a

week and cured me with their purring when I was desperate. Thank you for trusting me, being my babies and my therapists.

Last but not least, I am deeply indebted to my partner and my last words are dedicated to you, Dr Junjie Yang. Thank you for being my comrade and my companion for both PhD and life. Thank you for being my refuge every night I was on the verge of breaking down. Thank you for your care, motivation, inspiration and understanding during all these years. And most important of all, thank you for all your love.

Contents

List of Tables

List of Figures

Notation

Abbreviations

2D,3D	Two-dimensional and three-dimensional
BRB	Buckling resistance bracing
CB	Concentric bracing
DDBD	Direct displacement-based design
DL	Damage Limitation
DOF	Degree-of-freedom
EPP	Elasto-perfectly plastic
EVD	Equivalent viscous damping
FE	Finite element
FRP	Fibre-reinforced polymer
GA	Genetic algorithm
LS	Limit State
MDOF	Multi-degree-of-freedom
MLR	Multiple linear regression
MOP	Multi-objective optimisation problem
MR	Magnetorheological
NC	Near Collapse
NSGA	Nondominated sorting genetic algorithm
RC	Reinforced concrete
RMSE	Root mean square error
SD	Significant Damage
SDOF	Single-degree-of-freedom
SOP	Single-objective optimisation problem

Symbols introduced in Chapters 3 and 4

α	Inclination angle of the tension field
β	Degradation in compression coefficient
γ	Residual strength factor at the strain reversal point
η	Shear strength deviation parameter
θ	Angle between the corner brace and the vertical direction
κ	Degree of stiffness degradation
μ	Strain-hardening parameter in tension
ρ	Effective area factor
$\boldsymbol{\Phi}$	Response characteristics vector
χ	Buckling reduction factor
$A_{c(i)}, L_{c(i)}, K_{c(i)}$	Cross-section area, length and tangent stiffness of macroelement corner (internal) spring
$\{d\}$	Deformation vector
E_d^M, E_d^S	Dissipated energy of macroelement and shell element model
E_s	Elastic stiffness/steel Young's modulus
$\{f\}$	Component force vector
f_1, f_2	Objective function
f_1', f_2'	Relative objective function
f_{tp}, f_{cp}	Yield strength in tension and compression
f_y	Steel yield strength
F_y, F_{max}, F_{res}	Yielding force, maximum force and residual force after compression unloading
$[k]$	Element tangent stiffness matrix
$[K_t]$	Global level stiffness matrix
K_{in}, K_{fin}	Stiffness in the initial and final loading cycle
L, h, t	Steel plate length, height and thickness
L_e	Element length
l_{ij}, m_{ij}, n_{ij}	Direction cosines of element local x-axis
$\boldsymbol{p}$	Optimal set

$\{R\}$	Nodal force vector
$[T_r]$	Geometric transformation matrix
$\{u\}$	Macroelement DOF vector
$\boldsymbol{W}$	Weight matrix
(X_i, Y_i, Z_i)	Global coordinates

Symbols introduced in Chapters 2, 5 and 6

δ	Steel plate drift
δ_{dr}	Inter-storey drift
δ_{et}	Target elastic displacement
δ_n	Top displacement
δ_t	Displacement demand
δ_y	Yield displacement
ζ_{eq}	Equivalent viscous damping
ζ_f	Equivalent viscous damping of frame
ζ_{hyst}	Hysteretic damping
ζ_p	Equivalent viscous damping of plate
η	Damping correction factor
$\{\theta\}$	Regression coefficients
θ_{um}	Chord rotation capacity at ultimate
$\overline{\theta}_{y,i}, \overline{\theta}_{z,i}$	Chord rotation in local y and z directions at node i
μ	Ductility factor
μ_D	Ductility demand
Γ	Transformation factor
$\{\Phi\}, \Phi_i$	Eigenmode/displacement shape
ψ_E	Combination coefficient
D_{c0}	Initial deformation capacity
D_c	Deformation capacity
D_{d0}	Initial deformation demand
D_d	Deformation demand

d_{max}	Maximum displacement
E_D	Energy dissipated by damping
E_{s0}	Maximum strain energy
F	Lateral load
F_y	Yield force
f_1, f_2, f_3	Objective function
f_1', f_2', f_3'	Relative objective function
G_k, Q_k	Characteristic value of permanent and variable action
$K_{effective}$	Effective stiffness
L, h, t	Steel plate length, height and thickness
L_{span}	Length of the retrofitted span
$[m], m_i$	Storey seismic mass
m^*	Effective mass
S_a	Acceleration in capacity spectrum
S_d	Displacement in capacity spectrum
$S_e(T)$	Elastic acceleration spectrum
sp_{typ}	Steel plate infill type
T	Period
T_e	Effective period
T_n	Natural period
V	Shear force
V_b	Base shear force
V_R	Shear resistance
$V_{y,i}, V_{z,i}$	Shear forces in y and z directions at node i
x	Design variable

Chapter 1

Introduction

1.1 Background

Numerous reinforced concrete (RC) frame buildings suffered severe damage under earthquakes in the past decades. Most of such buildings were constructed prior to the implementation of modern seismic codes and were designed without consideration of seismic action. As a result, many substandard structures located in seismic regions and still in use do not possess enough resistance and stiffness to resist lateral seismic loading and sufficient dissipation capacity to absorb the energy transferred by earthquakes.

The pressing need for enhancing the seismic performance of deficient structures has led to a growth of interest in developing effective strengthening solutions. Typical strengthening strategies for RC frame buildings are based on local measures, such as bonding and jacketing, or global intervention by adding compact RC shear walls. Effective global strengthening can also be achieved by employing supplementary steel elements, including different types of

bracing systems, which generally lead to practical design, manufacturing and installation, and to cost savings and limited disruption during the strengthening operations (Castro et al., 2018).

A relatively recent strengthening solution utilising unstiffened thin steel shear walls has shown significant potential in previous experimental and numerical research (Timler and Kulak, 1983; Driver et al., 1997; Driver et al., 1998b; De Matteis et al., 2009; Li et al., 2015). In general, the addition of steel panels provides high lateral stiffness and shear strength to a deficient frame building. Moreover, the hysteretic energy dissipation capacity can be significantly increased by the formation of a post-buckling tension field mechanism within each steel wall panel subjected to in-plane loading. Previous research showed that the complex nonlinear response of steel shear walls can be accurately predicted using nonlinear finite element (FE) models with shell elements (Choi and Park, 2010; Guo et al., 2013). However, such a detailed modelling strategy allowing for material and geometric nonlinearity is associated with significant computational demand, which hinders its use in the analysis of realistic structures under earthquake loading. Thus, simpler and more efficient models are required for representing steel shear walls within large building models when investigating the seismic performance of retrofitted structures.

Efficient simplified descriptions for steel shear panels were proposed in previous studies, where several strips or trusses are employed to simulate the panel behaviour. These models are capable of accurately predicting the initial stiffness, ultimate strength and stiffness degradation under in-plane horizontal forces (Thorburn et al., 1983; Timler and Kulak, 1983; Driver et al., 1998a; Shishkin et al., 2009). Nevertheless, most previous simplified models for steel shear panels were developed to represent the response under monotonic loading conditions, and only a few attempts have been made to analyse the behaviour under cyclic loading (Shishkin et al., 2009; Choi and Park, 2010; Berman, 2011; Guo et al., 2013; Tian et al., 2015; Driver et al., 1998a). Besides, most previous studies applied hysteresis material relationships to multi-strip models, which are nevertheless difficult to assemble and computationally expensive. This lack of efficient but accurate simplified models for steel shear walls is one of the main drivers of the research carried out in the PhD and presented in this thesis.

The effect of seismic retrofitting largely depends on section sizes and configuration arrangement of the retrofit components. However, in most previous research and practical applications, the design of these elements, at least in the initial stages, has been addressed mainly by trial-and-error methods mostly based on engineering judgement. This process lacks systematic analysis and clear implementation procedures (Park et al., 2014). Optimal seismic retrofitting design with the aid of optimisation algorithms has been developed to overcome the above limitations. Genetic algorithm (GA) is commonly used to generate optimisation solutions to engineering problems. Some previous studies on the optimal design of retrofitting measures for existing buildings considered the layout and properties of dampers or isolators (Wongprasert and Symans, 2004; Charmpis et al., 2012; Charmpis et al., 2015; Kim and An, 2016; Cha and Agrawal, 2017), the amount and location of FRP jackets (Choi et al., 2014; Park et al., 2014; Choi, 2017; Choi et al., 2017), or the design of steel buckling restrained bracing components (Farhat et al., 2009; Park et al., 2015). Nevertheless, the optimisation of steel shear walls, including the thickness and location of infill panels, is yet to be investigated. The gaps in previous research on the optimal seismic retrofitting design using steel shear walls have been considered in the developments of the second part of this research as discussed in the following section.

1.2 Aims and scopes

This research deals with the seismic retrofitting of RC framed buildings using steel shear walls. The scope of this thesis includes the development and calibration of a simplified modelling strategy for steel shear walls, and the development and application of an optimal seismic retrofitting design procedure based on GA procedures.

The first stage of this work focuses on simplified macroscale modelling for steel shear walls with the following aims:

- Development of a macroelement formulation for steel shear walls which incorporates eight nodes and six nonlinear springs;
- Determination of the asymmetric constitutive material model for the macroelement to represent the nonlinear response under cyclic loading;

- Calibration of the macroelement by inverse analysis based on the results from detailed FE models with shell elements via the nondominated sorting genetic algorithm II (NSGA-II) (Deb et al., 2002);
- Development of simple functions to determine the material parameters of the constitutive model in terms of the steel plate geometrical properties for the ease of applying the macroelement in different models.

The second stage of this research focuses on optimal design for seismic retrofitting. Steel shear walls are considered as the retrofitting technique within the proposed optimal procedure, and macroelements are used to represent the steel panels. The specific aims of this part include:

- Development of an optimal seismic retrofitting procedure based on the capacity spectrum method for RC framed structures strengthened by steel shear walls;
- Development of the GA optimisation process to enable an automatic selection for steel infill plate lengths and thicknesses, while satisfying all the seismic performance requirements in the most efficient way;
- Application of the macroelement modelling method and optimal seismic retrofitting design to a selected case study.

1.3 Outline of thesis

This thesis is composed of seven chapters. Chapter 1 introduces the research background, the aims and the thesis outline. Chapter 2 presents a critical review of the relevant literature. Current seismic assessment strategies for existing RC framed structures are first introduced. Subsequently, seismic retrofitting of unqualified structures is discussed, presenting typical retrofitting strategies and local and global intervention techniques. Special attention is paid to the use of steel shear walls, which is the selected global retrofitting strategy in this thesis, and a detailed review of previous experimental and numerical studies on steel shear walls is carried out. At the end of Chapter 2, the concept of genetic algorithm (GA) is also discussed, followed by the introduction of GA applications in optimal seismic retrofitting design.

Chapter 3 proposes a new modelling strategy for steel shear walls with a novel macroelement formulation. A constitutive model is purposely designed to represent the shear behaviour of steel shear walls under cyclic loading. The formulation and material model of the proposed macroelement are first presented. This is followed by validation of the proposed macroelement against experimental data and numerical results using shell elements. Finally, preliminary tests are carried out to identify the most critical macroelement material parameters.

Chapter 4 performs calibration for the material parameters of the macroelement constitutive model in order to find the optimal combination which guarantees accurate predictions. The calibration methodology is first described by introducing detailed FE models with shell elements that provide baseline solutions for the calibration strategy. Subsequently, the calibration procedure is applied to steel shear wall samples with various geometric configurations to find estimated relationships for each material parameter via multiple linear regression. The regression results are then verified by comparing the calibrated macroelement models against the shell element models for a representative RC frame equipped with infill shear walls with different lengths.

In Chapter 5, an optimal seismic retrofitting design approach utilising steel shear walls is proposed with the aid of GA, which regards the selection and design of the retrofitting components as a multi-objective optimisation problem with constraints. An overview of the proposed procedure is first discussed in this chapter. Then, the determination of the deformation capacity for the retrofitted frame, allowing for local and global performance, is discussed in detail. The GA process of selecting optimal solutions and nonlinear regression for equivalent viscous damping of steel shear walls are also presented.

Based on the developments in Chapter 5, the optimal design procedure for seismic retrofitting is applied to a case study in Chapter 6, which is a regular 4-storey RC frame building. A basic description of the geometric and mechanical characteristics of this building is first introduced. Then, the seismic assessment of the original substandard frame structure is discussed, including the selection of design spectrum and accelerograms and the assessment results using the capacity spectrum method. The proposed optimal seismic retrofitting design procedure is then

applied to the 2D frames in perpendicular directions, and seismic assessment is carried out for the retrofitted structure.

Finally, Chapter 7 summarises the conclusions and achievements of the research work presented in this thesis. Furthermore, it provides recommendations for future work to extend the research outcomes.

Chapter 2

Literature Review

2.1 Introduction

In earthquake-prone zones, such as the Pacific region (e.g. Japan, the US West Coast) and the Balkan and Mediterranean countries (e.g. Italy, Greece and Turkey), reinforced concrete (RC) buildings suffered severe damage under earthquakes in the past decades. Most of these structures were built prior to the implementation of modern seismic codes, and they were designed without consideration of seismic actions. Therefore, they do not possess enough resistance and stiffness to lateral seismic loading or satisfactory plastic dissipation capacity to absorb the energy transferred by earthquakes. Such inadequate seismic performance caused many casualties and substantial economic losses. This problem has led to a growth of interest in developing effective strengthening solutions to improve stiffness, strength, ductility and hysteretic energy dissipation capacity of existing structures, ultimately aiming at enhancing their seismic performance, satisfying the safety requirements defined by current seismic design codes (e.g. EN1998-3 (2005)).

In this chapter, a brief review of the literature regarding existing seismic assessment and retrofitting strategies is presented. Previous studies on the use of steel shear walls as a global retrofitting solution and advanced optimisation procedures applied to seismic retrofitting are also presented and critically discussed, as they represent key background research for this thesis. Section 2.2 first performs a detailed review of the seismic assessment of existing structures. Global and local performance requirements for seismic assessment of existing RC framed structures are listed. Afterwards, displacement-based methods for the seismic assessment of existing structures are introduced, which differ from standard force-based seismic design procedures for new buildings. Then, seismic retrofitting of unqualified structures is discussed. Typical retrofitting strategies are introduced and the selection of suitable local and global intervention techniques is addressed in Section 2.3, focusing on steel shear walls which is the retrofitting technique studied further in this research. Subsequently, a detailed review of previous experimental and numerical studies on steel shear walls is carried out in Section 2.4. Finally, background information on genetic algorithm (GA) procedures and the use of GA for optimal seismic retrofitting is also provided in Section 2.5, as such a heuristic optimisation approach is extensively used in this research.

2.2 Seismic assessment of existing structures

Eurocode 8 – 3 (EN1998-3, 2005) defines the fundamental requirements for the global performance of existing structures by introducing three Limit States (LS), which are listed as follows:

- LS of Near Collapse (NC). The structure is heavily damaged and near collapse, with low residual lateral strength and stiffness. Most non-structural components have collapsed. Large permanent drifts are present.
- LS of Significant Damage (SD). The structure is significantly damaged and near collapse, with some residual lateral strength and stiffness. Non-structural components are damaged. Moderate permanent drifts are present. The structure may be uneconomic to repair.

- LS of Damage Limitation (DL). The structure is only slightly damaged, with structural elements retaining their strength and stiffness. Non-structural components may show some damage that could be economically repaired. Permanent drifts are negligible. The structure does not need repair.

For each LS, a return period of the seismic action is selected to provide appropriate protection, which is normally considered as 2.475 years for LS of NC, 475 years for LS of SD and 225 years for LS of DL, respectively. Seismic demands are evaluated based on the design of seismic action related to the limit state.

A quantitative procedure named seismic assessment is carried out in order to check if existing buildings meet code requirements under the seismic action related to the considered limit state. According to Eurocode 8 – 3 (EN1998-3, 2005), the assessment procedure includes a few steps, the first of which is collecting information on the analysed structure and selecting seismic action and load combination. Then, the building is represented by a numerical model under seismic loading. The seismic action effect can be evaluated using different approaches: (i) linear lateral force analysis, (ii) linear response spectrum analysis, (iii) nonlinear static (pushover) analysis or (iv) nonlinear dynamic analysis. Finally, decisions are taken for structural intervention based on the assessment results. Local or global retrofitting techniques are selected and designed to strengthen deficient structures enhancing their seismic performance.

2.2.1 Seismic assessment methods

The seismic design for new buildings generally follows a force-based procedure. According to this approach, the seismic force to be resisted by structures can be calculated as a function of the fundamental period and the total mass of the structure using a design acceleration spectrum. It is determined by introducing a force-reduction factor (e.g. q-factor in Eurocode 8 – 1 (EN1998-1, 2004)), which depends on the structural type and is related to the ductility demand. Capacity design rules and structural detailing provisions are followed to guarantee that local and global ductility capacities exceed the demands.

However, the implementation of standard force-based procedures for the seismic assessment of existing substandard structures is more problematic. Ductility capacity is not known in advance, thus very low behaviour factors can be adopted leading to a very conservative assessment. Therefore, current seismic codes recommend using displacement-based design procedures which require the generation of nonlinear structural capacity curves for the analysed structure. This process requires (i) performing a nonlinear static (pushover) analysis to obtain a lateral force – displacement curve, (ii) transforming the response of the multi-degree-of-freedom (MDOF) structure into an equivalent single-degree-of-freedom (SDOF) system, and (iii) reducing the design response spectrum to the corresponding damping level (Penelis and Penelis, 2019).

Current guidelines and seismic codes propose various displacement-based design methods. Three methods are presented in the following sections, including the N2 method, the capacity spectrum method and the direct displacement-based design (DDBD) approach. The capacity spectrum method is selected in this thesis because of the easy determination of equivalent viscous damping (EVD), previous research on which will be discussed later in Section 2.2.5.

2.2.2 N2 method

The N2 method was first proposed by Fajfar and Fischinger (1988) and Fajfar and Gašperšič (1996), and then adopted in Annex B of Eurocode 8 (EN1998-1, 2004; EN1998-3, 2005) as an informative procedure. The basic steps of this method are summarised below.

Step 1. Input data

The first step concerns data collection on the analysed structure, including geometry, loading condition, material properties and steel reinforcement characteristics for the different structural components (in the case of RC structures). Suitable numerical descriptions for nonlinear structural analysis are introduced for use in the following steps, which allow material and geometric nonlinearities with specific constitutive relationships at the material cross-sectional level, as the bending moment – rotation curve depicted in Fig. 2.1(b). Besides, the elastic

(pseudo) acceleration spectrum of seismic action associated with the location of the structure and the limit state under consideration is also established.

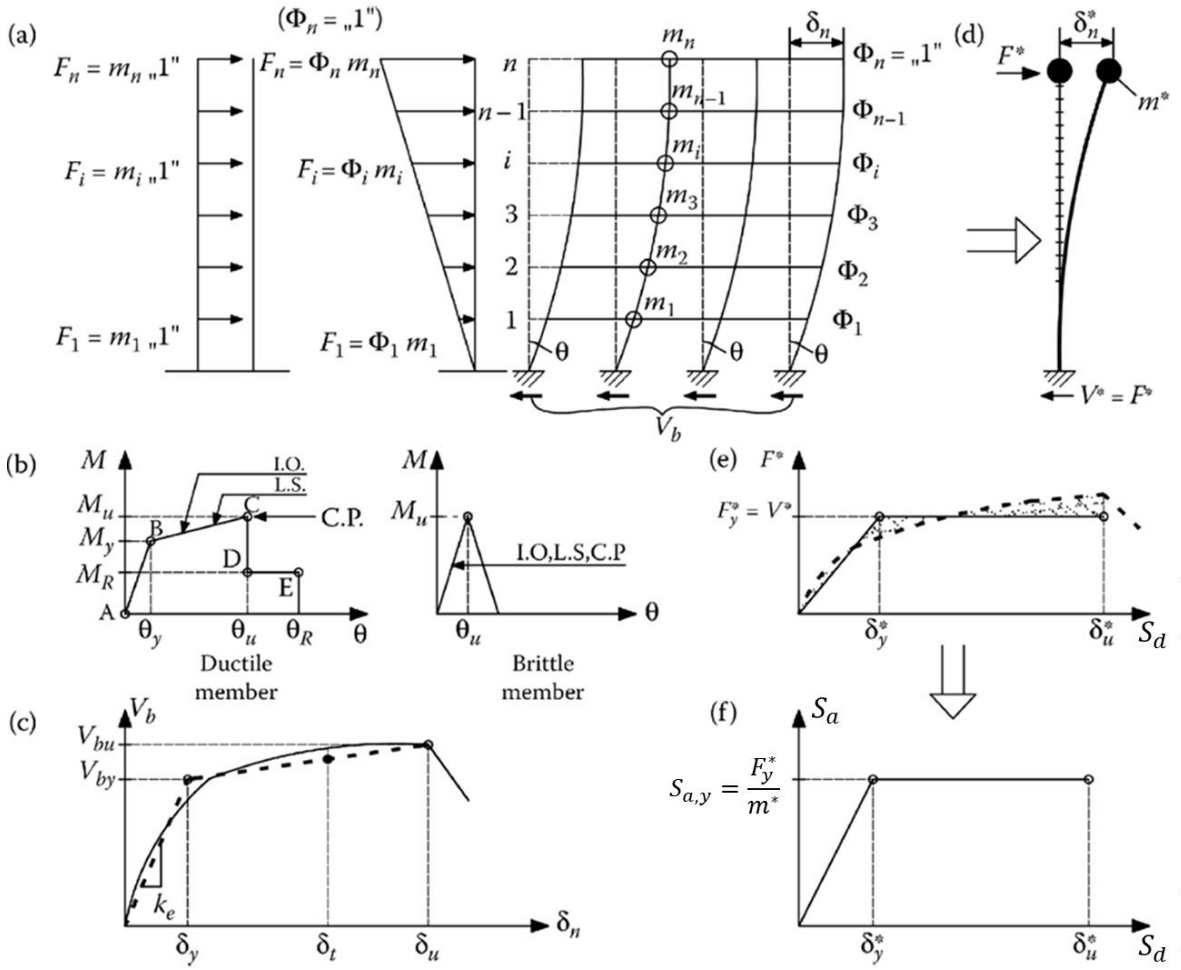

Fig. 2.1. Capacity curve transformation procedure (adapted from Penelis and Penelis (2019)):(a) Load patterns for pushover analysis of the MDOF model; (b) Input data for bending moment – member rotation curves; (c) Pushover curve of the MDOF system; (d) Equivalent SDOF model; (e) Capacity curve of the SDOF system; (f) Normalised capacity spectrum of the SDOF system

Step 2. Pushover analysis of MDOF model

Nonlinear static (pushover) analysis is then carried out for the n-storey structural system with the storey mass distribution $[m]$ and the first eigenmode $\{\Phi\}$ related to the fundamental period.

Increasing lateral loads are applied at each storey from zero values to collapse. Eurocode 8 (EN1998-1, 2004; EN1998-3, 2005) specifies two lateral load patterns for this analysis stage, as shown in Fig. 2.1(a): a 'uniform' pattern where the lateral force is proportional to the storey mass m_i; and a 'modal' pattern where the lateral load of the i-th storey is normal to the storey displacement shape Φ_i equal to

$$F_i = m_i \Phi_i \tag{2.1}$$

The base shear (V_b) – top displacement (δ_n) relationship is then determined as the pushover curve for the MDOF system (Fig. 2.1(c)).

Step 3. Transformation to equivalent SDOF model

As shown in Fig. 2.1(d) ~ (f), the pushover curve of the MDOF model is then transformed to the capacity spectrum of an equivalent SDOF model with the mass determined by

$$m^* = \sum m_i \Phi_i \tag{2.2}$$

The force and displacement of the SDOF system are calculated as

$$V^* = \frac{V_b}{\Gamma} \tag{2.3}$$

$$S_d = \frac{\delta_n}{\Gamma} \tag{2.4}$$

where Γ is the transformation factor which can be computed as

$$\Gamma = \frac{\sum m_i \Phi_i}{\sum m_i {\Phi_i}^2}$$

Afterwards, the pushover (F^*– δ^*) curve of the SDOF model is idealised as an elasto-perfectly plastic (EPP) diagram, as shown in Fig. 2.1(e). The fundamental period of this SDOF model is defined by

$$T^* = 2\pi\sqrt{\frac{m^*\delta_y{}^*}{F_y{}^*}} \tag{2.5}$$

where $\delta_y{}^*$ and $F_y{}^*$ are the yield displacement and yield force of the idealised SDOF system, respectively.

The EPP force – displacement relationship is then normalised in terms of acceleration as

$$S_a = \frac{V^*}{m^*} \tag{2.6}$$

The resultant S_a– S_d curve in Fig. 2.1(f) is the capacity spectrum of the equivalent SDOF model.

Step 4. Demand spectrum

The demand spectrum is in the pseudo acceleration – spectral displacement format and is transformed from the standard acceleration – period format by the equation

$$S_d = \frac{T^2}{4\pi^2}S_a \tag{2.7}$$

Fig. 2.2 plots the demand spectra for different ductility values in two formats.

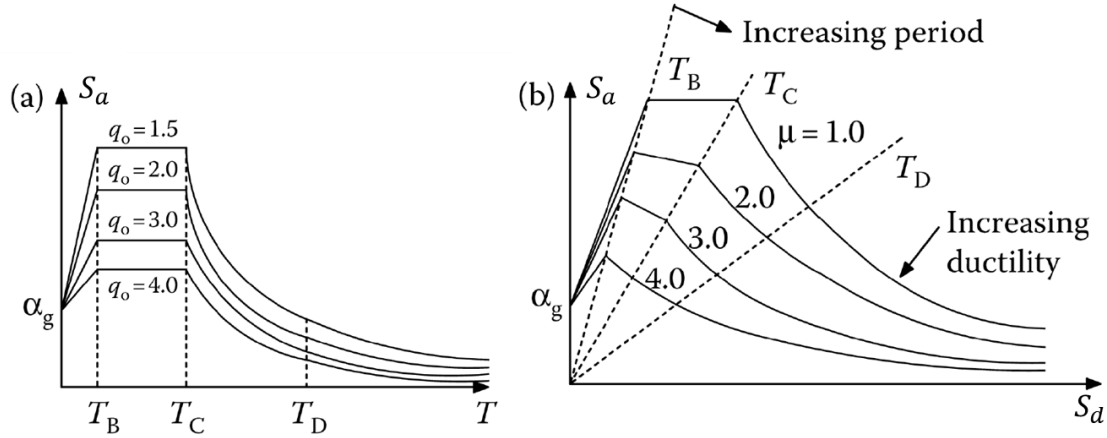

Fig. 2.2. Demand spectra for different ductility values adapted from Penelis and Penelis (2019): (a) Standard format in relation to period; (b) Acceleration – displacement format

Step 5. Seismic demand for SDOF model

Given the capacity spectrum and the elastic acceleration spectrum $S_e(T)$, the target displacement of the structure with period T^* and unlimited elastic behaviour can be determined by

$$\delta_{et}{}^* = S_e(T^*)\left[\frac{T^*}{2\pi}\right]^2 \tag{2.8}$$

For the calculation of the seismic demand, i.e. target displacement, for the SDOF system with inelastic behaviour, two expressions are adopted considering the structural period range in comparison with the corner period T_C, as illustrated in Fig. 2.3. For the short period range where $T^* < T_C$ and $F_y{}^*/m^* < S_e(T^*)$, the displacement demand is defined as

$$\delta_t{}^* = \frac{\delta_{et}{}^*}{q_u}\left(1 + (q_u - 1)\frac{T_C}{T^*}\right) \geq \delta_{et}{}^* \tag{2.9}$$

where $q_u = S_e(T^*)/\left(F_y{}^*/m^*\right)$.

On the other hand, for the short period range where $T^* < T_C$ and $F_y{}^*/m^* \geq S_e(T^*)$, and for the medium and long period range where $T^* \geq T_C$, the displacement demand for these two cases is

$$\delta_t{}^* = \delta_{et}{}^* \tag{2.10}$$

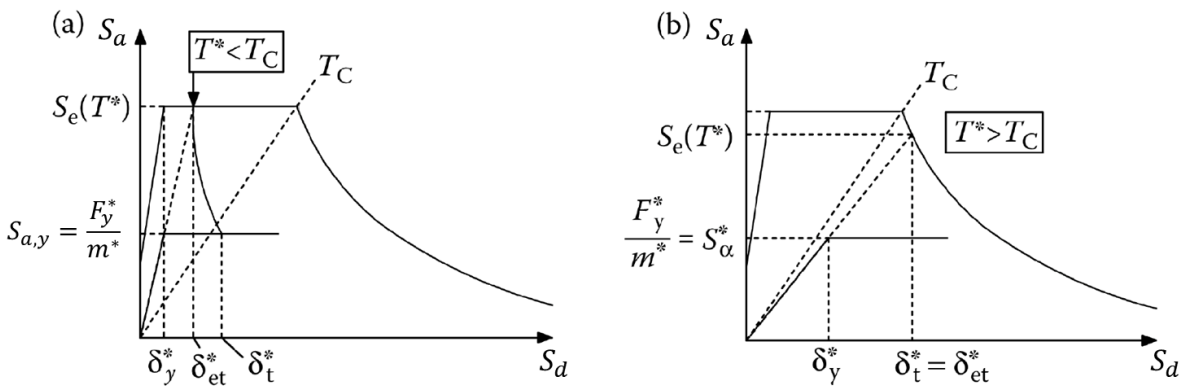

Fig. 2.3. Displacement demand for SDOF model adapted from Penelis and Penelis (2019): (a) Short period; (b) Medium and long period

Step 6. Global seismic demand for MDOF model

The seismic demand $\delta_t{}^*$ of the SDOF model is transformed to the top displacement δ_n of the MDOF model by the equation below:

$$\delta_n = \Gamma \delta_t{}^* \tag{2.11}$$

Step 7. Local seismic demand

The local deformation quantities, such as element rotations and storey drifts, and the local strength demands are determined by the pushover analysis of the MDOF system up to the displacement demand.

2.2.3 Capacity spectrum method

The capacity spectrum method is a procedure that compares the structural capacity curves to the response spectra representations of the seismic demand. It was adopted by the Applied Technology Council (ATC) in the guideline ATC-40 for seismic evaluation and retrofit of existing concrete buildings (ATC, 1996; Freeman, 2004). This method includes the following steps.

Step 1. Pushover analysis of MDOF model

This step is the same as Step 2 of the previous section.

Step 2. Transformation to equivalent SDOF model

The pushover curve of the MDOF model is transformed into the capacity spectrum of the equivalent SDOF model, following the procedure described in Step 3 of the previous section. Nevertheless, differences are noted comparing the two methods. First, the equivalent model mass is defined differently. This also affects the equations for S_a and S_d, which will be shown in Chapter 5. Besides, the pushover curve of the SDOF model is not transformed into an EPP curve in this method, resulting in a nonlinear capacity spectrum.

Step 3. Demand spectrum

The elastic demand spectrum in relation to displacement is transformed from the standard format in the same manner as in the previous section. Fig. 2.4 shows the demand spectra in the displacement format, each curve for a different damping ratio within the range between 5% (linearly elastic damping) and 30%.

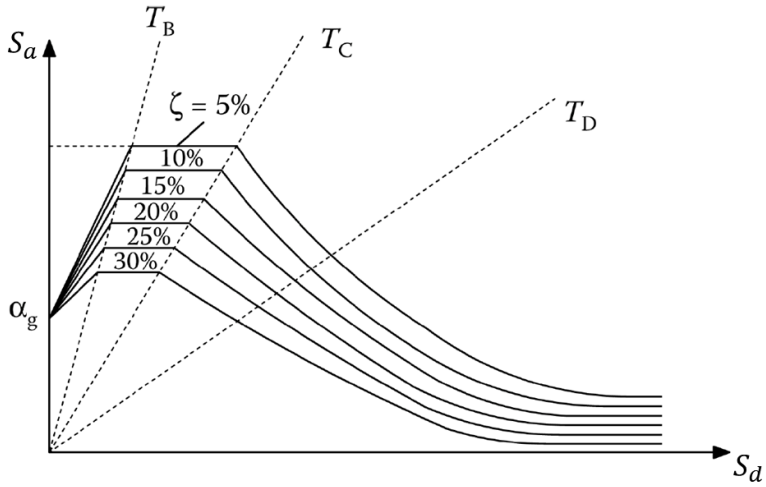

Fig. 2.4. Demand spectra with different damping ratios adapted from Penelis and Penelis (2019)

When reducing the elastic spectrum for the SDOF system, the EVD is considered, which is equal to a combination of damping ratio in the linearly elastic range (0.05) and hysteretic damping ζ_{hyst}:

$$\zeta_{eq} = 0.05 + \zeta_{hyst}$$
$$\zeta_{hyst} = \frac{1}{4\pi}\frac{E_D}{E_{s0}} \tag{2.12}$$

where E_D is the energy dissipated by damping and corresponds to the area enclosed by the hysteresis loop; $E_{s0} = K_{effective}{d_{pl}}^2/2$ is the strain energy with stiffness $K_{effective}$, as shown in Fig. 5.10. Literature for the equations of the hysteretic damping will be discussed later in Section 2.2.5.

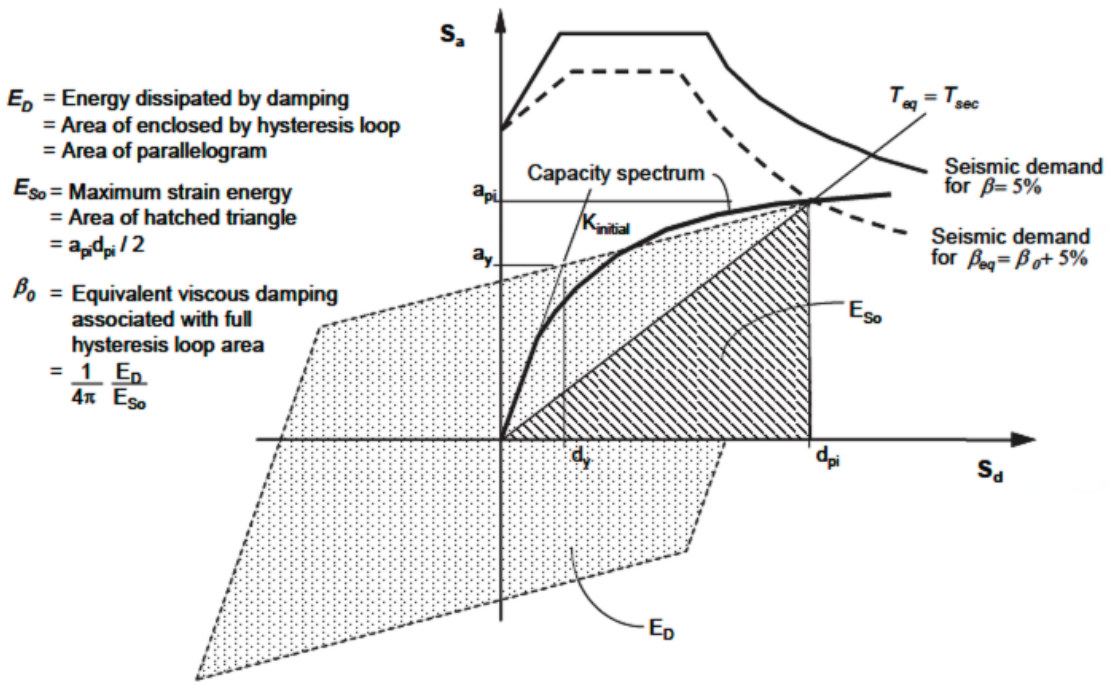

Fig. 2.5. Derivation of damping for spectral reduction (Security and Agency, 2013; ATC, 1996)

Step 4. Seismic demand for SDOF model

The capacity spectrum and the elastic demand spectrum are then plotted in the same graph. However, the intersection of two curves may not be the actual displacement demand because the damping of the demand spectrum can be different from the actual damping calculated by the intersected displacement. Therefore, ATC-40 suggests an iterative calculation to find the performance point, as illustrated in Fig. 2.6. This procedure starts from the estimated performance point using the elastic demand spectrum with 5% damping. Then the equivalent damping ratio is calculated with the plastic displacement equal to $S_{d,es}$. The reduced demand spectrum is developed accordingly, which intersects the capacity spectrum at the trial performance point $S_{d,tr}$. If $(S_{d,tr} - S_{d,es})/S_{d,tr} \leq$ tolerance, then the seismic demand of the SDOF model is taken as $S_{d,tr}$. Otherwise, iteration is needed until convergence (ATC, 1996; Chopra and Goel, 1999; Jing et al., 2011).

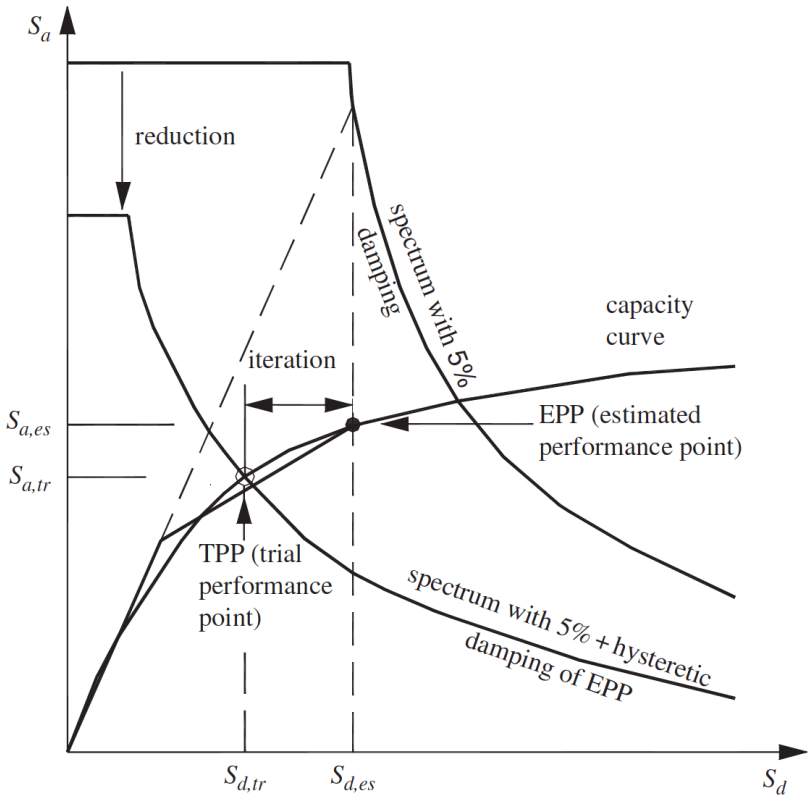

Fig. 2.6. Illustration of the iterative procedure to search for the performance point (Jing et al., 2011)

The steps for determining global seismic demand for the MDOF model and local seismic demands are the same as those in the previous section.

2.2.4 Direct displacement-based design (DDBD)

DDBD is developed to mitigate the deficiencies associated with the current force-based design, such as the inaccurate estimation of the initial stiffness and fundamental period. This method is presented in detail by Priestley et al. (2007). The displacement-based design considers the performance of an equivalent SDOF system at peak displacement rather than the initial elastic performance, which represents a key difference compared to force-based methods.

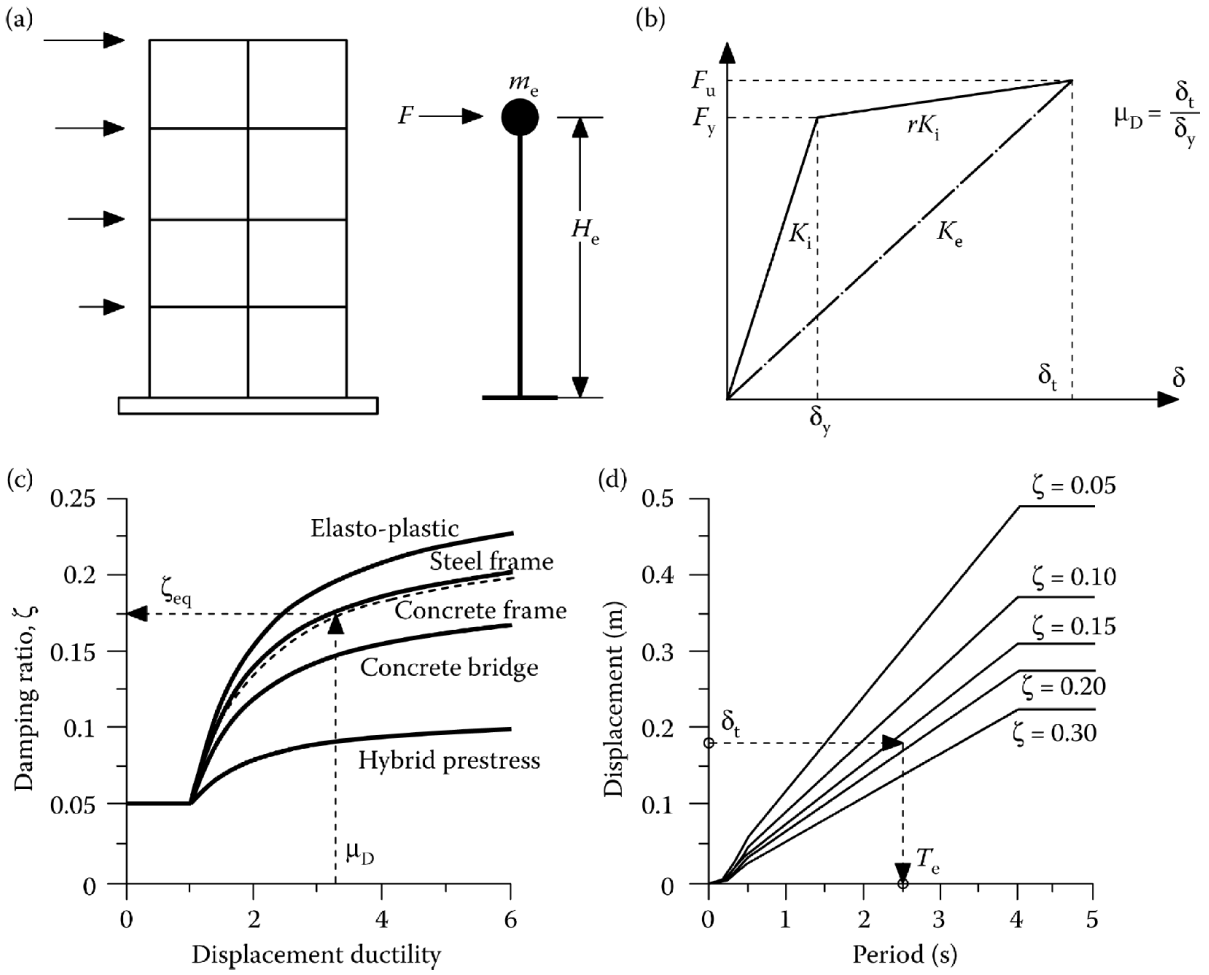

Fig. 2.7. Fundamentals of DDBD: (a) SDOF simulation; (b) Force – displacement response of the SDOF model; (c) Relationships between equivalent damping and ductility; (d) Design displacement spectra (Priestley et al., 2007; Penelis and Penelis, 2019)

Fig. 2.7 illustrates the fundamentals of the DDBD method. In the initial step, the analysed structure is represented as an SDOF model, as shown in Fig. 2.7(a). The lateral force – displacement response of the SDOF model is assumed as a bilinear curve with a predefined displacement demand δ_t (Fig. 2.7(b)), thus the ductility demand μ_D can be calculated. Based on the relationships between the equivalent damping ratio and the ductility, as shown in Fig. 2.7(c), the damping ratio ζ_{eq} is found for the ductility demand μ_D. The corresponding effective period T_e is then determined for the predefined δ_t and ζ_{eq} using the design displacement spectra in Fig. 2.7(d). Since the effective stiffness of the SDOF model can be obtained by

$$K_e = \frac{4\pi^2 m^*}{T_e^2} \tag{2.13}$$

the SDOF base shear is directly computed as

$$V_b = K_e \delta_t \tag{2.14}$$

Afterwards, V_b of the SDOF model is transformed into the base shear of the MDOF model, and distributed to the mass elements as inertial forces. The structure is then analysed and designed under this loading condition.

2.2.5 Estimation of hysteretic damping

Previous studies were conducted to estimate the EVD of structural components and systems, where the hysteretic part ζ_{hyst} of the EVD generally depends on the main features of the cyclic hysteresis response (Fig. 2.8) and the ductility of the system (Priestley et al., 2007). Dwairi et al. (2007) put forward a simple relationship for the hysteretic damping as

$$\zeta_{hyst} = C \cdot \left(\frac{\mu - 1}{\mu\pi}\right) \tag{2.15}$$

where μ is the ductility factor; C is a factor depending on the hysteresis rule which is assumed as 2 for elastic-perfectly plastic (EPP) components.

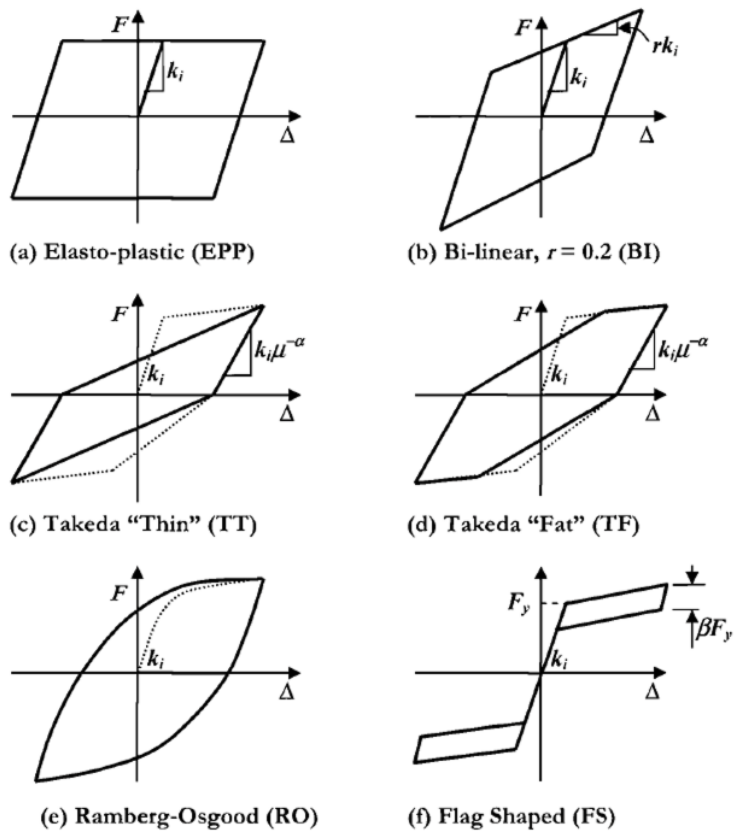

Fig. 2.8. Hysteresis rules considered in inelastic time-history analysis (Priestley et al., 2007)

Grant et al. (2005) provided a more complex equation for the hysteretic damping as

$$\zeta_{hyst} = a\left(1 - \frac{1}{\mu^b}\right)\left(1 + \frac{1}{(T_e + c)^d}\right) \tag{2.16}$$

where T_e is the effective period; the coefficients a, b, c and d vary for different hysteresis rules, In the case of EPP components, the coefficients are taken as $a = 0.224, b = 0.336, c = -0.002, d = 0.250$. Priestley et al. (2007) also introduced equations for ζ_{hyst} based on experimental results for different structural types. For an EPP system, the hysteresis damping value is estimated as

$$\zeta_{hyst,EPP} = 0.670 \cdot \left(\frac{\mu - 1}{\mu\pi}\right) \tag{2.17}$$

which tends to be more conservative compared with other works (Amadio et al., 2016)

FEMA-440 (Security and Agency, 2013) provided an improved procedure based on a modification of the capacity spectrum method with new equations for hysteresis damping. Corrective factors are introduced for the damping ratio considering the ductility level and the ratio between the effective period T_{eff} and the natural period T_0 of the system:

$$For\ 1.0 < \mu < 4.0: \quad \zeta_{hyst} = A(\mu - 1)^2 + B(\mu - 1)^3 \tag{2.18}$$

$$For\ 4.0 \leq \mu \leq 6.5: \quad \zeta_{hyst} = C + D(\mu - 1) \tag{2.19}$$

$$For\ \mu > 6.5: \quad \zeta_{hyst} = E\left[\frac{F(\mu-1)-1}{[F(\mu-1)]^2}\right]\left(\frac{T_{eff}}{T_0}\right)^2 \tag{2.20}$$

Coefficient values are provided for different bilinear and stiffness degrading inelastic behaviours with various post-elastic stiffness ratios. For an EPP system (bilinear behaviour with zero post-elastic stiffness), the coefficients are taken as $A = 3.2,\ B = -0.66,\ C = 11,\ D = 0.12,\ E = 19,\ F = 0.73$.

Table 2.1 compares the hysteretic damping ratios of an EPP system with three ductility values $\mu = 3, 5, 10$ based on the equations provided in the literature above. A significant difference can be observed from the data for all the ductility values.

Table 2.1. Comparison for hysteretic damping ratios with different ductility in literature

Ductility μ	Dwairi	Grant	Priestley	FEMA-440
3	0.4244	0.1661	0.1422	0.0752
5	0.5093	0.2176	0.1706	0.1148
10	0.5730	0.2700	0.1919	0.1122

2.2.6 Local requirements for structural members

When performing nonlinear static or dynamic analysis for structural assessment, local safety verifications need to be carried out by checking ductile and brittle mechanisms at structural member levels. Eurocode 8 – 3 (EN1998-3, 2005) classifies as 'ductile' failure mechanisms under flexure of beams and columns, and as 'brittle' mechanisms due to shear failure. To the extent of this thesis, capacity values for ductile and brittle mechanisms are provided only for LS of NC.

For the ductile mechanism under flexure loading, the deformation capacity of beams and columns is verified by checking the limit value of chord rotation, which is defined as the angle between the tangent to the axis at the yielding end and the chord connecting that end to the shear span end, i.e., the point of contraflexure. The ultimate chord rotation capacity of concrete beams and columns can be calculated from the empirical equation below (EN1998-3, 2005):

$$\theta_{um} = \frac{1}{\gamma_{el}} 0.016 \cdot (0.3^{\nu}) \left[\frac{max(0.01;\omega')}{max(0.01;\omega)} f_c\right]^{0.225} \cdot \left(min\left(9;\frac{L_V}{h}\right)\right)^{0.35} 25^{\left(\alpha\rho_{sx}\frac{f_{yw}}{f_c}\right)} (1.25^{100\rho_d}) \tag{2.21}$$

where γ_{el} is equal to 1.5 for primary seismic elements and to 1.0 for secondary seismic elements;

h is the cross-section depth;

$L_V = M/V$ is the shear span, which is equal to the ratio moment/shear at the end section;

$\nu = N/bhf_c$, where b is the width of the compression zone and N is the axial force (positive for compression);

$\omega = A_s f_{yw}/A_c f_c$, $\omega' = A'_s f_{yw}/A_c f_c$ are the mechanical reinforcement ratios of the tension and compression longitudinal reinforcement, respectively;

f_c and f_{yw} are the concrete compressive strength (MPa) and the stirrup yield strength (MPa);

$\rho_{sx} = A_{sx}/b_w s_h$ is the ratio of transverse steel parallel to the direction x of loading (s_h is the stirrup spacing);

ρ_d is the steel ratio of diagonal reinforcement (if any), in each diagonal direction;

α is the confinement effectiveness factor equal to:

$$\alpha = \left(1 - \frac{s_h}{2b_0}\right)\left(1 - \frac{s_h}{2h_0}\right)\left(1 - \frac{\sum b_i^2}{6h_0 b_0}\right) \tag{2.22}$$

where b_0 and h_0 are the dimensions of the confined core to the centerline of the loop; and b_i is centerline spacing of longitudinal bars (indexed by i) laterally restrained by a stirrup corner or a cross-tie along the perimeter of the cross-section.

For the brittle mechanism under shear, the expression below is used to predict the shear resistance (EN1998-3, 2005):

$$V_R = \frac{1}{\gamma_{el}}\left[\frac{h-x}{2L_v} min(N; 0.55A_c f_c) + \left(1 - 0.05\, min\left(5; \mu_\Delta^{pl}\right)\right)\right] \cdot \left[0.16\, max(0.5; 100\rho_{tot})\left(1 - 0.16\, min\left(5; \frac{L_V}{h}\right)\right)\sqrt{f_c}A_c + V_w\right] \tag{2.23}$$

where γ_{el} is equal to 1.15 for primary seismic elements and to 1.0 for secondary seismic elements;

h is the depth of cross-section;

x is the compression zone depth, which can be taken as $0.2d$ for simplicity;

N is the compressive axial force (positive, taken as being zero for tension);

$L_V = M/V$ is the ratio moment/shear at the end section;

A_c is the cross-section area, taken as being equal to $b_w d$ for cross-sections with rectangular web of width (thickness) b_w and structural depth d;

f_c is the concrete compressive strength;

μ_Δ^{pl} is the plastic ductility factor, which is calculated as the ratio of the plastic part of chord rotation normalised to the chord rotation at yielding;

ρ_{tot} is the total longitudinal reinforcement ratio;

V_w is the contribution of transverse reinforcement to shear resistance, given by the following equation for cross-sections with rectangular web of width (thickness) b_w:

$$V_w = \rho_w b_w z f_{yw} \tag{2.24}$$

where ρ_w is the transverse reinforcement ratio;

z is the length of the internal lever arm, taken as $d - d'$ in beams and columns, d and d' are the depths to the tension and compression reinforcement, respectively;

f_{yw} is the yield strength of the transverse reinforcement.

2.3 Seismic retrofitting of existing RC framed structures

After the quantitative seismic evaluation, retrofitting of substandard structures needs to be carried out to repair local members with deficiencies or damages and enhance the global seismic performance. In this section, a review of typical retrofit techniques, including local and global interventions for existing RC framed buildings is provided.

2.3.1 Retrofit strategies

Typical retrofit strategies

Retrofit strategies are adopted to address deficiencies of existing structures, the aims of which are (i) to recover original structural performance, (ii) to upgrade the performance leading to strength, stiffness or ductility enhancements, or (iii) to mitigate the seismic response of the original structure (Thermou and Elnashai, 2006; Sugano, 1996). The following strategies are typically employed to reduce earthquake vulnerability (ASCE, 2013):

- Local modification of components. This strategy includes local strengthening and local remedial. The former improves inadequate components or connections without affecting the overall seismic response, whereas the latter modifies the ductility or flexibility of the component.
- Removal or reduction of existing irregularities. Stiffness, mass and strength irregularities may be detected, reduced or removed to improve the seismic response.
- Global structural stiffening. This strategy is suitable for structures with deficiencies due to excessive lateral deflections, while critical components lack adequate ductility under the resultant deformations.
- Global structural strengthening. For structures with global deficiencies in structural strength, the global structural strengthening strategy is appropriate, which provides supplementary strength by means of adding shear walls or bracing systems.
- Mass reduction. If the seismic deficiencies are attributed to excessive structural mass and reduced global structural stiffness, mass reduction can reduce both strength and deformation seismic demands. As a result, this strategy can be used instead of strengthening and stiffening strategies to improve the seismic response.
- Seismic isolation. If contents and non-structural components of the retrofitted structure need protection from damage, compliant bearings can be inserted above the foundation, providing seismic isolation from the ground motion.

- Supplemental energy dissipation. This strategy applies special devices, which provide additional energy dissipation, to deficient structures experiencing excessive deformations under earthquake loading. These devices are capable of dissipating a substantial amount of the energy transferred by earthquakes in a controlled manner, generally leading to a significant reduction of the displacement demand to the existing structure.

Selection of retrofit strategies

When selecting a proper retrofit strategy, both socio-economic and technical issues should be considered. From a socio-economic point of view, the cost relative to the importance of the structure, workmanship availability, the level of quality control, the duration of the retrofit procedure, and the disruption of normal function to the occupants should all be considered. From a technical perspective, the selection is on the basis of structural compatibility with the existing system, the availability of the repair materials and technology, the damage control of non-structural components, the suitability and condition of the foundation system, and the presence of structural irregularities (Thermou and Elnashai, 2006).

Baros and Dritsos (2008) proposed a simplified procedure based on estimating the capacity curve of the initial structure, which allows comparisons among retrofit strategies to select an effective solution for an existing RC building. Retrofit strategies were divided into Groups A, B and C, which are associated with improved overall ductility, higher strength and stiffness, and improved strength, stiffness and ductility, respectively (Fig. 2.9).

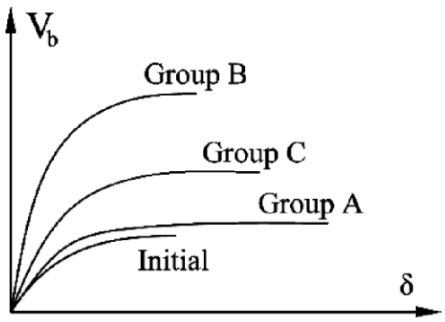

Fig. 2.9. Capacity curves representing the variation of base shear V_b against the roof lateral displacement δ of initial and retrofitted structures (Baros and Dritsos, 2008)

The pushover curves of three groups of retrofit strategies are converted to the estimated capacity spectra via the inelastic demand spectrum method. The force-displacement relationship of an MDOF system representing the original structure is converted into a bilinear capacity spectrum of the equivalent SDOF system. The capacity spectrum is then compared with both elastic and inelastic seismic demand spectra, providing an estimation of the extent of the structural deficiency. After that, the estimated bilinear capacity spectrum for Group A, B and C strategies can be determined with the assumptions of increasing overall ductility, strength or stiffness to the required performance point, as shown in Fig. 2.10.

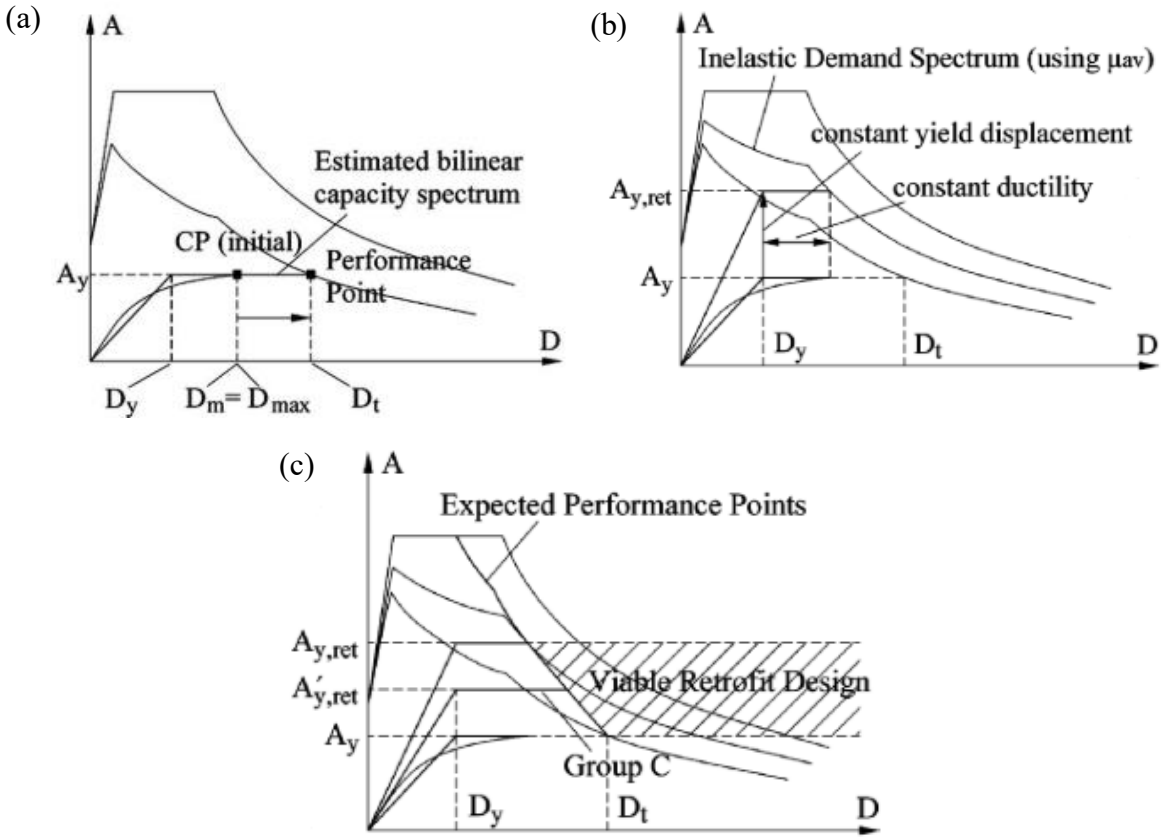

Fig. 2.10. Estimated capacity spectra for different group strategies: (a) Group A; (b) Group B; (c) Group C (Baros and Dritsos, 2008)

The proposed procedure included three steps. The seismic response of the original structure is first predicted using nonlinear static analysis in order to define the base shear – roof displacement relationship. Then the pushover curve is transformed into a capacity spectrum and compared with the estimated spectra of available retrofit strategies. The last step considers

the preliminary design of the selected intervention. Two ratios are explicitly defined to quantify the required increase in ductility and strength, respectively:

$$\lambda_D = \frac{\mu_{req}}{\mu_{av}} \tag{2.25}$$

$$\lambda_S = \frac{V_{b,ret}}{V_{b,av}} \tag{2.26}$$

where μ_{req} is the ductility demand factor, μ_{av} is the available ductility factor, $V_{b,ret}$ is the base shear of the retrofitted structure and $V_{b,av}$ is the available base shear of the initial structure. Based on the two ratios, Table 2.2 indicates the selection of suitable retrofit strategies (Group A, B, or C) for the existing RC building.

Table 2.2. Proposed selection of retrofit strategies for low, medium and high drift values (Baros and Dritsos, 2008)

Low drift value: drift (%) < 0.3 × maximum drift					
Strength Ratio λ_S	Ductility Ratio λ_D				
	$\lambda_D < 1.0$	$1.0 < \lambda_D < 1.4$	$1.4 < \lambda_D < 1.8$	$1.8 < \lambda_D < 2.5$	$2.5 < \lambda_D < 4.5$
$\lambda_S < 1.0$	No or light local intervention				
$1.0 < \lambda_S < 1.4$		A	A or C	B or C	B
$1.4 < \lambda_S < 1.7$		A	C	B or C	B or C
$1.7 < \lambda_S < 2.0$		A	C	B or C	C
$2.0 < \lambda_S < 3.0$		A or C	A or C	C	Rebuild
Medium drift value: 0.3 × maximum drift< drift (%) < 0.7 × maximum drift					
Strength Ratio λ_S	Ductility Ratio λ_D				
	$\lambda_D < 1.0$	$1.0 < \lambda_D < 1.4$	$1.4 < \lambda_D < 1.8$	$1.8 < \lambda_D < 2.5$	$2.5 < \lambda_D < 4.5$
$\lambda_S < 1.0$	No or light local intervention				
$1.0 < \lambda_S < 1.4$		A	C	B	B
$1.4 < \lambda_S < 1.7$		A or C	A or C	B	B
$1.7 < \lambda_S < 2.0$		A or C	A or C	B	B
$2.0 < \lambda_S < 3.0$		C	A	B	Rebuild
High drift value: drift (%) > 0.7 × maximum drift					
Strength Ratio λ_S	Ductility Ratio λ_D				
	$\lambda_D < 1.0$	$1.0 < \lambda_D < 1.4$	$1.4 < \lambda_D < 1.8$	$1.8 < \lambda_D < 2.5$	$2.5 < \lambda_D < 4.5$
$\lambda_S < 1.0$	No or light local intervention				
$1.0 < \lambda_S < 1.4$		A or C	C	B	B
$1.4 < \lambda_S < 1.7$		A or C	B or C	B	B
$1.7 < \lambda_S < 2.0$		A or C	B	B	B
$2.0 < \lambda_S < 3.0$		A or C	B	B	Rebuild

2.3.2 Retrofit techniques

Local intervention

Local interventions aim to enhance the ductility and strength of deficient components and improve their performance under earthquakes. Externally bonded FRP and RC jacketing are usually adopted for this purpose.

FRP is a relatively new material used in seismic retrofitting to increase the resistance and deformation capacity of flexural plastic hinges, and to improve the shear resistance of the components. FRP can be made of carbon (CFRP), glass (GFRP) or aramid (AFRP). Despite the high price per unit, FRP possesses a high strength-to-weight ratio. It guarantees reversibility of the application and good resistance to corrosion. In addition, the application of FRP elements is relatively simple, causing little disruption to the normal function of the retrofitted structures. These characteristics provide FRP with an advantage over other techniques, especially for the retrofit of cultural heritage or historic buildings (Fardis, 2009). Concerning the mechanical response, FRP has a linear elastic behaviour to failure without significant yielding or plastic deformation. Besides, some fibres of FRP are anisotropic in the aspects of strength and thermal expansion in the longitudinal and transverse directions. It may cause bond splitting of concrete, which should be considered during the application (Thermou and Elnashai, 2006).

RC jacketing is an alternative and popular seismic retrofit technique. It is the most suitable and cost-effective choice for strengthening severed damaged RC components. Besides, RC jacketing is the only technique to improve stiffness, shear strength, deformation capacity, moment resistance and reinforcement anchorage of RC members at the same time, and this multiple effectiveness distinguishes it from the other local intervention techniques. However, RC jacketing has certain drawbacks, including a considerable increase in the cross-section areas of RC components, which means a great loss in space and floor area, and a long disruption of occupancy (Fardis, 2009). It is worth noting that RC jacketing is considered as a local intervention only when the longitudinal reinforcement in the jacket is interrupted at the storey level, whereas it is counted as a global intervention technique if the reinforcement passes through the slab.

Global intervention

Global intervention techniques are selected for the RC buildings with high flexibility or without available transverse load paths. The most commonly used techniques include the addition of RC shear walls, metal shear panels, steel braces, dampers or isolators.

Adding RC shear walls is one of the most typical global intervention techniques for increasing the lateral stiffness and strength of existing RC framed structures. This intervention technique is usually introduced to RC structures through fully infilling selected bays of the existing frames with cast-in-place RC walls or pre-cast panels, and the added walls incorporate the surrounded frame members acting as boundary elements. RC shear walls are designed to develop substantial plastic deformations at their base. As a consequence, the cross-sections throughout the height should possess adequate shear capacity, and the parts above the plastic hinge region at the base should remain elastic in flexure. The introduction of RC shear walls substantially reduces the lateral drift under seismic loading and prevents structural damage. However, adding RC shear walls increases the overturning moment at the foundation level significantly. Because of the foundation enhancement cost, this global intervention technique is not suitable for existing structures with an insufficient foundation system (Thermou and Elnashai, 2006).

Metal shear panels, which experience large plastic deformations under earthquakes, are utilised as energy dissipative systems for seismic enhancement. Compared with RC shear walls, these devices have a number of advantages, including reduced self-weight, limited space occupation, the ease of construction and significant improvement in structural stiffness, lateral strength and energy dissipation capacity (Formisano et al., 2010). Unstiffened thin infill panels are inserted into a boundary supporting frame and connected to RC structures through steel boundary elements, as shown in Fig. 2.11. The panels are designed to buckle under small shear loads and then experience tension field action, resisting the lateral forces and dissipating the input energy through yielding of the panels in tension. Steel shear panels are the most typical kind of shear panels. Li et al. (2015) tested the thin steel panel performance and studied the effects of perforations by performing cyclic tests on both solid and perforated panels. The test results confirmed that thin steel shear panels improve lateral resistance, initial stiffness, and ductility.

In the tests, it was shown that the shear capacity of the perforated panels decreases by only around 25% in comparison with solid panels with the same thickness. Previous research investigated the seismic response of RC frames retrofitted with steel and aluminium panels (Formisano, 2007; Formisano et al., 2008; Mazzolani, 2008; De Matteis et al., 2009; Formisano et al., 2010). The preliminary design of both shear panels was first carried out based on experimental and numerical results of the bare RC frame. Numerical models of the retrofitted structure were then developed and used to evaluate the lateral resistance of the proposed shear panels. Experimental cyclic tests were performed on the full-scale RC frame with either steel or aluminium shear panels. The experimental results indicate that steel shear panels provide a superior enhancement in terms of strength and stiffness, whereas the aluminium ones improve the energy dissipation capacity more significantly.

Fig. 2.11. Example of an RC frame retrofitted with steel infill panels (Formisano et al., 2008)

Steel bracing system is another common technique for the seismic design of new buildings. It is also effective for global seismic retrofitting with the advantages of high lateral load resistance, relatively lightweight added to the original structures and easy arrangement for openings (Thermou and Elnashai, 2006). This technique for retrofitting RC frame structures usually employs concentric bracing (CB) or buckling resistance bracing (BRB). Both experimental and numerical research on seismic retrofitting of RC frames using the CB system showed that CB significantly increases the initial stiffness and ultimate strength, improves the seismic

performance and dissipates seismic energy via yielding in tension. However, buckling of the braces in compression might develop under cyclic loading, and the connections between CB and RC frames should be cautiously designed (Badoux and Jirsa, 1990; Bush et al., 1991; Masri and Goel, 1996; Abou-Elfath and Ghobarah, 2000). Concentric X-bracing configurations were studied through detailed numerical models. The results of nonlinear time-history analyses under earthquake loading showed that bracing configuration has an influence on the overall seismic response, the corresponding stress distribution in RC components and the amount of load transferred to foundations (Faella et al., 2014). Aiming to overcome the buckling of CB and provide larger energy dissipation capacity, BRBs with various cross-sections (Fig. 2.12) were developed. In general, they consist of a steel core resisting lateral loads and an external jacket restraining the buckling of the steel core (Abou-Elfath et al., 2017). Researchers have investigated the behaviour of existing RC structures retrofitted with BRB and indicated its effectiveness to enhance the seismic performance (Della Corte et al., 2015; Bai and Ou, 2016; Pan et al., 2016; Abou-Elfath et al., 2017). However, European standards still lack BRB design guidelines. Further studies about a simplified preliminary design for seismic retrofitting using BRB are still needed (Almeida et al., 2017).

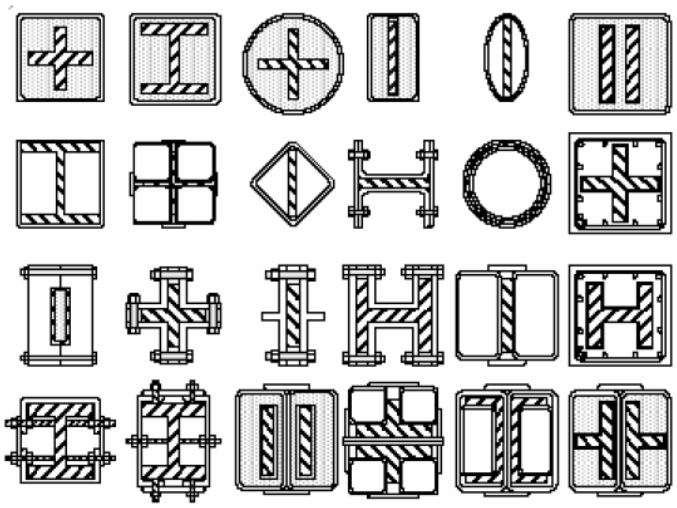

Fig. 2.12. Typical cross-sections of BRBs (Tsai et al., 2004)

Damping system is one commonly-used passive energy dissipation technique for seismic retrofitting, which includes viscous fluid dampers, viscoelastic solid dampers, friction dampers, metallic dampers, tuned mass or tuned liquid dampers, and semiactive dampers. The damping

system is adopted to decrease inelastic deformations of components and control seismic drifts of structures. Dampers are usually applied to the frame by connecting braces, resulting in hysteretic behaviour under cyclic loading (Symans et al., 2008).

Seismic isolators are the most suitable technique for the retrofit of critical structures and historic buildings, facilities with valuable contents and structures requiring higher performance levels. Isolation devices are commonly inserted at the top of the foundations or the first-storey columns, which can significantly reduce the earthquake damage to the structural and non-structural components. Nevertheless, the application of isolators is quite complex, which includes connecting all the columns above the isolators, cutting the structural components, temporarily supporting the whole above structure, adding the isolators at the top of foundations or columns and then releasing the above weight to the columns, meanwhile avoiding any damage to the structure (Thermou and Elnashai, 2006). In order to extend this technique to low-cost and public buildings, a research program called *Use of Rubber-Based Bearings for Earthquake Projection of Small Buildings* (UNIDO, 1991) was carried out. A relatively simple isolation system with high-damping natural rubber isolators was developed and applied to a four-storey RC frame building with masonry infill walls. The research showed that this system was both affordable and functional, and suitable for seismic retrofitting of small buildings in highly seismic regions (Taniwangsa, 2002).

2.4 Experimental and numerical studies for steel shear wall

Steel shear wall is one of the commonly used retrofitting strategies to improve the seismic performance of the existing framed structures designed without consideration of the earthquake loading (De Matteis et al., 2009; Li et al., 2015). The retrofitting system usually consists of infill steel panels connected to the surrounding boundary frame, and the infill panels can be either thick plates, stiffened plates or unstiffened thin plates. Prior to the research in the 1980s, the limit state of steel shear walls was considered as plate shear buckling, leading to a very conservative design using relatively thick steel panels or infill panels with heavy stiffeners (Bruneau et al., 2007). However, due to the development of the tension field in the thin steel plates, the post-buckling strength is considerable and should be fully utilised. Aiming to reduce cost and constructability, unstiffened thin steel panels have been widely researched in both

experimental and numerical studies, and proved to possess high initial stiffness, satisfying ductility and energy dissipation capacity.

2.4.1 Experimental studies

Experimental studies have been carried out to verify the post-buckling strength, hysteresis behaviour, energy dissipation capacity under seismic loading and practical design considerations of steel shear walls.

Timler and Kulak (1983) performed physical testing on full-scale single-storey specimens with 5 mm thick infill plates under cyclic loading to serviceability limit and failure load, respectively. These tests showed the formation of a tension filed by the distribution of principal surface stresses on steel shear walls, and the retaining stiffness and strength after plate buckling. Roberts and Ghomi (1991) carried out a set of experimental tests on unstiffened steel and aluminium shear panels with various aspect ratios and plate thickness. Quasi-static cyclic loading was applied to all the specimens along one panel diagonal direction. The test results showed that shear panels exhibited satisfying hysteresis characteristics, adequate ductility and good energy dissipation capacity. This experiment is followed by a series of tests on one-quarter-scale three-storey steel frame models with steel shear walls (Caccese et al., 1993; Elgaaly et al., 1993), a test on a large-scale four-storey steel specimen (Driver et al., 1998b), experiments on steel shear walls connected to concrete-infilled steel columns (Astaneh-Asl and Zhao, 2001), a full-scale RC frame test upgraded with steel shear panels (Formisano et al., 2008; Formisano et al., 2010), etc.

Besides, additional research has been carried out considering practical design for unstiffened steel shear walls, studying the effects of different boundary frame connections and perforations in the infill plates (Bruneau et al., 2007; Purba and Bruneau, 2009). Choi and Park (2009) performed an experimental study on three-storey specimens under controlled cyclic displacement. In the experimental programme, several design parameters for infill walls were considered, including welded or bolted connections to the boundary frame, full or partial welded connections, and solid infill plates or plates with openings (coupled walls). It was found that all the studied steel shear wall configurations can be effectively applied for seismic retrofitting leading to notable improvements in strength, stiffness, deformation and energy

dissipation capacities. Clayton et al. (2012a) proposed a new self-centring steel plate shear wall system, which combines the advantages of steel panels with the re-centring capability of posttensioned beam-to-column connections. Then, a series of experimental tests were carried out in order to investigate the behaviour of the overall system and components and the impact of geometry properties on performance (Clayton et al., 2012b; Clayton et al., 2013; Clayton et al., 2015)

2.4.2 Finite element models

Finite element (FE) modelling strategies using shell elements were used in previous research to predict the response of steel shear walls up to collapse. In FE models for steel shear wall panels, a number of shell elements allowing for material and geometric nonlinearity must be used to describe the complex response characterised by out-of-plane plate buckling and the formation of tension fields within the panel. Due to numerical convergence problems and the high computational cost, most previous studies using detailed FE models with nonlinear shell elements were limited to the investigation of the nonlinear response under monotonic loading.

Driver et al. (1998a) adopted eight-node quadratic shell elements in ABAQUS to model a four-storey steel frame specimen with steel shear walls (Driver et al., 1998b), using an elasto-plastic constitutive model with strain-hardening for the steel material of the plates. The results from nonlinear pushover analysis showed good agreement with the experimental data, especially in terms of initial stiffness and ultimate strength. Guo et al. (2013) developed FE models with shell elements in ANSYS, using the hysteretic description for infill steel plates put forward by Roberts and Ghomi (1991). The models were validated against experimental data first, and subsequently used in parametric studies varying the geometrical characteristics of the steel wall components including the height-to-thickness and span-to-height ratios of the steel plates and the minimum moment of inertia of the boundary columns.

2.4.3 Macroscale models

More efficient macroscale models for steel shear walls were developed in previous research. Thorburn et al. (1983) proposed a tension strip model, as shown in Fig. 2.13(a), where each panel is modelled as a series of tension-only strips assuming a specific inclination angle for the

tensile field. Such inclination angle was derived by minimising the internal work in the web plate and the boundary beams and columns subjected to axial forces. This multi-strip model is capable of representing the post-buckling strength, where at least ten equal-width strips are required to represent the tension field action within the steel plate. Timler and Kulak (1983) improved the definition of the inclination angle by considering the contribution of the bending strain energy in the columns. This enhanced multi-strip model was later verified against experimental results on single-storey and four-storey specimens carried out by Timler and Kulak (1983) and Driver et al. (1997), respectively. It is adopted by the Canadian standard CAN/CSA S16-01 (CAN, 2001) and the American AISC seismic provisions (AISC, 2016). One obvious disadvantage of such a description for steel shear walls is that the multi-strip model neglects the compressive resistance in the direction orthogonal to the tension field, which can be substantial in the corner area of the plate depending on the plate thickness (Shishkin et al., 2009).

A more efficient model with a single pin-ended diagonal truss member, as illustrated in Fig. 2.13(b), was proposed by Thorburn et al. (1983). This simplified model, which requires a simple definition of the model parameters, is capable of predicting the initial stiffness of steel shear walls accurately. It is recommended for the preliminary seismic design by CAN/CSA S16-01 (CAN, 2001). Nevertheless, the equivalent truss model does not allow for the local interaction between the steel plate and the surrounding beams and columns of the frame, and it also overestimates the ultimate strength when the length-to-height aspect ratio of the steel panels is different from 1(Berman and Bruneau, 2003; Choi and Park, 2010).

In a subsequent study, Shishkin et al. (2009) modified the multi-tension-strip model by adding a compression truss with the same cross-sectional area as the equivalent truss model. This modified strip model is shown in Fig. 2.13(c). Axial hinges, which are considered rigid until yielding, are positioned at the ends of both the tension strips and the compression struts to simulate strength deterioration caused by plate tearing in tension and buckling in compression. This modified strip model was verified against the experimental results under lateral loading obtained by Driver et al. (1998b). Tian et al. (2015) proposed an alternative three-strip model as shown in Fig. 2.13(d), where three tension strips are employed in the diagonal direction. The strips are connected to the opposite corner of the boundary frame and at the mid-span of beams and columns. The model provides good predictions for the storey stiffness and the reaction

forces in the boundary columns, as the more complex multi-strip models, but the ultimate strength estimate is less accurate.

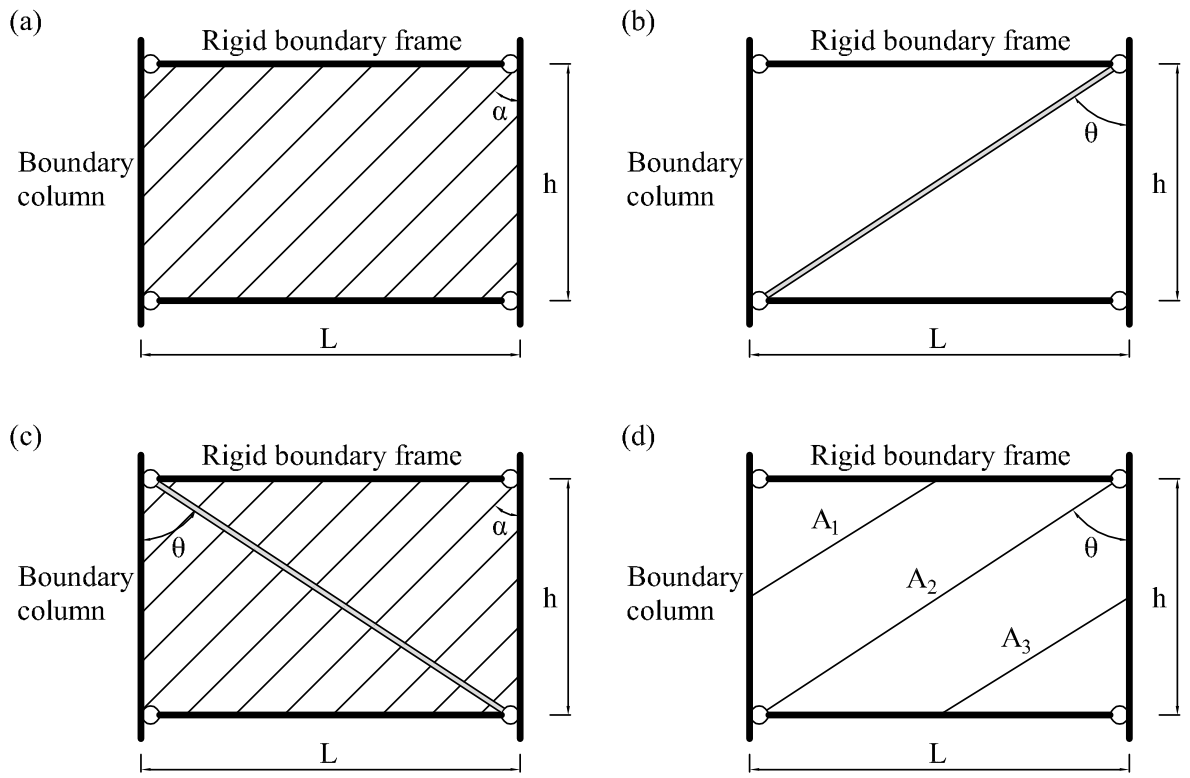

Fig. 2.13. Simplified models: (a) Multi-strip model (Thorburn et al., 1983); (b) Equivalent truss model (Thorburn et al., 1983); (c) Modified strip model (Shishkin et al., 2009); (d) Three-tension-strip model (Tian et al., 2015)

2.4.4 Hysteretic material models

To improve the accuracy of the numerical response predictions of steel shear walls under cyclic loading, enhanced hysteretic material descriptions for the tension strips and the equivalent trusses of macroscale steel shear wall models were developed in previous research.

Choi and Park (2010) proposed stress-strain relationships for strip elements allowing for plate buckling and material yielding, which define the maximum principal tension and compression stresses and tangent stiffness degradation in the steel panels under cyclic loading, as shown in

Fig. 2.14. This constitutive model was applied to the tension-strip macroscale models and validated against experimental tests and nonlinear finite element analysis.

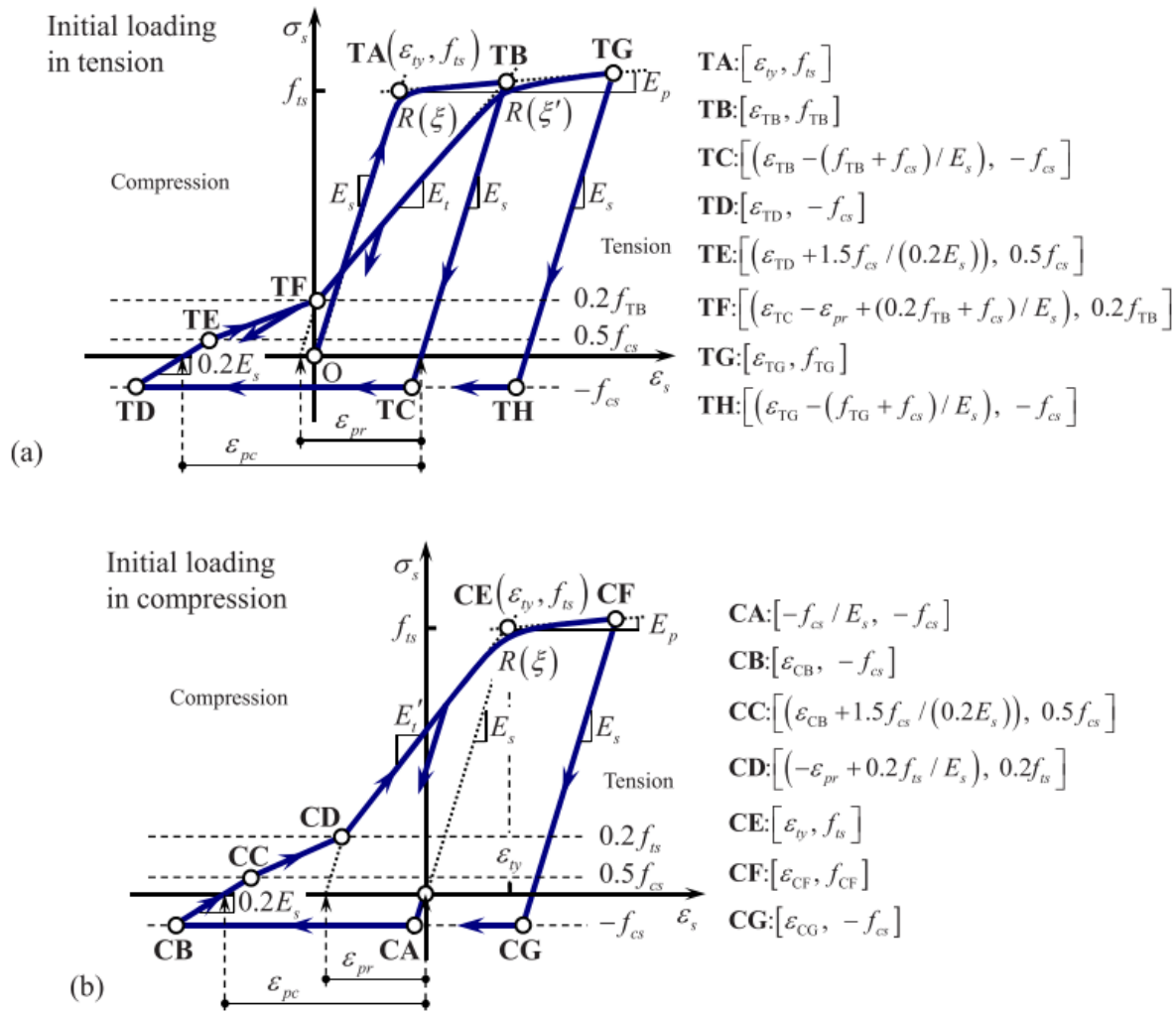

Fig. 2.14. Hysteresis model proposed by Choi and Park (2010): (a) Initial loading in tension; (b) Initial loading in compression.

Guo et al. (2013) defined the multi-strip model by introducing tension-only and tension-compression strips with specific constitutive relationships. This combined strip model considered the compressive strength contribution to the steel shear wall performance under cyclic loading obtaining a good representation of the hysteretic behaviour compared to experimental results.

Purba and Bruneau (2014) employed deterioration models for infill plates and boundary elements and model calibration based on the experimental results obtained from four steel shear wall specimens under cyclic loading.

Jalali and Banazadeh (2016) considered the Choi-Park (2010) model and the Purba-Bruneau (2014) model and proposed a new hysteresis model shown in Fig. 2.15, which allows for both in-cycle strength deterioration under monotonic loading and strength and stiffness degradation under cyclic loading. After validation against experimental results, it was demonstrated that this new material model can provide more accurate results compared with the previously developed Choi-Park (2010) and the Purba-Bruneau (2014) models.

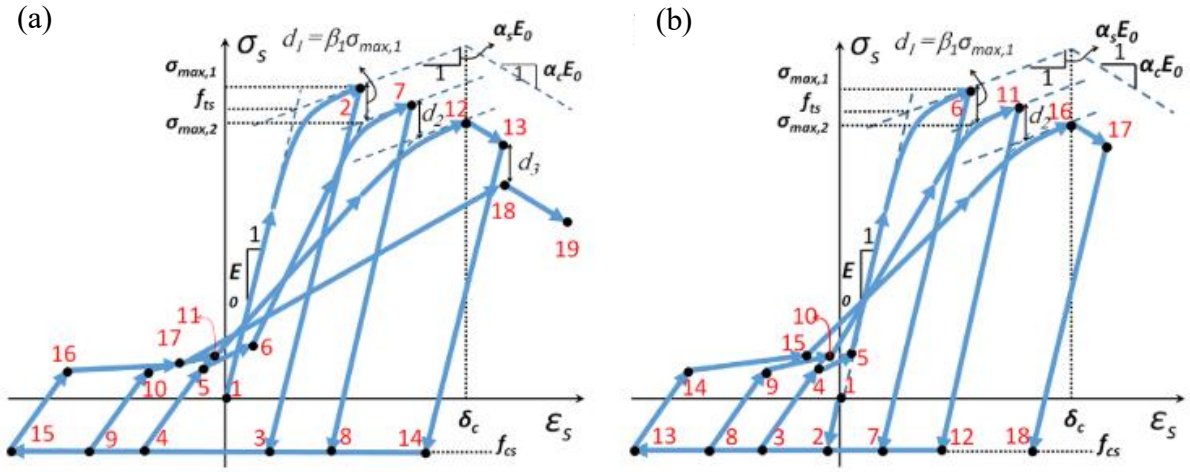

Fig. 2.15. Hysteresis model proposed by Jalali and Banazadeh (2016): (a) Initial loading in tension; (b) Initial loading in compression.

Wang and Yang (2018) built the hysteresis model based on the skeleton curves of different steel materials with quantified cyclic hardening characteristics, and took into consideration the compressive residual strength of the infill plate strips, as illustrated in Fig. 2.16. The proposed hysteresis model was applied to the multi-strip model and then verified against both experimental tests and shell element numerical models. The authors also conducted parametric studies on a range of steel shear walls with different plate thicknesses and loading patterns comparing the multi-strip models with the shell element models, which confirmed that the proposed hysteresis model can capture the actual cyclic behaviour of steel shear walls accurately.

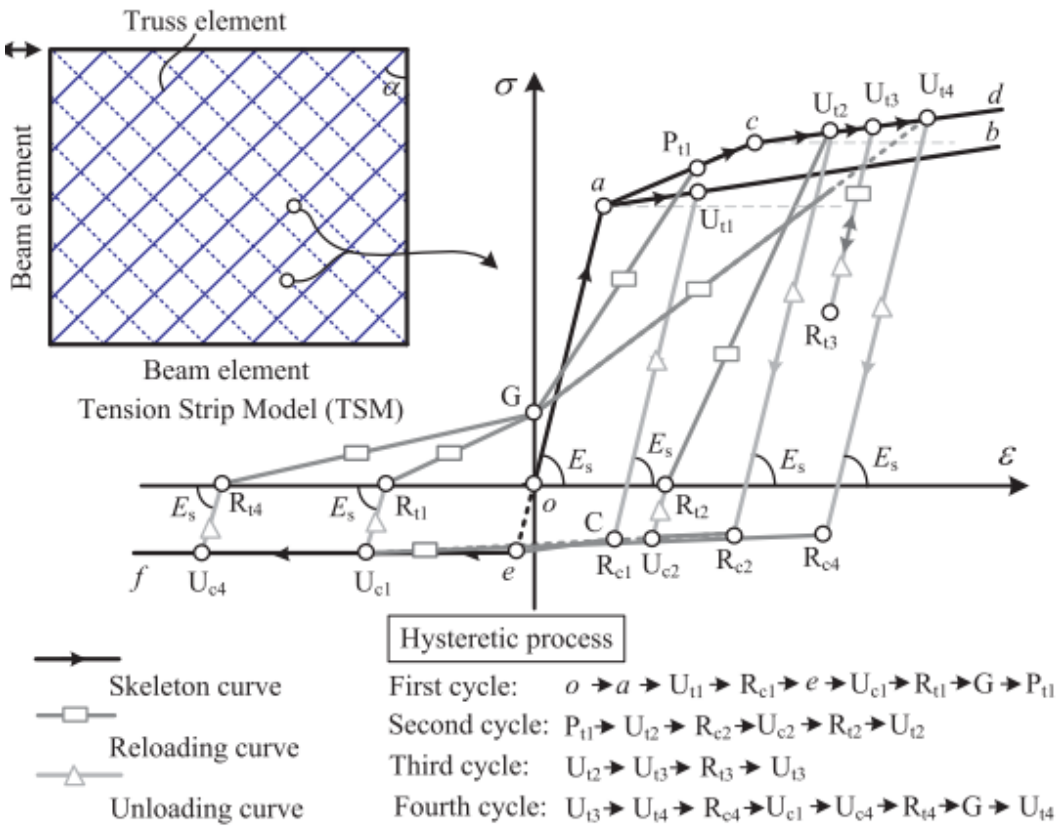

Fig. 2.16. Hysteresis model proposed by Wang and Yang (2018)

2.5 Genetic algorithm and application to optimal seismic retrofitting

2.5.1 Genetic Algorithm

Genetic Algorithm (GA) is one of the evolutionary algorithms inspired by Darwin's theory of biological evolution (Darwin, 2004). This algorithm was first presented by Holland (1975) in his book *Adaptation in natural and artificial systems*, which investigated the use of GA to transfer the evolutionary process in nature to artificial systems. GA is commonly used to generate solutions to optimisation problems by implementing the steps shown in the flowchart in Fig. 2.17.

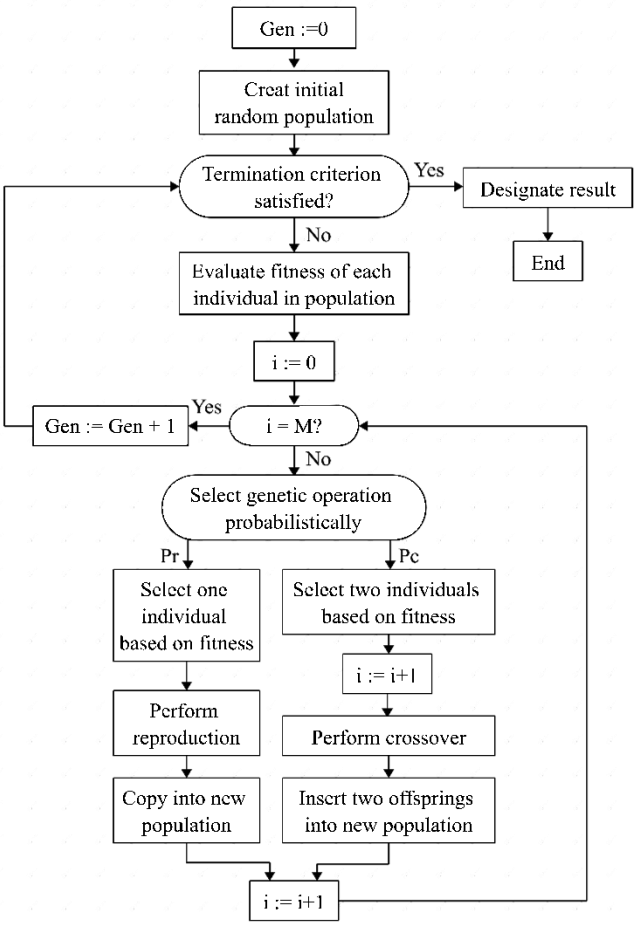

Fig. 2.17. Flowchart of GA programming (Koza, 1994)

An initial population is first generated randomly. The fitness measure of each individual in the population is computed to evaluate how well the individual performs in solving the given optimisation problem. A new population is then created by selecting individuals with high fitness and applying reproduction and crossover operations to the existing individuals. The last two steps are performed iteratively until the termination criteria are met. As a consequence, the fittest individual in all populations is considered as the solution or the approximate solution to the studied problem (Koza, 1994). Moreover, the mutation operator can be adopted to maintain good 'genetic material' of the poorly adapted individuals that may not be selected for selection and crossover, and to introduce diversity and more probability of exploring all the design regions. Random mutations are also needed to allow GA to avoid local optimal solutions and premature convergence (Falcone, 2018; Golberg, 1989).

An optimisation problem with multiple objectives subjected to certain inequality and equality constraints can be written as (Srinivas and Deb, 1994; Rao, 1983):

$$\begin{aligned} &\text{Minimise/Maximise } f_i(x) \quad i = 1,2,\dots,N \\ &\text{Subject to } g_j(x) \leq 0 \quad j = 1,2,\dots,J \\ &b_k(x) = 0 \quad k = 1,2,\dots,K \end{aligned} \tag{2.27}$$

For such multi-objective optimisation problems, a set of optimal solutions, namely Pareto-optimal solutions, are usually defined. The nondominated sorting genetic algorithm (NSGA) proposed by Srinivas and Deb (1994), which was later improved to NSGA-II by Deb et al. (2002), can be used to find the solutions. The term *nondominated* means that any member in the solution set is not somewhat less (greater) than any other member for a minimisation (maximisation) problem. The NSGA-II was developed considering a ranking selection method based on an individual nondominance in the population, and a crowded-comparison approach was introduced to maintain population diversity. Fig. 2.18 shows the NSGA-II procedure, where *P*, *Q*, *R* and *F* stand for the parent population, the offspring population, the combined population, and the nondominated set (Deb et al., 2002).

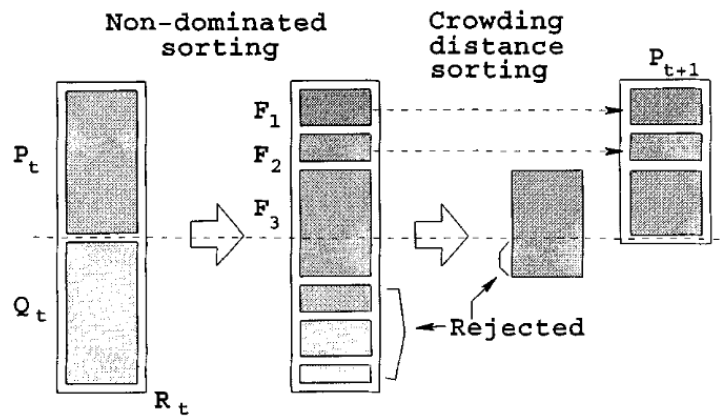

Fig. 2.18. NSGA-II procedure (Deb et al., 2002)

2.5.2 Optimal Seismic Retrofitting Using Dampers and Isolators

Previous work on optimal seismic retrofitting design mostly considered the use of dampers or isolators to dissipate the energy supplied by earthquakes, improving the seismic performance of existing RC frames.

Cha and Agrawal (2017) formulated a multi-objective optimisation method for the seismic upgrading of a nine-storey moment-resisting frame building. Magnetorheological (MR) dampers and a decentralised output feedback polynomial controller were applied to the retrofitting structure to improve the seismic response. This optimisation method provides a number of MR damper layouts satisfying the multiple design targets, which are obtained by minimising the number of MR dampers and the maximum inter-storey drift. Kim and An (2016) applied GA for determining the optimal slip-force distribution of friction dampers installed in the longitudinal direction of a 15-storey RC building. As shown in Fig. 2.19, to reduce the computational demand of nonlinear time-history analysis employed in combination with the GA procedure, the 15-storey model was simplified as a 15-degree-of-freedom (15-DOF) system to represent the maximum roof displacement under earthquake loading. This research showed that GA can be effectively used to find the optimal distribution of dampers.

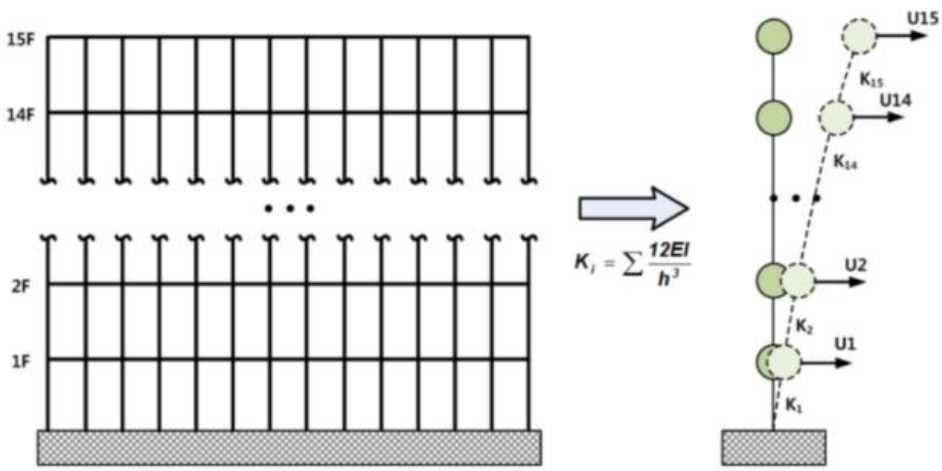

Fig. 2.19. Simplification of the model structure (Kim and An, 2016)

GA was also applied to determine the optimal configurations of isolators installed at different storeys for seismic retrofitting of multi-storey buildings (Charmpis et al., 2012). The solution

to this optimisation problem minimises the maximum floor acceleration by selecting the optimal number of isolation levels and the properties of each isolator. The structure was modelled as a multi-DOF system with equivalent mass, stiffness and viscous damping coefficient at each storey. This optimisation procedure identifies all feasible isolation configurations for seismic retrofitting of the studied structure.

2.5.3 Optimal Seismic Retrofitting Using FRP

Choi (2017) developed an optimisation approach for seismic retrofitting of existing non-ductile RC frames by applying FRP jackets to columns and beams. This strategy was aimed at determining the minimum amount of FRP jackets to minimise the cost of the retrofit solution while reducing the risk of collapse. The optimisation method adopted NSGA-II to obtain the optimal solution achieving two objectives. The proposed method was applied to a 3-storey RC frame structure. Compared with Choi et al. (2014), where FRP jackets were applied to columns only, the amount of FRP to retrofit both columns and beams was more than that to retrofit columns only. It suggested that retrofitting only columns is more economical if the criterion of the retrofit cost is more critical than other criteria.

Choi et al. (2017) also proposed an optimal method for retrofitting RC frames with masonry infill walls using FRP bracings, which act as tension ties and reduce the tension forces on the infill walls. The proposed method employs NSGA-II to obtain the optimal solution with the objectives of using the minimum amount of FRP and dissipating the maximum seismic energy. The results of the application of this method to a 5-storey and a 10-storey building indicate that a larger amount of FRP material leads to improved seismic performance, whereas the retrofit efficiency is reduced.

Chisari and Bedon (2017) performed an optimal performance-based design for existing RC frame structures using a retrofitting system made of FRP, aiming at minimising the retrofitting system cost, maximising the overall structural ductility and satisfying all the inter-storey drift constraints at different levels considering seismic loading provided by current design codes.

2.5.4 Optimal Seismic Retrofitting Using Bracing Systems

Farhat et al. (2009) proposed a systematic methodology for the optimal seismic retrofitting design of existing structures using buckling restrained braces (BRBs). A single-objective optimisation problem (SOP) and a multi-objective optimisation problem (MOP) were adopted in their study, with the constraints of the minimum structural performance requirements. The objective function of the former optimisation problem was cost, while the latter considered objective functions for cost and damage. GA was applied for the solutions to both problems, and nonlinear time-history analyses were carried out to estimate the structural performance under the designed earthquake ground motion without and with seismic retrofitting systems. With the aim of reducing analysis time, only material nonlinearity was considered, ignoring geometric nonlinearity and second-order ($P - \delta$) effects. A preliminary procedure was also employed to reduce the number of possible solutions in MOP, improving the performance of GA without excluding any possible optimal solutions. As a result, the optimal cross-sectional areas of the BRBs with four different sections assigned in the studied 2D RC frame model, as shown in Fig. 2.20, were determined.

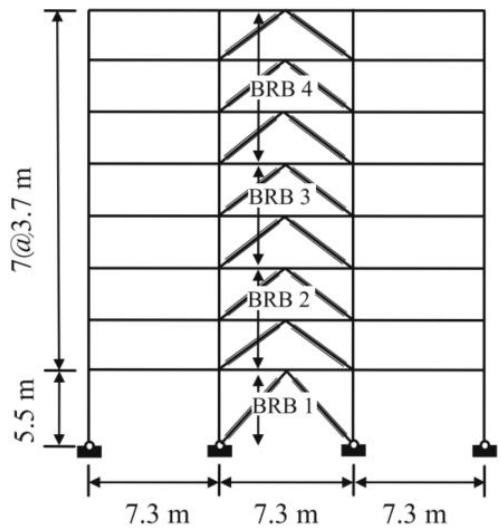

Fig. 2.20. The studied 2D RC frame model (Farhat et al., 2009)

Park et al. (2015) studied the optimal retrofit design for the configurations and cross-sectional sizes of BRBs using NSGA-II. Two objective functions were set as the minimum cost of both the initial BRB installation and the seismic damage during the structural life cycle. This

optimisation procedure was applied to a 2D regular steel frame structure and a 3D irregular RC frame, where the structural response was investigated using nonlinear static and nonlinear dynamic analysis, respectively. Besides, the researchers adopted a distributed algorithm on a cluster of commercial multi-core PCs to decrease the computational time of the optimisation problems. The performance of the proposed distributed algorithm was evaluated by global convergence, computing efficiency and accuracy of the optimal solutions.

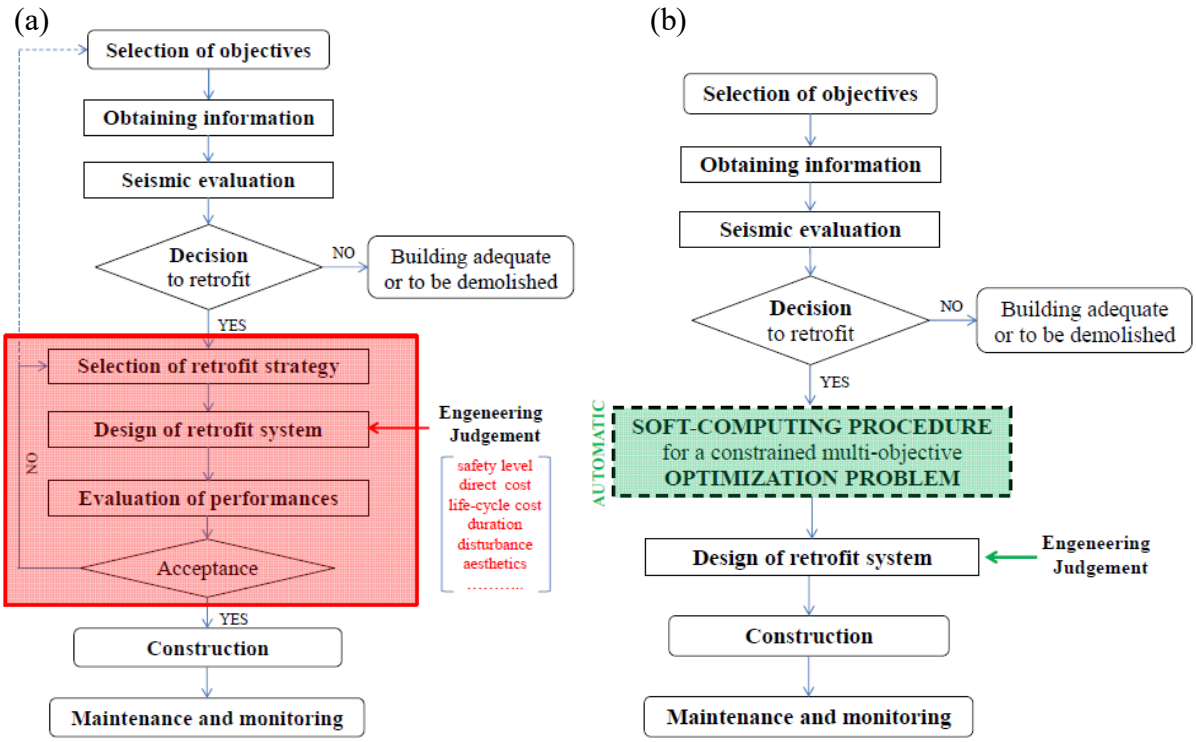

Fig. 2.21. Flowcharts for seismic retrofitting design using: (a) Conventional trail-and-error method; (b) Computing-aided method (Falcone, 2018)

Falcone developed a complete GA-based procedure for the optimal retrofitting design of existing RC buildings using FRP jacketing of columns as local intervention and concentric X-shape steel bracing as global intervention (Falcone, 2018; Falcone et al., 2019). A computing-aided method was proposed to replace the conventional trial-and-error method. The flowchart of the method is shown in Fig. 2.21, where it is compared against a standard trial-and-error approach. Detailed descriptions were shown in this work, including encoding the intervention methods to decimal genotype, modification of FE models corresponding to decision variables, and definition of main GA operators, i.e. selection, crossover and mutation operators. The

proposed optimal design procedure was then applied to a 3D model of a 4-storey RC framed structure using pushover analysis and the N2 method (Section 2.2.2). The single optimisation objective is set mainly considering the cost of FRP sheets, steel bracing and foundation strengthening.

2.6 Summary

A complete review of previous research on seismic assessment and retrofitting of existing RC buildings has been presented in this chapter. Focus has been placed on the use of steel shear walls and optimal seismic retrofitting design to identify potential research gaps. The main findings are listed below:

- Seismic assessment of existing RC framed structures is carried out not only based on global performance requirements, but also allowing for local brittle and ductile failure.
- Unlike the seismic design of new buildings that follows simplified force-based procedures, accurate seismic assessment of existing structures requires the use of displacement-based methods, including the N2 method, capacity spectrum method and direct displacement-based design (DDBD) approach. The capacity spectrum method is selected in this thesis because of the easy determination of equivalent viscous damping (EVD), which represents the hysteretic characteristics under the cyclic response of the analysed system defining the global displacement demand. Many rules have been presented in the literature to determine the hysteretic part of the EVD showing contrasting results. Besides, none of the existing hysteresis rules fully allow for the distinct features of the response of steel shear walls under cyclic loading.
- The seismic performance of unqualified structures can be enhanced by global or local retrofitting strategies. Steel shear wall is an effective global retrofitting technique, which has the advantage of reduced self-weight and guarantees a significant improvement of the overall structural stiffness, lateral strength and energy dissipation capacity.
- The behaviour of steel shear walls under cyclic loading is relatively complex. Most of the previous research represents steel wall panels using nonlinear FE models with shell elements, which requires relatively high computational demand. Macroscale models

were also developed using multi strips, equivalent trusses or three tension strips to represent the steel plates, where specific hysteresis models can be used to improve the simulation accuracy. However, most of the previous studies applied the hysteresis material models to the multi-strip model, which usually needs to define many strips and is difficult to assemble. Besides, the existing hysteresis models predefined material parameters for all the cases and did not consider compressive strength reduction and different levels of stiffness degradation when increasing the number of loading cycles.

- Genetic algorithms are commonly used to perform optimal seismic retrofitting design. However, most previous research focused on the use of dampers, FRP or bracing systems, but not steel shear walls as retrofitting solutions and some studies were based upon single-objective optimisation procedures.

Chapter 3

Macroelement Formulation for Steel Shear Walls

3.1 Introduction

As discussed in Chapter 2, finite element (FE) models with shell elements allowing for material and geometric nonlinearity provide an accurate representation of the buckling and plastic behaviour of steel shear walls. Such detailed models, however, are associated with significant computational cost, which renders their use impractical for the nonlinear analysis of large structures and extensive parametric studies. As a result, simpler and more efficient modelling strategies are needed to represent the response of steel shear walls up to failure. Efficient representations incorporating several strips or braces to simulate one-bay one-storey steel wall components were proposed in previous studies (Thorburn et al., 1983; Timler and Kulak, 1983; Shishkin et al., 2009; Tian et al., 2015). Such existing simplified models generally lead to accurate predictions of the initial stiffness and ultimate resistance under monotonic in-plane

horizontal forces. Later research developed enhanced hysteresis models to improve the predictions under cyclic loading (Choi and Park, 2010; Jalali and Banazadeh, 2016; Wang and Yang, 2018). However, as already discussed in Chapter 2, most of the previous studies applied hysteresis material relationships to multi-strip models (Thorburn et al., 1983), which are nevertheless difficult to assemble and computationally expensive.

In this chapter, a modelling strategy for steel shear walls utilising a novel efficient macroelement formulation is proposed. The main features of the developed macroelement are presented first in Sections 3.2 to 3.4. Subsequently, the macroelement is validated against previous experimental results on a thin steel panel subjected to in-plane cyclic loading and numerical results obtained by employing detailed nonlinear shell element models in Section 3.5. Finally, the outcomes from preliminary numerical tests carried out to identify the most critical macroelement model parameters are presented and critically discussed in Section 3.6.

3.2 Macroelement formulation

The developed macroelement for a generic one-bay one-storey steel wall element incorporates six nonlinear springs with asymmetric constitutive relationships to represent the cyclic nonlinear response. It introduces a number of advantages and novel features as listed below:

- The macroelement is developed based on standard FE procedures, thus can be easily implemented into any FEM software;
- The connectivity of the macroelement is realised via eight nodes along the four edges of the rectangular macroelement, which can be easily defined and conveniently connected to the beams and columns of a frame model;
- The constitutive relationship for the nonlinear springs of the macroelement allows for the main characteristics of the shear behaviour of steel wall components under cyclic loading;
- The inherent computational efficiency makes the proposed macroelement a suitable alternative to more expensive models with nonlinear shell elements for the simulation of large-scale structures under seismic loading.

The 8-noded macroelement formulation includes four internal and two corner nonlinear springs, as sketched in Fig. 3.1(a). Each spring represents an equivalent component of the braced model depicted in Fig. 3.1(b).

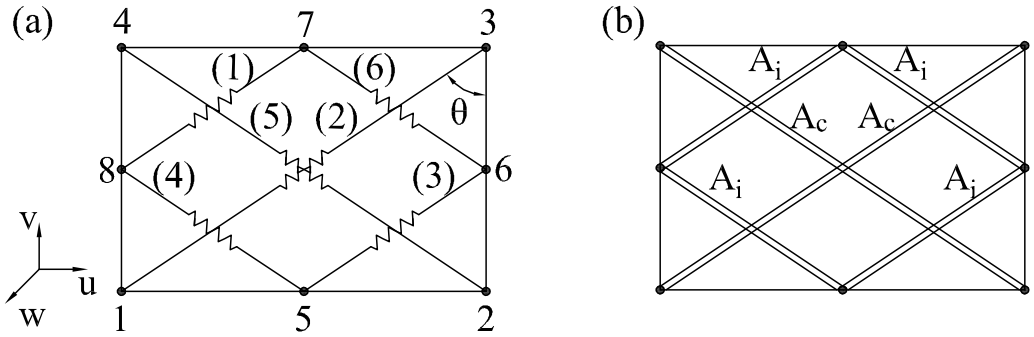

Fig. 3.1. (a) Steel shear wall macroelement; (b) Equivalent six-brace model

The tangent stiffness of each spring is determined as:

$$K_{c(i)} = \frac{S \cdot A_{c(i)}}{L_{c(i)}} \tag{3.1}$$

where S is the material tangent stiffness depending on the adopted constitutive relationship; $A_{c(i)}$ is the cross-section area of the equivalent corner (c) or internal (i) brace component; $L_c = \sqrt{L^2 + h^2}$ and $L_i = \sqrt{L^2 + h^2}/2$ represent the length of the corner and internal springs, respectively. The axial force for each spring is given by the stress defined by the material model multiplied by the cross-section area, denoted as:

$$F = \sigma \cdot A_{c(i)} \tag{3.2}$$

The equivalent brace areas A_c and A_i are set according to the three-strip model proposed by Tian et al. (2015), using the following expressions:

$$A_c = \frac{htsin^2\alpha\ cos^2\alpha}{sin\ \theta\ cos^2\theta} - \frac{2htsin^3\alpha\ cos\ \alpha}{3sin^2\theta\ cos\ \theta} \tag{3.3}$$

$$A_i = \frac{2htsin^3\alpha\ cos\ \alpha}{3sin^2\theta\ cos\ \theta} \tag{3.4}$$

where L, h, t are the length, height and thickness of the infill steel wall; $\theta = \tan^{-1}(L/h)$ is the angle between the corner brace and the vertical direction; α is the inclination angle of the tension field, which is derived by minimising the internal work due to the tension field within the steel panel component, and it can be determined according to Timler and Kulak (1983) as:

$$\alpha = tan^{-1}\sqrt[4]{\frac{1 + \frac{tL}{2A_{col}}}{1 + th\left(\frac{1}{A_{bm}} + \frac{h^3}{360I_{col}L}\right)}} \tag{3.5}$$

where I_{col} is the moment of inertia of the boundary beam; A_{bm} and A_{col} are the cross-section areas of the boundary beam and column, respectively.

3.3 Connectivity, kinematics and compatibility

The macroelement is developed according to a 3D FE framework and implemented in ADAPTIC (Izzuddin, 1991), a FE program for nonlinear analysis of structures under extreme loading conditions. The eight nodes are arranged on the external edges of the steel wall panel. The order of the node connectivity is shown in Fig. 3.1(a). Each node is characterised by three translational degrees of freedoms (DOFs) noted as u, v, w in the local element coordinate system. The element DOF vector (24×1) is therefore noted as

$$\{u\} = \{u_1, v_1, w_1, u_2, v_2, w_2, \dots, u_8, v_8, w_8\}^T \tag{3.6}$$

Six nonlinear springs connect different pairs of the corner and mid-edge nodes assuming a specific constitutive relationship allowing for degradation of strength and stiffness under cyclic

loading, as discussed in the following section. The compatibility conditions of the macroelement are expressed as:

$$\{d\} = [T_r]\{u\} \tag{3.7}$$

where $\{d\}$ (6×1) is the deformation vector collecting the axial deformations of the springs.

As illustrated in Fig. 3.2, a single bar element with local nodes *1* and *2*, which correspond to global nodes *i* and *j* respectively, is subjected to nodal displacements in the global X, Y and Z directions. The displacement vector of the two nodes in the local coordinate system can be obtained from the global displacement vector as:

$$\begin{Bmatrix} {u_1}^e \\ {u_2}^e \end{Bmatrix} = [T_r]^e \{u_i, v_i, w_i, u_j, v_j, w_j\}^T \tag{3.8}$$

Based on first order kinematics under small displacements, the transformation matrix of the 3D bar element is given by (The-Crankshaft-Publishing):

$$[T_r]^e = \begin{bmatrix} l_{ij} & m_{ij} & n_{ij} & 0 & 0 & 0 \\ 0 & 0 & 0 & l_{ij} & m_{ij} & n_{ij} \end{bmatrix} \tag{3.9}$$

in which l_{ij}, m_{ij}, n_{ij} are the direction cosines of the local *x*-axis of the element (Fig. 3.2) and can be written according to the global coordinates of two nodes (X_i, Y_i, Z_i) and (X_j, Y_j, Z_j) as:

$$l_{ij} = \frac{X_j - X_i}{L_e} \tag{3.10}$$

$$m_{ij} = \frac{Y_j - Y_i}{L_e} \tag{3.11}$$

$$n_{ij} = \frac{Z_j - Z_i}{L_e} \tag{3.12}$$

The length of the element L_e is obtained from the global nodal coordinates as:

$$L_e = \sqrt{\left(X_j - X_i\right)^2 + \left(Y_j - Y_i\right)^2 + \left(Z_j - Z_i\right)^2} \tag{3.13}$$

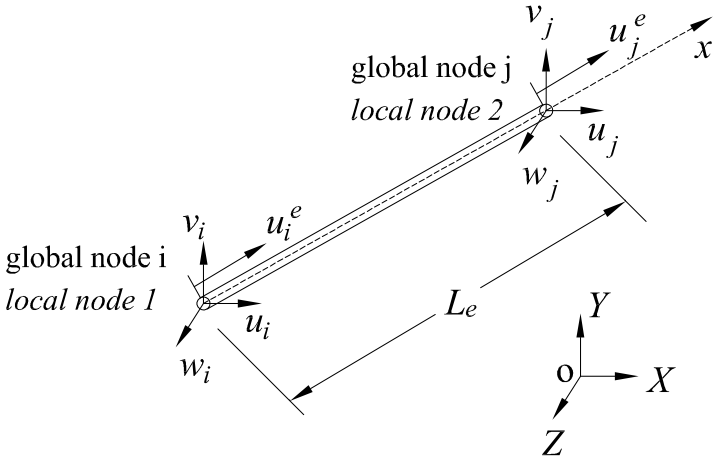

Fig. 3.2. 3D bar element associated with a generic spring of the macroelement (The-Crankshaft-Publishing)

As a result, the deformation of the bar element can be expressed as:

$$\begin{aligned} d^e &= {u_2}^e - {u_1}^e \\ &= \{-l_{ij}, -m_{ij}, -n_{ij}, l_{ij}, m_{ij}, n_{ij}\}\{u_i, v_i, w_i, u_j, v_j, w_j\}^T \end{aligned} \tag{3.14}$$

Furthermore, considering the element connectivity, the geometric transformation matrix $[T_r]$ (6×24) of the proposed macroelement can be derived as:

$$
[T_r] = \begin{bmatrix}
0 & 0 & 0 & 0 & 0 & 0 & \dots & \dots & 0 & 0 & 0 & 0 & 0 & 0 & \dots & \dots & 0 & 0 & 0 & 0 & 0 & 0 & \dots \\
\frac{X_1 - X_3}{L_c} & \frac{Y_1 - Y_3}{L_c} & \frac{Z_1 - Z_3}{L_c} & 0 & 0 & 0 & \dots & \dots & \frac{X_3 - X_1}{L_c} & \frac{Y_3 - Y_1}{L_c} & \frac{Z_3 - Z_1}{L_c} & 0 & 0 & 0 & \dots & \dots & 0 & 0 & 0 & 0 & 0 & 0 & \dots \\
0 & 0 & 0 & 0 & 0 & 0 & \dots & \dots & 0 & 0 & 0 & 0 & 0 & 0 & \dots & \dots & 0 & 0 & 0 & 0 & 0 & 0 & \dots \\
0 & 0 & 0 & 0 & 0 & 0 & \dots & \dots & 0 & 0 & 0 & 0 & 0 & 0 & \dots & \dots & 0 & 0 & 0 & 0 & 0 & 0 & \dots \\
0 & 0 & 0 & \frac{X_2 - X_4}{L_c} & \frac{Y_2 - Y_4}{L_c} & \frac{Z_2 - Z_4}{L_c} & \dots & \dots & 0 & 0 & 0 & \frac{X_4 - X_2}{L_c} & \frac{Y_4 - Y_2}{L_c} & \frac{Z_4 - Z_2}{L_c} & \dots & \dots & 0 & 0 & 0 & \frac{X_5 - X_6}{L_i} & \frac{Y_5 - Y_6}{L_i} & \frac{Z_5 - Z_6}{L_i} & \dots \\
0 & 0 & 0 & 0 & 0 & 0 & \dots & \dots & 0 & 0 & 0 & 0 & 0 & 0 & \dots & \dots & 0 & 0 & 0 & \frac{X_5 - X_8}{L_i} & \frac{Y_5 - Y_8}{L_i} & \frac{Z_5 - Z_8}{L_i} & \dots \\
 & & & & & & & & & & & & & & & & 0 & 0 & 0 & 0 & 0 & 0 & \dots \\
 & & & & & & & & & & & & & & & & 0 & 0 & 0 & \frac{X_6 - X_7}{L_i} & \frac{Y_6 - Y_7}{L_i} & \frac{Z_6 - Z_7}{L_i} & \dots \\
 & & & & & & & & & & & & & & & & \frac{X_7 - X_8}{L_i} & \frac{Y_7 - Y_8}{L_i} & \frac{Z_7 - Z_8}{L_i} & \frac{X_8 - X_7}{L_i} & \frac{Y_8 - Y_7}{L_i} & \frac{Z_8 - Z_7}{L_i} & \dots \\
 & & & & & & & & & & & & & & & & 0 & 0 & 0 & 0 & 0 & 0 & \dots \\
 & & & & & & & & & & & & & & & & 0 & 0 & 0 & 0 & 0 & 0 & \dots \\
 & & & & & & & & & & & & & & & & 0 & 0 & 0 & \frac{X_8 - X_5}{L_i} & \frac{Y_8 - Y_5}{L_i} & \frac{Z_8 - Z_5}{L_i} & \dots \\
 & & & & & & & & & & & & & & & & 0 & 0 & 0 & 0 & 0 & 0 & \dots \\
 & & & & & & & & & & & & & & & & \frac{X_7 - X_6}{L_i} & \frac{Y_7 - Y_6}{L_i} & \frac{Z_7 - Z_6}{L_i} & 0 & 0 & 0 &
\end{bmatrix}
\tag{3.15}
$$

After defining the deformation vector $\{d\}$, the component forces of the springs $\{f\}$ (6×1) can be obtained as

$$\{f\} = [k]\{d\} \tag{3.16}$$

where the element tangent stiffness matrix $[k]$ is a 6×6 diagonal matrix expressed as

$$[k] = \begin{bmatrix} K_i & & & & & \\ & K_c & & & & \\ & & K_i & & & \\ & & & K_i & & \\ & & & & K_c & \\ & & & & & K_i \end{bmatrix} \tag{3.17}$$

K_c, K_i are the tangent stiffness for diagonal and corner springs, respectively, as defined in Eq. (3.1).

The nodal force vector $\{R\}$ (6×1) and global level stiffness matrix $[K_t]$ (24×24) can be then obtained according to the equilibrium conditions as

$$\{R\} = [T_r]^T\{f\} \tag{3.18}$$

$$[K_t] = [T_r]^T[k][T_r] \tag{3.19}$$

3.4 Constitutive material model

The constitutive material model for the diagonal springs of the macroelement is developed to represent the typical response characteristics of steel shear walls under in-plane cyclic loading (Fig. 3.3), which derive from a complex interaction between plate buckling and steel yielding, including:

- the strain-hardening after yielding;

- residual shear force after each loading cycle;
- elastic stiffness degradation under cyclic loading; and
- pinching and sliding upon reloading.

The adopted constitutive model derives from the hysteretic uniaxial stress-strain law put forward by Choi and Park (2010). It is governed by a set of material parameters: $\{E_s, f_{tp}, f_{cp}, \mu, \beta, \gamma, \kappa\}$. E_s represents the elastic stiffness; f_{tp} and f_{cp} are the yield strength in tension and compression; μ and β correspond to the strain-hardening in tension and the degradation in compression coefficients; γ and κ are two factors which control the residual strength at the strain reversal point and the degree of stiffness degradation, respectively.

Fig. 3.3(a) schematically shows the evolution of the stress-strain relationship starting from loading in tension. In the first loading cycle, a bilinear curve is followed with initial elastic stiffness E_s up to yielding at strain $\varepsilon_{t0} = f_{tp}/E_s$ (point TA) and reduced stiffness μE_s for larger deformations. When unloading after yielding, stresses reduce linearly from the stress at point TB $[\varepsilon_{TB}, f_{TB}]$ following a linear branch with stiffness equal to the elastic stiffness E_s. After reaching the compressive strength limit f_{cp} at TC, the compressive stress degrades with a slope of βE_s. When the strain increment changes sign from point TD, the stress increases linearly to the strain reversal point TE $[0, \gamma f_{TB}]$ where the second cycle starts. With increasing tensile strain, the elastic tensile stress grows until it reaches the plastic tensile curve at TF. The yielding tensile strain value in the second cycle ε_{TF} considers the degree of stiffness reduction κ and it is defined by $\varepsilon_{TF} = \varepsilon_{t0} + \kappa(\varepsilon_{TB} - \varepsilon_{t0})$. After the yield point, the stress-strain relationship follows the same rule as for the first loading cycle.

Fig. 3.3(b) displays the cyclic behaviour starting from loading in compression. Also in this case the initial elastic stiffness corresponds to E_s and a reduced softening stiffness βE_s is assumed after yielding in compression from point CA at $\varepsilon_{c0} = f_{cp}/E_s$. Unloading from CB follows a linear branch up to the strain reversal point CC $[0, \gamma f_{tp}]$. Then, the tensile yielding point CD $[\varepsilon_{t0}, f_{tp}]$ is reached following a linear branch with reduced stiffness μE_s.

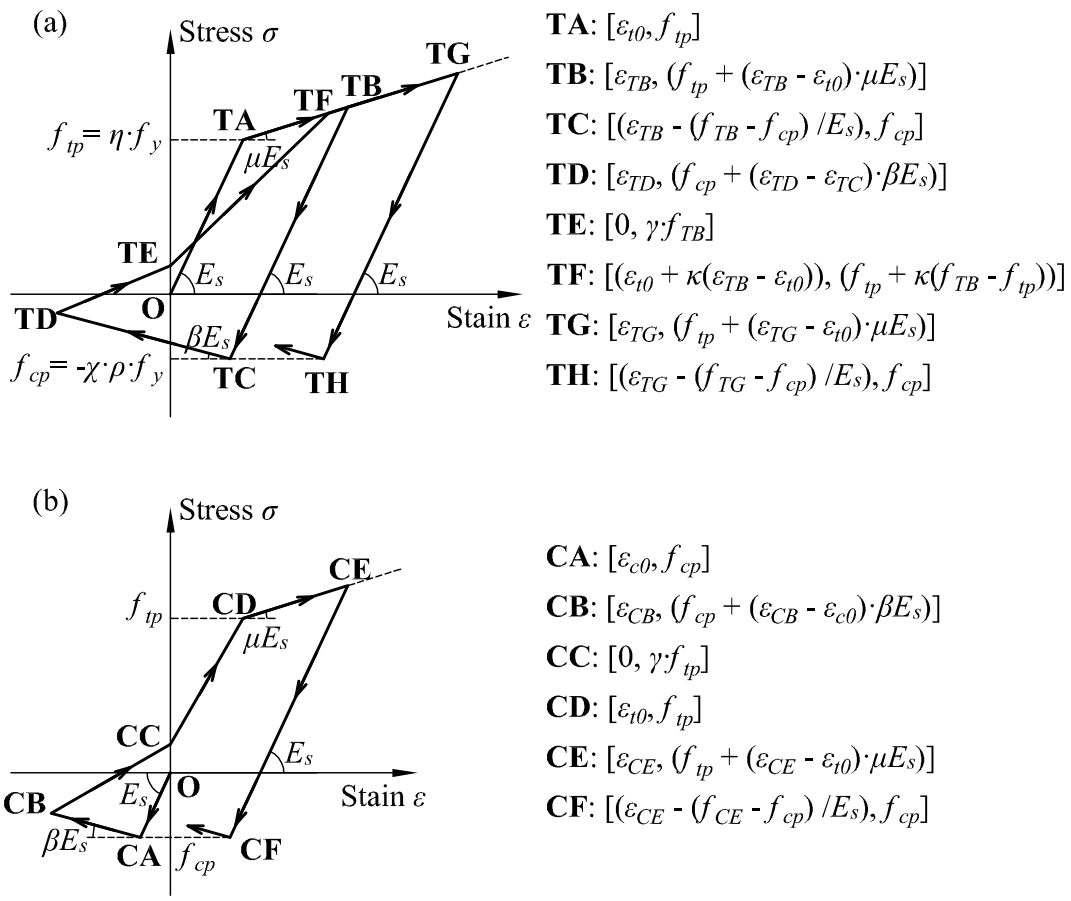

Fig. 3.3. Material constitutive model: initial loading in (a) tension and (b) compression

The material parameters are determined allowing for the material characteristics of structural steel and the geometry of the analysed steel shear wall. Importantly, due to the phenomenological nature of the proposed modelling strategy, some of the material parameters require also model calibration based on data from physical tests or numerical results from detailed nonlinear FE models for steel walls under cyclic loading. More specifically, the assumed elastic stiffness E_s corresponds to Young's modulus of structural steel. The tensile strength f_{tp} is obtained from the yield strength of structural steel f_y using the relationship:

$$f_{tp} = \eta f_y \tag{3.20}$$

where η is the shear strength deviation factor, which corresponds to the ratio between the shear strength prediction provided by a detailed multi-strip model (Berman and Bruneau (2003) and

that offered by a more efficient three-strip description (Tian et al., 2015), and it is given by the expression:

$$\eta = \frac{sin\,2\theta}{sin\,2\alpha} \tag{3.21}$$

where θ and α have been introduced previously.

The strength in compression f_{cp} for the corner and internal springs, which is associated with the buckling resistance of the internal and corner braces, is calculated assuming a rectangular cross-section for the braces (Fig. 3.1(b)) with the same thickness t as the analysed steel wall and a width $b_{c(i)}$ given by:

$$b_{c(i)} = \frac{A_{c(i)}}{t} \tag{3.22}$$

Besides, the expression recommended by Eurocode 3 (EN1993-1-1, 2005; EN1993-1-5, 2005) to calculate compressive strength allowing for bulking is adopted:

$$f_{cp} = \chi \rho f_y \tag{3.23}$$

in which ρ is the effective area factor for Class 4 cross-sections (EN1993-1-1, 2005; EN1993-1-5, 2005) and χ is the buckling coefficient:

$$\chi = \frac{1}{\phi + \sqrt{\phi^2 - \bar{\lambda}^2}} \leq 1 \tag{3.24}$$

where $\phi = 0.5\left[1 + 0.21\left(\bar{\lambda} - 0.2\right) + \bar{\lambda}^2\right]$;

$\bar{\lambda} = \sqrt{\frac{A_{eff} f_y}{N_{cr}}}$;

$$N_{cr} = \frac{\pi^2 EI}{(kL)^2};$$

$$\rho = \frac{\overline{\lambda_p} - 0.055(3+\psi)}{\overline{\lambda_p}^2} \leq 1 \; for \; \overline{\lambda_p} > 0.5 + \sqrt{0.085 - 0.055\psi}$$

$$\overline{\lambda_p} = \sqrt{\frac{f_y}{\sigma_{cr}}} = \frac{\frac{b}{t}}{28.4\varepsilon\sqrt{k_\sigma}} \; ;$$

or $\rho = 1.0$ for internal braces

It is important to point out that the slenderness $\bar{\lambda}$ depends upon the assumed effective length of the equivalent brace which is related to the unsupported length and the end restraints. These are linked to the proposed simplified phenomenological representation with six braces for describing the complex strain/strain field developing within the steel panel under shear. For an initial estimate of f_{cp}, an effective length factor k = 0.5 is assumed, where the effective length is taken as half of the actual brace length. A more refined estimate for f_{cp} within the interval $[\chi\rho f_y, \rho f_y]$ together with the definition of all the remaining material model parameters governing degradation of strength and stiffness are addressed in Chapter 4 based on detailed model calibration.

3.5 Model validation and numerical tests with shell elements

The ability of the macroelement model to represent the actual shear behaviour of steel panels under cyclic loading is assessed in comparisons against experimental results and detailed FE models with nonlinear shell elements. In the following, the experimental test on an unstiffened thin steel panel under shear, which has been considered for model validation, is introduced. Subsequently, FE models with shell elements simulating the experimental test are developed and the numerical results are compared against experimental data. Finally, numerical predictions achieved by using the proposed macroelement formulation are matched against numerical curves obtained by employing shell element models to identify the role played by model material parameters in determining the key response characteristics of unstiffened steel plates under cyclic loading conditions.

3.5.1 Experimental test

The experimental test carried out by Roberts and Ghomi (1991) on specimen SW2 shown in Fig. 3.4(a) has been selected for model validation. The test was performed on an unstiffened thin steel panel applying cyclic loading along the diagonal direction of the panel. The 300×300 mm^2 steel panel with 0.83 mm thickness was mounted on a boundary square frame with steel members of 70×40 mm^2 rectangular cross-section linked at the four corners by pinned joints. The steel panel was bolted to the boundary frame using high strength 8 mm bolts assuring rigid connectivity between the panel and the frame. In the test, the specimen was pinned to a strong floor at one corner, while at the opposite corner a force along the diagonal direction was applied quasi-statically with controlled target displacements of ±1.6 mm, 2.0 mm, 2.4 mm and 2.8 mm.

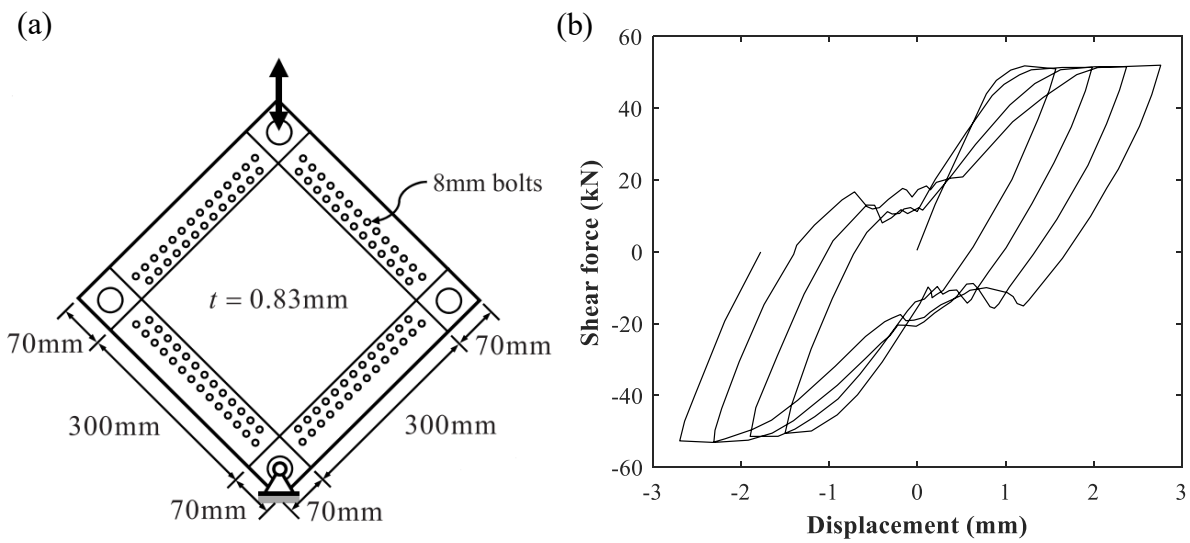

Fig. 3.4. (a) Experimental specimen; (b) Experimental load-displacement curve (Roberts and Ghomi, 1991)

The experimental results are shown in Fig. 3.4(b), where the applied force is plotted against the displacement along the diagonal direction at the load position. The experimental curve shows a stable cyclic behaviour with high initial stiffness, significant ductility and high hysteretic energy dissipation capacity. Shear strength remains practically constant also for large plastic deformations, but a non-negligible degradation of stiffness develops by increasing the

number of cycles. A pinching behaviour can be also observed when unloading before reloading in the opposite direction.

3.5.2 Numerical simulations with nonlinear shell elements

Initial numerical simulations are performed using FE models with shell elements. They provide an explicit description of the steel panel geometrical characteristics and require only basic material properties enabling accurate predictions of the cyclic response when geometric nonlinearity is allowed for and a suitable elasto-plastic material description for steel is used.

The members of the boundary frame of the SW2 specimen are modelled using the cubic elasto-plastic beam-column elements 'cbp3' available in ADAPTIC (Izzuddin, 1991), while 9-noded co-rotational shell elements 'cvs9' (Izzuddin and Liang, 2020) are employed to represent the steel panel. Pinned joints are introduced to connect the beam elements at the four corners of the frame. To represent the no-slip rigid connection offered by the high-strength bolts in the physical specimen, the nodes of the beam elements of the boundary frame are rigidly connected to the nodes of the shell elements at the perimeter of the panel.

The adopted shell element is the H3O9 variant of the 'cvs9' element (Izzuddin and Liang, 2020), which is based on a novel hierarchic optimisation process for eliminating various locking phenomena and the 4-noded quadrilateral flat shell element proposed by Izzuddin (2005), and it is suitable for modelling geometric nonlinearity effects in steel panels subjected to shear loading. A bisector co-rotational system is employed enabling nonlinear kinematic transformations of local displacements related to global nodal coordinates. As shown in Fig. 3.5, (X, Y, Z) and (x, y, z) are the global and local co-rotational coordinate systems, respectively. The x-axis and y-axis of the local coordinate system are defined so as to superpose the bisectors of the diagonals generated from the four corner nodes in the current configuration, eliminating the effect of rigid body rotations of the local elements. The co-rotational method enables solving a large-displacement small-strain problem based on the solution of the associated small-displacement small-strain problem at the local element level, where low-order kinematics can be used (Izzuddin and Liang, 2020).

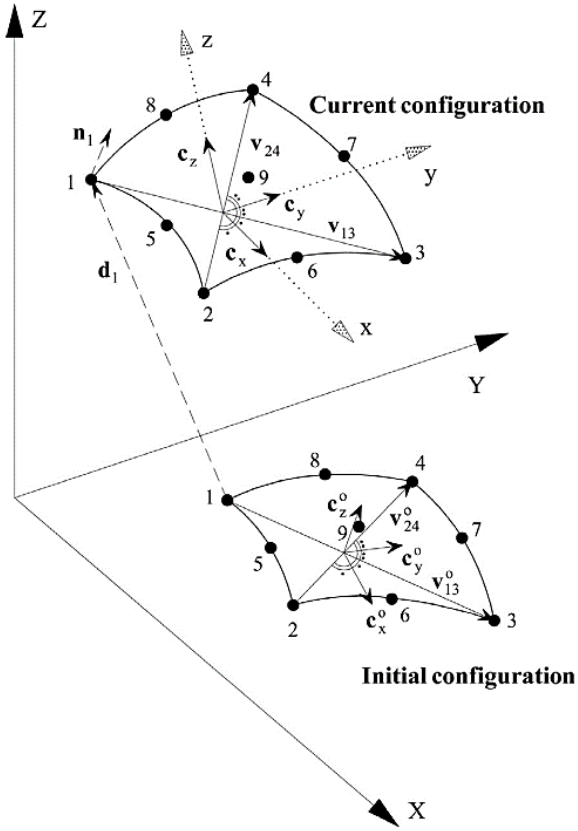

Fig. 3.5. The bisector co-rotational shell element (Izzuddin and Liang, 2017)

The material models 'stl1' and 'bnsk' shown in Fig. 3.6(a) and (b) are employed to take into account material nonlinearity in the beam-column and shell elements, respectively. The adopted yield strength 219 N/mm^2 and Young's modulus 202000 N/mm^2 correspond to the values obtained from tensile coupon tests on the structural steel of specimen SW2 as reported in Roberts and Ghomi (1991). The strain hardening factor μ is assumed as 0.01, while the strain limit at the onset of strain hardening used in model 'bnsk' is taken as ε_h= 0.002, which is the typical limit employed for most steel materials.

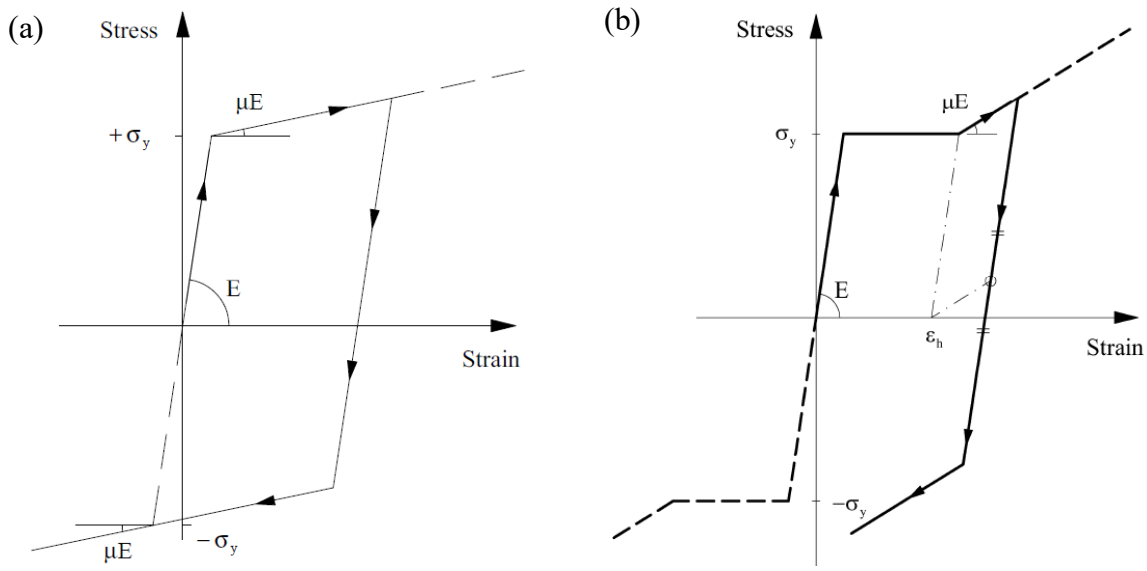

Fig. 3.6. Material model for frame and plate: (a) 'stl1'; (b) 'bnsk' (Izzuddin, 2019)

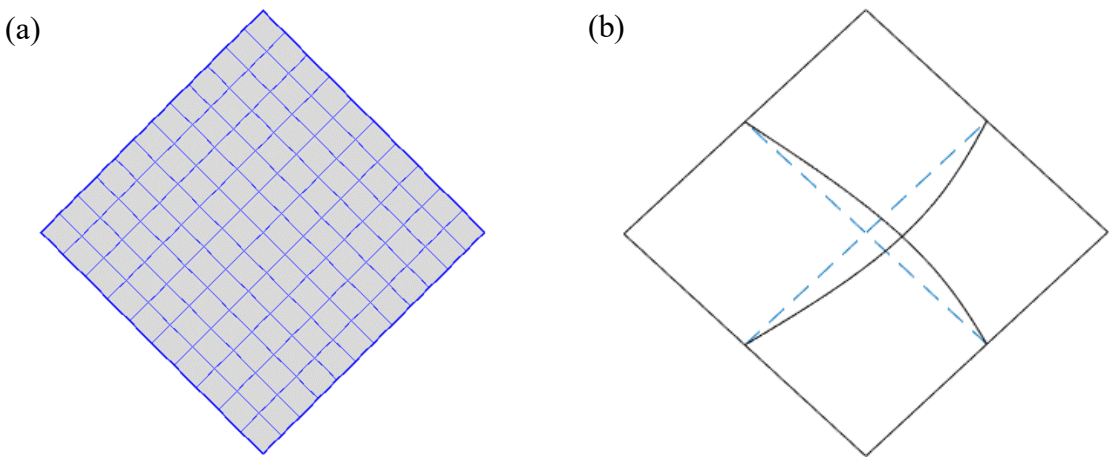

Fig. 3.7. (a) FE model of SW2 specimen*; (b) Initial imperfections shape*

Fig. 3.7(a) displays the FE mesh with 12×10 shell elements for the steel panel and beam elements for the external frame representing specimen SW2. Fig. 3.7(b) shows the adopted initial out-of-plane imperfections based on half sinusoidal shapes in the two main directions of the panel with a maximum imperfection of 1 mm at the central node. They have been introduced to capture geometric nonlinear effects due to the out-of-plane buckling of the panel as observed in the experimental test.

3.5.3 Numerical results

To investigate the cyclic response of the specimen, nonlinear simulations have been carried out prescribing the displacement at the corner top node following the displacement history indicated the Fig. 3.8.

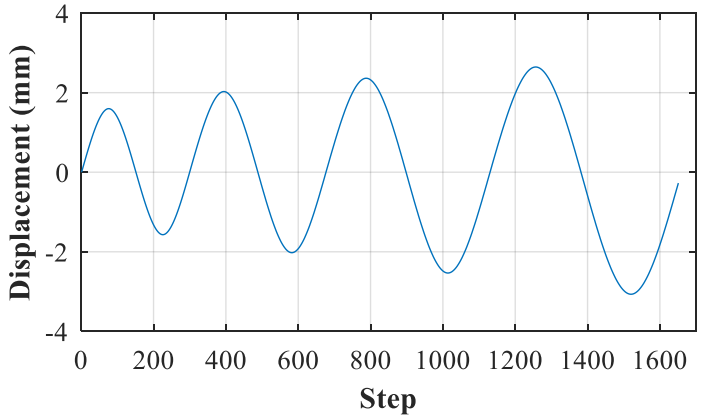

Fig. 3.8. Cyclic displacement history used in the nonlinear simulation of specimen SW2

The numerical response curve obtained using the developed FE model is shown in Fig. 3.9, where it is compared against the experimental data. Several crucial engineering features are compared between the experimental results and the shell element results in Table 3.1, including yield strength, ultimate shear strength (maximum strength), residual strength at the end of cyclic loading, and tangent stiffness (slope) of the final cycle. From the results shown in the figure and the table, a good agreement can be observed. The ADAPTIC FE model leads to an accurate prediction of the panel stiffness and shear capacity and the main features of the cyclic response including the pinching behaviour and the degradation of stiffness by increasing the number of cycles. The main discrepancy is related to the over-prediction of the elastic stiffness when unloading after yielding. This has been found also by other researchers (Guo et al., 2013) in the analysis of the same steel panel specimen using FE models with shell elements.

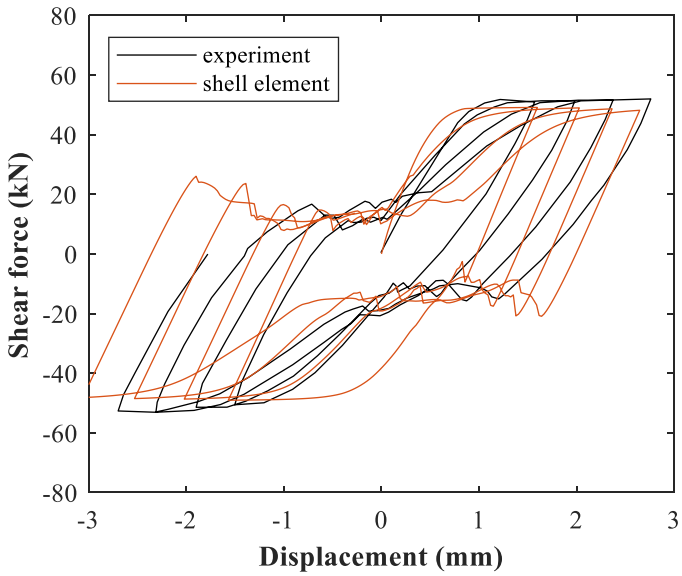

Fig. 3.9. Comparison between experimental and FE results using nonlinear shell elements

Table 3.1. Selected engineering features and deviation between experimental results and shell element results

	Yield strength (kN)	Ultimate strength (kN)	Residual strength (kN)	Stiffness at final cycle (kN/mm)
Experiment	51.80	51.98	17.35	10.46
Shell	46.44	49.29	19.53	10.44

Further numerical investigations have been carried out to assess the influence of the assumed material parameters and the mesh characteristics. The results from FE models with different values of the strain hardening parameter μ = 0.005, 0.01 and 0.015 are compared in Fig. 3.10. The three models provide very similar load-displacement curves with minor differences in the post yielding behaviour and ultimate strength.

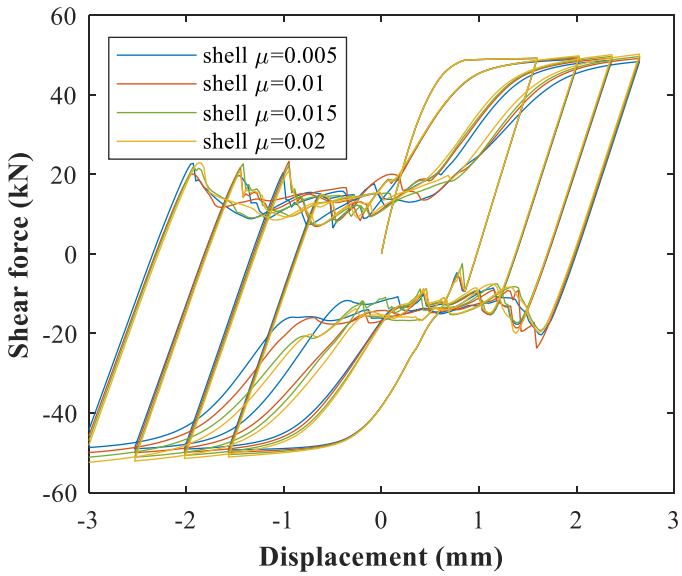

Fig. 3.10. Numerical curves obtained using the FE model with nonlinear shell elements with different strain hardening factors

The influence of the mesh characteristics has been analysed while setting the strain hardening parameter μ as 0.01. In Fig. 3.11(a) the numerical curves achieved using FE models with meshes of 6×5, 12×10 and 24×20 shell elements are compared, while Fig. 3.11(b-d) show the deformed shapes predicted by the 3 meshes at a 2.8 mm displacement at the top corner where the load is applied. It can be seen that the numerical response curve computed by the model with the 6×5 mesh does not provide an accurate representation of actual response and buckling shape under cyclic loading, whereas the models with 12×10 and 24×20 meshes provide very similar results and are close to the experimental data.

Table 3.2 lists the computational costs for the different mesh sizes. It is evident the analysis time and the allocated memory increases dramatically when employing the finest mesh with the largest number of shell elements. Therefore, it can be concluded that the moderate mesh size 12×10 represents a suitable balance between modelling accuracy and computation efficiency. Thus, such mesh density has been considered in subsequent numerical investigations.

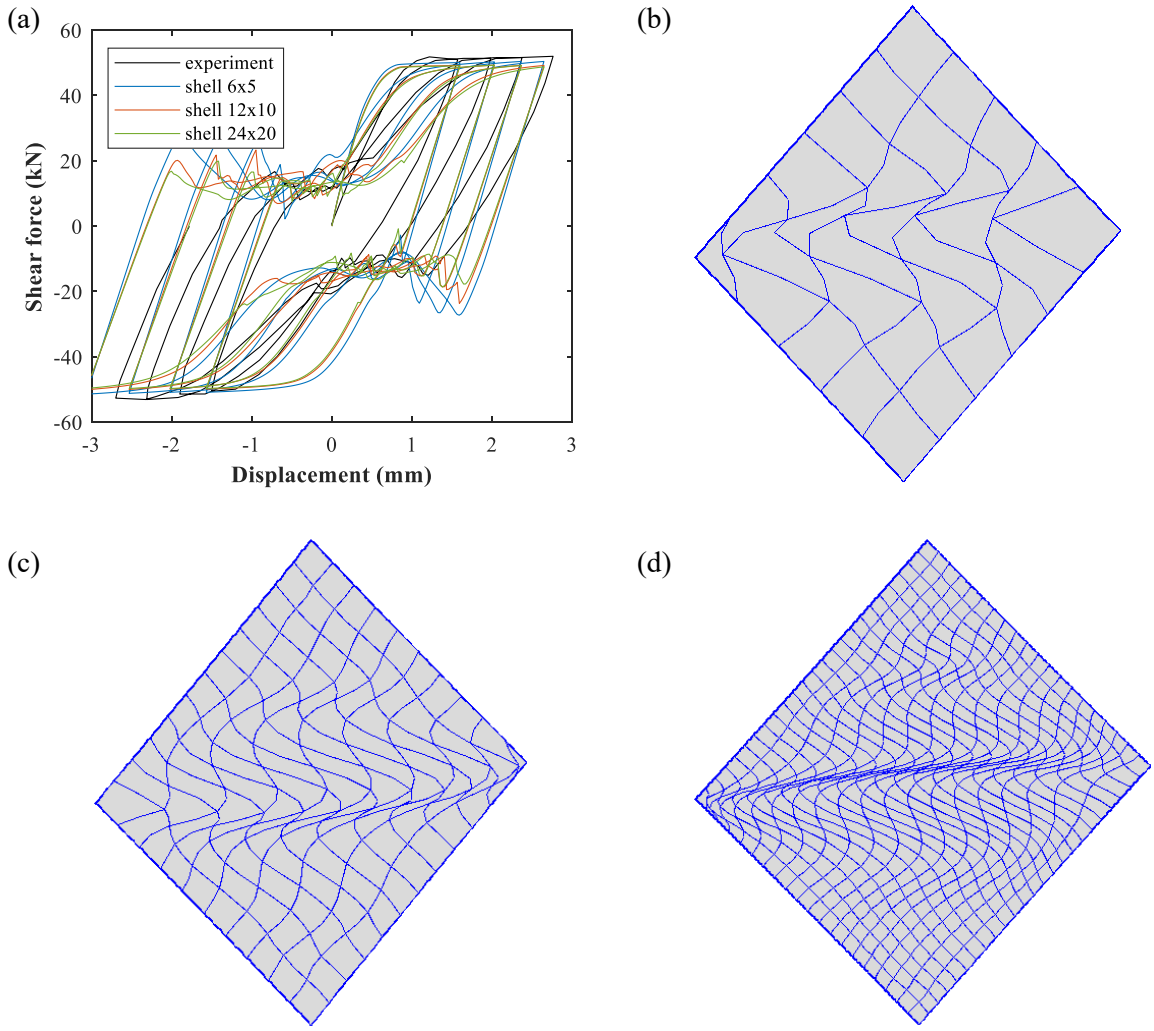

Fig. 3.11. (a) Comparison between experimental and numerical results with different mesh sizes; Deformed shape of (b) 6×5 mesh, (c) 12×10 mesh and (d) 24×20 mesh at 2.8 mm displacement

Table 3.2. Computational cost for different mesh sizes

Mesh size	Analysis time	Allocated memory
6×5	6 min	7 MB
12×10	30 min	26 MB
24×20	128 min	78 MB

3.6 Numerical tests with macroelement models

The previous numerical simulations have confirmed that FE models with shell elements allowing for geometric and material nonlinearity enable accurate predictions of the main response characteristics of steel panels subject to in-plane cyclic loading. On the other hand, detailed FE models for steel panels are computationally demanding, thus they are not suitable to represent realistic steel shear walls within 3D models for framed buildings under earthquake loading. However, such models are based on an objective description of the physical panels, thus they can be used to validate and calibrate more efficient phenomenological models considering the variation of geometry and material properties for the steel wall components. Obviously, the calibration of phenomenological efficient models, as the developed macroscale formulation, could be based also on experimental data, but this is not feasible due to the lack of experimental tests on steel wall panels under cyclic loading.

In initial numerical tests, the developed macroelement has been employed to simulate the shear response of the steel panel of the SW2 specimen introduced previously assuming different values for some key model material parameters, and the numerical results are compared against the numerical curves obtained by the validated FE model assumed as the baseline model.

The FE model with a 12×10 mesh of shell elements is restrained at the base, and a horizontal in-plane displacement is applied at the top edge considering the cyclic displacement history in Fig. 3.8. A linear variation of horizontal displacement from the bottom to the top edge is considered to impose shear deformations on the panel. The same material parameters employed in the previous comparisons against experimental data for the validation of the FE model with shell elements are adopted also in this numerical study. Fig. 3.12 shows the deformed shape predicted by the FE model at 2.8 mm top displacement which indicates clear out-of-plane buckling of the plate.

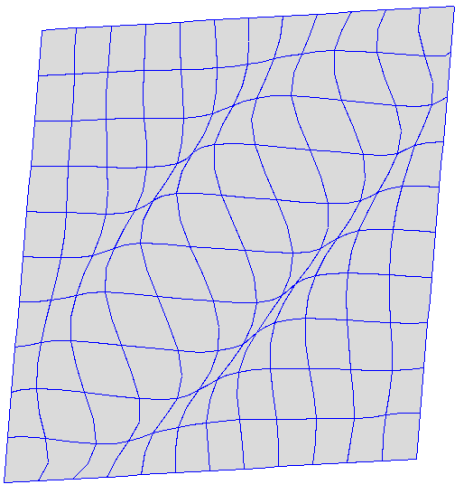

Fig. 3.12. Deformed shape of the FE model at 2.8 mm displacement

A macroelement model for the steel plate has been developed and then subjected to the same displacement history at the top edge. The model material parameters for the internal and corner spring components $\{E_s,\ f_{tp},\ f_{cp},\ \mu,\ \beta,\ \gamma,\ \kappa\}$ have been derived following the recommendations in Section 3.4. More specifically, the inclination angle of the tension field is taken as $\alpha = tan^{-1}\sqrt[4]{1} = 45°$, which is a simplified assumption for the case without boundary beams or columns. Since the plate is square, the angle θ is equal to 45°. As a result, the shear strength deviation factor and tensile yield strength for the material model are calculated as $\eta = sin\,2\theta/sin\,2\alpha = 1$, $f_{tp} = \eta f_y = 219\ \mathrm{N/mm^2}$. Using Eqs (3.3) and (3.4), the cross-sectional areas of the corner and internal braces are calculated as $A_c = 72.4\ \mathrm{mm^2}$ and $A_i = 144.8\ \mathrm{mm^2}$, respectively. The effective area factors and the buckling reduction factors of the two types of braces are $\rho_c = 0.4910$, $\chi_c = 0.0152$ and $\rho_i = 0.2627$, $\chi_i = 0.1081$. The strain hardening in tension and strength degradation in compression is assumed as $\mu = 0.01$ and $\beta = -0.005$, repevtively. Referring to Choi-Park constitutive model, the residual strength parameter at the strain reversal point is initially taken as $\gamma = 0.2$ (Choi and Park, 2010). Different values for the yield strength in compression f_{cp} and the degree of stiffness reduction κ have been assumed in a parametric study and the results are compared against the numerical curves provided by the validated FE model with shell elements.

To investigate the influence of f_{cp}, three different cases were considered:

- Case 1, $f_{cp} = 0$ (Fig. 3.13(a)). Compression strength is completely ignored, which corresponds to what is assumed in the strip models put forward by Timler and Kulak (1983) and Tian et al. (2015);
- Case 2, $f_{cp} = \rho f_y$ (Fig. 3.13(b)). Compression resistance for Class 4 cross-sections (EN1993-1-1, 2005; EN1993-1-5, 2005) is assumed;
- Case 3, $f_{cp} = \chi \rho f_y$ (Fig. 3.13(c)). Out-of-plane buckling resistance for Class 4 cross-sections is employed.

In further numerical simulations, f_{cp} was set as $\chi \rho f_y$ and three different degrees of stiffness reduction factors were considered:

- Case 3, $\kappa = 1$ (Fig. 3.13(c)). Full stiffness reduction is assumed, meaning that the yield point for a new cycle corresponds to the point at the maximum stress (post yielding) in the previous cycle;
- Case 4, $\kappa = 0.5$ (Fig. 3.13(d)). Half stiffness reduction is considered, thus the yield point of the new cycle locates at the mid-point between the initial yield point and the maximum stress point of the previous cycle;
- Case 5, $\kappa = 0$ (Fig. 3.13(e)). Stiffness reduction is ignored and the yield point remains unchanged for all the cycles.

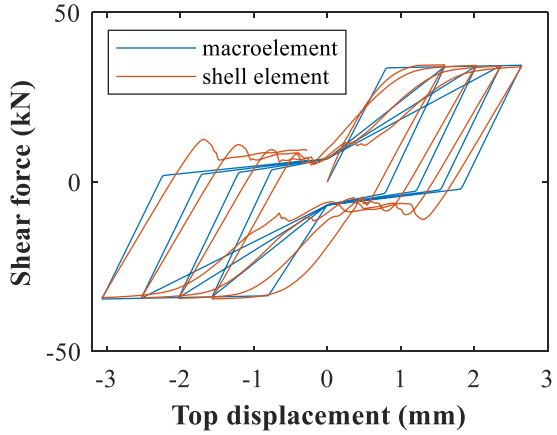

(a) Case 1: $f_{cp} = 0, \kappa = 1$

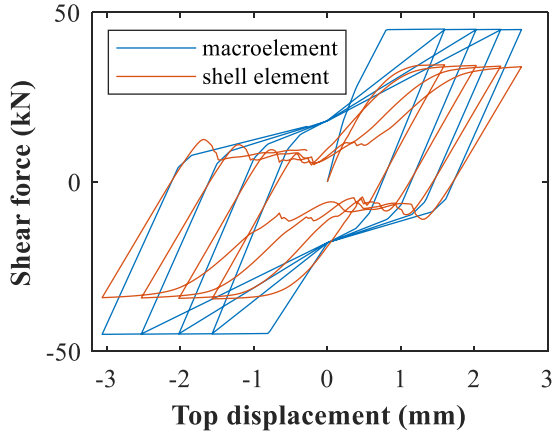

(b) Case 2: $f_{cp} = \rho f_y, \kappa = 1$

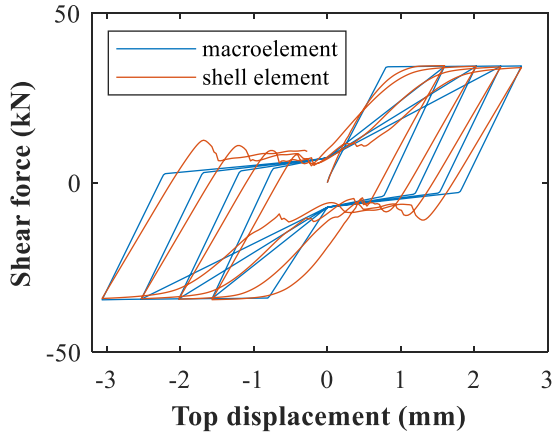

(c) Case 3: $f_{cp} = \chi \rho f_y, \kappa = 1$

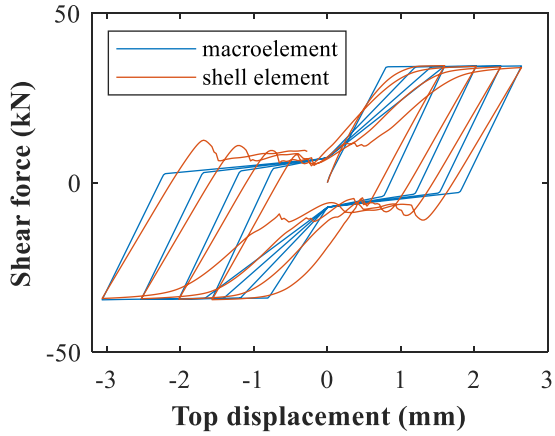

(d) Case 4: $f_{cp} = \chi \rho f_y, \kappa = 0.5$

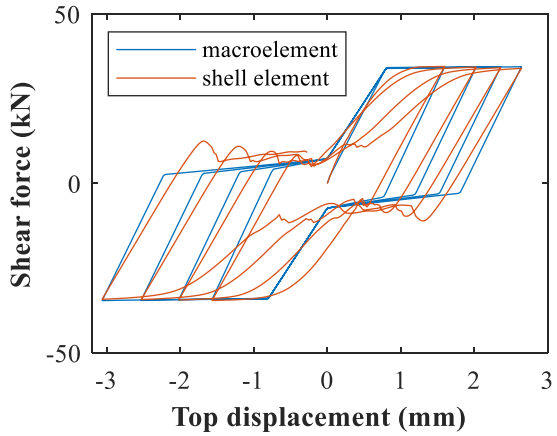

(e) Case 5: $f_{cp} = \chi \rho f_y, \kappa = 0$

Fig. 3.13. Load displacement curve obtained by using macroelement models with different model material parameters

Several crucial features are compared between the results of macroelement and shell element. Deviations of the macroelement results from the shell element result are calculated in the same process when comparing the experimental and shell element results, and the calculation values are listed in Table 3.3. The calculation process is straightforward, e.g. the equation for dissipated energy (E_d) deviation can be written as $(E_d^M - E_d^S)/E_d^S \times 100\%$, where the macroelement and shell element model are indicated by subscript M and S, respectively.

It can be noted that Case 1 and Case 3 provide a good estimate for yield strength, ultimate strength and residual strength whilst underestimating the dissipated energy. Case 2 overestimates all the critical strength features resulting in an excessively large prediction for the dissipated energy. This indicates that compressive yield strength f_{cp} should be taken as a value between $\chi\rho f_y$ and ρf_y limits. Cases 3, 4 and 5 indicate that the factor κ affects not also stiffness degradation, but also residual strength and that a value in the range 0.7~0.8 should be used to achieve accurate results.

Table 3.3. Deviations of macroelement results from shell element model

Deviation	Dissipated energy	Yield strength	Ultimate strength	Residual strength	Stiffness in final cycle
Case 1	-9.01%	3.03%	-0.34%	-2.22%	-12.22%
Case 2	43.04%	37.57%	30.60%	60.09%	-13.81%
Case 3	-6.43%	4.71%	-0.25%	3.20%	-13.28%
Case 4	5.60%	4.71%	-0.25%	4.68%	28.43%
Case 5	17.63%	4.71%	-0.25%	8.79%	151.22%

3.7 Concluding remarks

In this chapter, a novel simplified 8-noded macroelement formulation for unstiffened thin steel shear walls is proposed. It includes six nonlinear springs with a newly defined asymmetric constitutive model. The proposed macroelement is inspired by the Tian's three-strip model (Tian et al., 2015) and the Choi-Park's material model (Choi and Park, 2010), and it is developed within a 3D FE framework. The model is capable of representing the cyclic nonlinear response of steel panels, including the strain-hardening, residual shear strength by increasing the loading cycles, elastic stiffness degradation and pinching effects. Furthermore, the macroelement formulation guarantees computational efficiency, making it suitable for modelling large-scale structures under seismic loading.

The phenomenological formulation of the macroelement is discussed in detail. It allows for the development of a tension field within a steel panel and the contribution of the compressed parts of the panel when it is subjected to shear loading. The nonlinear constitutive model proposed for the nonlinear springs of the macroelement is also described, and the different model material parameters are specified.

Because of the lack of extensive experimental results that may be used for the calibration of phenomenological simplified models, a detailed FE description with nonlinear 9-noded shell elements has been introduced first. This was validated against experimental results and employed as a baseline model in subsequent numerical tests for the verification of the developed macroelement. The test results indicate that the macroelement with the initial assumptions for model material parameters cannot fully represent all the key response characteristics of steel shear wall components, indicating the need for detailed model calibration which will be addressed in Chapter 4.

Chapter 4

Calibration of the Macroelement for Steel Shear Walls

4.1 Introduction

The preliminary tests on the proposed macroelement in Chapter 3 have shown that a straightforward definition of the model material parameters may lead to inaccurate predictions of the main response characteristics of steel wall panels under cyclic loading. Thus, more detailed model calibration is required to improve accuracy.

The calibration of the macroelement material parameters is treated as a multi-objective optimisation problem in this research, where an equivalence between macroelement and shell element models is assumed based on virtual tests representing steel panels under cyclic shear loading. As pointed out in Chapter 3, FE models with shell elements, though computationally

expensive, provide an objective description of the panel response, so they can make up for the lack of experimental data in the calibration of more efficient phenomenological models.

For the ease of applying the proposed macroelement description in nonlinear simulations of structures incorporating steel shear walls under earthquake loading, simple expressions have been determined to derive the material model parameters from the main geometrical characteristics of steel wall elements using multiple linear regression. To achieve this, model calibration on a large population of realistic panel configurations with various lengths, heights and thicknesses has been carried out to find optimal sets of material parameters.

In this chapter, the calibration methodology is described first in Section 4.2. Subsequently, Sections 4.3 and 4.4 apply the calibration to the numerical example investigated in Section 3.5 and to steel shear wall samples to derive simple relationships for the model material parameters, respectively. Finally, the calibrated macroelements are compared against detailed FE models with shell elements in nonlinear simulations of a representative substandard RC frame equipped with different types of steel shear walls in Section 4.5.

4.2 Calibration methodology

The model calibration strategy concerns the following set of material parameters for the nonlinear springs of the developed macroelement introduced in Chapter 3:

- strain-hardening parameter in tension μ;
- degradation in compression coefficient β;
- residual strength factor at strain reversal factor γ;
- shear strength deviation parameter η;
- buckling reduction factor χ;
- degree of stiffness degradation κ.

The non-dominated sorting genetic algorithm NSGA-II (Deb et al., 2002) for multi-objective optimisation is applied to find the solutions to the optimisation problem for model calibration. The optimal set of material parameters $\boldsymbol{p} = \{\mu,\ \beta,\ \gamma,\ \chi,\ \eta,\ \kappa\}$ for a given panel configuration is obtained by minimising objective functions representing discrepancies between some response characteristics predicted by the baseline FE model with shell elements and the macroelement counterpart. Thus, the first step of the calibration procedure requires the development of a FE model with shell elements and an equivalent macroelement model to simulate the response of a steel panel under shear cyclic loading.

The transition from the shell element to the macroelement first considers the dissipated energy equivalence for the steel shear wall component, which can be achieved by equating the work done by the total shear force for the analysed steel panel. Thus, the first objective function f_1 considers the discrepancy in dissipated energy between the macroelement and the shell element models according to the procedure put forward in Chisari et al. (2019) and Chisari et al. (2020):

$$f_1(\boldsymbol{p}) = \int_0^T [dW^M(\boldsymbol{p}, t)/dt - dW^S(t)/dt]^2 dt \tag{4.1}$$

where $dW(t)$ is the incremental work done by the base shear force $F(t)$ for the lateral displacement during the time $[0, T]$. The subscripts M and S indicate the macroelement and shell element model, respectively. In the case of lateral-displacement-only boundary conditions, identical incremental lateral displacement du/dt at each step and loading application to the same nodes of two models, Eq. 4.1 can be simplified as:

$$\begin{aligned} f_1(\boldsymbol{p}) &= \int_0^T [dW^M(\boldsymbol{p}, t) - dW^S(t)]^2 \\ &= \int_0^T \left[\left(F^M(\boldsymbol{p}, t) - F^S(t)\right) du/dt\right]^2 dt \end{aligned} \tag{4.2}$$

However, minimising only the energy discrepancy f_1 may result in an inconsistent shape of the macroelement force-displacement curve. Since the single-objective optimisation searches only for the best fit with the closest area enclosed by the curve, preliminary studies have shown that

the numerical curve could end up with relatively large tension ultimate strength and stiffness but underestimated tension yield strength, compression strength and residual strength, although the enclosed area is still quite close to the target value, or vice versa (Chisari et al., 2020). Besides, as there are six variables in this optimisation problem, adopting only one objective function may lead to difficulties in achieving convergence within an acceptable maximum number of iterations.

As a result, additional response characteristics are introduced into the optimisation formulation by defining a second objective function f_2. Some engineering features $\boldsymbol{\Phi}$ are extracted from the shear force – displacement curves for both shell element and macroelement models. They include elastic stiffness, yielding force, maximum force and residual force after compression unloading. The second objective function is thus defined as (Chisari et al., 2020):

$$f_2(\boldsymbol{p}) = (\boldsymbol{\Phi}^M(\boldsymbol{p}) - \boldsymbol{\Phi}^S)^T \cdot \boldsymbol{W} \cdot (\boldsymbol{\Phi}^M(\boldsymbol{p}) - \boldsymbol{\Phi}^S) \tag{4.3}$$

where $\boldsymbol{\Phi} = \{K_{in}\ \ K_{fin}\ \ F_y\ \ F_{max}\ \ F_{res}\}^{\mathrm{T}}$ is the response characteristics vector;

- K_{in}, K_{fin} are stiffness values in the initial and final loading cycle, respectively;
- F_y, F_{max}, F_{res} are yielding force, maximum force and residual force after compression unloading;
- $\boldsymbol{W} = diag\left[\left(F_{max}^S / K_{in}^S\right)^2\ \ \left(F_{max}^S / K_{in}^S\right)^2\ \ 1\ \ 1\ \ 1\right]$ is the weight matrix considering different physical units in $\boldsymbol{\Phi}$.

In conclusion, the studied multi-objective optimisation problem can be written as:

$$\begin{cases} Find\ \ \boldsymbol{p} = \{\mu, \beta, \gamma, \chi, \eta, \kappa\} \\ min\ \ f_1(\boldsymbol{p}) = \int_0^T \left[\left(F^M(\boldsymbol{p}, t) - F^S(t)\right) du/dt\right]^2 dt \\ min\ \ f_2(\boldsymbol{p}) = (\boldsymbol{\Phi}^M(\boldsymbol{p}) - \boldsymbol{\Phi}^S)^T \cdot \boldsymbol{W} \cdot (\boldsymbol{\Phi}^M(\boldsymbol{p}) - \boldsymbol{\Phi}^S) \end{cases} \tag{4.4}$$

the solutions of which are included in the Pareto Front. Genetic Algorithms (GAs) are employed to find the optimal sets of material parameters. The MATLAB function '*gamultiobj*' available in the *Global Optimisation Toolbox* (MathWorks, 2020) is applied, which is based upon the NSGA-II procedure (Deb et al., 2002). Considering the definition of the parameters and engineering judgement, the searching bounds for the material parameters are set as $\mu \in [0,0.1]$, $\beta \in [-0.1,0]$, $\gamma \in [0,1]$, $\chi \in [0,1]$, $\eta \in [0,2]$, $\kappa \in [0,1]$. Population size, crossover ratio, and the maximum number of iterations are set as 200, 0.8 and 1200, respectively, which are the recommended values for an optimisation problem with six variables (MathWorks, 2020). For the mutation of this optimisation problem with constraints, the adaptive feasible function method is selected to generate mutations randomly while still satisfying bounds and linear constraints.

4.3 Numerical example

The numerical example in Section 3.5, which is based on the experimental test on the SW2 specimen carried out by Roberts and Ghomi (1991), is selected to test the proposed calibration procedure. For the ease of evaluating the errors of the two objective functions and selecting the optimal case on the Pareto front, the objectives for each case on the Pareto Front are transformed to relative values, which can be written as:

$$\begin{cases} f_1'(\boldsymbol{p}) = \dfrac{\int_0^T \left[\left(F^M(\boldsymbol{p},t) - F^S(t)\right)du/dt\right]^2 dt}{\int_0^T (F^S(t)\cdot du/dt)^2\, dt} \\ f_2'(\boldsymbol{p}) = \dfrac{(\boldsymbol{\Phi}^M(\boldsymbol{p}) - \boldsymbol{\Phi}^S)^T \cdot \boldsymbol{W} \cdot (\boldsymbol{\Phi}^M(\boldsymbol{p}) - \boldsymbol{\Phi}^S)}{(\boldsymbol{\Phi}^S)^T \cdot \boldsymbol{W} \cdot \boldsymbol{\Phi}^S} \end{cases} \tag{4.5}$$

Fig. 4.1 and Fig. 4.2 show the Pareto Front of the optimisation problem and the corresponding macroelement results with the material parameter equal to the Pareto Front solutions compared with the shell element results. As observed from the figures, the relative errors of both objectives are negligible for all the cases on the Pareto Front, and the macroelement numerical curves are practically identical. The two figures indicate that GA returns a suitable optimal result for the multi-objective optimisation problem. For a definitive selection, the case with the

minimum summation of the 1st and 2nd relative objective values, which is marked with a black circle in Fig. 4.1, is chosen as the representative solution of the Pareto Front cases.

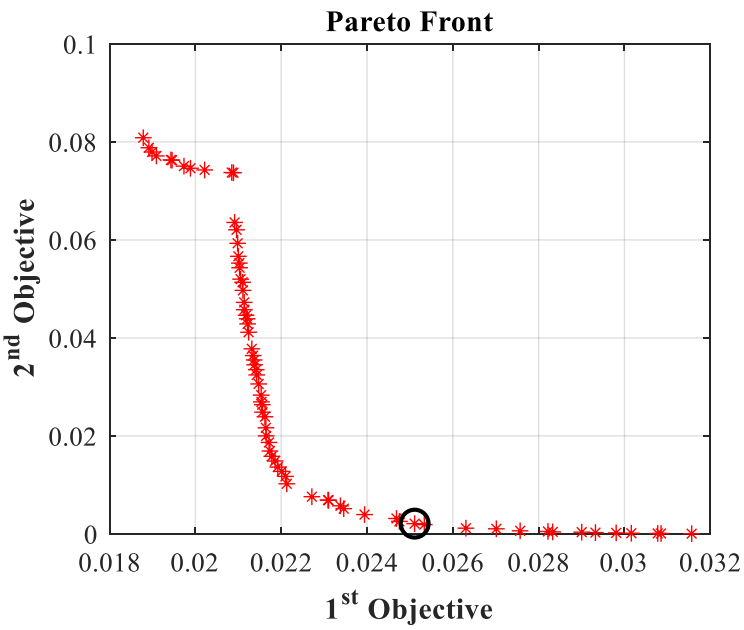

Fig. 4.1. The optimisation Pareto Front for $\boldsymbol{p} = \{\mu, \beta, \gamma, \chi, \eta, \kappa\}$

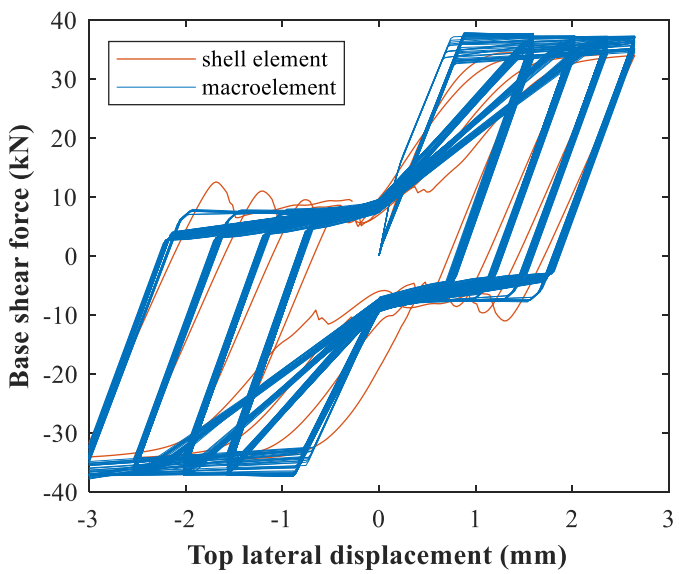

Fig. 4.2. Optimal solutions on Pareto Front in comparison with shell element results

Fig. 4.3 shows the numerical result comparison of the selected optimal case, the material parameters of which are $\mu = 0.0253$, $\beta = -0.0406$, $\gamma = 0.2165$, $\chi = 0.0459$, $\eta = 0.9676$ and $\kappa = 0.7760$. It is obvious that the proposed macroelement with the calibrated material parameters provides a good representation of the nonlinear response of the analysed steel shear wall, as predicted by the more detailed shell element model, including elastic stiffness, maximum shear force and stiffness degradation upon unloading and subsequent reloading.

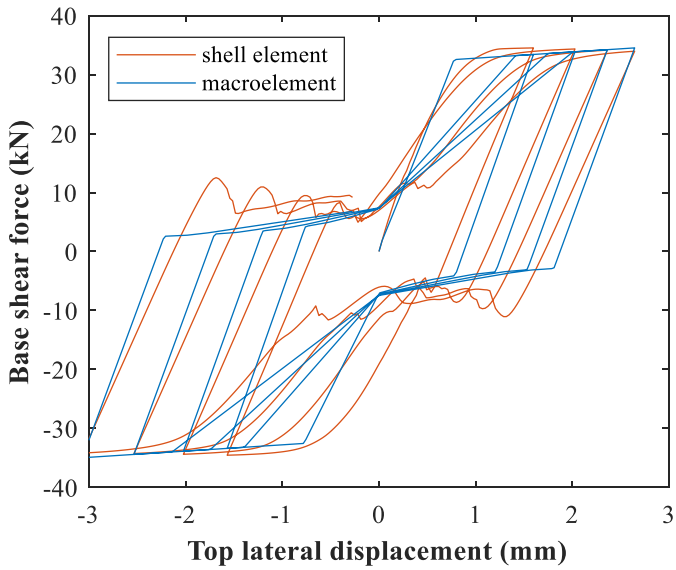

Fig. 4.3. Numerical result comparison of the selected optimal case

In a subsequent verification study, the material parameters of the optimal solution have been considered in the simulation of the SW2 specimen with boundary frame elements (Roberts and Ghomi, 1991). The force – top displacement curve determined by the model with the calibrated macroelement for the steel panel is compared against both experimental and numerical shell model results in Fig. 4.4. A good agreement between the three curves confirms that the macroelement with calibrated material parameters is capable of accurately representing the steel shear wall response.

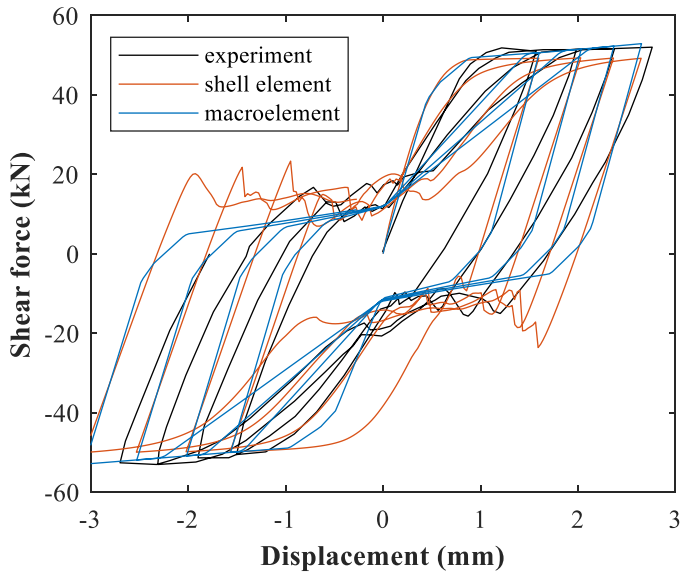

Fig. 4.4. Comparison among experiment, shell element and macroelement results for SW2 specimen with boundary frame (Roberts and Ghomi, 1991)

4.4 Multiple linear regression for material parameters

The calibration procedure for the material parameters of the macroelement model for steel shear wall panels has been applied to numerous samples with various lengths L, heights h and thicknesses t. The calibration results for the large population of realistic panel configurations have been further processed by multiple linear regression (MLR) to establish simple relationships for the material parameter set $\{\mu,\ \beta,\ \gamma,\ \chi,\ \eta,\ \kappa\}$ in terms of $(L,\ h,\ t)$.

4.4.1 Basic concept of multiple linear regression

MLR is a method for fitting a linear model between one dependent variable or response and more than one independent or regressor variable (Montgomery and Runger, 2010). In general, the relationship between one dependent variable Y and k independent variables x_j $(j = 1,2,\dots,k)$ can be written as:

$$Y = \theta_0 + \theta_1 x_1 + \theta_2 x_2 + \cdots + \theta_k x_k \tag{4.6}$$

where the parameters θ_j $(j = 0,1, \dots, k)$ are the so-called regression coefficients. MLR has been widely used to analyse multifactor effects.

Higher-order models with multiple variables representing interaction effects can also be analysed by MLR as long as the approximation is linear in terms of the regression coefficients θ_j. An example of a complete quadratic model with two variables can be typically written as:

$$Y = \theta_0 + \theta_1 x_1 + \theta_2 x_2 + \theta_{11} {x_1}^2 + \theta_{22} {x_2}^2 + \theta_{12} x_1 x_2 \tag{4.7}$$

If x_3, x_4, x_5 are assigned as ${x_1}^2, {x_2}^2, x_1 x_2$, respectively, and $\theta_{11}, \theta_{22}, \theta_{12}$ are substituted by $\theta_3, \theta_4, \theta_5$, Eq. 4.7 can be rewritten as an MLR model:

$$Y = \theta_0 + \theta_1 x_1 + \theta_2 x_2 + \theta_3 x_3 + \theta_4 x_4 + \theta_5 x_5 \tag{4.8}$$

The regression coefficients are commonly estimated by the least-squares method. Suppose an MLR model with $n > k$ observed responses denoted as $(x_{i1}, x_{i2}, \dots, x_{ik}, y_i)$, $i = 1, 2, \dots, n$. Each observed response can be written as:

$$\begin{aligned} y_i &= \theta_0 + \theta_1 x_{i1} + \theta_2 x_{i2} + \cdots + \theta_k x_{ik} + \varepsilon_i \\ &= \theta_0 + \sum_{j=1}^{k} \theta_j x_{ij} + \varepsilon_i \end{aligned} \tag{4.9}$$

where ε_i is the residual, which is the difference between the observation y_i and the fitted value $\hat{y}_i$ estimated by the MLR model. The least-squares function is considered as the sum of the squared residuals for all cases, which is:

$$L(\theta) = \sum_{i=1}^{n} {\varepsilon_i}^2 = \sum_{i=1}^{n} (y_i - \theta_0 - \sum_{j=1}^{k} \theta_j x_{ij})^2 \tag{4.10}$$

By minimising $L(\theta)$ for each θ_j, the following equations are adopted to solve the regression coefficients $\hat{\theta}_0, \hat{\theta}_1, \dots \hat{\theta}_k$:

$$\frac{\partial L(\theta)}{\partial \theta_0} = -2\sum_{i=1}^{n}\left(y_i - \hat{\theta}_0 - \sum_{j=1}^{k}\hat{\theta}_j x_{ij}\right) = 0$$
$$\frac{\partial L(\theta)}{\partial \theta_j} = -2\sum_{i=1}^{n}\left(y_i - \hat{\theta}_0 - \sum_{j=1}^{k}\hat{\theta}_j x_{ij}\right)x_{ij} = 0 \quad j = 1, 2, \dots, k \tag{4.11}$$

The regression coefficients can also be solved by the normal equation method, which starts by expressing the MLR model in Eq. 4.9 in matrix notations as:

$$\{y\} = [X]\{\theta\} + \{\varepsilon\} \tag{4.12}$$

where $\{y\} = \begin{Bmatrix} y_1 \\ y_2 \\ \vdots \\ y_n \end{Bmatrix}$ $[X] = \begin{bmatrix} 1 & x_{11} & x_{12} & \dots & x_{1k} \\ 1 & x_{21} & x_{22} & \dots & x_{2k} \\ \vdots & \vdots & \vdots & & \vdots \\ 1 & x_{n1} & x_{n2} & \dots & x_{nk} \end{bmatrix}$ $\{\theta\} = \begin{Bmatrix} \theta_1 \\ \theta_2 \\ \vdots \\ \theta_k \end{Bmatrix}$ and $\{\varepsilon\} = \begin{Bmatrix} \varepsilon_1 \\ \varepsilon_2 \\ \vdots \\ \varepsilon_n \end{Bmatrix}$

The least-squares function can be written as:

$$L(\theta) = [\{y\} - [X]\{\theta\}]^T[\{y\} - [X]\{\theta\}] \tag{4.13}$$

The regression coefficient matrix $\{\hat{\theta}\}$ is the solution of $\partial L(\theta) \,/\, \partial\{\hat{\theta}\} = 0$. Using the normal equation method, $\{\hat{\theta}\}$ can be solved as:

$$\{\hat{\theta}\} = ([X]^T[X])^{-1}[X]^T\{y\} \tag{4.14}$$

The MLR is carried out and verified under supervised machine learning concepts (Alpaydin, 2020). The observation dataset is divided into two parts, a training set and a testing set. The training set is adopted to find solutions for the hypothetical MLR function, whereas the testing

set is used to evaluate how well the hypothesis performs on new instances by reporting the generalisation error of the test data. It is worth noting that if the given training set contains only a small part of all possible cases, an ill-posed problem will arise where the data is insufficient to solve the regression function. Increasing the amount of training data returns a more accurate fit, although the generalisation error usually increases at the same time. The complexity of the hypothesis function also affects the fitting accuracy. Underfitting may happen if the hypothesis is expressed as a polynomial of lower order than that of the function underlying the data. When the hypothesis complexity is increased, the error of the training set decreases, indicating that the hypothetical function leads to an improved representation of the training data. However, overfitting will happen if the hypothesis is too complex and considers the noise in the data. This problem can be avoided by examining the generalisation error using the testing set. In collusion, there is a trade-off between three factors, namely the triple trade-off (Dietterich, 1997; Dietterich, 2003):

- the training data size;
- the complexity of the hypothesis; and
- the generalisation error on new data.

4.4.2 Virtual tests on shell element models

Virtual tests using shell elements are first performed to represent the response of steel shear walls under a shear deformation mode, because of the impracticality of using data from experimental tests. Then the calibration procedure is carried out based on the results obtained by shell element models.

For the selection of numerical samples for the virtual tests, the steel wall height L is set as 500 mm to 6000 mm with a 500 interval, namely 500 mm, 1000 mm, 1500 mm, …, 6000 mm. Considering the general design requirements and drift limits of boundary elements referred to ANSI/AISC 341-16 (AISC, 2016), the aspect ratios of length over height and length over thickness are typically limited to $0.8 \leq L/h \leq 2.5$ and $250 \leq L/t \leq 1000$, respectively. Therefore, for each length L, the height h is generated between $L/2.5$ and $L/0.8$ with 20 evenly spaced values rounded to centimetre and no larger than 4000 mm in view of realistic

storey heights. Up to 10 equal-difference values of thickness t are selected within the range $L/1000$ and $L/250$ and rounded to integer numbers.

A mesh of 12×10 9-noded shell elements (Izzuddin and Liang, 2020) is adopted to model each sample, where Young's modulus and yield strength of the steel material model is equal to 235 MPa and 210000 MPa, respectively. The shell element model is fully restrained at the bottom edge. Considering the rehabilitation drift requirements for RC framed structures under collapse performance level (FEMA, 2000) and experimental test records (Choi and Park, 2009), the maximum lateral drift is limited to 6.0% of the steel panel height, which corresponds to the inter-storey height of the retrofitted frame building. As a result, the sampling model is subjected to lateral cyclic displacements set at the top edge as $\pm 0.2\%$, 0.4%, 0.8%, 1.2%, 1.6%, 2.0%, 3.0%, 4.0%, 5.0% and 6.0% of the steel panel height. The shear force – top displacement cyclic curves for each sample are obtained by performing nonlinear simulations using ADAPTIC (Izzuddin, 1991).

4.4.3 Regression for material parameters of constitutive model

Based on each shell element result, six critical material parameters of the macroelement constitutive model are calibrated following the procedure in Section 4.2. The optimal calibration results for the parameter set $\{\mu,\ \beta,\ \gamma,\ \chi,\ \eta,\ \kappa\}$ are stored together with the steel panel properties $(L,\ h,\ t)$ as the regression dataset.

The dataset obtained from the macroelement calibration procedure is then randomly separated into 85% for training and 15% for testing. For the training set, the linear regression model '*fitlm*' available in MATLAB *Statistic and Machine Learning Toolbox* (MathWorks, 2020) is first applied to find initial relationships with only linear and first-order terms of $(L,\ h,\ t)$. The function '*step*' is then used to automatically adjust the regression models to include up to cubic terms, so that only highly correlated 2nd and 3rd order predictors are added to the functions. Afterwards, the test data is substituted into the regression models to obtain predicted values which are compared with calibrated values, aiming to examine the fitness of the regression model. Root mean square errors (RMSEs) for each material parameter of both the training and testing dataset are listed in Table 4.1. RMSEs of testing data are slightly larger than those of

training data, and all the values are relatively small compared with the parameter value range, indicating that the regression models can provide a good fitting but not overfitting for the analysed data. Table 4.2 shows the estimated regression coefficients of the MLR functions for each material parameter with highly related higher-order terms selected by '*step*', where the slash sign '/' indicates that one predictor is not included in the regression function. Fig. 4.5 and Fig. 4.6 indicate the linear regression results (surfaces and lines) in comparison with the calibration results (blue dots) of the samples with 3000 mm length and 3000 mm height 10 mm thickness, respectively. Both figures prove that all the regression models are capable of capturing the variation trends of the material parameters.

Table 4.1. RMSE for material parameters

	μ	β	γ	χ	η	κ
Training data RMSE	0.0033	0.0106	0.0560	0.0347	0.0562	0.0924
Testing data RMSE	0.0033	0.0109	0.0578	0.0389	0.0590	0.0947

Table 4.2. Regression coefficients of MLR functions for material parameters

	μ	β	γ	χ	η	κ
Intercept	8.966e-03	-8.445e-02	3.748e-01	7.383e-01	8.816e-01	9.520e-01
L	1.667e-06	2.248e-05	1.948e-05	2.031e-04	-3.360e-04	-2.299e-04
h	-9.318e-07	3.586e-05	-1.517e-04	-4.351e-04	5.572e-04	1.418e-05
t	8.590e-04	/	6.151e-02	-5.969e-02	-1.429e-02	-4.289e-02
$L \cdot h$	-5.651e-10	-1.530e-08	3.955e-08	-1.636e-07	2.649e-07	/
$L \cdot t$	/	/	1.533e-06	/	9.844e-07	-1.778e-05
$h \cdot t$	/	/	-1.238e-05	1.400e-05	-6.636e-06	1.959e-05
L^2	/	/	-1.558e-08	1.378e-08	-3.482e-08	6.806e-08
h^2	5.337e-10	1.031e-09	/	1.972e-07	-3.238e-07	-2.795e-09
t^2	-5.814e-05	/	-2.394e-03	2.250e-03	1.664e-03	3.561e-03
$L \cdot h \cdot t$	/	/	/	/	1.155e-09	/
$L^2 \cdot h$	/	/	/	5.997e-12	-2.403e-11	/
$L^2 \cdot t$	/	/	/	/	/	1.450e-09
$L \cdot h^2$	/	2.554e-12	/	1.410e-11	/	/
$L \cdot t^2$	/	/	/	/	-2.245e-07	/
$h^2 \cdot t$	/	/	/	-1.955e-09	/	-2.364e-09
$h \cdot t^2$	/	/	3.659e-07	/	/	/
L^3	/	/	/	-1.692e-12	6.732e-12	-5.778e-12
h^3	/	-1.460e-12	/	-2.201e-11	2.985e-11	/
t^3	1.140e-06	/	2.477e-05	-5.553e-05	/	-7.527e-05

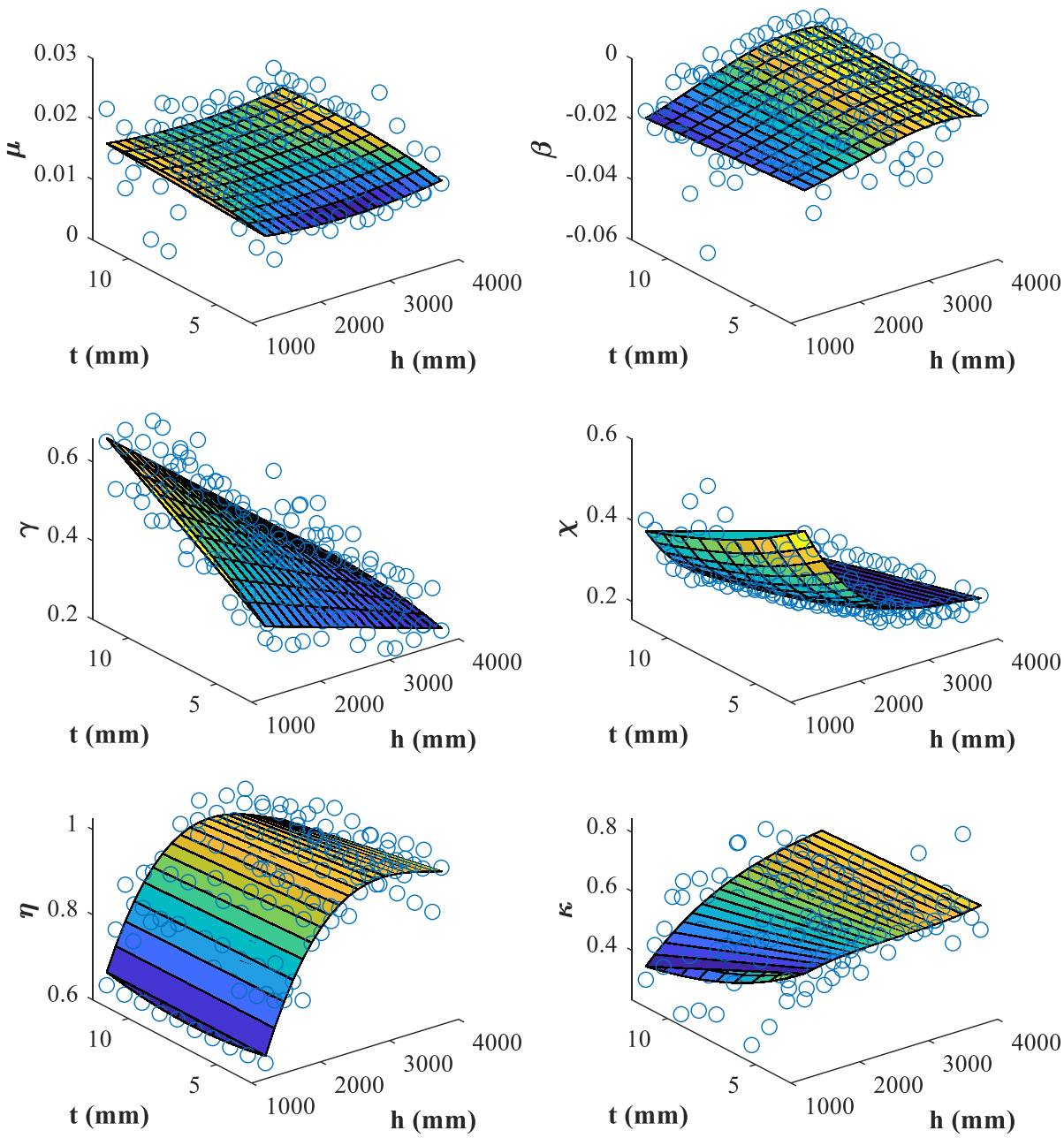

Fig. 4.5. Regression results for L = 3000 mm

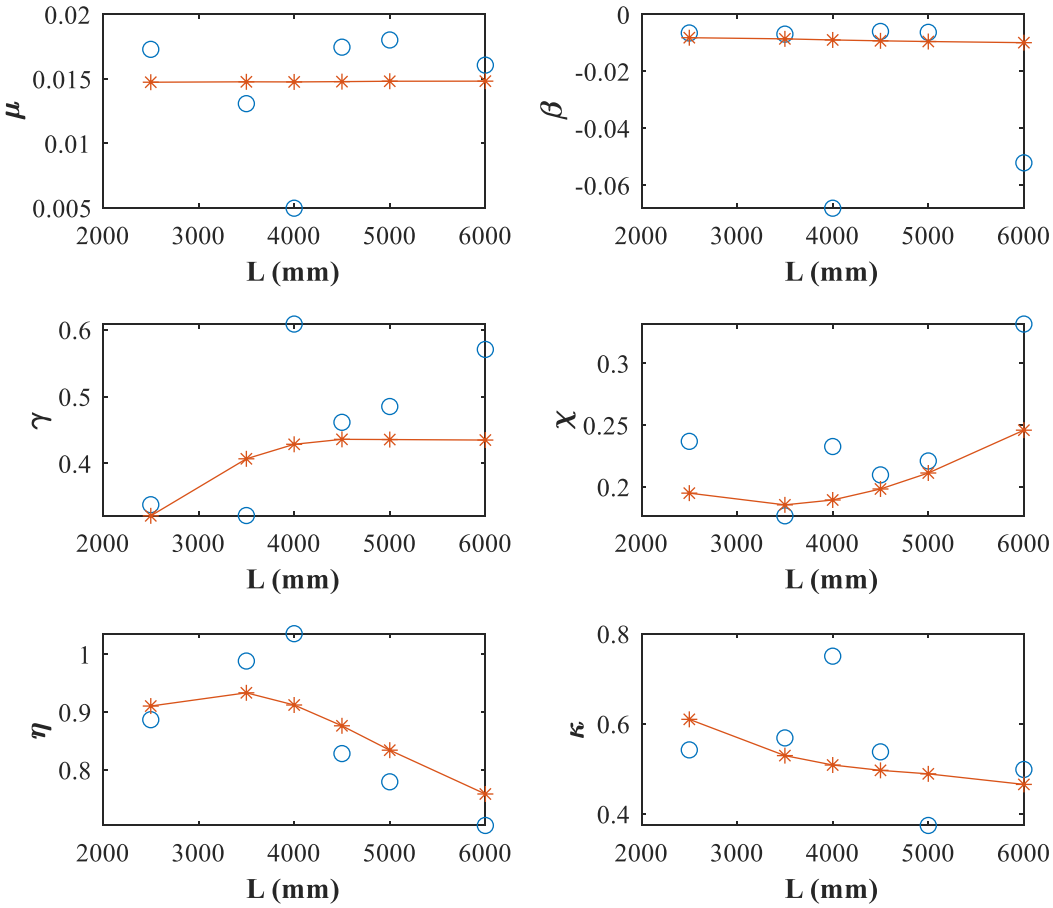

Fig. 4.6. Regression results for h = 3000 mm, t = 10 mm

Energy dissipation capacity is one of the most critical characteristics of steel shear walls under cyclic loading. As a result, the dissipated energy, which is the area enclosed by the base shear force – lateral displacement curve, is selected to measure the residuals of the regression models. The difference in dissipated energy is calculated for each case for the shell element model (indicated by subscript s) and the macroelement model using calibrated (mc) or predicted (mp) material parameters, respectively. Fig. 4.7 (c) presents the total residuals of dissipated energy for the predicted models of all the samples in comparison with the original data from the shell element model, which are induced by the errors stemming from both the calibration procedure shown in Fig. 4.7 (a) and the regression estimation illustrated in Fig. 4.7 (b). The total residual of most samples is in the range between a 3% overestimation and a 15% underestimation, indicating that the regression models for material parameters are quite satisfying and able to capture the energy dissipation level of steel shear walls.

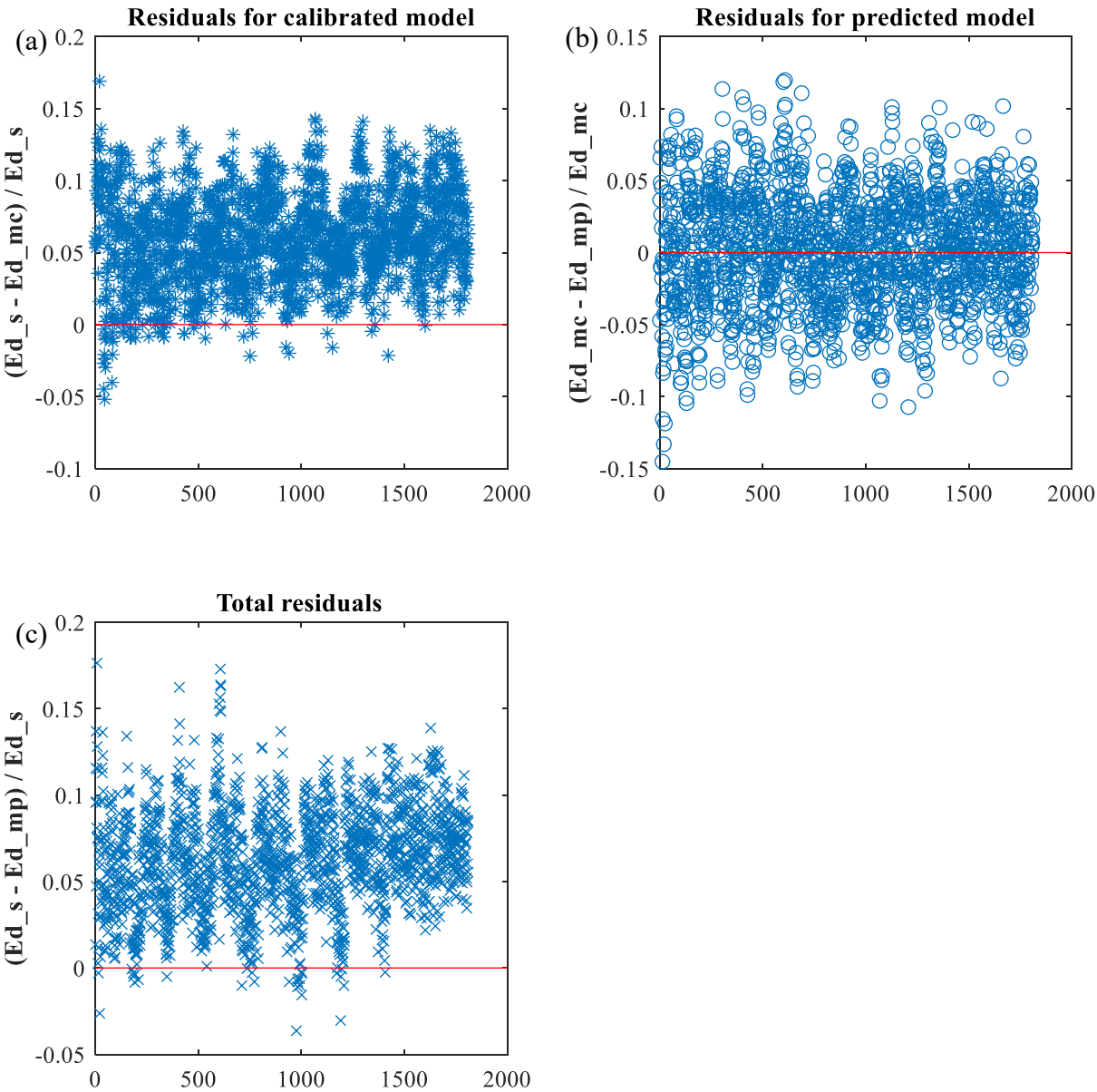

Fig. 4.7. Residuals of dissipated energy: (a) Residuals for calibrated models in comparison with shell element models; (b) Residuals for predicted models in comparison with calibrated models; (c) Total residuals for predicted models in comparison with shell element models

4.5 Numerical simulations of a 2-storey RC frame with steel shear wall

4.5.1 Numerical models for the RC frame and the steel shear walls

In order to assess further the accuracy and efficiency of the proposed modelling strategy for steel shear walls, the macroelement model has been employed in this study to represent steel shear wall panels within a retrofitted 2-storey RC frame. The numerical results under cyclic loading have been compared against the numerical predictions obtained by representing the steel shear wall elements by a FE mesh with nonlinear shell elements.

The analysed 2D RC frame has been extracted from a realistic substandard 4-storey RC framed building built in Italy in the 1960s and investigated numerically under seismic loading in previous research (Masjuki, 2017). The dimensions of the frame are shown in Fig. 4.8, where the FE mesh for the bare frame with nonlinear beam-column elements used for the nonlinear simulations is also displayed. Table 4.3 lists the geometrical characteristics of the RC columns and beams. Fig. 4.9 and Fig. 4.10 show the reinforcement details of columns and beams.

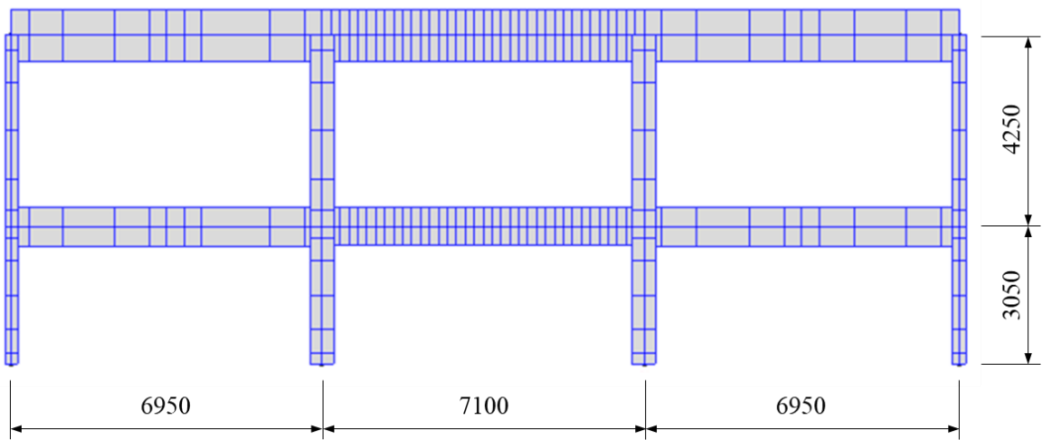

Fig. 4.8. FE mesh of the 2-storey RC frame (dimensions in mm)

Table 4.3. Geometrical characteristics of RC members of the 2-storey frame

Member ID		Width (mm)	Depth (mm)
Columns	C31	650	300
	C32	550	550
	C33	550	550
	C34	650	300
Beams	B3231	300	850
	B3332	300	850
	B3433	300	850

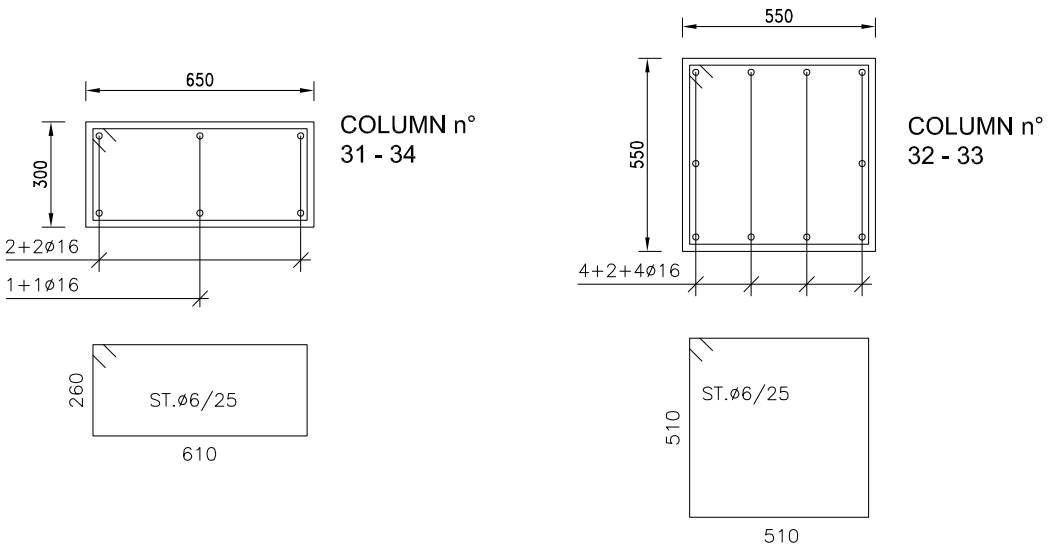

Fig. 4.9. Reinforcement details of columns on the 1st and 2nd floor (dimensions in mm) (Masjuki, 2017)

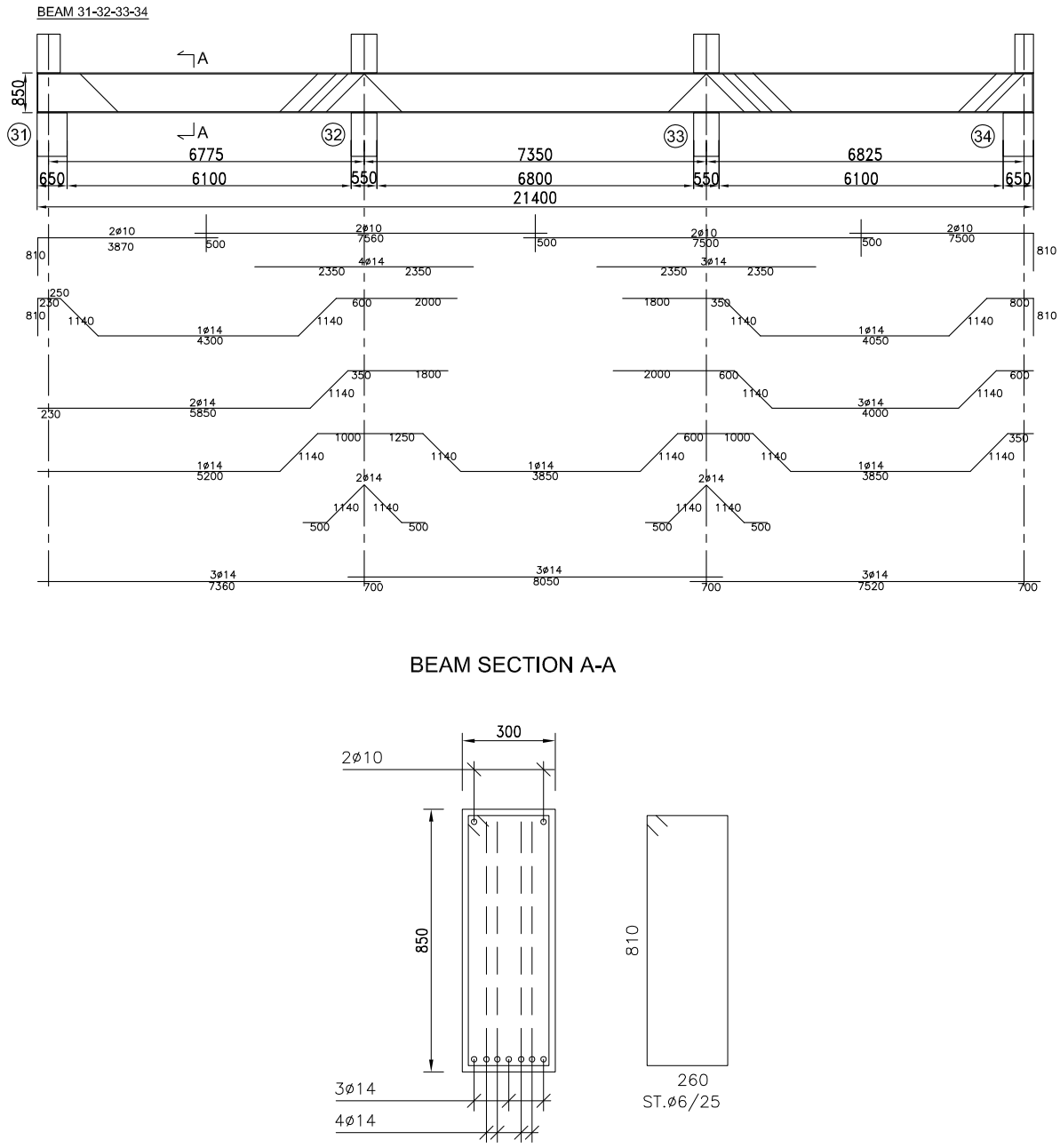

Fig. 4.10. Reinforcement details of Beam 31-32-33-34 on the 1st and 2nd floor (dimensions in mm) (Masjuki, 2017)

In the FE model for the frame (Fig. 4.8), RC beams and columns are represented using the fibre-type elasto-plastic beam-column elements 'cbp3' (Izzuddin and Lloyd Smith, 2000) in ADAPTIC. These elements allow not only for geometric nonlinearity effects utilising a co-rotation approach, but also for material nonlinearity of steel reinforcement and concrete. Cubic

shape functions are assumed for the transverse displacements $v(x)$ and $w(x)$ and six local freedoms and two Gauss points are set for each element, as shown in Fig. 4.11 where $\{\theta_{y1}, \theta_{z1}, \theta_{y2}, \theta_{z2}\}$ are the local rotations at the nodes, and $\{\Delta, \theta_T\}$ are the relative axial displacement and twist rotation, respectively. The cross section of each RC beam and column at each Gauss point is discretised into three parts with monitoring areas (Fig. 4.12), defining the behaviour of unconfined concrete, confined concrete and steel reinforcement separately.

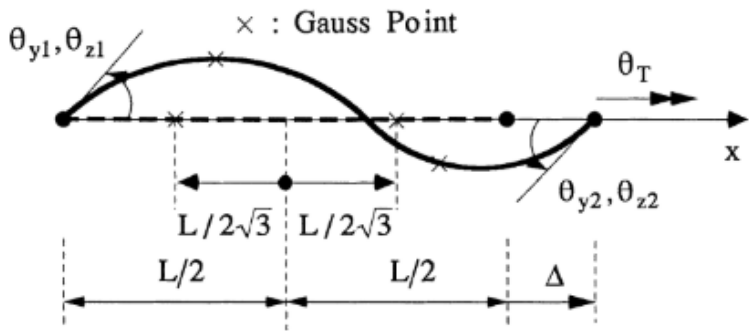

Fig. 4.11. Local freedoms and Gauss points of the elasto-plastic beam-column element (Izzuddin and Lloyd Smith, 2000)

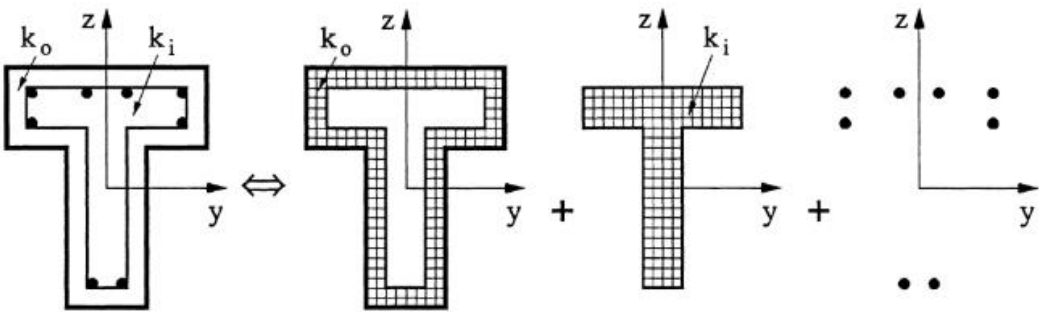

Fig. 4.12. Monitoring areas for RC sections (Izzuddin and Lloyd Smith, 2000)

The adopted material model for steel reinforcement corresponds to the bilinear model 'stl1' in ADAPTIC (Fig. 3.6(a)), while the elasto-plastic behaviour of concrete is represented by the concrete model 'con1' (Fig. 4.13) which is characterised by softening branches in tension and compression to allow for concrete cracking and crushing. Table 4.4 reports the material properties for the RC frame members and the material model parameters utilised in the numerical simulations.

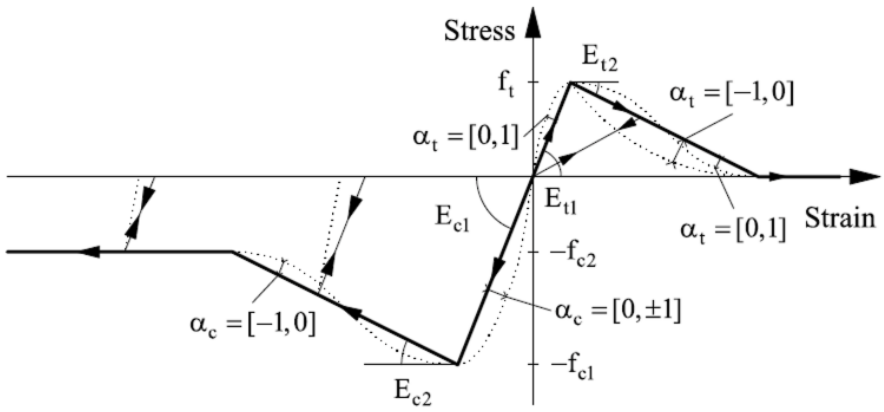

Fig. 4.13. Concrete material model 'con1' in ADAPTIC (Izzuddin, 2019)

Table 4.4. Material properties for concrete and steel reinforcement

Concrete compressive strength, f_{c1}	18.7 MPa
Concrete residual compressive strength, f_{c2}	18.7 MPa
Concrete tensile strength, f_t	0.001 MPa
Concrete secant stiffness E_{c1}, E_{t1}	26544 MPa
Concrete softening stiffness E_{c2}, E_{t2}	0 MPa
Steel reinforcement yield strength, f_y	382.5 MPa
Steel Young's modulus, E_s	210000 MPa

Steel shear walls with fully-infilled or partially-infilled plates have been considered in this numerical example. In both cases, the plates are 10 mm thick and made of structural steel with 235 MPa yield strength. The length of the fully-infilled walls corresponds to the bay length equal to 7100 mm, while the partially-filled wall is 2367 mm long (1/3 of the span). The two retrofitted frames are modelled using either one macroelement of a mesh of shell elements for each steel shear wall component at the two floor levels. Fig. 4.14 shows frame models with macroelements to represent fully-infilled and partially-infilled steel shear walls, while Fig. 4.15 displays retrofitted frame models where the steel shear walls are described by a mesh of shell elements.

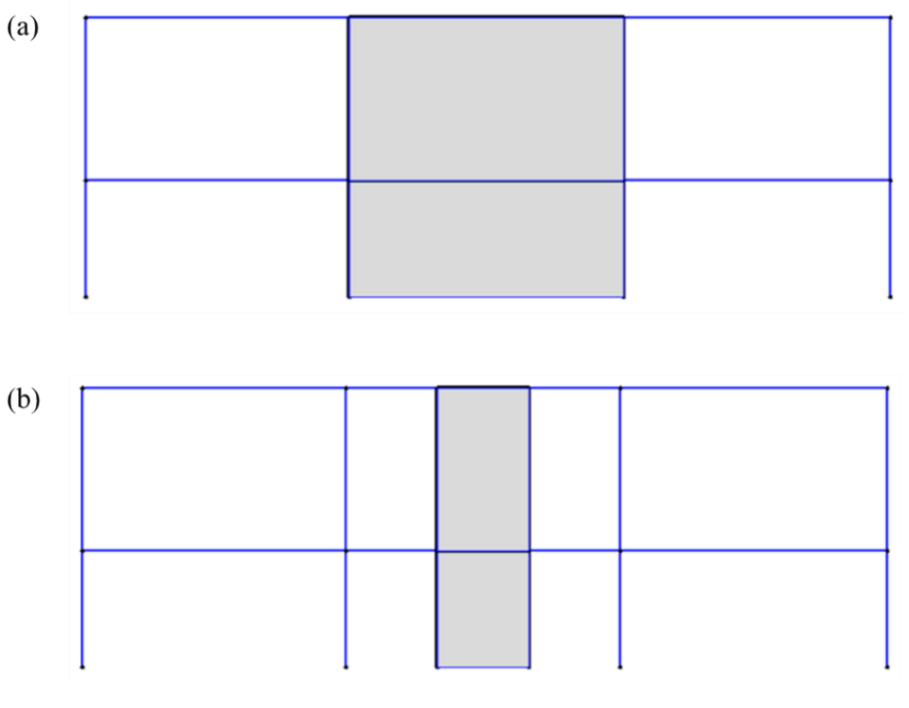

Fig. 4.14. Frame models with macroelements for the steel wall components: (a) Fully-infilled steel shear wall; (b) Partially-infilled steel shear wall

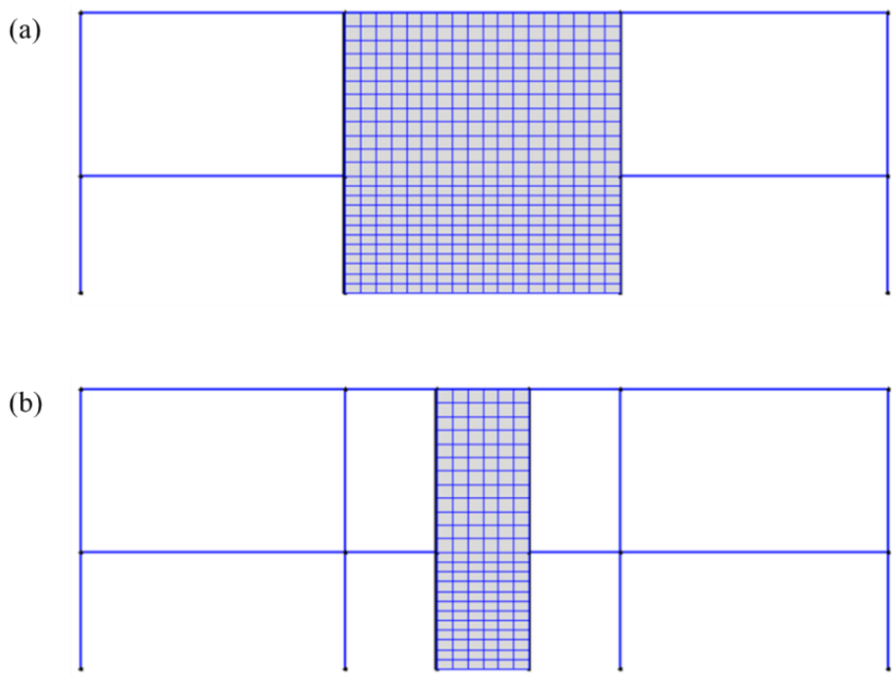

Fig. 4.15. Frame models with shell elements for the steel wall components: (a) Fully-infilled steel shear wall; (b) Partially-infilled steel shear wall

The material parameters for the nonlinear springs of the macroelements, which are reported in Table 4.5, have been determined using the MLR functions established in the previous section based on the geometrical characteristics of the two steel shear wall components. Furthermore, to avoid introducing unrealistically high concentrated forces to the members of the RC frame which are directly connected to the steel shear wall elements, only the four corner nodes of the macroelement are directly linked to the boundary frame, while the middle nodes on the four edges are connected to the corner nodes via link elements, which are pinned to the top and bottom nodes of the two boundary columns and have elastic axial stiffness and rigid twisting stiffness. The axial stiffness has been assumed as the axial stiffness of a bar element with an area equal to one-quarter of the cross-section area of the steel plate. Conversely, in the model with shell elements for the steel shear wall components, the shell elements are connected directed to the nodes of the boundary beams along the members in the horizontal direction while the same link elements as the macroelement models are applied to the boundary nodes in the vertical direction.

Table 4.5. Predicted material parameters for nonlinear springs of macroelements in fully-infilled and partially-infilled models

Model	Storey ID	μ	β	γ	χ	η	κ
Fully-infilled	1	0.0138	-0.0088	0.3741	0.2703	0.7325	0.4267
	2	0.0128	-0.0020	0.4044	0.2668	0.8007	0.4608
Partially-infilled	1	0.0157	-0.0087	0.2656	0.2002	0.8391	0.6425
	2	0.0173	-0.0119	0.1591	0.1565	0.7324	0.6766

4.5.2 Numerical results

Nonlinear simulations have been carried out employing the two alternative descriptions with macroelements and shell elements. The cyclic horizontal displacement history shown in Fig. 4.16 has been applied at the top beam restraining the out-of-plane displacements at the nodes where beams and columns connected at the two floor levels.

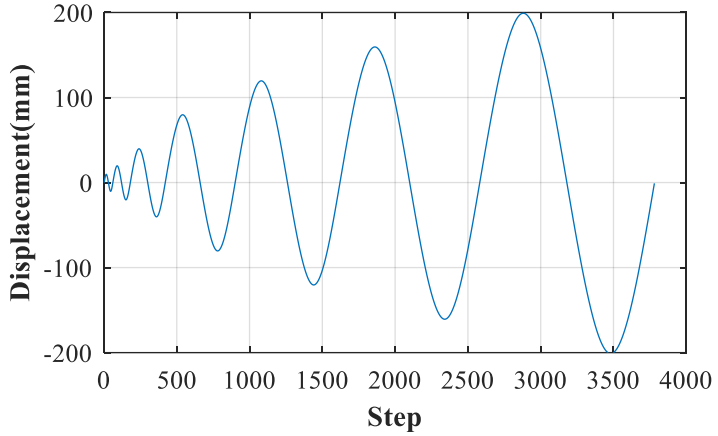

Fig. 4.16. Cyclic displacement history applied at the top beam of the RC frame with a steel shear wall

Fig. 4.17 compares the base shear – top displacement curves obtained by using the two alternative models. It can be seen that using macroelement models for both the fully-infilled and partially-infilled cases leads to numerical predictions close to the baseline curves of the shell element models, with very good estimates of the initial stiffness and yielding force. However, the level of stiffness degradation by increasing the number of cycles is underestimated and the post-yielding behaviour is characterised by higher forces in the case of the fully-infilled frame. This may result from the different connectivity between the steel shear wall and the RC frame components in the shell element and macroelement models. On the other hand, the macroelement model guarantees a good estimation of the energy dissipated by the retrofitted frame under cyclic loading, with an overprediction of 0.90% for the fully-infilled case and an underprediction of 1.22% for the partially-infilled frame.

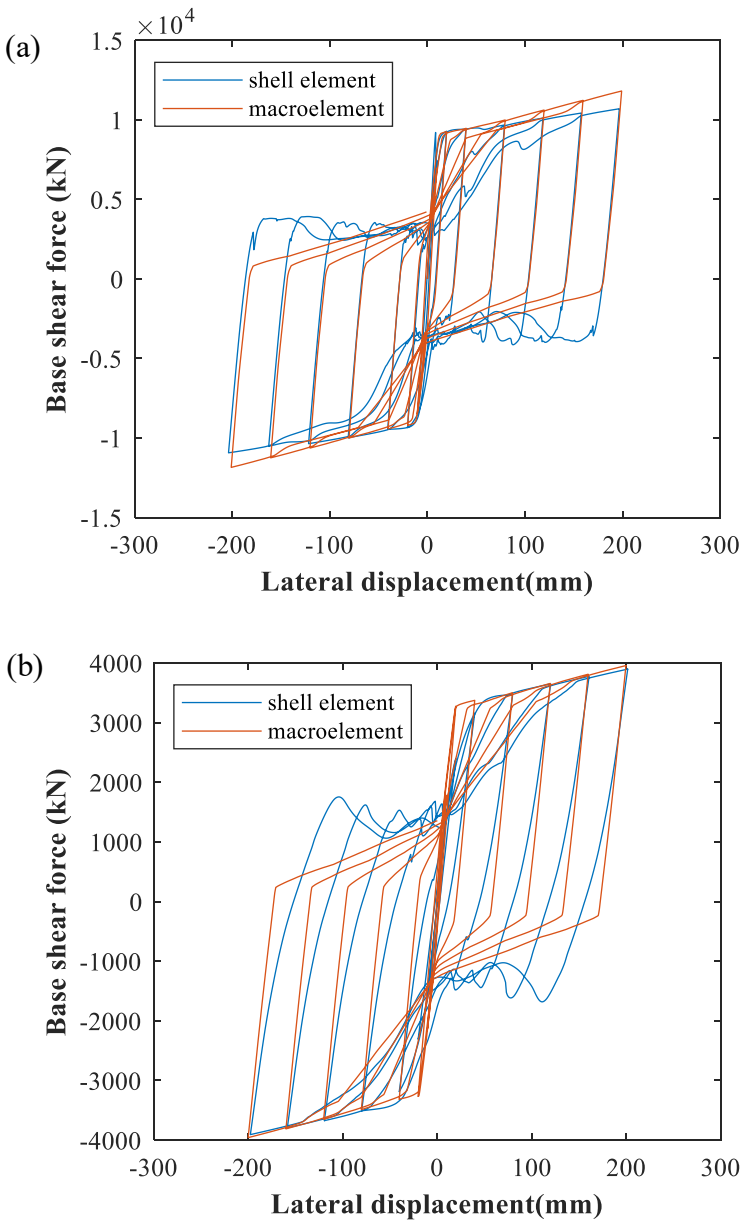

Fig. 4.17. Comparison between shell element and macroelement results for: (a) Fully-infilled model; (b) Partially-infilled model

Table 4.6 compares the computational costs for the numerical models in terms of wall-clock time and allocated memory. It can be noted that the computational demand is significantly reduced when simulating steel shear walls by macroelements instead of shell elements.

Table 4.6. Computational costs for the numerical models with different elements

Model	Analysis time	Allocated memory
Fully-infilled shell element	451 min	85 MB
Fully-infilled macroelement	3 min	7 MB
Partially-infilled shell element	131 min	35 MB
Partially -infilled macroelement	3 min	6 MB

Finally, it is worth comparing the distribution of internal forces due to the interaction between the frame components and the steel shear wall. Fig. 4.18 and Fig. 4.19 show contour plots of the bending moment distribution in the beams and columns for the frame models with shell elements and macroelements at the maximum horizontal displacement. The macroelement models exhibit lower bending moments along the beams and higher bending moments at the column ends in the members directly connected to the steel shear walls. On the other hand, similar internal forces are predicted in the other beam-column elements of the frame which are not directly connected to the steel wall. Under 15% difference is observed when comparing the shear forces and the chord rotations for the frame members of both cases between the macroelement and shell element models.

This indicates that the use of the proposed macroelement strategy is suitable for the seismic assessment of retrofitted RC frame buildings, when local checks for brittle failure modes (e.g. shear forces in beams and columns) and ductile failure modes (e.g. chord rotations) are limited to the elements not directed connected to steel shear walls. It is deemed adequate as beams and columns connected to steel wall components are generally reinforced to allow for connectivity to the steel panels. On the other hand, it can be argued that local effects due to the interaction between steel walls and connected RC frame components can be investigated only using detailed models, such as the FE model with nonlinear shell elements.

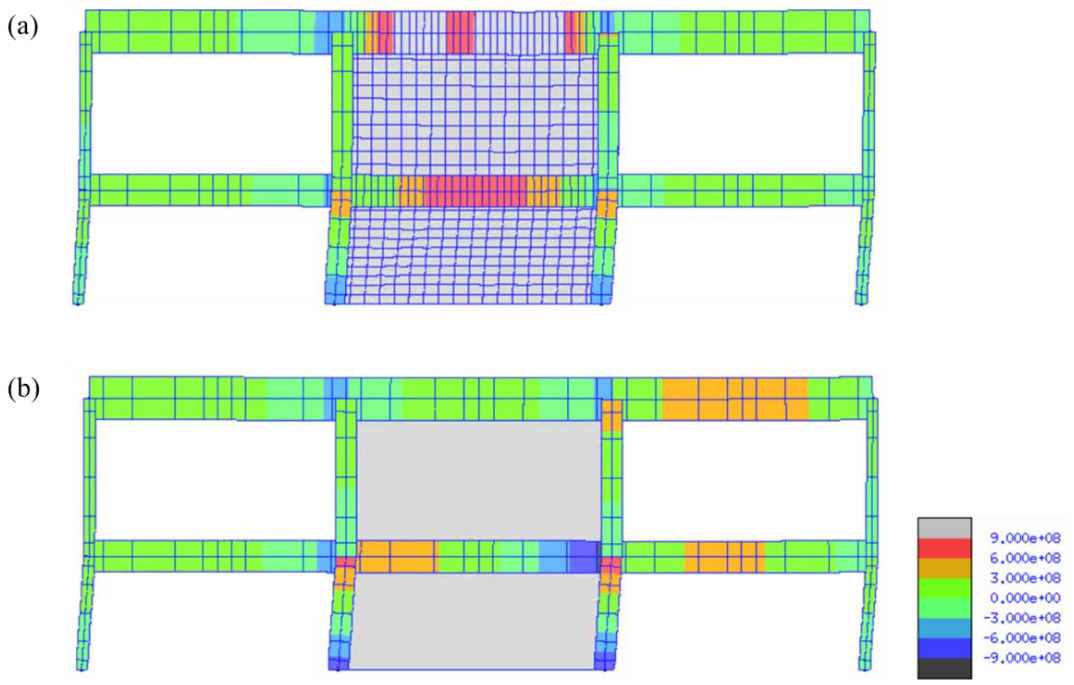

Fig. 4.18. Bending moment distributions in the components of the fully-infilled frame: (a) Macroelement model; (b) Shell element model

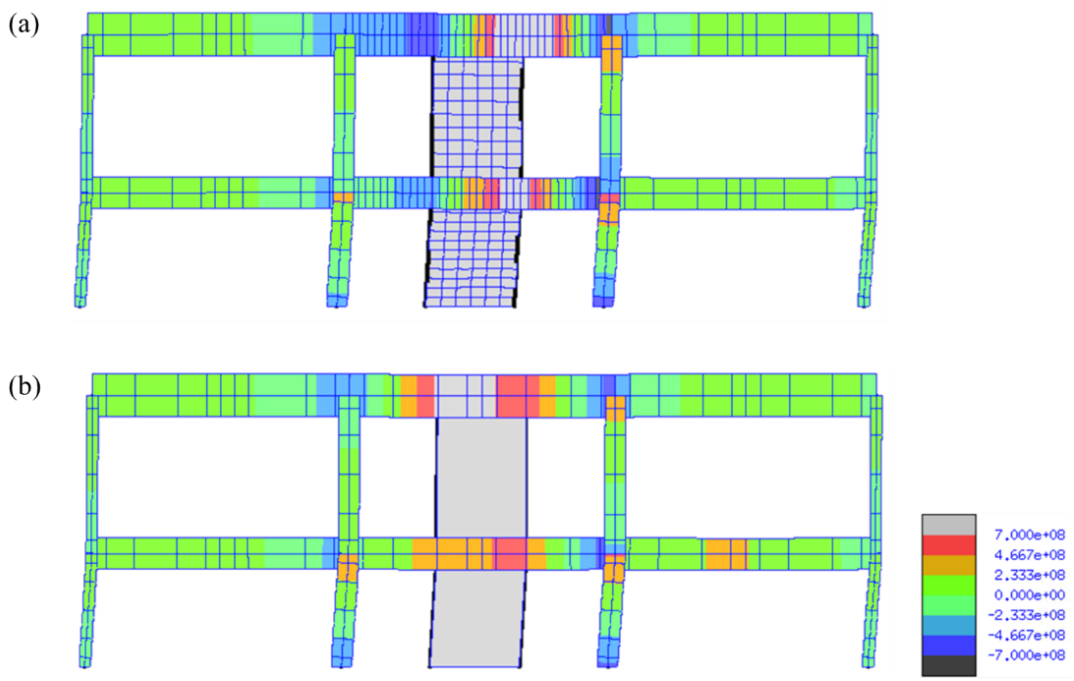

Fig. 4.19. Bending moment distributions in the components of the partially-infilled frame: (a) Macroelement model; (b) Shell element model

4.6 Concluding remarks

In this chapter, a calibration procedure is proposed for the material parameters of the macroelement developed for steel shear walls. This procedure is aimed at finding optimal sets of material parameters leading to response predictions close to those provided by detailed FE models with shell elements. The calibration is treated as a multi-objective optimisation problem considering the discrepancies of dissipated energy and selected engineering features between the macroelement and shell element results. The calibration procedure is applied to numerous samples of steel infill plates with various lengths, heights and thicknesses under a shear deformation mode. Subsequently, the calibration results are processed by MLR to determine simple functions for the practical calculation of macroelement material parameters in terms of the steel plate geometric properties.

The accuracy of the calibration results and the MLR functions have been assessed in the analysis of a substandard RC frame equipped with fully-infilled and partially-infilled steel shear walls modelled with macroelements or shell elements. It has been found that the results provided by the macroelement models are in good agreement with those of the shell element models, confirming the ability and computational efficiency of the developed macroelement in representing steel shear walls within retrofitted RC frames subjected to cyclic loading.

Chapter 5

Optimal Seismic Retrofitting Design for RC Frame Structures

5.1 Introduction

Seismic retrofitting design is currently based upon trial-and-error procedures, which are mainly driven by practical engineering judgment lacking systematic analysis. In this chapter, computer-aided optimal retrofitting design is developed to overcome some inherent limitations of standard design approaches, focusing on the use of steel shear walls to enhance the performance of substandard RC framed buildings.

The seismic response of deficient RC buildings retrofitted with steel shear walls largely depends on the geometrical and mechanical characterises of the steel walls and their location

within the strengthened structure. In this research, the selection and design of the retrofitting steel wall components is regarded as a multi-objective optimisation problem with constraints, where genetic algorithm (GA) procedures are conveniently used to generate Pareto front solutions. Engineering judgement is then introduced to select the most suitable solution for the specific retrofitting operation, which will be discussed in the application to the numerical examples in Chapter 6. The proposed approach presents some novel features including improvement of lateral stiffness, shear strength and satisfied energy dissipation capacity compared to existing optimal seismic retrofitting design methods, which consider the use of dampers, FRP elements and bracing systems. Some of the studies limit to the single-objective optimisation as well (Farhat et al., 2009; Charmpis et al., 2012; Park et al., 2015; Kim and An, 2016; Cha and Agrawal, 2017; Chisari and Bedon, 2017; Choi et al., 2017; Falcone, 2018).

Current codes of practice for seismic design of new buildings (e.g. Eurocode 8 – 1 (EN1998-1, 2004)) mostly follow force-based approaches. Seismic forces are established considering a design spectrum allowing for specific global ductility demand depending on the structural type. Compliance with structural detailing rules and capacity design provisions guarantees that local and global ductility capacities will not exceed the demands leading to a safe design. Existing structures built prior to the advent of modern seismic design codes usually do not inherently meet local and global ductility requirements which prevent a straightforward application of standard force-based analysis methods. Thus, displacement-based procedures are generally used for the assessment of existing buildings and for the design of retrofitting solutions. In this research, the capacity spectrum method originally introduced in ATC 40 – 1996 (ATC, 1996; Chopra and Goel, 1999) is selected for the seismic retrofitting design of existing RC framed buildings using steel shear walls. This approach explicitly allows for the energy dissipation characteristics of the analysed structure by introducing an equivalent viscous damping (EVD) ratio, which is related to the dissipated hysteretic energy in the cycle at the maximum displacement. On the other hand, other approaches also based on nonlinear static analysis like the N2 method (Fajfar and Fischinger, 1988) could be used as viable alternatives within the proposed retrofitting design strategy but are outside the scope of this research.

The developed optimal seismic retrofitting design approach is first discussed in Section 5.2, which provides an overview of the proposed procedure. Afterwards, Section 5.3 explains how

to determine the deformation capacity in detail, taking into account global and local deformation and local strength performance. Subsequently, Section 5.4 elaborates on the GA process for selecting optimal retrofitting solutions, indicating the basic steps of the proposed process including the definition of design variables and objective functions. Since the EVD for steel shear walls needs to be estimated within the optimal procedure, nonlinear regression for the EVD is presented in Section 5.5. This is undertaken based on virtual tests under cyclic loading using macroelement models to represent different steel shear wall configurations subjected to varying drift levels. As a result, a practical expression is established to calculate the equivalent damping ratio for steel shear wall components as a function of the geometry of the steel panels and the drift demand.

5.2 Design procedure

5.2.1 Steps for optimal seismic retrofitting design

The developed optimal seismic retrofitting design strategy introduces some novel features:

- The proposed procedure enables the automatic definition of optimal infill plate length and thickness;
- The optimisation objectives are selected considering local and global seismic performance requirements, minimising the amount of steel material for the added shear wall components and drift uniformity along the height;
- The developed macroelements for steel shear walls with varying geometrical parameters are adopted in the optimal design, providing an efficient yet accurate representation for each possible solution.

Fig. 5.1 shows the flowchart of the design procedure based on the capacity spectrum method, which involves a series of steps:

- Perform pushover analysis on the bare frame model and obtain the base shear force – top displacement diagram ($V_b - \delta_n$), and then convert it into the frame capacity diagram in the $S_a - S_d$ format. The transformation process will be described in Section 5.2.2.
- Obtain the damped demand diagram in the $S_a - S_d$ format, which can be derived from the elastic response spectrum $S_a - T_n$ by introducing the EVD coefficient of the bare RC frame (Section 5.2.3).
- Determine the initial deformation demand D_{d0} at the intersection between the frame capacity diagram and the damped demand diagram. If such an intersection does not exist, the global deformation performance requirement is not satisfied, and the frame requires retrofitting. On the other hand, if the initial deformation demand D_{d0} can be established, determine the initial deformation capacity D_{c0} by checking for local seismic performance requirements at the member level at each step of the pushover analysis for the bare frame (Section 5.3). If $D_{c0} < D_{d0}$, the RC frame does not meet the seismic local performance requirements and needs retrofitting. Otherwise, the frame is safe.
- If the frame requires retrofitting, GA is applied to generate optimal solutions for the seismic retrofitting problem adding steel shear wall elements to the existing RC framed structure (Section 5.4). For each population, macroelements representing steel shear walls in different configurations are introduced into the frame model. Pushover analysis is then carried out on the new models. Besides, the EVD of the frame equipped with steel shear walls model ξ_{eq} is estimated (Section 5.5). As a result, new capacity and demand diagrams are determined leading to updated deformation capacity D_c and demand D_d. The aim of the optimisation process is to select cases with the minimum gap between seismic deformation capacity and demand, with the capacity larger than the demand, while using the minimum amount of steel for the shear wall components and achieving a uniform distribution of inter-storey drift along the height.
- Select one of the most suitable solutions from the Pareto front generated by GA. This process needs engineering judgement giving priority to key objectives depending on the specific practical case, and this will be discussed in the application to numerical examples in Chapter 6.

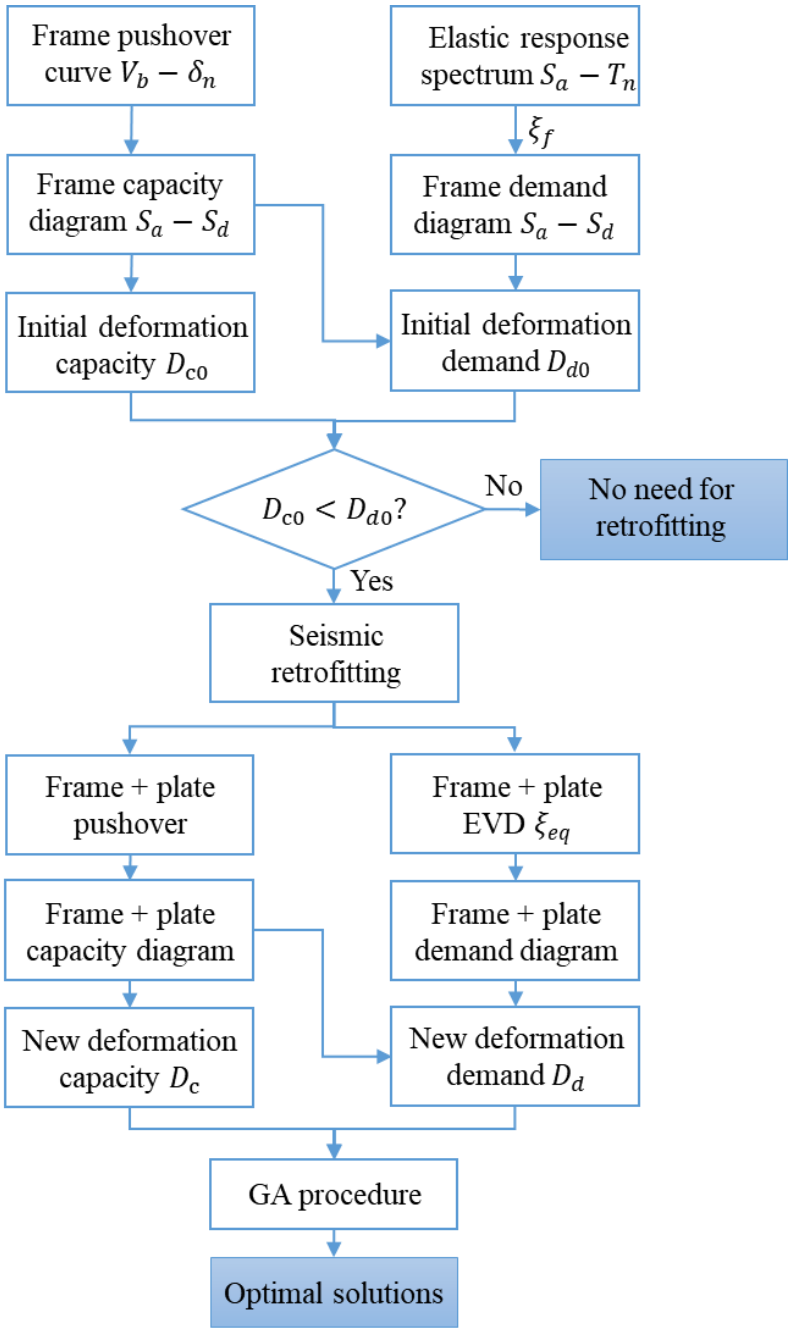

Fig. 5.1. Flowchart for the proposed optimal seismic retrofitting design based on capacity spectrum method

5.2.2 Conversion of capacity diagram

The pushover curve is first developed, which is the relationship between the base shear force V_b and the top (n-th storey) displacement δ_n. Then the MDOF structure is transformed into an equivalent SDOF model, as discussed in Section 2.2, with effective mass:

$$m^* = \frac{(\sum m_i \Phi_i)^2}{\sum m_i {\Phi_i}^2} \tag{5.1}$$

and transformation factor:

$$\Gamma = \frac{\sum m_i \Phi_i}{\sum m_i {\Phi_i}^2} \tag{5.2}$$

For regular framed structures, the displacement shape Φ_i relates to the first eignmode and can be estimated for design purposes as (Priestley et al., 2007):

$$\begin{gathered} \text{For } n \leq 4\text{: } \Phi_i = \frac{H_i}{H_n} \\ \text{For } n > 4\text{: } \Phi_i = \frac{4}{3} \cdot \left(\frac{H_i}{H_n}\right) \cdot \left(1 - \frac{H_i}{4H_n}\right) \end{gathered} \tag{5.3}$$

where H_i and H_n are the i-th and n-th (roof) storey heights, respectively.

Afterwards, as shown in Fig. 5.2, the capacity diagram in the $S_a - S_d$ format can be obtained by:

$$S_a = \frac{V_b}{m^*}, \quad S_d = \frac{\delta_n}{\Gamma \Phi_n} \tag{5.4}$$

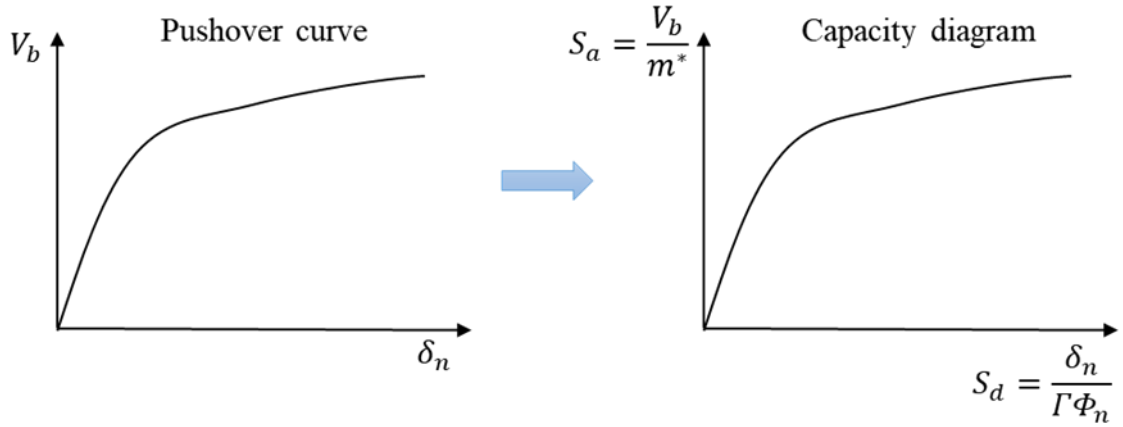

Fig. 5.2. Conversion of pushover curve to capacity diagram (Chopra and Goel, 1999)

5.2.3 Conversion of demand diagram

The demand diagram in the $S_a - S_d$ format is converted from the standard $S_a - T_n$ format, as shown in Fig. 5.3, by using the equation

$$S_d = \frac{T_n^2}{4\pi^2} S_a \tag{5.5}$$

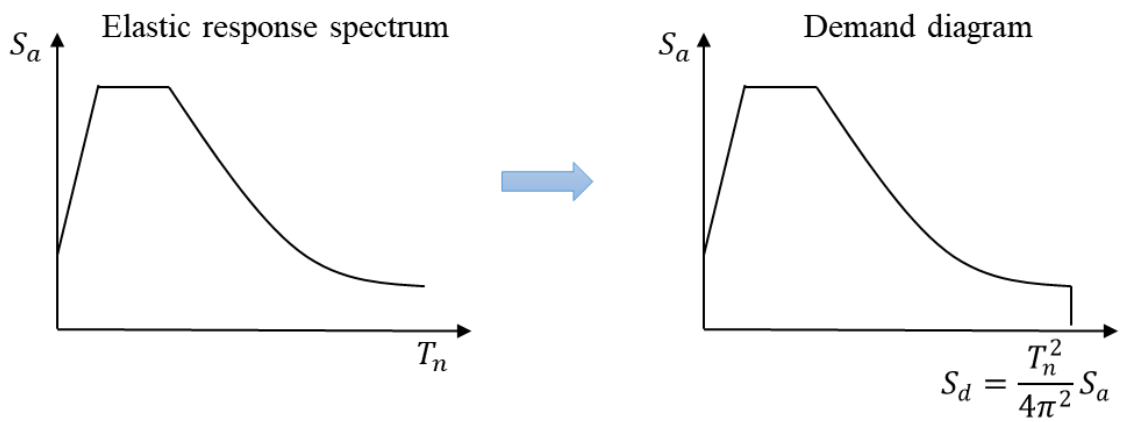

Fig. 5.3. Conversion of the elastic response spectrum to the demand diagram (Chopra and Goel, 1999)

When converting the 5% elastic response spectrum to the reduced spectrum, the EVD of the frame is taken into account considering the structural types. For well-detailed RC frame buildings, the EVD coefficient can be estimated as (Priestley et al., 2007):

$$\zeta_f = 0.05 + 0.565\left(\frac{\mu - 1}{\mu\pi}\right) \tag{5.6}$$

where μ is the ductility factor equal to the ultimate displacement divided by the yield displacement. In this work, the equation above is adopted also for substandard RC frames considered in the optimal retrofitting design as a practical approximated way to estimate the frame damping ratio.

For the general case of a multi-degree-of-freedom structure where the structural elements have different strength V_i, displacement δ_i and damping ζ_i, the global EVD ζ_{eq} can be a weighted average according to the dissipated energy (Priestley et al., 2007) leading to:

$$\zeta_{eq} = \frac{\sum(V_i\delta_i\zeta_i)}{\sum(V_i\delta_i)} \tag{5.7}$$

When calculating the damping of the retrofitted frame with added steel plates, the overall structure can be treated as the bare RC frame in parallel with several bays of steel shear walls. One bay of steel shear walls is composed of several in-series single steel shear wall components at the different floor levels. The estimation of EVD for a single steel shear wall element will be discussed in detail in Section 5.5, where a function for the damping ratio is derived based on the steel plate dimensions and drift demand.

After obtaining the overall equivalent damping ratio, the reduced spectrum can be calculated as the 5% elastic spectrum multiplied by the damping correction factor η equal to (EN1998-1, 2004):

$$\eta = \sqrt{10/(5 + 100 \cdot \zeta_{eq})} \tag{5.8}$$

5.3 Determination of deformation capacity

The deformation capacity of an RC frame is assessed from global deformation performance and local ductile and brittle performance (Penelis and Penelis, 2019). Global performance is satisfied if the capacity diagram has an intersection with the demand diagram, which can be checked following the procedure presented in the previous section. On the other hand, local performance requirements are verified considering ductile and brittle mechanisms at the member level. It requires comparing the demand and capacity values for chord rotation and shear force at the ends of each member of the retrofitted RC frame structure. According to the proposed procedure, chord rotations and shear forces of RC beams and columns are calculated from the results of the nonlinear pushover analysis at the end of each step of the incremental solution procedure. These values are subsequently compared against the chord rotation and shear capacities of the RC beams and columns of the frame (see Section 2.2.6). The smallest displacement at which chord rotation and/or shear force exceeds the corresponding limit is assumed as the deformation capacity of the RC frame.

5.3.1 Chord rotation limit check

As pointed out before, local ductile performance is determined based on chord rotations checks at the member level. The chord rotation is defined as the angle between the tangent to the member axis at the end section and the chord connecting the end section to the contraflexure point with zero bending moment, as shown in Fig. 5.4 (Mpampatsikos et al., 2008). Thus, the overall chord rotation is composed of the nodal rotations and the drift angle due to gravity or seismic loads.

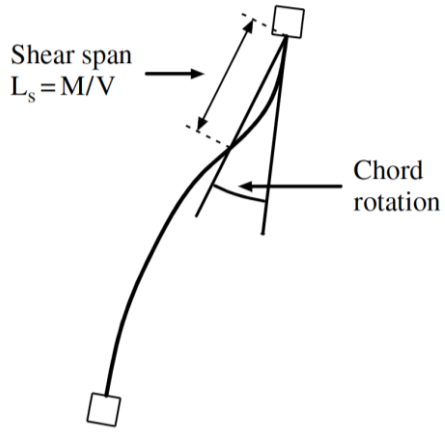

Fig. 5.4. Definition of chord rotation (Mpampatsikos et al., 2008)

According to the adopted modelling strategy, where a mesh of several corotational 3D beam elements is used to represent each beam and column (Section 4.5) of an RC framed structure, the chord rotation θ_{rot} at the two ends of each member includes three parts as illustrated in Fig. 5.5: (i) the end nodal rotation θ_1 in the element local reference system x, y, z; (ii) the end element rotation θ_2 in the global reference system X, Y, Z; and (iii) the overall deformed angle θ_3 of the entire member due to relative nodal displacements in the global reference system X, Y, Z. The nodal rotations at two ends *1* and *2* of the adopted elasto-plastic cubic beam-column elements are shown in Fig. 5.6. The nodal rotations are noted as the angles $\theta_{y1}, \theta_{z1}, \theta_{y2}$, and θ_{z2}, respectively, in the local reference system.

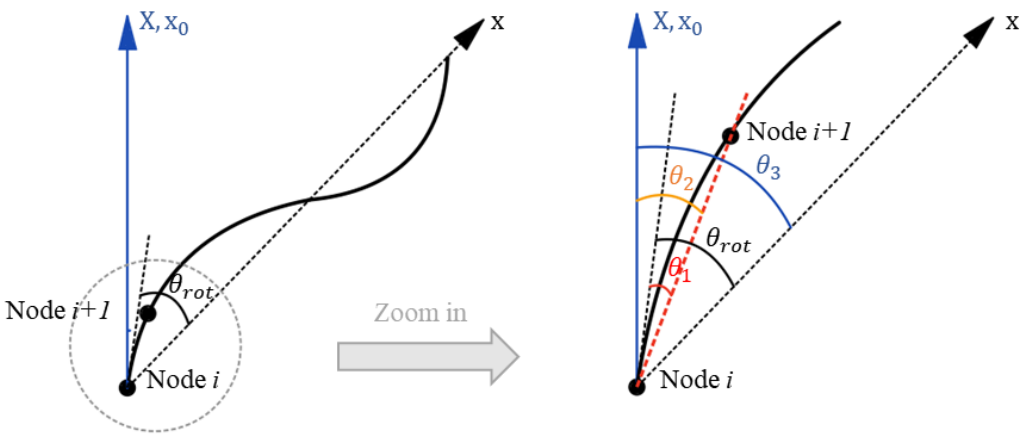

Fig. 5.5. Illustration for chord rotation calculation

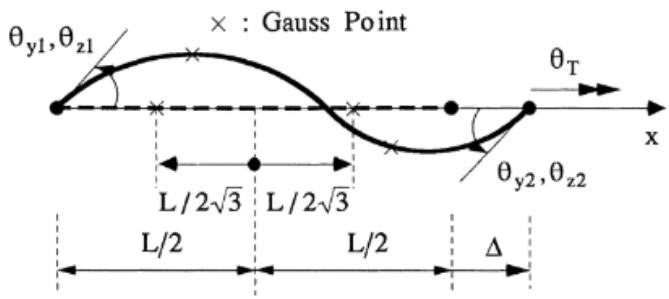

Fig. 5.6. Local freedoms of the cubic elasto-plastic beam-column element (Izzuddin and Lloyd Smith, 2000)

When calculating the chord rotations of the beam/column members with several elements, the contraflexure point can be simply assumed at the intersection of the chord between the two end elements and the deflected shape. The calculation also takes into account the orientation of beams and columns corresponding to the global reference system. For the specific case of member orientation shown in Fig. 5.7, the chord rotation at two end nodes *i* and *j* of each beam and column in the two planes of bending can be obtained from the formulas below (Masjuki, 2017):

Chord rotations for columns:

At node i,

$$\overline{\theta}_{y,i} = \theta_{y,i} + \left(\frac{U_{X,i+1} - U_{X,i}}{L_i}\right) - \left(\frac{U_{X,j} - U_{X,i}}{L_{ij}}\right) \tag{5.9}$$

$$\overline{\theta}_{z,i} = \theta_{z,i} + \left(\frac{U_{Y,i+1} - U_{Y,i}}{L_i}\right) - \left(\frac{U_{Y,j} - U_{Y,i}}{L_{ij}}\right) \tag{5.10}$$

At node j,

$$\overline{\theta}_{y,j} = \theta_{y,j} + \left(\frac{U_{X,j} - U_{X,j-1}}{L_j}\right) - \left(\frac{U_{X,j} - U_{X,i}}{L_{ij}}\right) \tag{5.11}$$

$$\overline{\theta}_{z,j} = \theta_{z,j} + \left(\frac{U_{Y,j} - U_{Y,j-1}}{L_j}\right) - \left(\frac{U_{Y,j} - U_{Y,i}}{L_{ij}}\right) \tag{5.12}$$

Chord rotations for beams along X-axis:

$$\overline{\theta}_{y,i} = \theta_{y,i} + \left(\frac{U_{Z,i+1} - U_{Z,i}}{L_i}\right) - \left(\frac{U_{Z,j} - U_{Z,i}}{L_{ij}}\right) \tag{5.13}$$

At node i,

$$\overline{\theta}_{z,i} = \theta_{z,i} - \left(\frac{U_{Y,i+1} - U_{Y,i}}{L_i}\right) + \left(\frac{U_{Y,j} - U_{Y,i}}{L_{ij}}\right) \tag{5.14}$$

$$\overline{\theta}_{y,j} = \theta_{y,j} + \left(\frac{U_{Z,j} - U_{Z,j-1}}{L_j}\right) - \left(\frac{U_{Z,j} - U_{Z,i}}{L_{ij}}\right) \tag{5.15}$$

At node j,

$$\overline{\theta}_{z,j} = \theta_{z,j} - \left(\frac{U_{Y,j} - U_{Y,j-1}}{L_j}\right) + \left(\frac{U_{Y,j} - U_{Y,i}}{L_{ij}}\right) \tag{5.16}$$

Chord rotations for beams along Y-axis:

$$\overline{\theta}_{y,i} = \theta_{y,i} + \left(\frac{U_{Z,i+1} - U_{Z,i}}{L_i}\right) - \left(\frac{U_{Z,j} - U_{Z,i}}{L_{ij}}\right) \tag{5.17}$$

At node i,

$$\overline{\theta}_{z,i} = \theta_{z,i} + \left(\frac{U_{X,i+1} - U_{X,i}}{L_i}\right) - \left(\frac{U_{X,j} - U_{X,i}}{L_{ij}}\right) \tag{5.18}$$

$$\overline{\theta}_{y,j} = \theta_{y,j} + \left(\frac{U_{Z,j} - U_{Z,j-1}}{L_j}\right) - \left(\frac{U_{Z,j} - U_{Z,i}}{L_{ij}}\right) \tag{5.19}$$

At node j,

$$\overline{\theta}_{z,j} = \theta_{z,j} + \left(\frac{U_{X,j} - U_{X,j-1}}{L_j}\right) - \left(\frac{U_{X,j} - U_{X,i}}{L_{ij}}\right) \tag{5.20}$$

where $\theta_{y,i}$, $\theta_{z,i}$, $\theta_{y,j}$, $\theta_{z,j}$ are the nodal rotations in the local reference system; $U_{X,i(j)}$, $U_{Y,i(j)}$, $U_{Z,i(j)}$ are the nodal displacements at nodes *i*(*j*) in the global reference systems; node *i+1* and node *j-1* are the nodes following node *i* and prior to node *j*, respectively; L_i and L_j represent the beam-column end element length; L_{ij} represents the overall member length of the RC columns or beams.

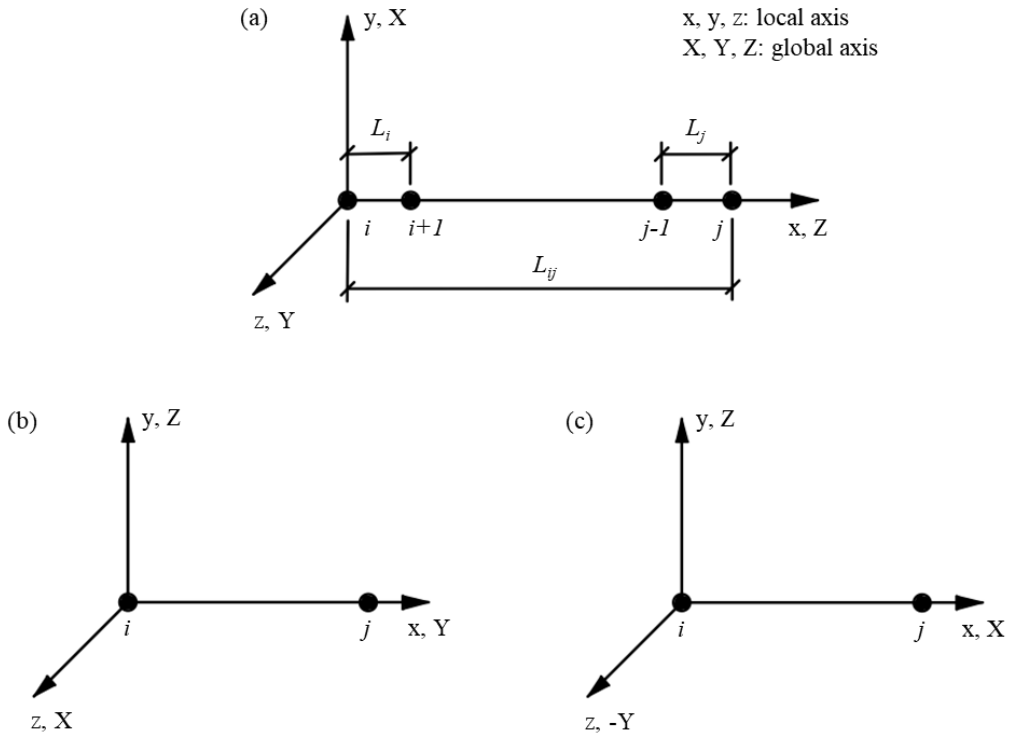

Fig. 5.7. Specific orientation of (a) columns, (b) beams along Y-axis, and (c) beams along X-axis for a 3D frame model (Masjuki, 2017)

5.3.2 Shear limit check

For the local brittle deformation capacity check, the shear forces are calculated based on the bending moment distribution for each beam and column assuming that the bending moment changes linearly along the end elements of the member. Therefore, the shear forces at the two end nodes *i* and *j* can be simply calculated as:

At node i,

$$V_{y,i} = \frac{M_{y,i} + M_{y,i+1}}{L_i} \tag{5.21}$$

$$V_{z,i} = \frac{M_{z,i} + M_{z,i+1}}{L_i} \tag{5.22}$$

At node j,

$$V_{y,j} = \frac{M_{y,j-1} + M_{y,j}}{L_j} \tag{5.23}$$

$$V_{z,j} = \frac{M_{z,j-1} + M_{z,j}}{L_j} \tag{5.24}$$

given that M_y, M_z are the member bending moments in the local reference system in y and z directions, respectively.

5.4 GA process of selecting optimal solutions

The GA procedure is developed with the aid of the MATLAB function '*gamultiobj*', which is available in the *Global Optimisation Toolbox* (MathWorks, 2020). Furthermore, MATLAB is utilised to (i) create ADAPTIC input files for the analysed structure, (ii) process the results of the nonlinear simulations, and (iii) evaluate the objective functions.

MATLAB provides the built-in *Parallel Computing Toolbox* allowing users to establish a parallel pool of several workers suitable for multicore processors. A simple command '*parpool*' is added before calling the GA solver, and the needed number of local workers can be set. Then '*UseParallel*' is set as '*true*' in the option of multi-objective GA '*gamultiobj*'. These commands divide the solutions of the population into several groups so that each worker can analyse one individual solution in parallel independently. Parallel computing leads to a significant speed-up of the GA process.

Fig. 5.8 summarises the GA process for the selection of optimal retrofitting solutions. A more detailed description of the main steps for this process is provided in the following.

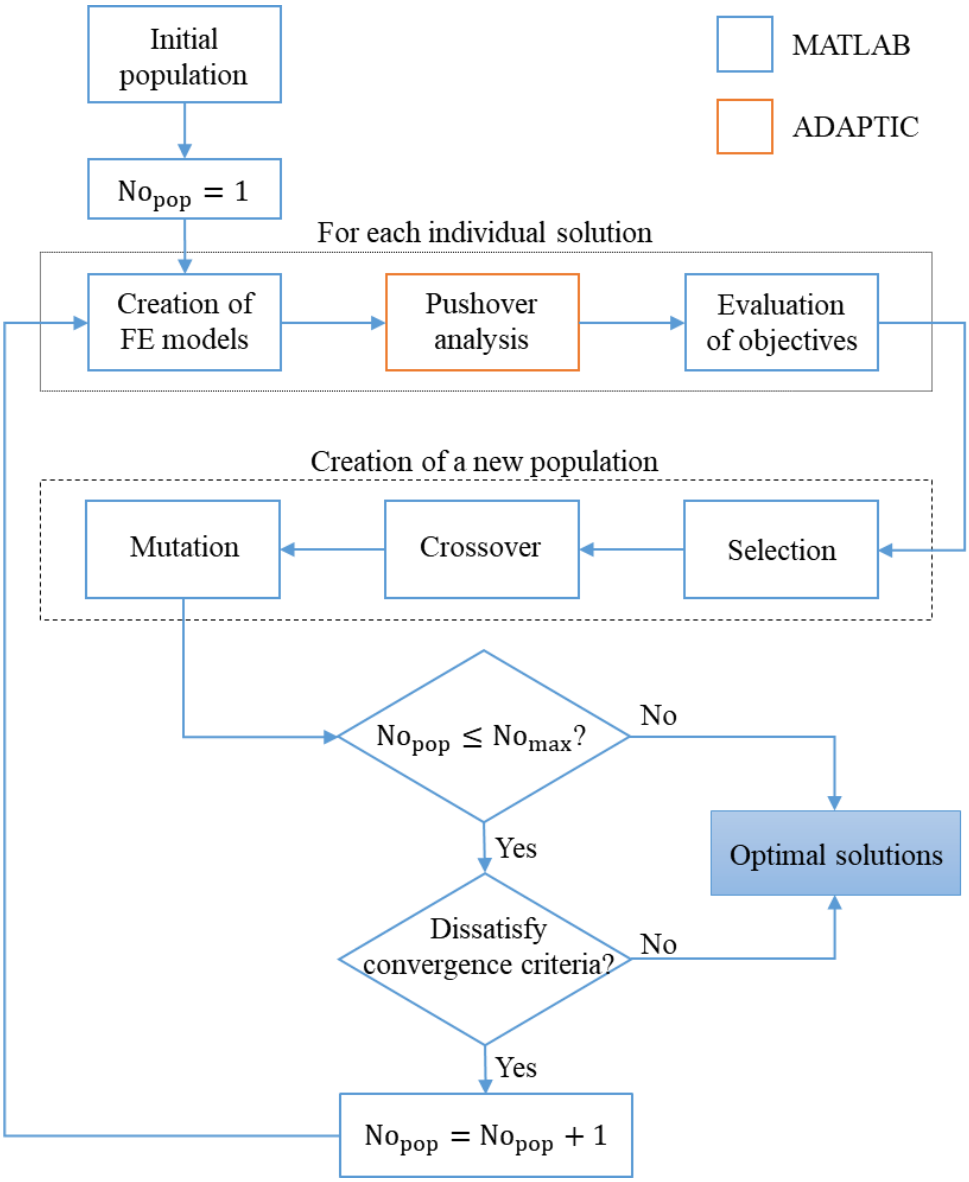

Fig. 5.8. Flowchart for the GA selection process

Step 1. Population representation and initialisation

The GA selection process starts from the generation of the initial population, which contains a set of randomly generated potential solutions. For an *n*-storey RC frame equipped with a steel shear wall inserted into the frame at a generic bay, *n*+1 design variables are selected to represent each solution, including steel plate type sp_{typ} (e.g. fully-infilled or partially-infilled) and plate thickness on each floor $(t_1, t_2, \ldots, t_n)$:

$$x = [sp_{typ};\ t_1;\ t_2;\ \ldots; t_n] \tag{5.25}$$

Bounds and constraints for the variables are set according to the length-to-height aspect ratio limits $0.8 \leq L/h \leq 2.5$ and the length-to-thickness ratio limits $250 \leq L/t \leq 1000$ for the steel plate (AISC, 2016). The bound of sp_{typ} is set as [1,3] and then rounded to the closest integer during the GA process. The rounded value equal to 1, 2 and 3 represents '1/3 infill', '2/3 infill' and 'full infill', respectively, indicating the ratio of the steel plate length divided by the overall length of the bay where the steel wall component is installed. The plate thickness of the *i*-th floor t_i is selected within the range $[L_{span}/1000, L_{span}/250]$, where L_{span} is the length of the retrofitted span, and rounded to the millimetre for practical reasons. Linear inequality constraints $A \cdot x \leq b$ are also added to achieve a different limit value for the maximum thickness considering different infill types. The plate thickness t_i is constrained to be no larger than $(sp_{typ} + 1) \times L_{span}/1000$, which can be written as:

$$\begin{bmatrix} -\frac{L_{span}}{1000} & 1 & & \\ -\frac{L_{span}}{1000} & & 1 & \\ \vdots & & & \ddots \\ -\frac{L_{span}}{1000} & & & 1 \end{bmatrix} \cdot \begin{bmatrix} sp_{typ} \\ t_1 \\ t_2 \\ \vdots \\ t_n \end{bmatrix} \leq \begin{bmatrix} \frac{L_{span}}{1000} \\ \frac{L_{span}}{1000} \\ \vdots \\ \frac{L_{span}}{1000} \end{bmatrix} \tag{5.26}$$

After defining the representation for each individual, the first population is generated randomly. Population size is set as 100 if the total number of variables is no larger than 5; otherwise, it is set as 200, which is a typical value suggested in the MATLAB documentation (MathWorks, 2020). In the initial population for each individual, a finite element description for the retrofitted frame is developed utilising the modelling strategy for RC frames with infilled steel walls introduced in Section 4.5, where steel shear wall components are represented using the developed macroelement model. Different variable values for each model are assumed and the models are analysed and evaluated consequently as discussed in Step 2.

Step 2. Creation of FE models

The second step of the GA selection process is the creation of FE models based on the optimal variables. Steel shear walls with lengths corresponding to sp_{typ} and different thicknesses for different floors corresponding to t_i are added to the specific bay of the original RC frame model. The model creation procedure utilises a MATLAB subroutine that modifies existing input files representing the physical RC frame in ADAPTIC. Fig. 5.9 illustrates the different cases for mapping sp_{typ} to infilled wall type in the FE models.

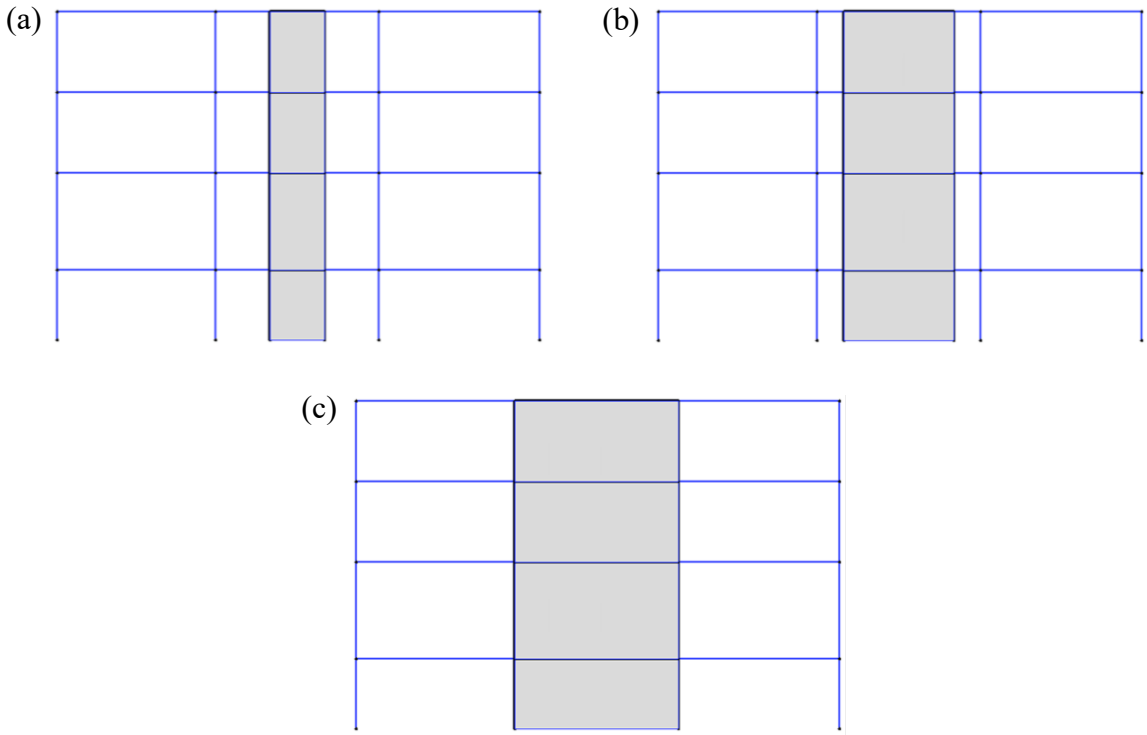

Fig. 5.9. Mapping sp_{typ} to infill type in the FE models for the case: (a) $sp_{typ} = 1 \rightarrow '1/3\ infill'$; (b) $sp_{typ} = 2 \rightarrow '2/3\ infill'$; (c) $sp_{typ} = 3 \rightarrow 'full\ infill'$

In practical applications, the beams of the retrofitted bay are typically strengthened to allow for connectivity with the steel plate components. Member strengthening is not explicitly represented in the FE models for the retrofitted frame, but the members directly connected to the wall components are assumed as elastic to prevent unrealistic local failure. As specified in Section 4.5, the connectivity between the FE mesh for the bare frame and the macroelements

representing the different parts of steel shear walls is achieved by introducing specific link elements available in ADAPTIC.

Step 3. Analysis of FE models

Pushover nonlinear simulations are carried out using ADAPTIC to assess the seismic performance of the retrofitted structures according to the capacity spectrum method as discussed in Section 2.2.3 (ATC, 1996; Chopra and Goel, 1999). More specifically, nonlinear simulations are performed prescribing monotonically increasing horizontal displacements at a control node on the roof level. A spreader element in ADAPTIC (Izzuddin, 2019) is used to distribute the resultant force at the beam-to-column connection nodes on each floor following the distribution ratio proportional to the storey mass multiplied by the displacement shape, as indicated in Fig. 2.1(a).

Step 4. Evaluation of objectives

The results from the nonlinear simulations in ADAPTIC are processed using an optimisation procedure developed in MATLAB. The calculated nodal displacements and forces are utilised in the definition of objective functions for the solution of the optimisation problem.

The pushover curve for the retrofitted frame with steel shear walls, which indicates the relationship between base shear force V_b and top displacement δ_n, is obtained from the ADAPTIC output files. The inter-storey drift for the i-th floor $\delta_{dr,i}$ is also recorded. Following the steps described in Section 5.2.1, the pushover curve is then converted to the new capacity diagram, and a new demand diagram is obtained considering the EVD of added steel shear walls. Consequently, the new deformation demand D_d, which is the intersection of the capacity diagram and the demand diagram, can be calculated. It is worth mentioning that when calculating the effective masses of the model for the retrofitted frame with steel shear wall components, the mass of the steel panels is added to the original mass of the bare frame model. On the other hand, the new deformation capacity D_c of the retrofitted frame is determined considering chord rotation and shear force limits for each frame member at each step of the incremental nonlinear simulation.

Three objective functions are defined to address the design of the retrofitting system with steel shear walls. The first objective Eq. (5.27) is introduced to minimise the gap between D_d and D_c while the second objective Eq. (5.28) concerns the amount of steel material for the additional wall components. The third objective Eq. (5.29) is aimed at achieving a uniform distribution of drift along the height of the framed structure by minimising the difference between lateral drifts $\delta_{dr,i}$ at adjacent storeys, aiming to avoid localisation of plastic deformation demand at a specific floor level. The three functions are given by the expressions:

$$f_1 = (D_c - D_d)/D_d \tag{5.27}$$

$$f_2 = \sum_{i=1}^{n} (L_i \cdot t_i) \tag{5.28}$$

$$f_3 = \sum_{i=1}^{n-1} (\delta_{dr,i+1} - \delta_{dr,i})^2 \tag{5.29}$$

where L_i and t_i are length and thickness of the steel plate on the i-th floor and n is the total number of storeys.

Since only the individuals where the deformation capacity is larger than or equal to seismic demand are considered as feasible solutions, constraints are also added to the optimisation problem. However, as GA can be applied only to unconstrained optimisation, a penalty function is introduced to penalise infeasible solutions converting the original constrained optimisation problem to an unconstrained one (Falcone, 2018). As a result, a large penalty term P (e.g. $P = 10000$) is added to infeasible solutions modifying Eq. (5.27) as:

$$f_1 = \begin{cases} (D_c - D_d)/D_d & if\ D_c \geq D_d \\ (D_c - D_d)/D_d + P & if\ D_c < D_d \end{cases} \tag{5.30}$$

Step 5. Creation of a new population

After evaluating the given population, a new population is created through the processes of selection, crossover and mutation. The individuals with minimum objectives are selected as 'parents' and mixed together to extract new individuals, i.e. 'offspring', setting the crossover as 0.8. Mutation points are then generated randomly by the adaptive feasible function method while still satisfying the bounds and the linear constraints for the variables (MathWorks, 2020).

Step 6. Convergence criteria

For the new population, Step 2 to Step 5 are repeated until the convergence criteria are met. The algorithm terminates if the number of the population exceeds the maximum generation, which is set equal to 200 times the total number of variables. The algorithm also stops if the average relative change in the best fitness function value over the generation is less than or equal to the tolerance value, which is generally set as 1e-4 for a typical multi-objective optimisation problem using GA (MathWorks, 2020).

Step 7. Processing of optimal solutions on Pareto Front

Solutions on the Pareto front are saved, including the values of all the variables and objectives. For the ease of selecting one optimal case, the objectives for each solution are transformed into relative values f_j', which are equal to the original objectives f_j divided by the minimum objective value, $\min(f_j)$, among all the solutions on the Pareto front:

$$f_j' = \frac{f_j}{min(f_j)} \quad j = 1,2,3 \tag{5.31}$$

Consequently, engineering considerations are involved in this step, and the best solution is selected considering different priorities for the different design objectives. This concept will be discussed when applying the proposed procedure to numerical examples in Chapter 6.

5.5 Nonlinear regression for equivalent viscous damping of steel shear walls

While using the capacity spectrum method within the developed optimal seismic retrofitting design strategy, the EVD for the retrofitted system must be determined to obtain the global deformation demand. In this respect, a simple function providing EVD for a generic steel shear wall panel has been established by using nonlinear regression to fit the results obtained in virtual tests, where the developed macroelement model is used to represent unstiffened steel plates with different geometrical characteristics and subjected to cyclic shear loading at different drift levels. In the following, some basic concepts of nonlinear regression are presented first and then applied to calculate EVD functions for steel shear wall elements.

5.5.1 Basic concept of nonlinear regression

For the cases where the dependent variable y cannot be predicted by linear terms of the independent variables X, nonlinear regression is needed to fit nonlinear models, which can be generally written as (MathWorks, 2021)

$$\{y\} = f([X], \{\theta\}) + \{\varepsilon\} \tag{5.32}$$

where $\{y\} = \begin{Bmatrix} y_1 \\ y_2 \\ \vdots \\ y_n \end{Bmatrix}$ is n observations of the dependent (response) variable;

f is the nonlinear function of $[X]$ and $\{\theta\}$ that evaluates each row of $[X]$ using the value of the parameter vector $\{\theta\}$;

$[X] = \begin{bmatrix} 1 & x_{11} & x_{12} & \dots & x_{1k} \\ 1 & x_{21} & x_{22} & \dots & x_{2k} \\ \vdots & \vdots & \vdots & & \vdots \\ 1 & x_{n1} & x_{n2} & \dots & x_{nk} \end{bmatrix}$ is the matrix of the independent variables (predictors);

$\{\theta\} = \begin{Bmatrix} \theta_1 \\ \theta_2 \\ \vdots \\ \theta_k \end{Bmatrix}$ is the regression coefficients, i.e. the unknown parameters in the function;

$\{\varepsilon\} = \begin{Bmatrix} \varepsilon_1 \\ \varepsilon_2 \\ \vdots \\ \varepsilon_n \end{Bmatrix}$ is the residuals/disturbances, which should be independent and identically random distributed.

Similar to linear regression, nonlinear regression also aims at finding the fittest regression coefficients by minimising the least-squares function, which is the sum of the squared values of the residuals. The main steps of the nonlinear regression are listed below (MathWorks, 2021):

- Prepare the input data including all sets of independent variables and the corresponding dependent variables;
- Predict the nonlinear model for the data, and select an initial set of values for function parameters as the starting point;
- Use a nonlinear regression function, e.g. '*fitnlm*' in Matlab, to fit the nonlinear model to the data;
- Examine the quality of the regression results by slice plots to visualise the effect and performance of each predictor, and by predicting for a new dataset.

5.5.2 Virtual tests on macroelement models

Virtual tests using macroelements are first performed to represent the response of steel shear walls with different properties under different drift levels. The selection of numerical sample properties for the virtual tests follows the same rules mentioned in Section 4.4.2. The steel wall height L is set as 500 mm to 6000 mm with a 500 mm interval. For each length L, height h is generated between $L/2.5$ and $L/0.8$ and is limited to 4000 mm. Plate thickness t is selected within the range $L/1000$ and $L/250$ and rounded to integer numbers. The drift value δ is selected as 0.1% to 6% with a 0.1% interval.

For each test sample with different plate L, h, t and δ, three cycles of lateral cyclic displacements with amplitude d_{max} equal to $\delta \cdot h$ are applied to the top nodes of the macroelement. A linear variation of lateral displacements is set along the two vertical edges

while the three nodes at the bottom edge are fully restrained to form a pure shear mode giving the lateral force – top displacement relationship for the plate.

Previous research about displacement-based seismic design provided a simplified way to estimate the EVD for a structural element, which is composed of a damping ratio in the linear elastic range and a hysteretic damping ratio ζ_{hyst} (Chopra and Goel, 1999; Priestley et al., 2007). The damping ratio in the linear elastic range can be taken as 0.05, thus the EVD of the plate is equal to:

$$\zeta_p = 0.05 + \zeta_{hyst} \tag{5.33}$$

$$\zeta_{hyst} = \frac{1}{4\pi}\frac{E_D}{E_{s0}} \tag{5.34}$$

where E_D is energy dissipated by damping, which is the average area enclosed by the 2nd and 3rd hysteresis loops aiming to avoid overestimation considering the stiffness degradation of steel shear walls under cyclic loading; $E_{s0} = K_{effective}{d_{max}}^2/2$ is the strain energy with stiffness $K_{effective}$, as shown in Fig. 5.10.

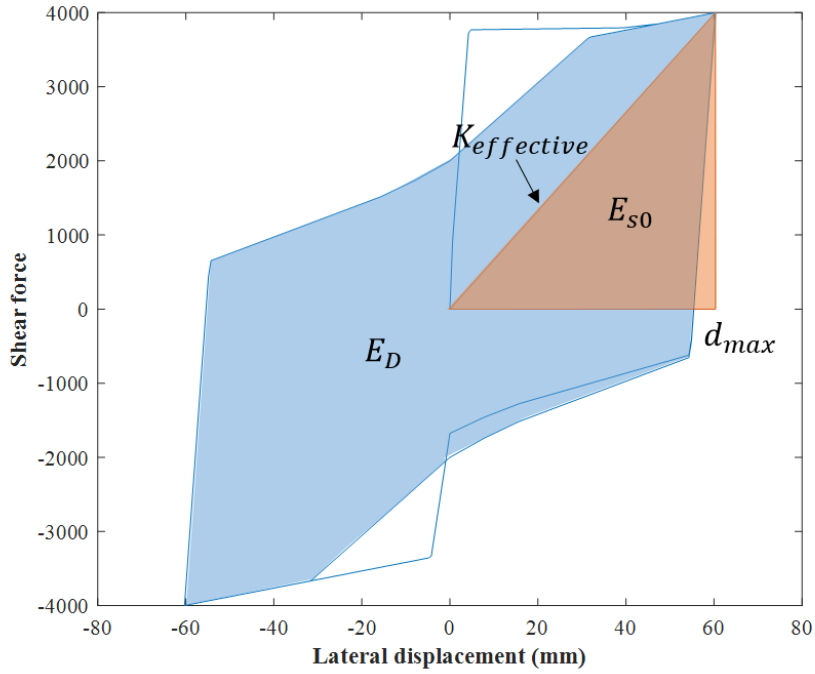

Fig. 5.10. Derivation of hysteretic damping ratio

5.5.3 Regression for hysteretic damping of steel shear walls

The dataset obtained from the macroelement virtual tests is then randomly separated into two parts, 85% as training data and 15% as testing data. For the training set, '*fitnlm*' available in the MATLAB *Statistic and Machine Learning Toolbox* (MathWorks, 2020) is used to find nonlinear relationships between ζ_{hyst} and $(L,\ h,\ t,\ \delta)$. Referring to the relationships provided by previous research (Chopra and Goel, 1999; Priestley et al., 2007; Dwairi et al., 2007; Penelis and Penelis, 2019), the hysteretic damping ζ_{hyst} is predicted by up to quadratic terms of the variables $(L,\ h,\ t)$ and $1/x$ term of (δ). The nonlinear regression function for ζ_{hyst} is herein written as:

$$\zeta_{hyst} = (\theta_0 + \theta_1 L + \theta_2 h + \theta_3 t + \theta_4 Lh + \theta_5 Lt + \theta_6 ht + \theta_7 L^2 + \theta_8 h^2 + \theta_9 t^2)\frac{\theta_{10} + \delta}{\theta_{11}\delta} \tag{5.35}$$

where θ_i is the unknown coefficient for each term. Nonlinear regression is carried out resulting in the estimated coefficients listed in Table 5.1.

Table 5.1. Estimated coefficients for nonlinear regression function

$\boldsymbol{\theta_0}$	9.388e+02	$\boldsymbol{\theta_6}$	-4.704e-03
$\boldsymbol{\theta_1}$	5.231e-02	$\boldsymbol{\theta_7}$	-1.625e-05
$\boldsymbol{\theta_2}$	-1.478e-01	$\boldsymbol{\theta_8}$	-1.551e-06
$\boldsymbol{\theta_3}$	3.667e+01	$\boldsymbol{\theta_9}$	-5.973e-01
$\boldsymbol{\theta_4}$	3.110e-05	$\boldsymbol{\theta_{10}}$	-1.074e-03
$\boldsymbol{\theta_5}$	1.099e-03	$\boldsymbol{\theta_{11}}$	3.086e+03

Afterwards, the testing set is substituted into the regression model to obtain predicted values for ζ_{hyst}, which are then compared with calculated ones aiming to examine the fitness of the regression model. Root mean square errors (RMSEs) of both training and testing data are shown in Table 4.1. The RMSE of testing data is slightly larger than that of training data, while it is still relatively small considering the range of ζ_{hyst} as [0,0.4].

Table 5.2. RMSE for hysteresis damping estimation

Training data	0.0084	**Testing data**	0.0172

Fig. 5.11 to Fig. 5.14 show some regression results for the relationships between the hysteretic damping ζ_{hyst} and the variable L, h, t and δ. In each figure, ζ_{hyst} is plotted against a specific variable, while all the other parameters are set as constant. Then the estimation values provided by the regression function (shown as orange star markers) are compared against the observation values (shown as blue circle markers). All the following figures and the RMSE table above

illustrate that the regression model provides an accurate estimate for the hysteretic damping of a generic steel shear wall component for a given drift level.

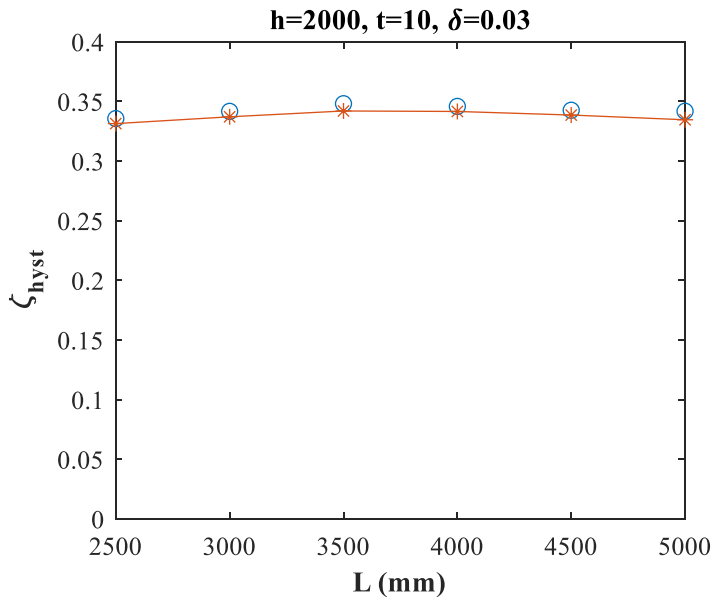

Fig. 5.11. Regression results of ζ_{hyst} *versus L for* $h = 2000\ mm, t = 10\ mm,\ \delta = 0.03$

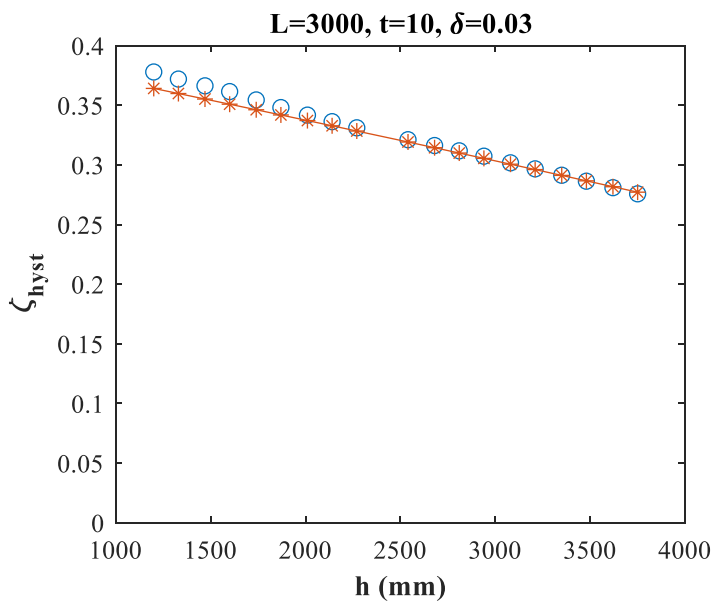

Fig. 5.12. Regression results of ζ_{hyst} *versus h for* $L = 3000\ mm, t = 10\ mm,\ \delta = 0.03$

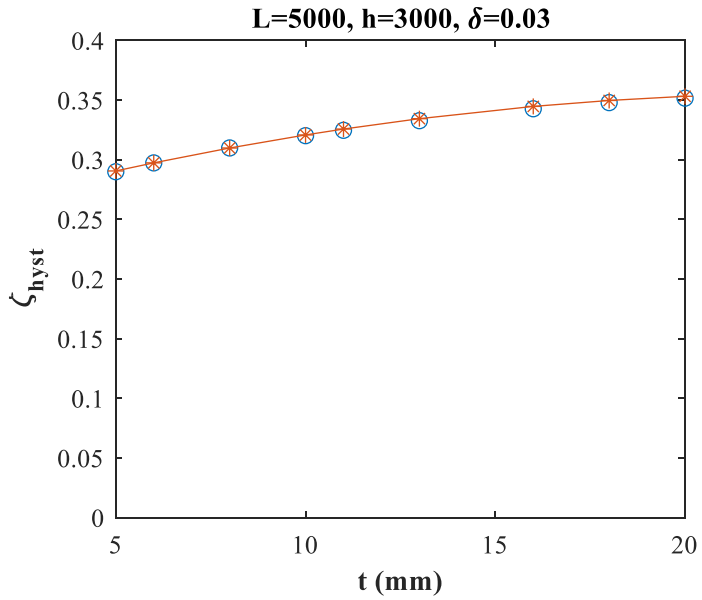

Fig. 5.13. Regression results of ζ_{hyst} *versus* t *for* $L = 5000\ mm, h = 3000\ mm,\ \delta = 0.03$

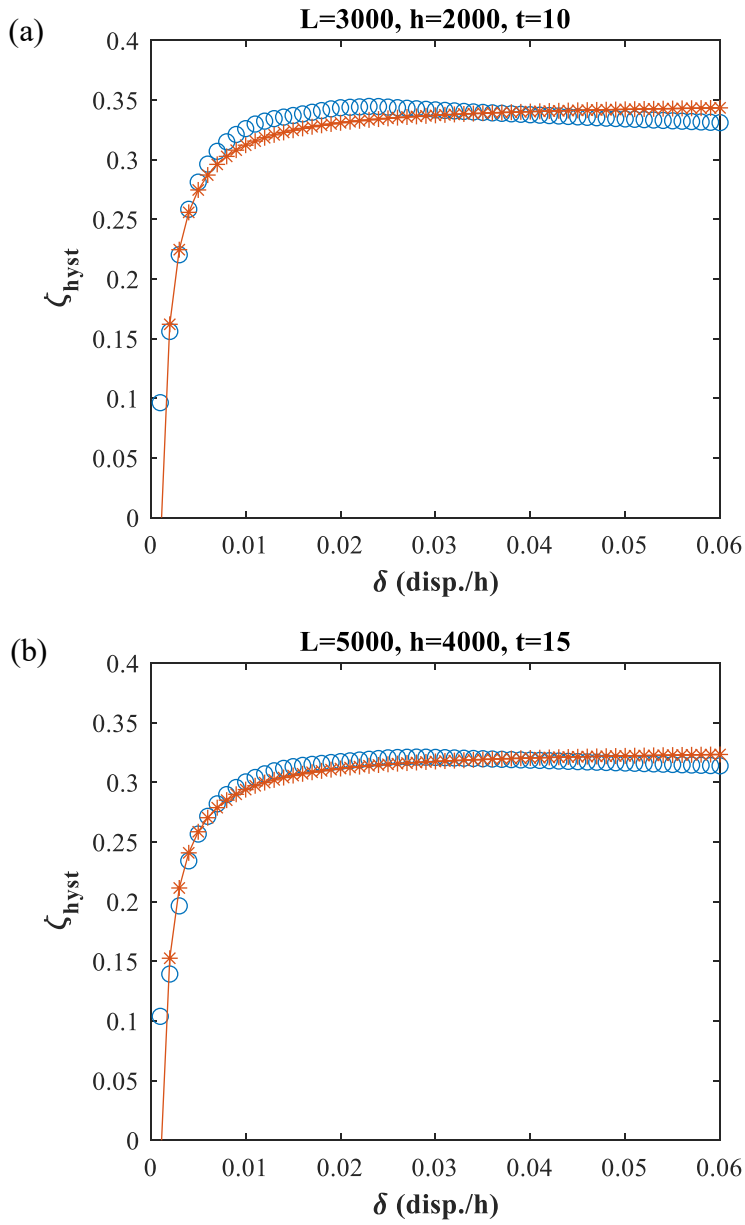

Fig. 5.14. Regression results of ζ_{hyst} versus δ for: (a) $L = 3000\ mm,\ h = 2000\ mm,\ t = 10\ mm$; (b) $L = 5000\ mm,\ h = 4000\ mm,\ t = 15\ mm$

For the selected two cases in Fig. 5.14, the regression results for hysteresis damping are transformed from $\zeta_{hyst} - \delta$ to $\zeta_{hyst} - \mu$ to compare against literature equations, which have been discussed in Section 2.2.5. The stiffness degrading (SD) system with 2% post-elastic stiffness in FEMA-440 (Security and Agency, 2013), the Takeda 'Fat' (TF) rule proposed by Grant et al. (2005) and the original function for the elastic-perfectly plastic (EPP) rule (Dwairi

et al., 2007) are selected as references. Fig. 5.15 shows the comparisons for the two cases, which confirm that the regression results are within the limits defined by existing models while providing a more accurate definition of the equivalent damping based on the specific characteristics of the cyclic response of steel shear wall components.

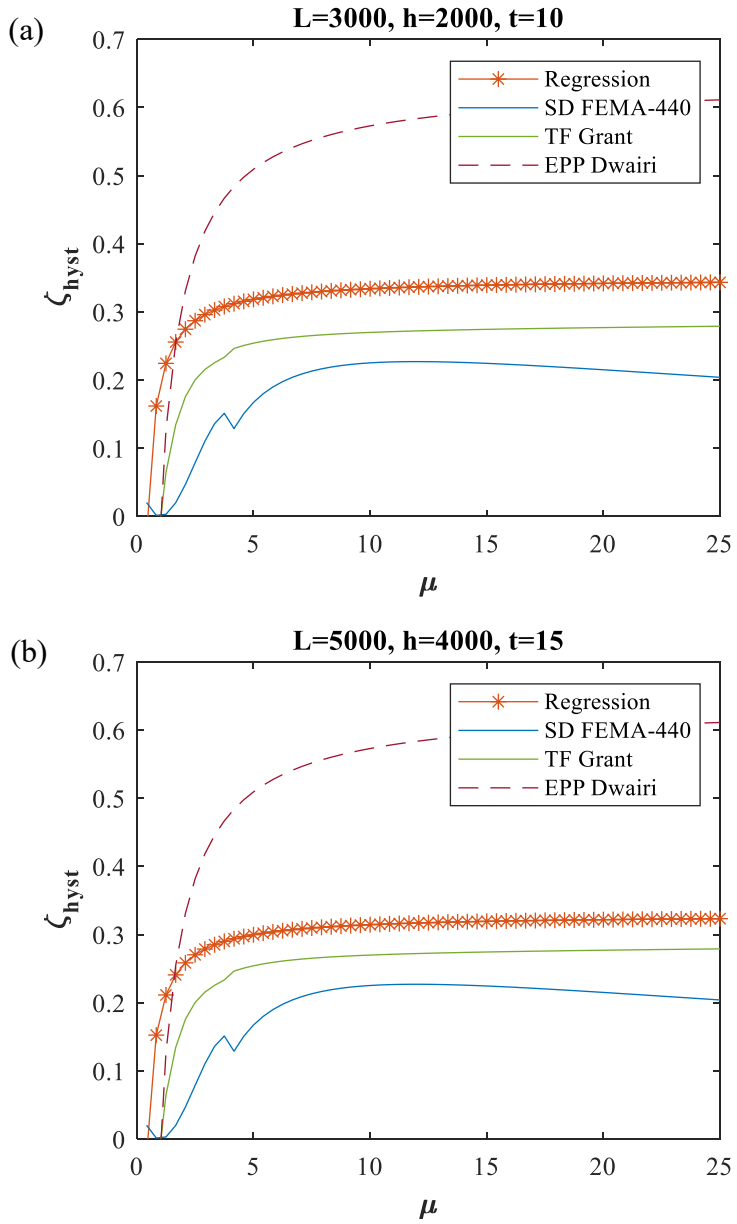

Fig. 5.15. Regression results of ζ_{hyst} versus μ in comparison with literature results for: (a) $L = 3000\ mm,\ h = 2000\ mm,\ t = 10\ mm$; (b) $L = 5000\ mm,\ h = 4000\ mm,\ t = 15\ mm$

5.6 Concluding remarks

In this chapter, a new optimal design procedure for the seismic retrofitting of RC framed structures is proposed. It translates the seismic retrofitting design using steel shear walls to a multi-objective optimisation problem enabling automatic selection for the infill type and thickness of steel shear walls. An overview of the developed strategy is first provided, where the capacity spectrum method is adopted for assessing the seismic performance of retrofitted systems. Afterwards, the determination of the bare and retrofitted frame deformation capacity is described, which is assessed by checking chord rotation and shear force limits for each RC beam and column of the original substandard frame at the end of each analysis step. The definition and evaluation of chord rotation angels and shear forces are presented in detail.

For the selection of optimal solutions, a GA procedure is developed with the aid of the MATLAB *Global Optimisation Toolbox* (MathWorks, 2020). The main steps of the optimisation strategy are described including population representation and initialisation, analysis and objective evaluation for each individual solution, creation of a new population, and convergence criteria. After generating the Pareto front and achieving a set of optimal solutions, engineering judgement is considered to select the best solution for the specific retrofitting problem.

As the damping ratio of the retrofitted structure is needed in the capacity spectrum method, the EVD of steel shear walls is estimated in the final part of the chapter. Virtual tests are first performed for steel wall macroelement models with different properties under different drift levels. Then nonlinear regression is carried out in order to obtain a nonlinear function for the damping ratio in terms of plate length, height, thickness and drift demand. Comparisons between estimation and observation data confirm that the adopted regression model provides a very good estimate for the steel shear wall equivalent damping.

Chapter 6

Application of Optimal Seismic Retrofitting Design to a Deficient RC Building

6.1 Introduction

The optimal procedure for seismic retrofitting design presented in Chapter 5 is applied to a case study in this chapter. A four-storey RC framed building is assessed under earthquake loading at the near-collapse (NC) limit state. The results of nonlinear dynamic simulations utilising a set of natural ground acceleration records have confirmed that the analysed structure is unsafe. Thus seismic retrofitting using steel shear walls is applied to enhance the seismic performance. Due to the regularity characteristics of the analysed structure, the proposed optimal seismic retrofitting design is applied onto 2D RC frames along the two main in-plane directions of the building. Pareto fronts for the retrofitted frames are obtained using the developed MATLAB code, and optimal solutions are selected based on engineering judgement. The effectiveness of the proposed optimal design strategy is verified by performing nonlinear dynamic simulations

of the 2D retrofitted frames and the whole 3D building under earthquake loading, where the developed macroelement model is employed for representing the optimal steel shear wall components.

In the following, Section 6.2 first provides a basic description of the geometric and mechanical characteristics of analysed RC frame building, illustrating also the modelling strategy in ADAPTIC (Izzuddin, 1991) utilised for nonlinear static and dynamic simulations. Subsequently, the seismic assessment of the bare frame and the results from optimal retrofitting design are presented and discussed in Sections 6.3 and 6.4. Finally, the outcomes of the seismic assessment for the retrofitted 3D building, where macroelements are employed to describe steel shear walls with optimal geometrical characteristics, are presented in Section 6.5.

6.2 RC frame building

6.2.1 Building characteristics

A regular 4-storey RC building is selected as a case study to investigate the effectiveness of the proposed optimal seismic retrofitting design procedure. The framed building sample corresponds to a portion of a larger school building designed considering gravity and wind loading but not seismic action and built in Italy in the 1960s, which was investigated under earthquake loading in previous research (Masjuki, 2017). The analysed building structure is characterised by RC floors with ribbed one-way spanning slabs. It is composed of five identical 3-bay RC frames along the X direction in Fig. 6.1 supporting the floor slabs and two additional perimetric 4-bay frames with a uniform span length of 5650 mm in the perpendicular direction (Y direction in Fig. 6.1). A 2-storey part of the generic X-frame has been analysed in Section 4.5, where the steel reinforcement details of representative columns and beams are also shown in Fig. 4.9 and Fig. 4.10. The heights of the 1st, 2nd, 3rd and 4th storey are given as 3.05 m, 4.25 m, 3.51 m and 3.51 m, respectively.

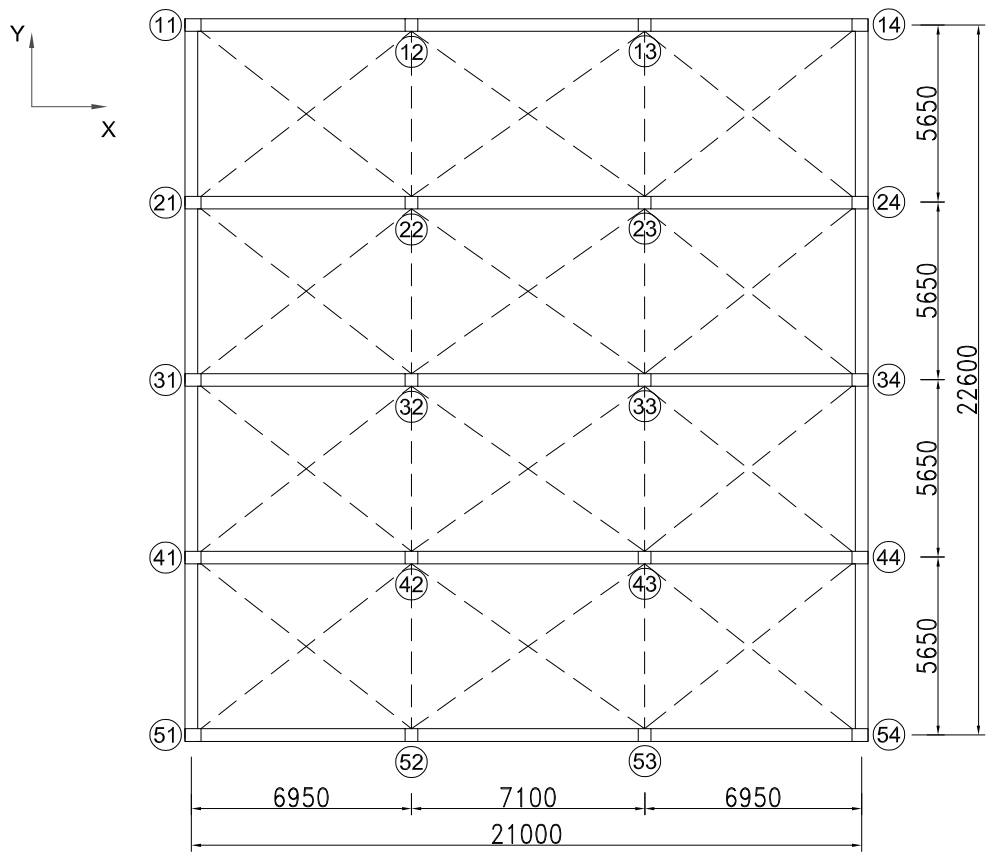

Fig. 6.1. Structural plan with column numbering for the RC frame building and floor regions (all dimensions in mm)

Fig. 6.1 showing the plan view of the analysed frame building illustrates the arrangement of beams and columns with the column numbering adopted in the numerical model in ADAPTIC. It refers to the column numbering adopted in the 3D model for the larger building investigated in Masjuki (2017). Table 6.1 and Table 6.2 list the geometrical characteristics, connectivity and gravity loading for columns and beams on different floors.

Table 6.1. Geometrical characteristics for RC columns

Floor ID	Column ID	Width (mm)	Depth (mm)	Number bars
1; 2	31	650	300	4
	32	550	550	6
	33	550	550	6
	34	650	300	4
3; 4	31	500	300	4
	32	400	400	3
	33	400	400	3
	34	500	300	4

Table 6.2. Geometrical characteristics, connectivity and gravity loading for RC beams

Storey ID	Joint 1	Joint 2	Width (mm)	Depth (mm)	UDL (kN/m)	Mass (kN/g/mm)	Number bars
1; 2	31	32	300	850	-33.74	0.003439	3
	32	33	300	850	-46.08	0.004697	4
	33	34	300	850	-46.08	0.004697	4
	31	21	300	850	-8.10	0.000826	3
3; 4	31	32	400	850	-31.36	0.003197	4
	32	33	400	850	-38.62	0.003937	3
	33	34	400	850	-38.62	0.003937	3
	31	21	400	850	-14.00	0.001427	4

In the calculations, the permanent and the variable floor loads are assumed as 4.6 kN/m^2 and 3.0 kN/m^2, respectively, while the variable load applied on the roof due to snow is set as 0.8

kN/m^2. According to Eurocode 8 – 1 (EN1998-1, 2004), the seismic mass used in the simulations under earthquake loading is given by:

$$\sum G_k + \sum \psi_E \cdot Q_k \tag{6.1}$$

where G_k and Q_k represents the characteristic value of permanent and variable action, respectively; ψ_E is the combination coefficient considering the likelihood of the variable loads not being present during the earthquakes. In this case study, ψ_E is simply taken as 0 for the roof (the 4th storey) and 0.3 for the other storeys, which are typical values for a school building recommended in Eurocode 0 (EN1990, 2002).

6.2.2 3D building model

The 3D numerical model in ADAPTIC is shown in Fig. 6.2. The modelling strategy described in Section 4.5 is utilised to represent the beams and columns of the building with the same material characteristics reported in Table 4.4.

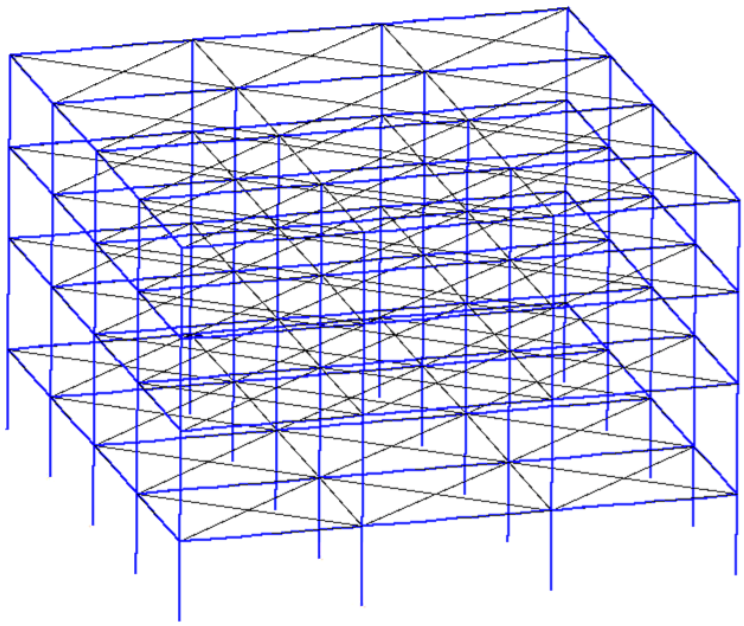

Fig. 6.2. 3D frame building model in ADAPTIC

On the other hand, the diaphragm action due to the floor slab is explicitly taken into account in the 3D building model modelling the top solid parts of the ribbed floor slabs by a set of 3D link elements representing peripheral frame components and diagonal braces (Fig. 6.1 and Fig. 6.2) with flexural and axial stiffness values given by (Masjuki, 2017; Yettram and Husain, 1966):

$$EI_f = \frac{Eh}{60} l_x^2 l_y \tag{6.2}$$

$$EA_f = \frac{Ehl_y}{2}\left[1 - 0.2\left(\frac{l_x}{l_y}\right)^2\right] \tag{6.3}$$

$$EA_d = \frac{Eh}{10}\left(\frac{l_x^2 + l_y^2}{l_x l_y}\right)^{\frac{3}{2}} \tag{6.4}$$

where EI_f and EA_f are the flexural and axial rigidities of the frame links, respectively; EA_d is the axial rigidity of the diagonal braces; E is Young's modulus of the concrete material of the floor slab; l_x, l_y and h are the in-plane dimensions and the top thickness of the floor slab rectangular regions defined by the column grid as shown in Fig. 6.1.

In the numerical simulations, a partitioned modelling strategy (Jokhio and Izzuddin, 2013) implemented in ADAPTIC using domain decomposition is adopted to improve the computation efficiency. According to this approach, which allows for parallel computation, the analysed large structure is modelled as a parent structure with a number of placeholder super-elements representing the partitioned subdomains, named as the child partitions. Each child partition simulates parts of the main structural system and is analysed separately, where a dual super-element links the interface boundary of the child partition to the parent structure. Two-way communication between the parent structure and the child partitions is realised by providing iterative displacements U_i of the placeholder super-elements in the parent structure to the corresponding dual super-elements in the child partitions, after which resistance forces R_i and tangent stiffness K_i are returned to the parent structure, as schematically illustrated in Fig. 6.3 (Izzuddin et al., 2013). Both parent structure and child partitions can be analysed in the same

finite element analysis programme using the same library of materials, elements and solution methods (Jokhio and Izzuddin, 2015).

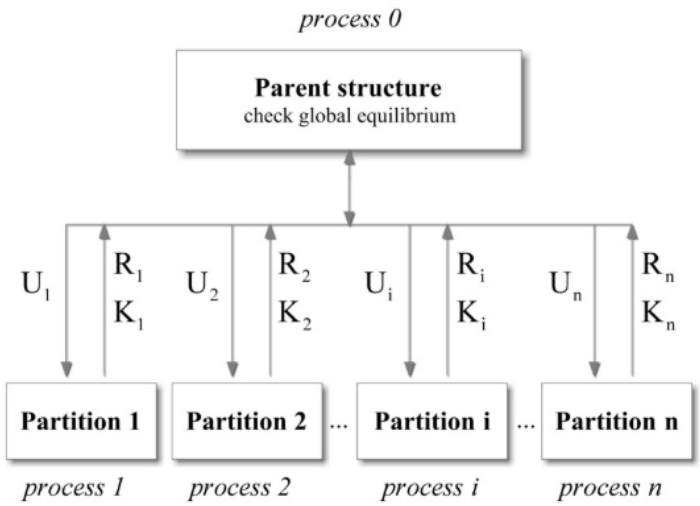

Fig. 6.3. Two-way communication of partitioned modelling method (Izzuddin et al., 2013)

6.3 Seismic assessment of the RC building

6.3.1 Design spectrum and accelerograms

The seismic performance of the RC buildings at the NC limit state has been investigated by nonlinear dynamic simulations considering the set of ground acceleration records used in a previous numerical study on the larger school building (Masjuki, 2017). They are based on the design spectrum shown in *Fig.* 6.4 and have been generated using REXEL (Iervolino et al., 2009) considering the following recommendations in Eurocode 8 (EN1998-1, 2004; EN1998-3, 2005):

- The mean of the zero-period spectral response acceleration values should not be smaller than the value of $a_g \cdot S$ for the site in question, where S is the soil factor;
- The accelerograms should be in the range of periods between $0.2T_1$ and $2T_1$, where T_1 is the fundamental period of the structure in the direction where the accelerogram will be applied; no value of the mean 5% damping elastic spectrum, calculated from all-

time histories, should be less than 90% of the corresponding value of the 5% damping elastic response spectrum.

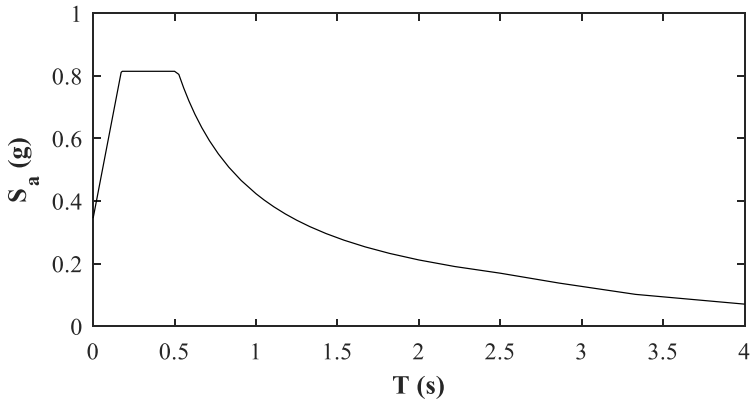

Fig. 6.4. Design elastic response spectrum

Table 6.3 reports basic information for the building site and the adopted design elastic response spectrum from the Italian seismic code (NTC, 2008). The design peak ground acceleration on ground type A is set as $a_g = 0.283g$ and the soil factor for the assumed ground type C is $S = 1.15$. Seven sets of the accelerograms each containing two acceleration time-history components along the horizontal X and Y directions of the RC frame building have been considered for the nonlinear dynamic simulations. The spectrum compatibility is shown in Fig. 6.5, while the main characteristics of the selected ground acceleration histories are reported in Table 6.4 and Table 6.5, and time-acceleration curves are shown in Fig. 6.6 (Masjuki, 2017).

Table 6.3. Site and design spectrum data

Lon (°)	Lat (°)	Site class	Top cat.	V_n	CU	a_g (g)
13.394	42.366	C	T1	50 years	II	0.283

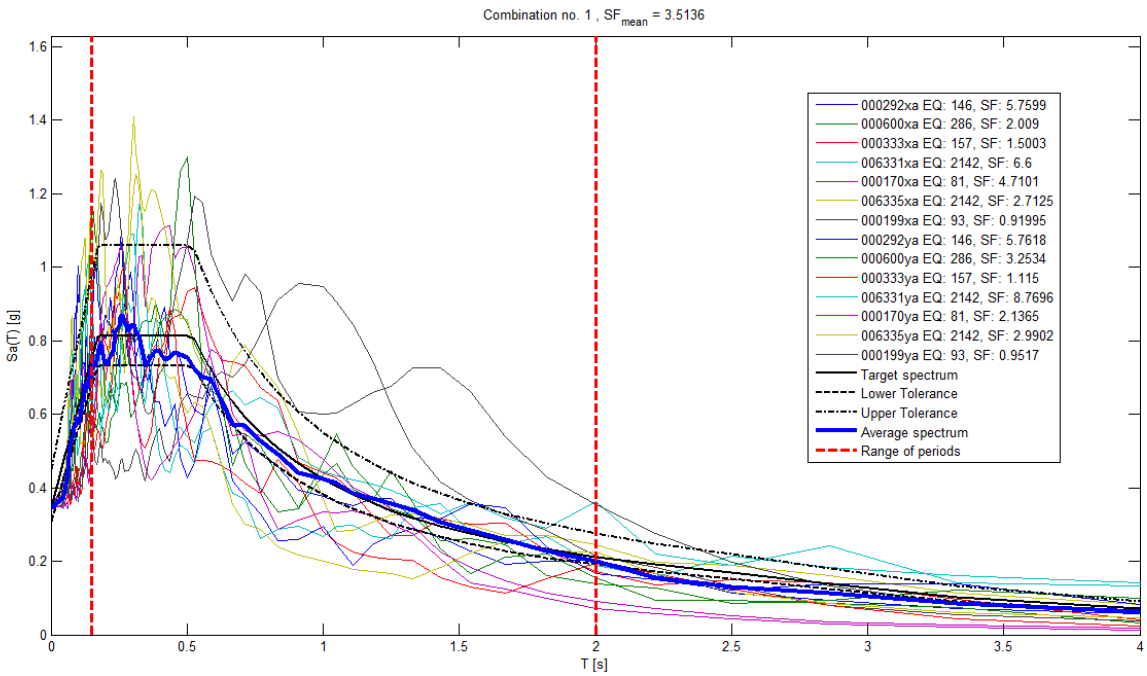

Fig. 6.5. Spectrum compatibility in X and Y directions (Masjuki, 2017)

Table 6.4. Main characteristics of the selected accelerograms (I) (Masjuki, 2017)

Waveform ID	Earthquake ID	Station ID	Earthquake Name	Date	Mw	Fault Mechanism	Epicentral Distance (km)	EC8 Site class
170	81	ST46	Basso Tirreno	15/04/1978	6	oblique	18	C
199	93	ST67	Montenegro	15/04/1979	6.9	thrust	16	B
292	146	ST98	Campano Lucano	23/11/1980	6.9	normal	25	A
333	157	ST121	Alkion	24/02/1981	6.6	normal	20	C
600	286	ST223	Umbria Marche	26/09/1997	6	normal	22	C
6331	2142	ST2486	South Iceland (aftershock)	21/06/2000	6.4	strike-slip	22	A
6335	2142	ST2557	South Iceland (aftershock)	21/06/2000	6.4	strike-slip	15	A
Means					6.46		19.7143	

Table 6.5 Main characteristics of the selected accelerograms (II) (Masjuki, 2017)

Waveform ID	PGA_X [m/s^2]	PGA_Y [m/s^2]	PGV_X [m/s]	PGV_Y [m/s]	ID_X	ID_Y	Np_X	Np_Y
170	0.7188	1.5846	0.0619	0.1543	10.7925	4.7453	0.5245	1.0578
199	3.6801	3.5573	0.4210	0.5202	7.9992	10.2063	1.1525	0.8440
292	0.5878	0.5878	0.0436	0.0585	16.3510	13.7949	0.6554	1.1620
333	2.2566	3.0363	0.2234	0.2262	7.9202	7.4474	0.7593	0.7789
600	1.6852	1.0406	0.1449	0.1176	8.7515	11.1211	0.6406	0.4604
6331	0.5130	0.3860	0.0572	0.0397	6.5052	7.1010	1.0681	0.7664
6335	1.2481	1.1322	0.1659	0.1083	6.4075	7.0906	0.7804	0.6190
Means	1.5271	1.6178	0.1597	0.1750	9.2467	8.7867	0.7972	0.8126

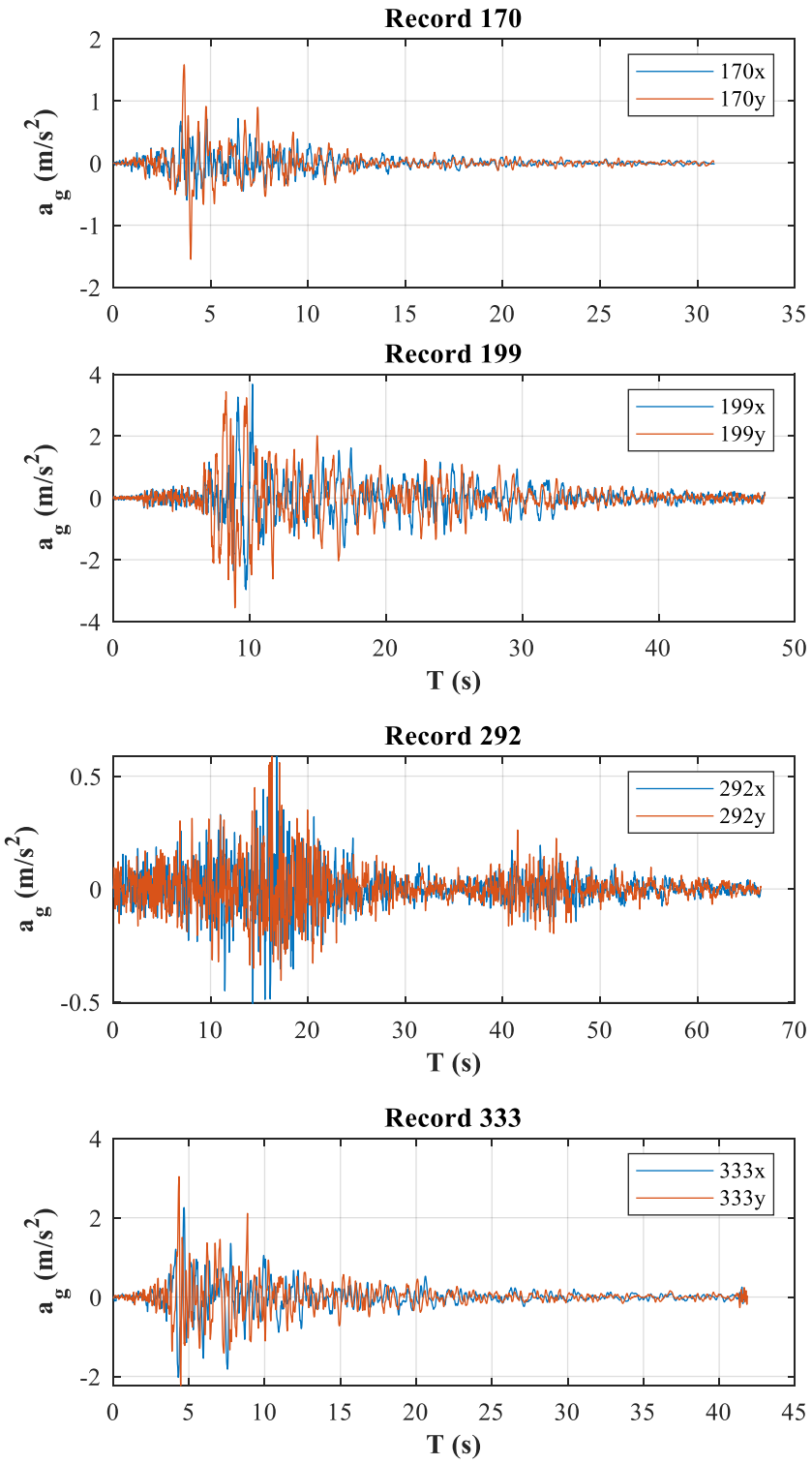

Fig. 6.6. Accelerograms for each record in X and Y direction (Cont'd)

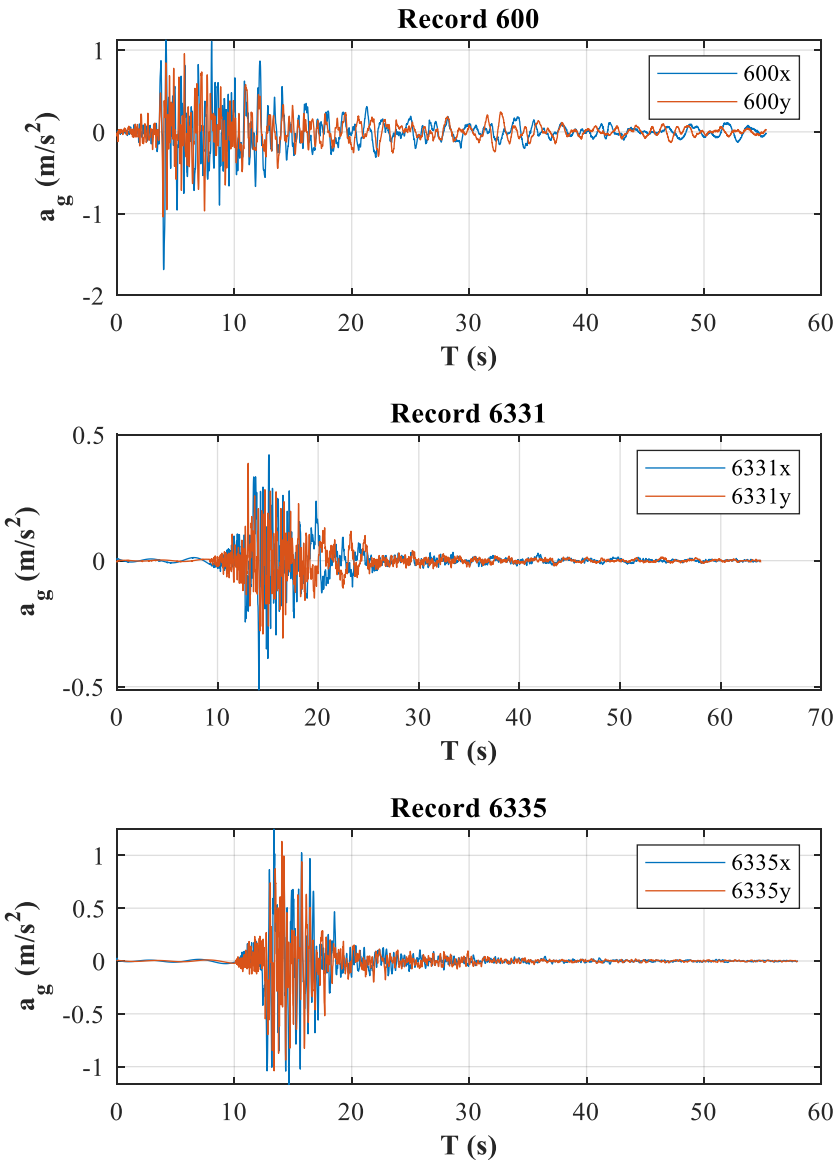

Fig. 6.6. Accelerograms for each record in X and Y directions

6.3.2 Seismic performance of the bare frame

The 3D model of the 4-storey building has been divided into 4 partitions using the partitioning approach introduced previously. Each child partition encompasses beams, columns and floor components for each storey of the building model, while the parent partition includes the nodes at the top of each column of storey 1, 2 and 3. Seven nonlinear dynamic analyses of the 3D building have been performed by applying the seven different pairs of acceleration – time

histories at the base of the columns of the building. The effects due to accidental torsional eccentricities have not been considered in this numerical example.

The performance of the structure at the NC limit state has been assessed by checking local ductile and brittle failure modes in terms of demand-to-capacity ratios for chord rotations and shear forces in beams and columns. As seven distinct simulations have been carried out, mean results can be considered in the seismic assessment of the building according to Eurocode 8 (EN1998-1, 2004; EN1998-3, 2005). They have been calculated considering the mean of the maximum chord rotations and shear forces at each step of the dynamic nonlinear time-history analyses. As in the 3D simulations, the members of the frames of the building (especially the columns) are subjected to bending and shear forces along the two main directions X and Y, circular interaction diagrams have been considered to represent equivalent chord rotations and shear forces under biaxial bending as recommended in Fardis (2009). The circular interaction relationships for the chord rotation and shear force checks are given by:

$$\sqrt{\left(\frac{\overline{\theta}_y}{\theta_{um,y}}\right)^2 + \left(\frac{\overline{\theta}_z}{\theta_{um,z}}\right)^2} \leq 1 \tag{6.5}$$

$$\sqrt{\left(\frac{V_y}{V_{R,y}}\right)^2 + \left(\frac{V_z}{V_{R,z}}\right)^2} \leq 1 \tag{6.6}$$

where $\overline{\theta}_y$, $\overline{\theta}_z$ and V_y, V_z are the uniaxial chord rotations and shear forces along the local y and z axes respectively, which can be calculated as discussed in Section 5.3; $\theta_{um,y}$, $\theta_{um,z}$ and $V_{R,y}$, $V_{R,z}$ are the uniaxial ultimate chord rotation capacities and shear resistances introduced in Section 2.2.6.

The results summarising the seismic assessment of the building concerning local ductile and brittle failure checks are shown in Fig. 6.7, Fig. 6.8, Fig. 6.9 and Fig. 6.10, where the mean demand-to-capacity ratios for chord rotations and shear forces of the RC columns and beams are shown. The results under each individual set of earthquake records are included in the Appendix. In the figures, the label for each rectangular bar refers to a specific column or beam

in the building, where the first digit corresponds to the floor number followed by the column ID (Table 6.1) for the column bars and the number of the two joints (Table 6.2) at the ends of each beam for the beam bars.

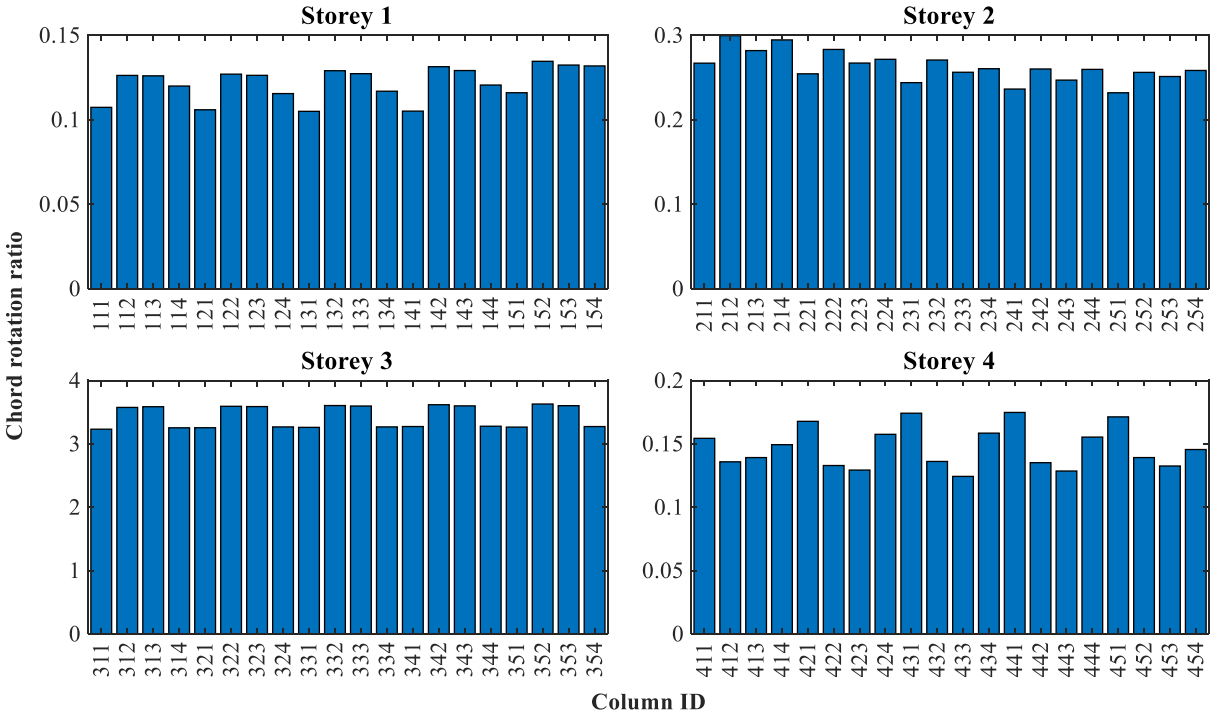

Fig. 6.7. Mean chord rotation ratios for the columns of the 3D bare building model

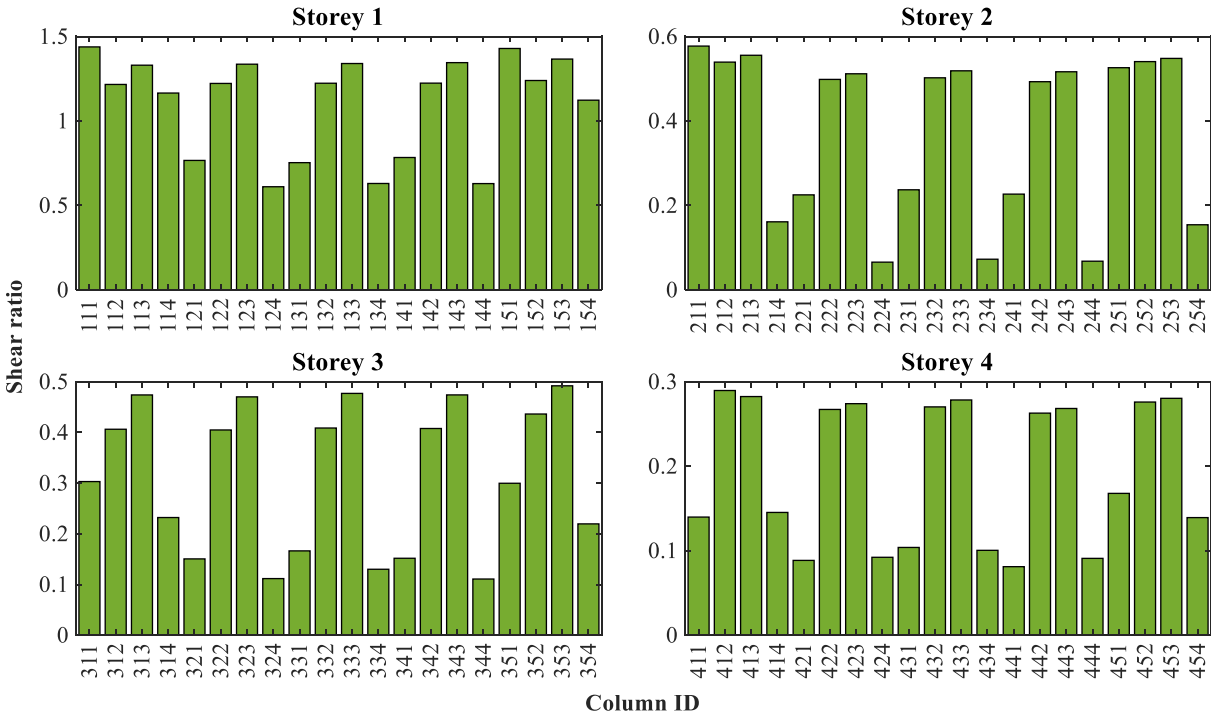

Fig. 6.8. Mean shear force ratios for the columns of the 3D bare building model

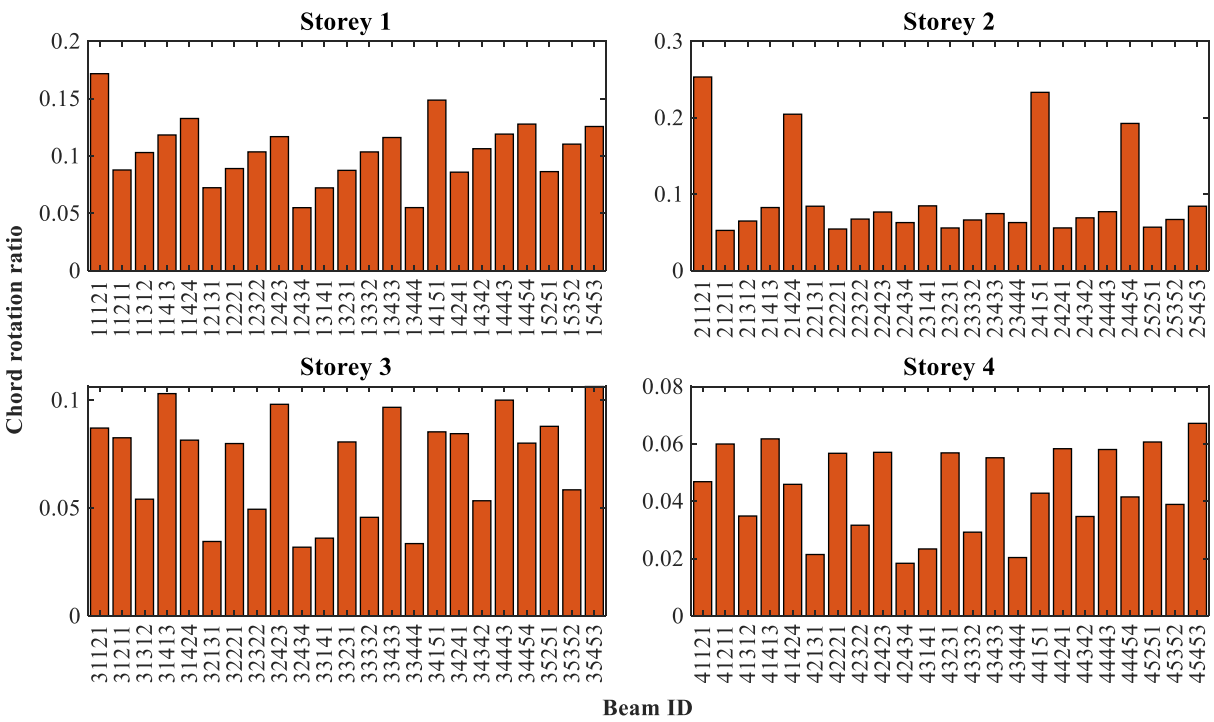

Fig. 6.9. Mean chord rotation ratios for the beams of the 3D bare building model

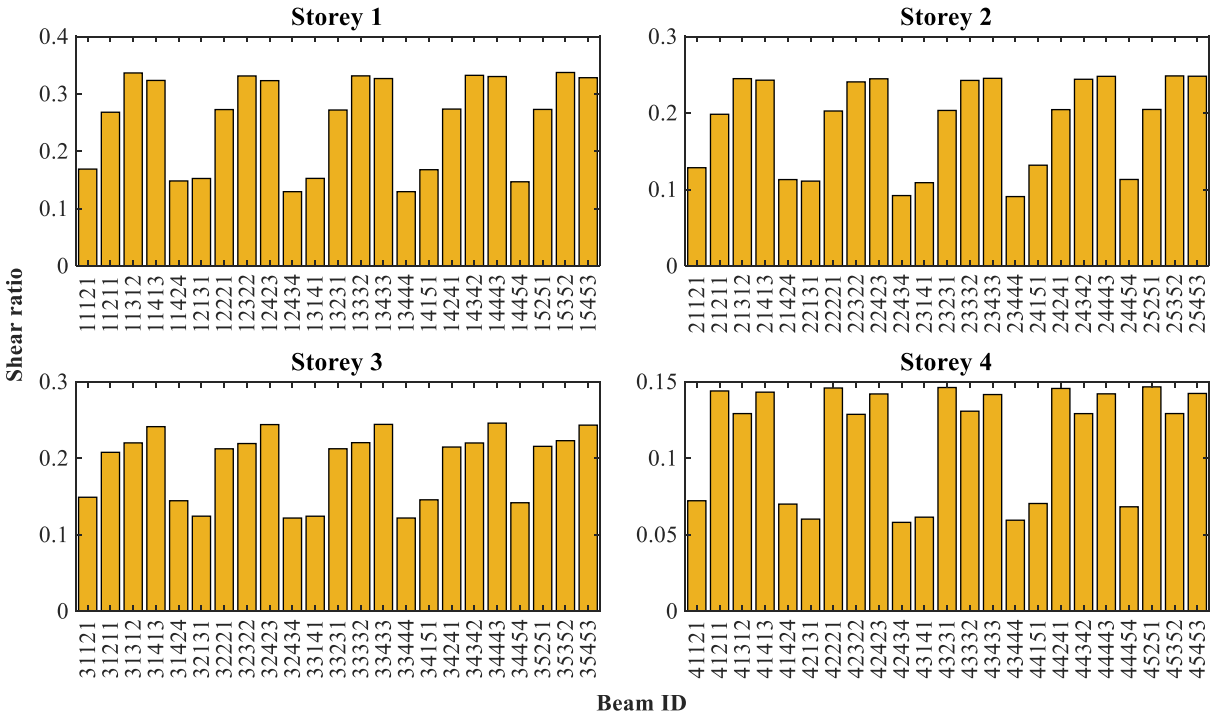

Fig. 6.10. Mean shear force ratios for the beams of the 3D bare building model

All the chord rotation ratios of the columns on the 3rd floor are much larger than 1 (Fig. 6.7) indicating local ductile failure in these elements and the formation of a storey mechanism. Furthermore, the shear ratios for most of the columns at the 1st-floor level exceed 1 (Fig. 6.8) which implies local brittle failure on the ground floor. On the other hand, the results of the nonlinear dynamic analyses suggest that the beams do not develop any ductile or brittle failure under earthquake loading at the NC limit state, as all the beam demand-capacity ratios are smaller than 1.

Fig. 6.11 shows the deformed shape of the 3D building model predicted by ADAPTIC under the ground accelerations Record 199 at a generic time step, where the development of a storey mechanism at the 3rd-floor level can be seen.

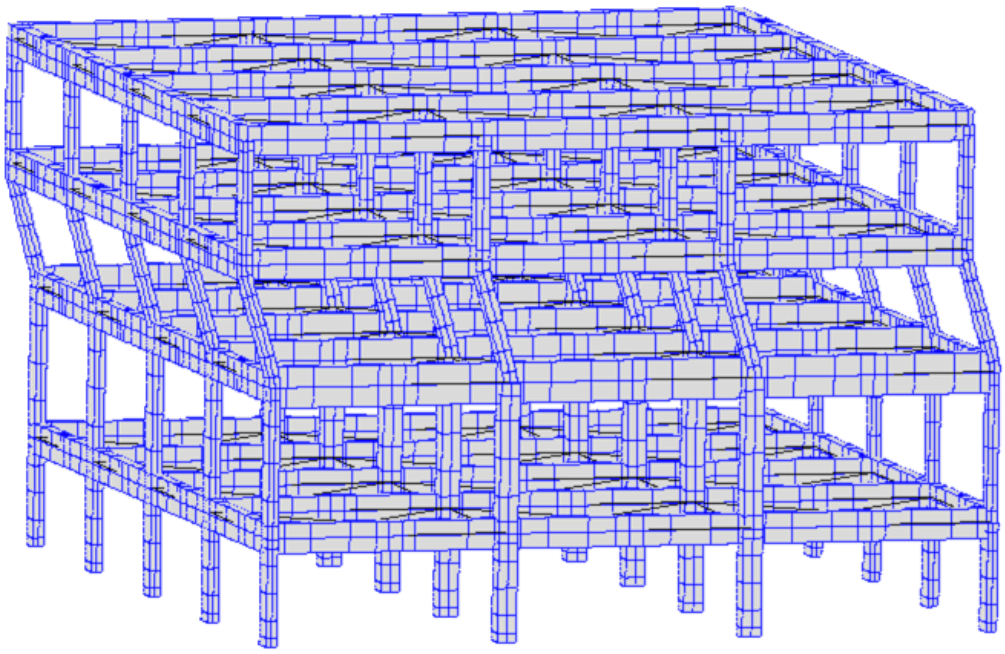

Fig. 6.11. Deformed shape of 3D bare building model under Record 199 acceleration

Further nonlinear dynamic simulations have been conducted on 2D frame models. Due to the regularity characteristics of the 3D building, one X-fame with columns 11, 12 and 13 (Fig. 6.1) and one Y-frame with columns 11, 21, 31, 41 and 51 (Fig. 6.1) have been analysed separately, applying the acceleration histories at the base of the columns along the longitudinal direction of the frames and restraining the out-of-plane displacements at the four levels.

The results displayed in Fig. 6.12 and Fig. 6.13 are similar to the outcomes from the assessment by the 3D building model. Also in this case, local ductile failure develops in the 3rd-floor columns and shear failure occurs in the columns. This confirms the suitability of simplified 2D assessment, as the effects due to biaxial bending interaction that are explicitly allowed for only in 3D simulations lead to increased demand–capacity ratios, but not to a change in the local failure modes. These results also confirm that the design of potential strengthening can be addressed via nonlinear 2D analyses, which is expected due to the regularity characteristics of the building.

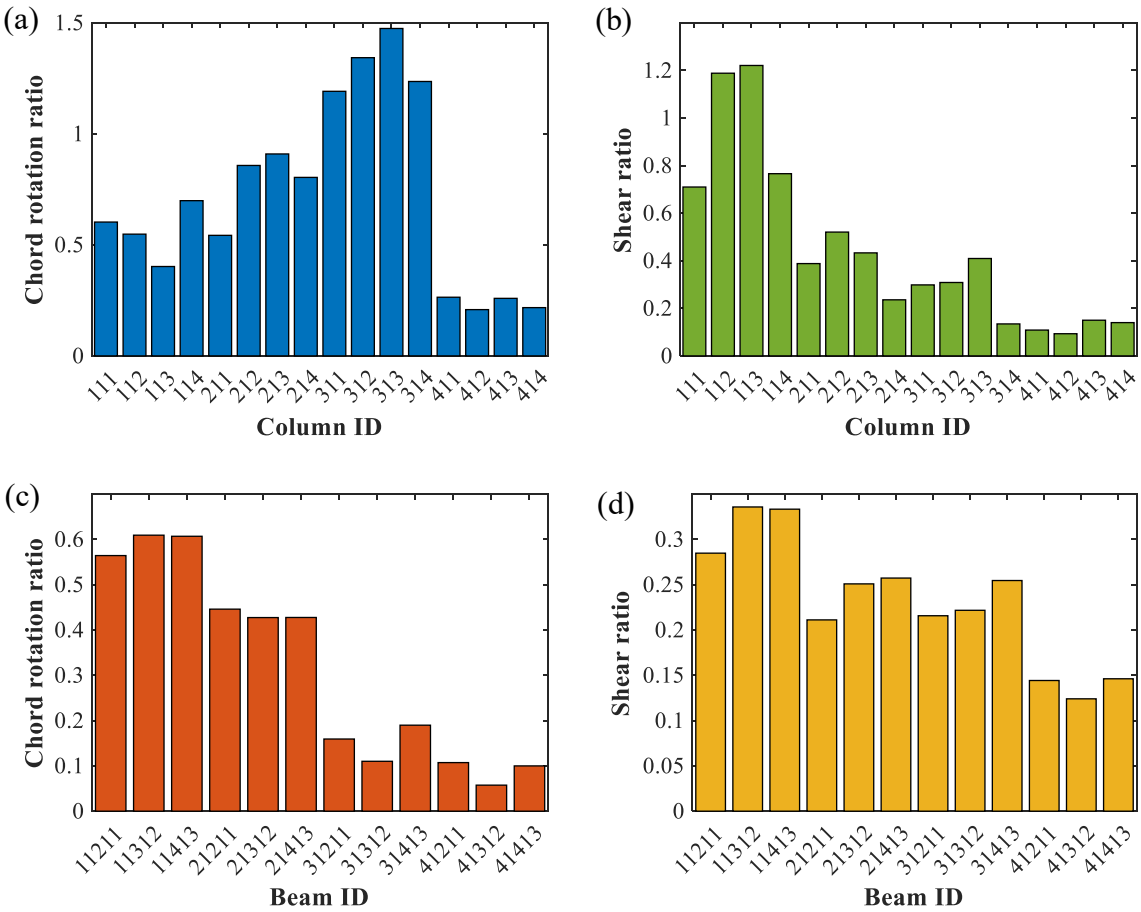

Fig. 6.12. Seismic assessment results for the bare X-frame: (a) Column chord rotation ratios; (b) Column shear ratios; (c) Beam chord rotation ratios; (d) Beam shear ratios

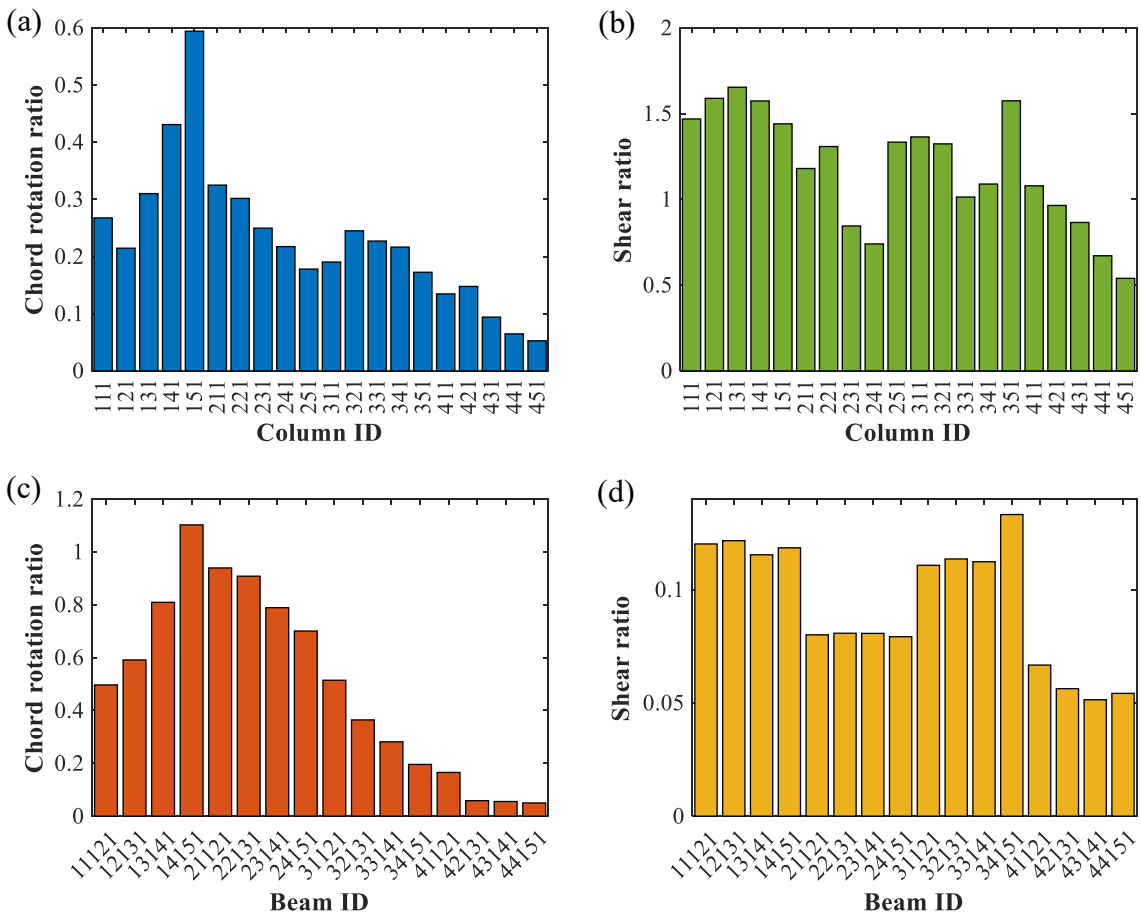

Fig. 6.13. Seismic assessment results for the bare Y-frame: (a) Column chord rotation ratios; (b) Column shear ratios; (c) Beam chord rotation ratios; (d) Beam shear ratios

Fig. 6.14 and Fig. 6.15 show the deformed shapes under Record 199 at the time steps of maximum top displacements predicted by the X-frame and Y-frame models, denoting high local ductility demands in the columns on the 3rd floor in the X-direction.

The results of the seismic assessment conducted by performing 3D and 2D nonlinear dynamic simulations indicate that retrofitting is required. It is addressed in the following section, where optimal seismic retrofitting design is carried out to enhance the performance of the substandard RC frame building.

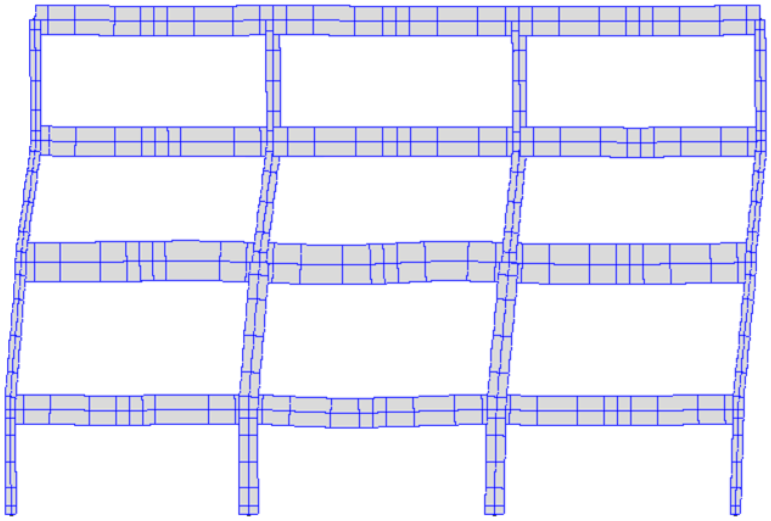

Fig. 6.14. Deformed shape of 2D X-frame under Record 199 accelerations at the maximum top displacement of 114.0 mm

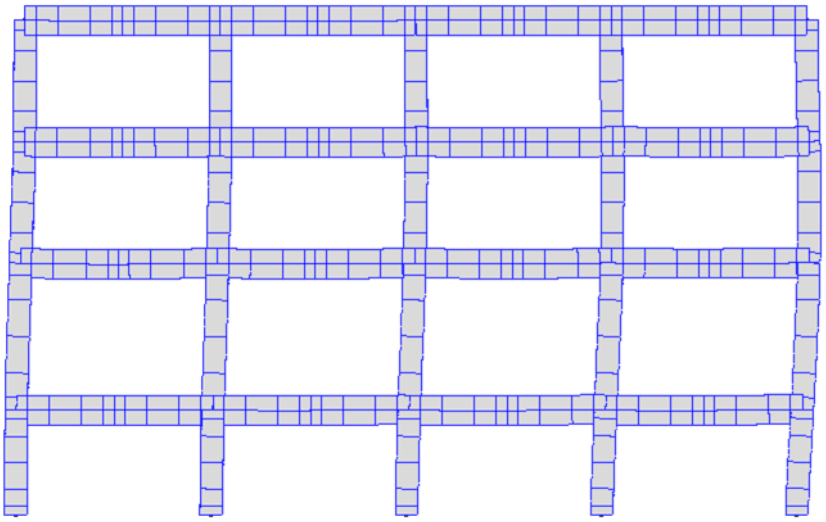

Fig. 6.15. Deformed shape of 2D Y-frame under Record 199 accelerations at the maximum top displacement of 150.9 mm

6.4 Optimal seismic retrofitting design

The substandard RC frame building is retrofitted using steel shear walls. To avoid detrimental torsional eccentricity effects, the steel shear walls are arranged symmetrically on the four sides

of the building. Thus, optimal seismic retrofitting design is applied to one X-frame and one Y-frame, separately.

6.4.1 Optimal retrofitting design for X-frame

Pushover analysis is first performed on the bare X-frame model. A spreader element available in ADAPTIC is employed to distribute the base shear force according to the 'modal' pattern shown in Fig. 2.1(a) while controlling the horizontal displacement at a master node at the top of the frame. The assumed spread force ratio is equal to $m_i\Phi_i/\sum m_i\Phi_i$ at each storey, where m_i and Φ_i are the storey seismic mass and displacement shape, respectively. Table 6.6 reports the calculation results for the loads, seismic masses and spread ratios at the different floor levels.

Table 6.6. Loads, seismic masses and spread ratios

Floor	Storey height (m)	G_k (kN)	Q_k (kN)	Load Combination (kN)	Seismic mass m_i (ton)	Φ_i	Spread ratio
1	3.05	3852.3	1779.8	4386.2	447.1	0.213	0.091
2	4.25	3880.9	1779.8	4414.8	450.0	0.51	0.219
3	3.51	3893.5	1779.8	4427.4	451.3	0.755	0.325
4	3.51	3757.5	474.6	3757.5	383.0	1	0.365

After conducting the pushover analysis, the shear force – top displacement curve for the X-frame is converted into the capacity diagram. Only the seismic mass for one single bare frame associated with the portion of the floor directly supported by the frame is considered at this stage. The deformation capacity is determined as $D_{c0} = 31.4$ mm by checking the chord rotation and shear force limits at every step of the pushover analysis. On the other hand, the demand diagram is converted from the elastic response spectrum introduced in Section 6.1 considering the damping of the bare X-frame calculated using Eq. (5.6) as $\zeta_f = 0.197$. The intersection of the capacity and demand diagrams is defined as the deformation demand $D_{d0} = 176.1$ mm, which is much higher than the deformation capacity.

Therefore, the X-frame model needs to be retrofitted. Fig. 6.16 displays the curves described above.

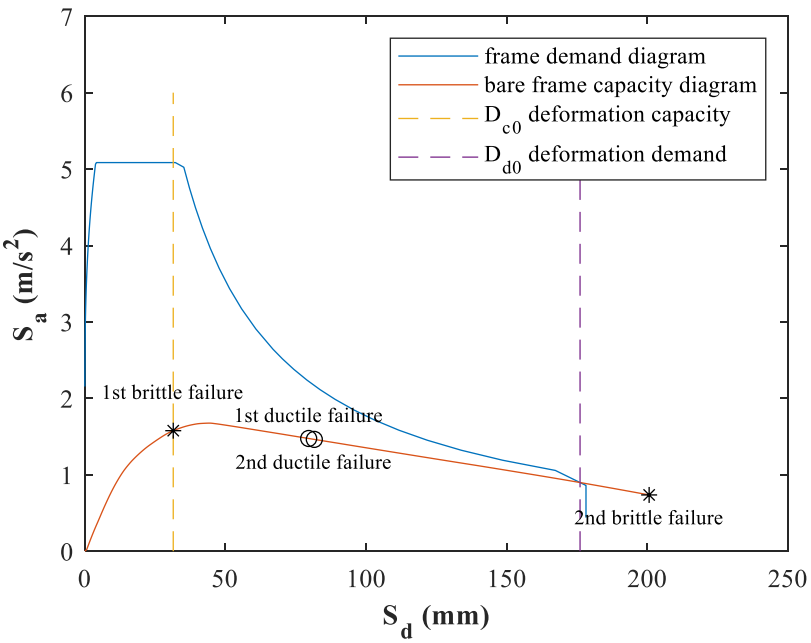

Fig. 6.16. Demand and capacity diagram of the bare X-frame model

The optimal seismic design procedure is carried out on the 2D X-frame following the steps presented in Section 5.2 by adding steel shear wall components into the mid-bay of the perimetric X-frames of the buildings (i.e. in the bays between Columns 12, 13 and between Columns 52, 53). In the calculations, it is assumed that the stiffness to horizontal earthquake loading of the retrofitted frames with steel shear walls is much higher than the original individual bare frames, so half of the mass of the whole building is applied to the two 2D frames equipped with steel wall components.

The design variables for the X-frame equipped with steel shear walls are set as:

$$x = [sp_{typ};\ t_1;\ t_2;\ t_3\ ;t_4] \tag{6.7}$$

where sp_{typ} is the steel plate type indicating the length of the infill panel; $t_1 \sim t_4$ is the plate thickness of the 1st ~ 4th floor, respectively. The initial population is generated by randomly selecting the design variables. Creation and analysis of the FE models for the X-frame with added steel shear wall macroelements are carried out, as discussed in Chapter 5. When evaluating the FE results for objective functions, the pushover curve of the X-frame with plates is first converted to a new capacity diagram considering the increased seismic mass and equivalent EVD ζ_{eq} of the overall system. After obtaining the EVD of the frame ζ_f and calculating the EVD $\zeta_{p,i}$ of the i-th storey plate using the nonlinear regression function in Eq. (5.35), a simplified method is employed for the calculation of ζ_{eq}, which treats the damping of the plates in the same bay on different floors as a set of dampers in series, and the damping of the bare frame and one bay of steel plates as dampers in parallel. As a result, the global equivalent EVD can be obtained as:

$$\zeta_{eq} = \zeta_f + 1 \Big/ \sum_{i=1}^{4} \frac{1}{\zeta_{p,i}} \tag{6.8}$$

As mentioned in Section 5.4, the optimisation aim is to minimise (i) the gap between seismic capacity D_c and seismic demand D_d, (ii) the amount of added steel shear walls and (iii) drift uniformity measure, which corresponds to minimising the 3 objective functions f_1, f_2 and f_3 shown in Eq. (5.28) to (5.30). New populations are created via the GA process until the convergence criteria are met, and the Pareto front is generated. The objectives are then transferred to relative values to select optimal cases:

$$f_j' = \frac{f_j}{min(f_j)} \quad j = 1,2,3 \tag{6.9}$$

Fig. 6.17 shows the Pareto front for the X-frame optimisation results setting the figure axes as the relative values of each objective. Engineering judgement is involved when selecting an optimal solution from the Pareto front cases. Different criteria are adopted considering the specific retrofitting aims of the real projects referring to the relative objective values. If the retrofitting project needs a balanced solution with minimum demand-capacity gap, minimum

amount of added steel and most uniform inter-storey drifts, the case with the minimum summation of the three objectives is selected, as the solution circled in black in Fig. 6.17. Fig. 6.18 illustrates the new capacity and demand diagram for this case. One-third of the retrofitted bay is infilled by the steel shear walls and the plate thickness on each floor is equal to 2, 7, 3, 2 mm, respectively. If the retrofitting target is adding the minimum amount of steel plates to minimise the cost, the optimal case with the minimum f_2' is selected, as shown in Fig. 6.19. The infill type parameter sp_{typ} is rounded to 1 ('1/3' infill) while the infill plates are 3, 2, 2, 2 mm thick. It is worth mentioning that the stiffness of the retrofitted model is smaller than the bare frame model. The reason is that different masses are assumed when converting the pushover curves to the capacity diagrams. The seismic mass for the bare frame model only takes into account the loads on that bay, while half of the mass of the whole building is considered for the retrofitted frame model assuming that the earthquake loading is resisted only by the two retrofitted bays with increased stiffness. Alternatively, Fig. 6.20 shows the optimal case with minimum f_3' indicating the retrofitted frame with the most uniform inter-storey drift and lateral stiffness distribution along the height of the building. This case can be selected for a retrofitting design aiming to prevent the formation of local soft-storey mechanisms.

Table 6.7 lists the equivalent damping ζ_{eq}, deformation capacity and demand D_c and D_d, the volume of the added plates and drift uniformity measure f_3 for the three selected optimal cases. From the figures and the table, it can be seen that the damping increases when the amount of steel plates increases, and the damping ratio increases leading to a more reduced demand diagram. Meanwhile, the capacity diagram rises and thus the deformation demand decreases. The overall stiffness becomes higher resulting in a lower f_3. In general, the deformation capacity should increase with thicker infill plates. However, the added plates may change the distribution of bending moments and shear forces on the frame and change the chord rotation and shear ratios of beams and columns, giving rise to unpredictable deformation capacity.

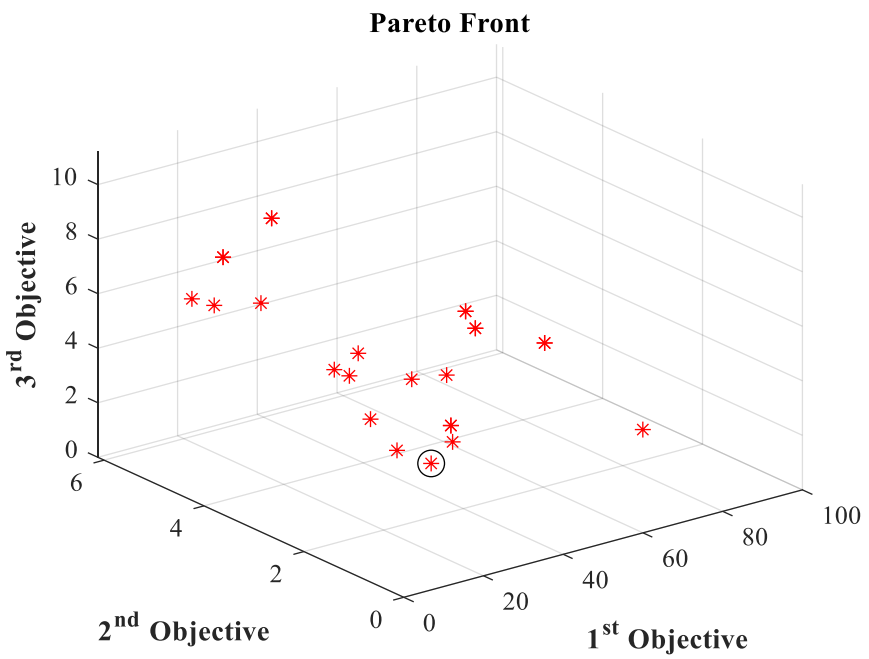

Fig. 6.17. Pareto front for X-frame optimisation

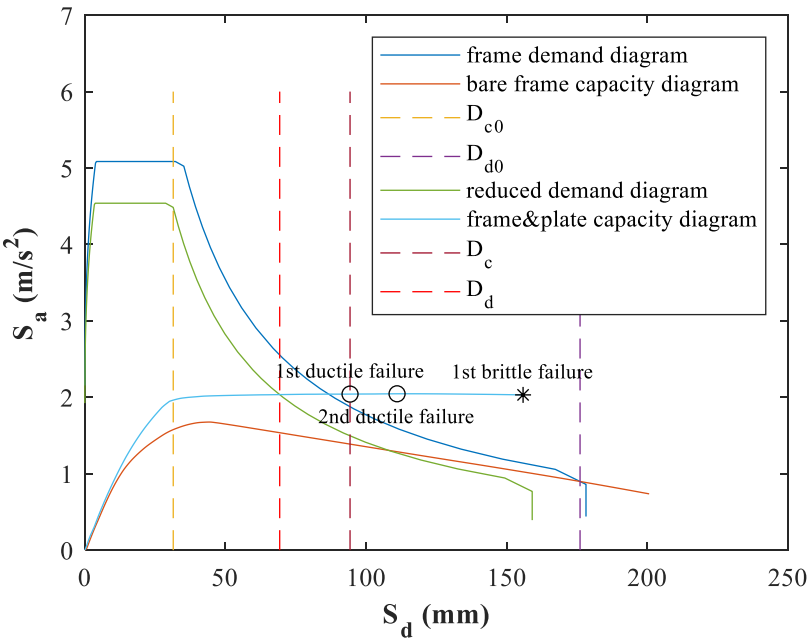

Fig. 6.18. Demand and capacity diagram of the optimal case for X-frame optimisation with min $(f_1' + f_2' + f_3')$*:* $sp_{typ} = 1, t = 2,7,3,2$ *mm*

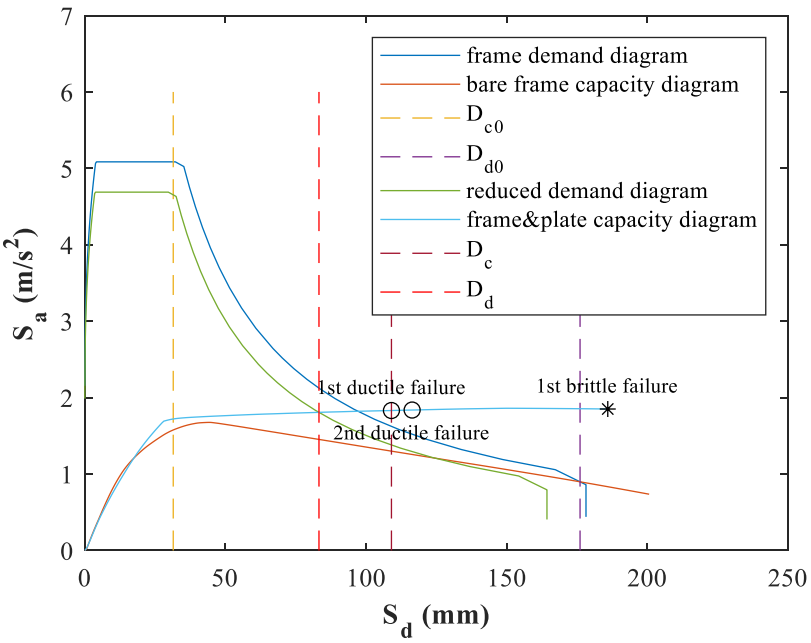

Fig. 6.19. Demand and capacity diagram of the optimal case for X-frame optimisation with min (f_2'): $sp_{typ} = 1, t = 3, 2, 2, 2$ mm

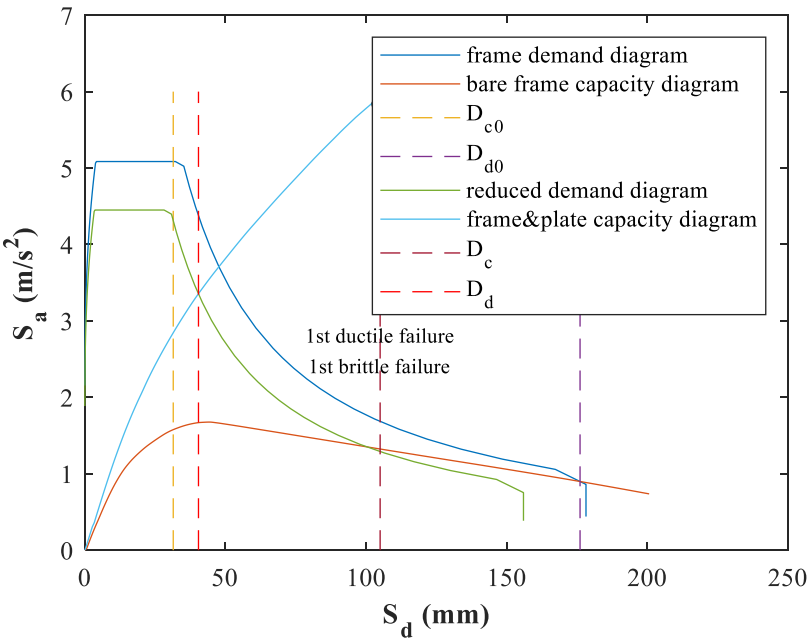

Fig. 6.20. Demand and capacity diagram of the optimal case for X-frame optimisation with min (f_3'): $sp_{typ} = 1, t = 12, 13, 9, 7$ mm

Table 6.7. Results of selected optimal cases for X-frame optimisation

Optimal case	ζ_{eq}	D_c (mm)	D_d (mm)	Plate volume (mm^3)	Drift uniformity measure f_3
min ($f'_1 + f'_2 + f'_3$)	0.261	99.0	69.5	1.27e+08	2.97e+04
min (f'_2)	0.247	112.4	82.4	7.55e+07	8.02e+04
min (f'_3)	0.272	105.0	40.4	3.53e+08	1.43e+04

2D nonlinear dynamic simulations using the seven different ground acceleration time histories have been performed on the retrofitted case with minimum summation targets, where the infill type sp_{typ} is 1 and the infill plate thicknesses are 2, 7, 3, 2 mm. The average results of the seismic assessment focusing on local brittle and ductile failure checks at the member level are shown in Fig. 6.21. It can be noticed all the demand-capacity ratios are below 1 with the maximum ratio equal to 0.74 confirming the safety of the retrofitted structure considering the effects of ground seismic accelerations in the X-direction.

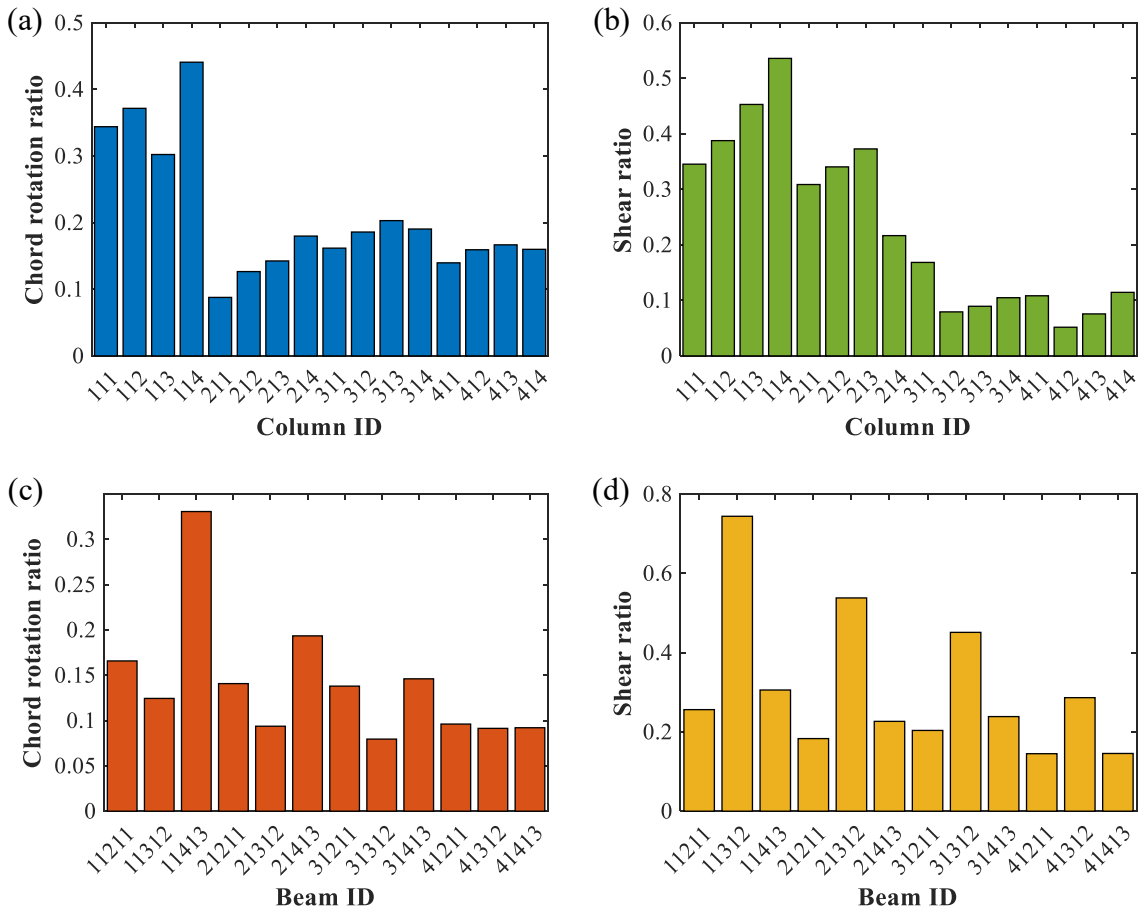

Fig. 6.21. Mean seismic assessment results for retrofitted X-frame: (a) Column chord rotation ratio; (b) Column shear ratio; (c) Beam chord rotation ratio; (d) Beam shear ratio

6.4.2 Application of optimal seismic retrofitting design to Y-frame

The same procedure as described in the previous section is applied to the Y-frame. Pushover analysis is first conducted on the bare Y-frame model, resulting in deformation capacity and demand of $D_{c0} = 15.4$ mm, $D_{d0} = 178.5$ mm, as shown in Fig. 6.22. The Y-frame does not satisfy the seismic requirement, thus it requires retrofitting.

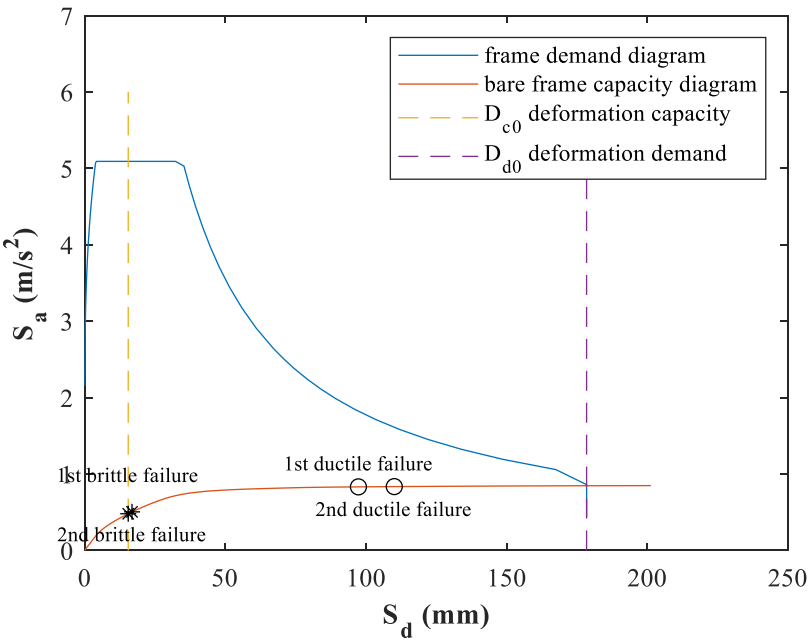

Fig. 6.22. Demand and capacity diagram of the bare Y-frame model

The optimal seismic design procedure is carried out on the 2D Y-frame inserting steel shear walls into the middle two bays of both Y-frames, i.e. the bays between Columns 21, 31, 41 and between Columns 24, 34, 44. For the ease of the study, the same infill type parameter and the same plate thickness are adopted for the bays at the same storey. As a result, the design variables for the Y-frame are identical to those for the X-frame. Since the steel shear walls are added to two bays in the frame, the global equivalent EVD is calculated as

$$\zeta_{eq} = \zeta_f + 2 \times 1 \Big/ \sum_{i=1}^{4} \frac{1}{\zeta_{p,i}} \tag{6.10}$$

The optimal cases are selected using the same criterion as for the X-frame case and the results are shown in Fig. 6.23, Fig. 6.24, Fig. 6.25, Fig. 6.26 and Table 6.8.

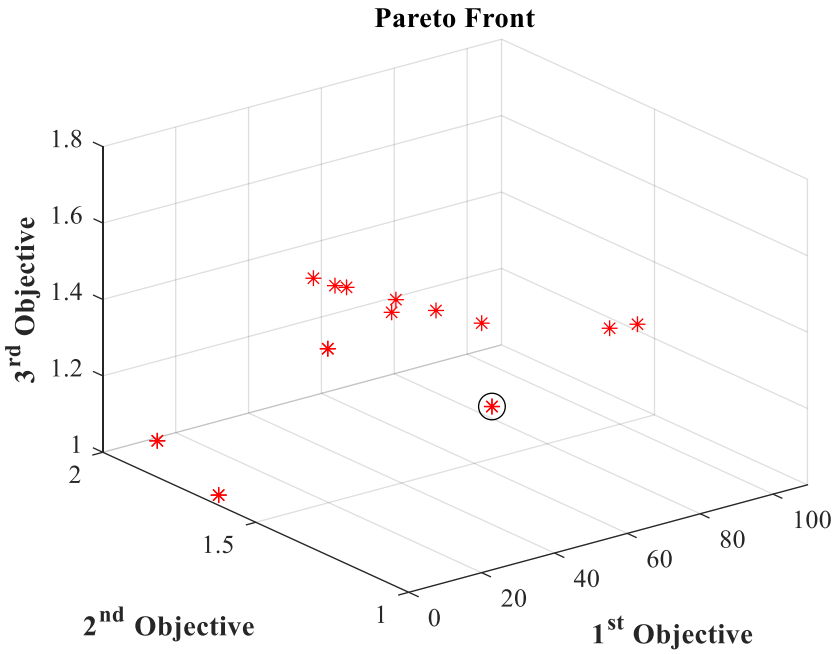

Fig. 6.23. Pareto front for Y-frame optimisation

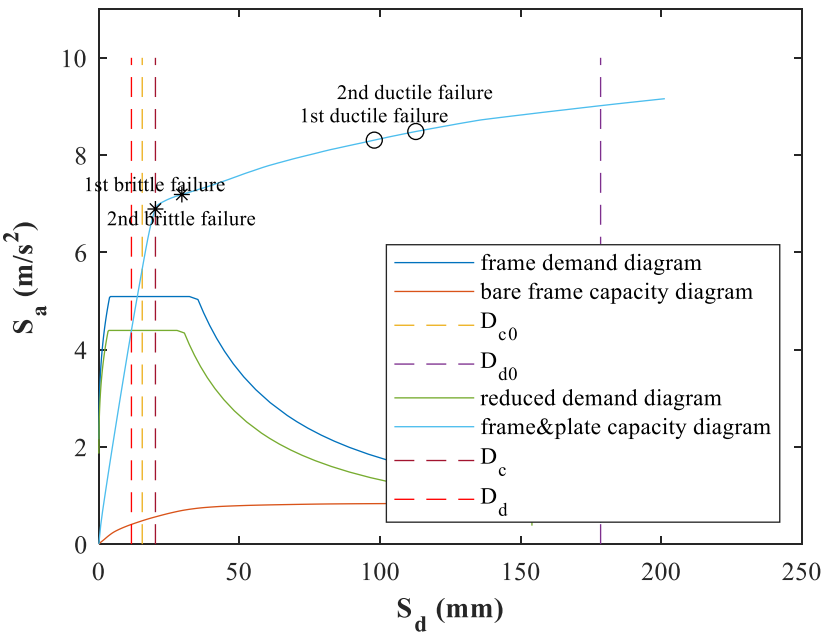

Fig. 6.24. Demand and capacity diagram of the optimal case for Y-frame optimisation with min $(f_1' + f_2' + f_3')$*:* $sp_{typ} = 2, t = 3, 4, 2, 2$ *mm*

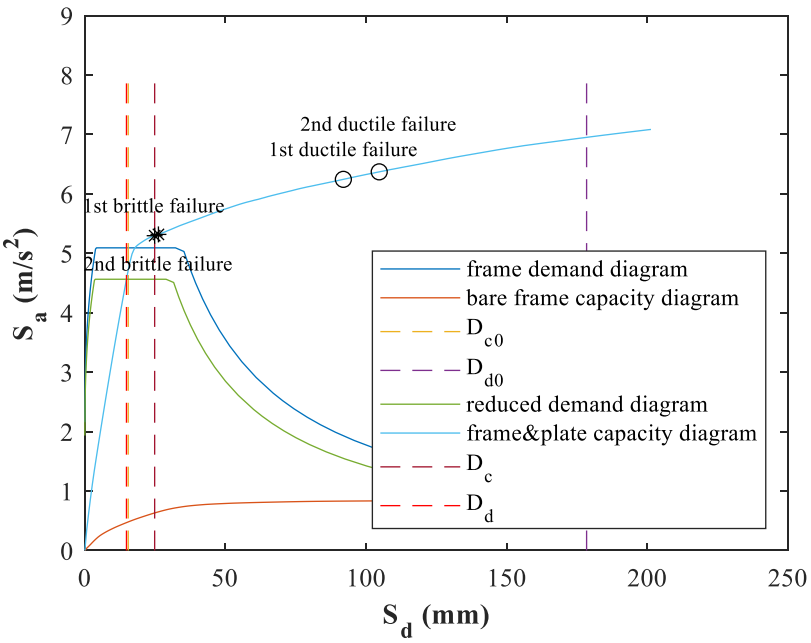

Fig. 6.25. Demand and capacity diagram of the optimal case for Y-frame optimisation with min (f_2'): $sp_{typ} = 2, t = 2, 3, 2, 2$ mm

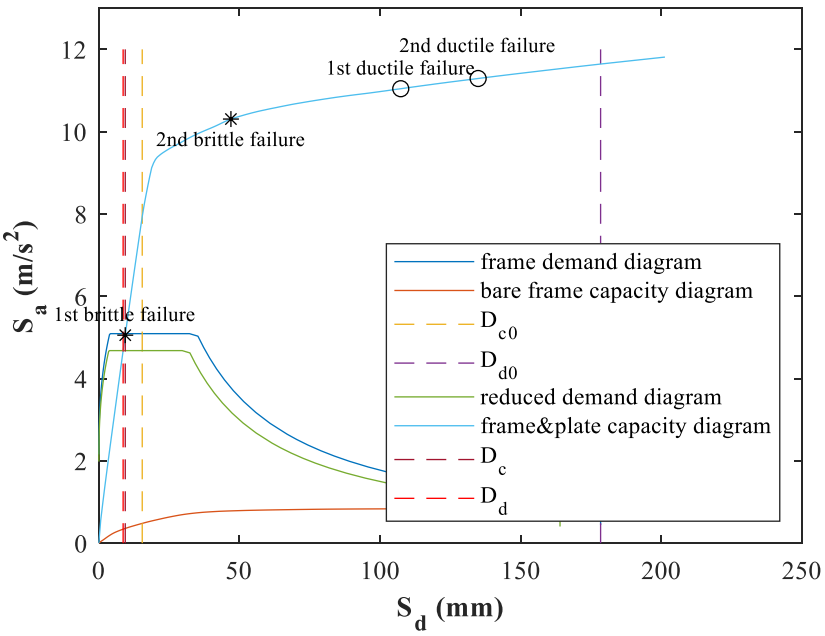

Fig. 6.26. Demand and capacity diagram of the optimal case for Y-frame optimisation with min (f_3'): $sp_{typ} = 3, t = 3, 3, 2, 2$ mm

Table 6.8. Results of selected optimal cases for Y-frame optimisation

Optimal case	ζ_{eq}	D_c (mm)	D_d (mm)	Plate volume (mm^3)	Drift uniformity measure f_3
min ($f'_1 + f'_2 + f'_3$)	0.282	19.5	12.9	3.03e+08	6.05e+04
min (f'_2)	0.260	19.5	16.3	2.48e+08	7.70e+04
min (f'_3)	0.241	9.5	9.4	4.06e+08	4.66e+04

Then, nonlinear dynamic simulations using the earthquake ground acceleration have been performed on the first retrofitted case ($sp_{typ} = 2, t = 3, 4, 2, 2$ mm) and the average results are shown in Fig. 6.27. It can be noticed all the demand-capacity ratios are below the limit with the maximum ratio equal to 0.55 confirming the safety of the retrofitted structure considering the effects of ground seismic accelerations in the Y direction. However, the seismic assessment results are quite small in comparison with the limit 1. The reason is that two centre bays are selected for adding steel panels leading to this conservative design. The optimal procedure will be carried out to the Y-frame with one bay of infill panels in further studies.

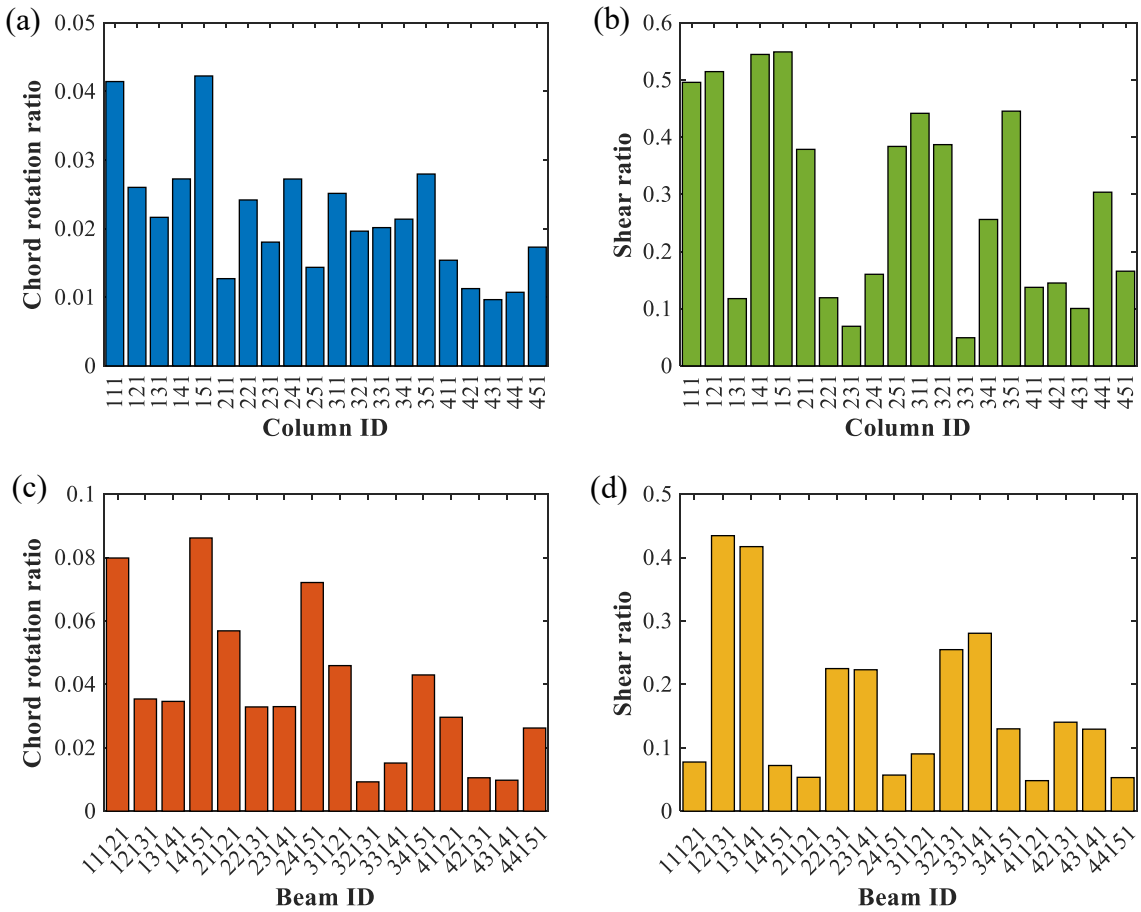

Fig. 6.27. Mean seismic assessment results for retrofitted Y-frame: (a) Column chord rotation ratio; (b) Column shear ratio; (c) Beam chord rotation ratio; (d) Beam shear ratio

6.5 Seismic assessment of retrofitted building

The selected optimal seismic solutions for the X- and Y-frame with minimum summation of three relative objective values are applied to the 3D frame model as a verification for the optimal design. 1/3 of the middle bay in the first and last X-direction frames are infilled by steel shear walls, while 2/3 of the middle two bays in the Y-frames are infilled. The thicknesses of the steel plates in the X and Y directions at each storey are $t_x = 2, 7, 3, 2$ mm and $t_y = 3, 4, 2, 2$ mm, respectively. Fig. 6.28 shows the retrofitted frame model with the steel shear wall macroelements in ADAPTIC.

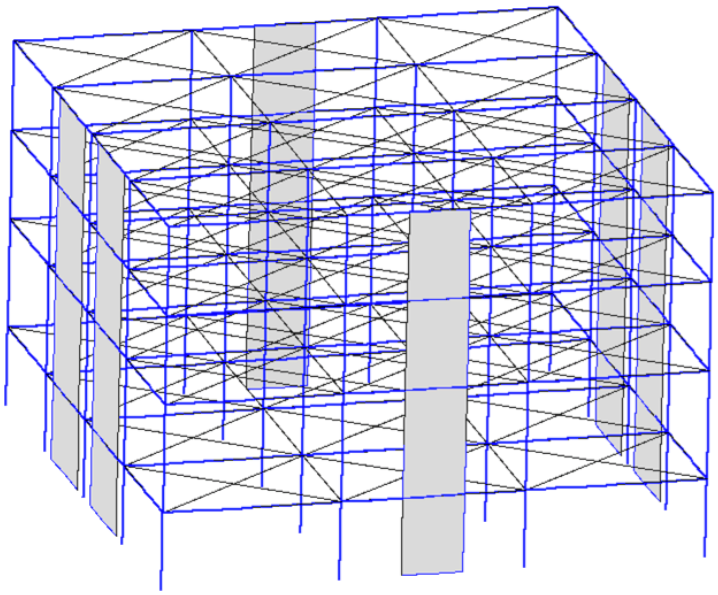

Fig. 6.28. 3D retrofitted frame model in ADAPTIC

The selected seven sets of accelerograms are applied to the retrofitted frame model for nonlinear dynamic analysis. Then, seismic assessment is conducted for each seismic record, aiming to verify the designed optimal seismic retrofitting design procedure. The retrofitted frame does not experience any collapse under all the seismic records. Only the assessment results for the average response quantities are shown and discussed here. The results under each record are displayed in Appendix.

A significant enhancement of the seismic response can be observed when comparing the results for the bare frame and those for the retrofitted frame. Fig. 6.29 to Fig. 6.32 show the average seismic assessment results for seven sets of accelerograms, where all values for every member are under the limit of 1. The average responses suggest that both columns and beams of the retrofitted structure do not experience local ductile and brittle failures. The infilled steel shear walls possess satisfying dissipation capacity for the energy induced by the earthquake while increasing the overall stiffness and strength at the same time. Therefore, the seismic performance of the retrofitted structure has been significantly improved, and the strengthened frame model with steel shear walls satisfies the retrofitting requirements. Besides, some of the assessment results for the 3D retrofitted frame are larger when compared with those for the 2D

X- and Y-frames. This is because the 3D case considers the biaxial bending which affects the seismic assessment ratios. The proposed optimal design procedure could be further developed for the direct application to the 3D frame in the future for a more accurate result, but the procedure will need much more computational resources referring to the analysis time for each numerical model in Table 6.9.

Considering the mean response results, as discussed before, and comparing the figures for every single record in Appendix, it can be concluded that adding steel shear walls to the selected RC framed building can provide significant enhancement of the seismic performance. It prevents global collapse and local failures in the beams and columns.

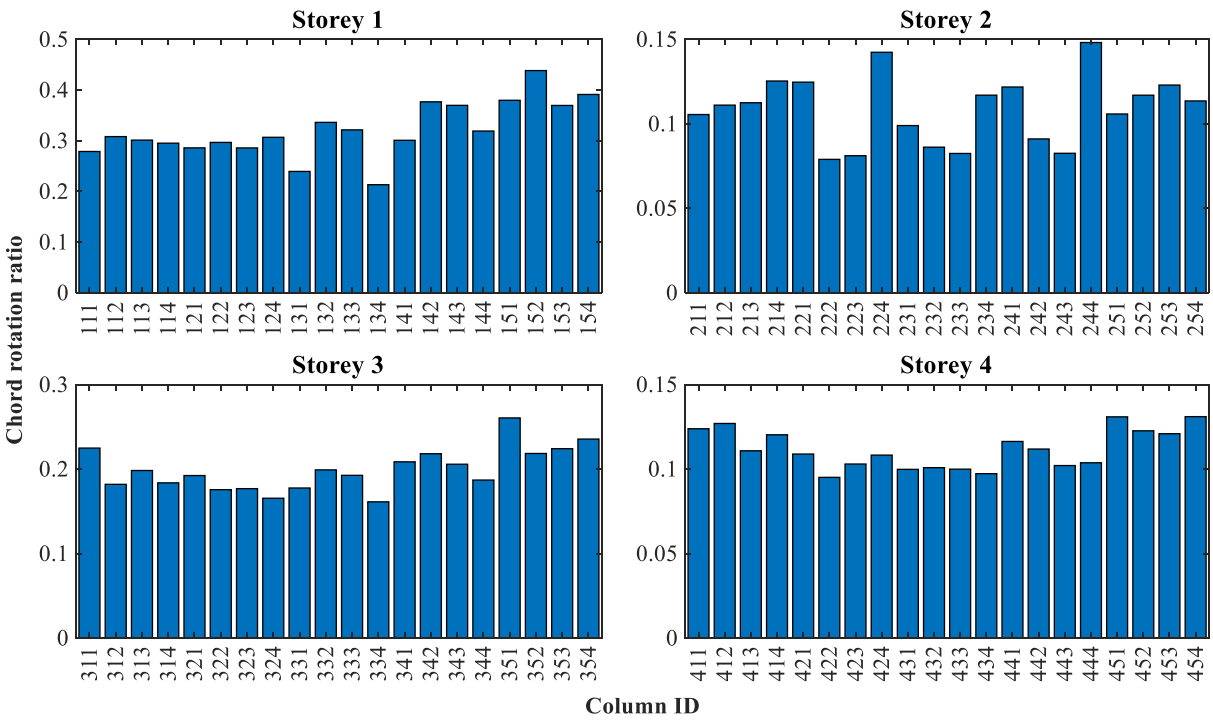

Fig. 6.29. Mean chord rotation ratios for the columns of the 3D retrofitted building model

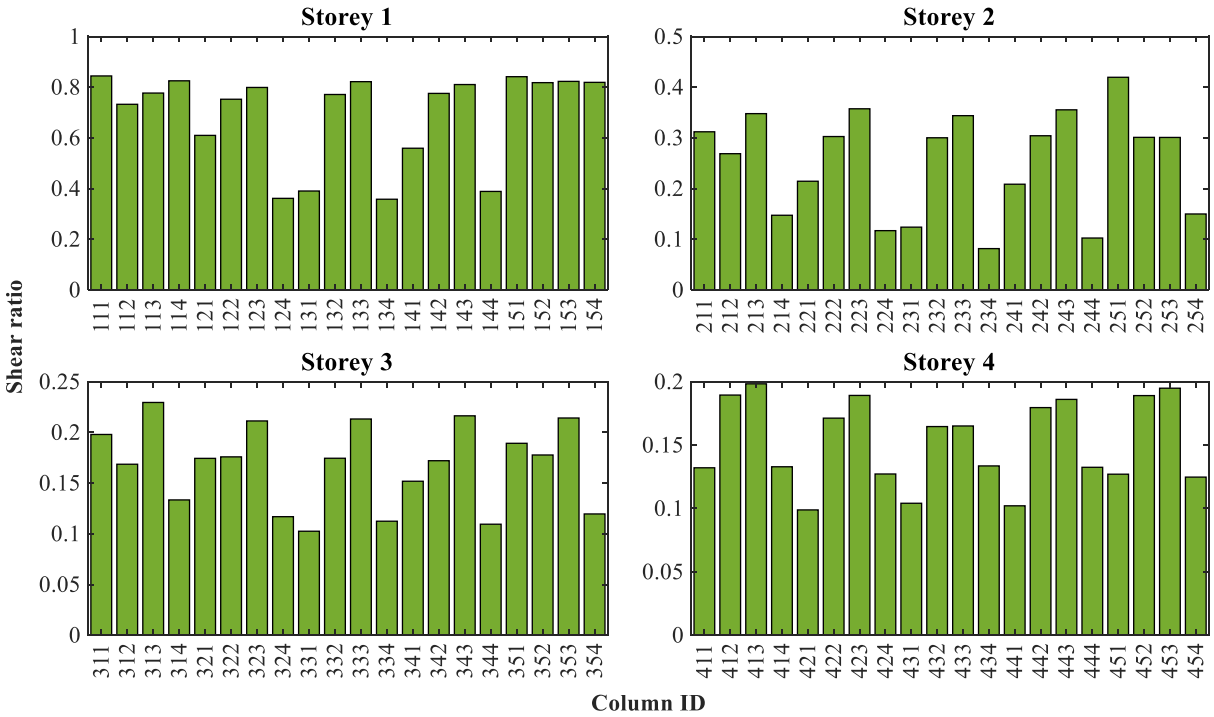

Fig. 6.30. Mean shear force ratios for the columns of the 3D retrofitted building model

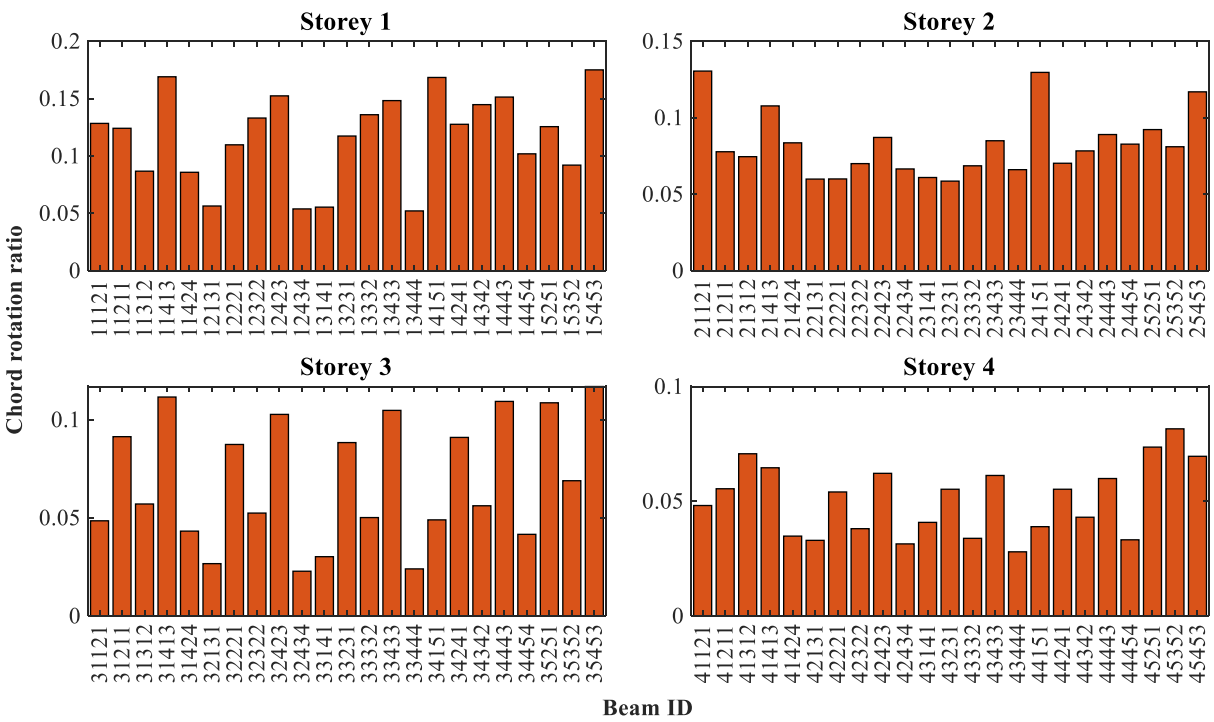

Fig. 6.31. Mean chord rotation ratios for the beams of the 3D retrofitted building model

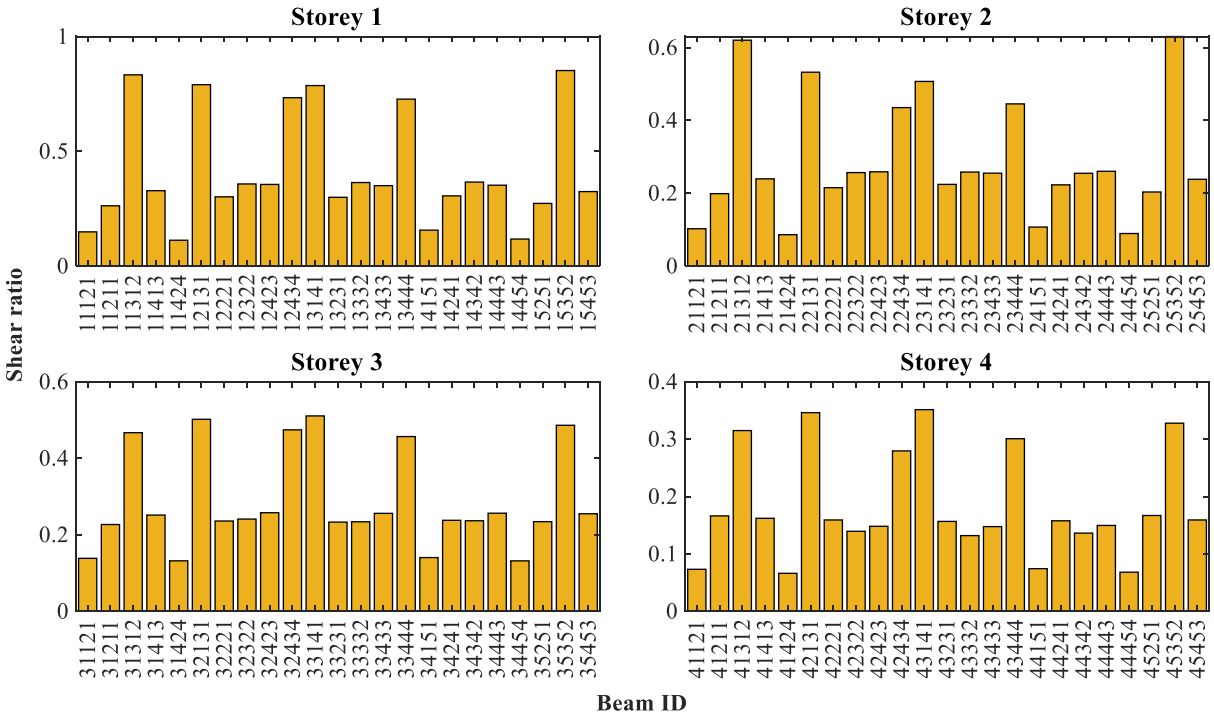

Fig. 6.32. Mean shear force ratios for the beams of the 3D retrofitted building model

Table 6.9. Analysis time for the numerical models

Model	Analysis time	Model	Analysis time
3D bare building under Record 199	252 min	3D retrofitted building under Record 199	412 min
2D bare X-frame under Record 199	2 min	2D retrofitted X-frame under Record 199	2 min
2D bare Y-frame under Record 199	2 min	2D retrofitted Y-frame under Record 199	3 min
2D bare X-frame under pushover	1 min	2D retrofitted X-frame under pushover	1~3 min
2D bare Y-frame under pushover	1 min	2D retrofitted Y-frame under pushover	1~3 min

6.6 Concluding remarks

A regular 4-storey 3D RC framed building is selected as a case study in this chapter for the application and verification of the proposed optimal seismic retrofitting design. A numerical model for the studied frame building is developed in ADAPTIC allowing material and geometric nonlinearity. Accelerograms matching the design spectrum are selected following Eurocode 8 (EN1998-1, 2004; EN1998-3, 2005), and then applied to the bare frame model for seismic assessment. Since the bare frame fails to meet the chord rotation and shear requirements under the seismic records, seismic retrofitting is carried out using the proposed optimal design procedure. Independent design for 2D frames along the X- and Y- direction is considered thanks to the regularity characteristics of the building. Optimal solutions are selected from the Pareto front referring to relative values of optimisation objectives. It has been observed that the deformation demand decreases, and the overall stiffness rises while increasing the overall volume of steel plates. However, the deformation capacity does not always increase with thicker infill plates because bending moment and shear force distributions along the frame may change.

The optimal solutions with a minimum summation of three relative objective values are applied to the 3D frame model under the selected accelerograms. Seismic assessment is conducted for the retrofitted structure, and a significant enhancement of the seismic performance can be observed. The added steel shear walls can prevent global collapse and local ductile and brittle failures in beams and columns. Differences can be noticed when comparing the assessment results for the 3D frame with those for the 2D frames, which is caused by taking biaxial bending into account in the 3D case. This observation leads to further research about applying the proposed optimal procedure directly to 3D frames, which may however result in a significant larger computational cost.

Chapter 7

Conclusions and Future Work

7.1 Conclusions

This research is motivated by the demand for simplified macroscale formulations for steel shear walls under cyclic loading, and optimal seismic retrofitting design procedures for existing framed structures. For this purpose, a novel macroelement model with calibrated constitutive material relationships for steel shear wall panels has been developed in this work. Besides, an enhanced optimal seismic retrofitting design procedure utilising steel shear walls as a global strengthening solution has been also put forward. It enables an automatic selection for steel infill plate lengths and thicknesses while satisfying global and local seismic performance requirements. The main results obtained in the research are summarised in the following.

7.1.1 Macroelement development and calibration

As highlighted in Chapter 2, the use of nonlinear shell element models for representing steel shear walls under earthquake loading is associated with a relatively high computational demand. Previous research considered the use of multi-strip macroscale models (Thorburn et al., 1983) with complex hysteresis material relationships, which are nevertheless difficult to assemble within a frame description for nonlinear simulations under earthquake loading. Therefore, Chapter 3 proposes a novel simplified 8-noded macroelement formulation for unstiffened thin steel shear walls including six nonlinear springs with a newly defined asymmetric constitutive relationship. The developed macroelement model is computationally efficient and capable of representing the cyclic nonlinear response of steel panels, including the pinching characteristics, the strain-hardening effects and the stiffness degradation when increasing the number of cycles. The phenomenological formulation of the macroelement allows for the development of tension fields within the panel of a steel shear wall and the contribution of the compressed parts of the panel when it is subjected to shear loading.

A detailed FE description with nonlinear 9-noded shell elements has been introduced for the calibration of the proposed phenomenological simplified model. After validation against experimental results, shell element models are employed to generate baseline solutions for the subsequent calibration of the macroelement model in Chapter 4. It is aimed at finding optimal sets of material parameters that can provide response predictions close to nonlinear shell element results. The calibration is treated as a multi-objective optimisation problem considering the discrepancies of dissipated energy and selected engineering features between the macroelement and shell element models. Subsequently, simple functions are put forward for the practical calculation of the macroelement material parameters in terms of the steel plate geometrical properties. At last, a substandard RC frame equipped with fully-infilled and partially-infilled steel shear walls is modelled with macroelements and shell elements, respectively, to assess the accuracy of the calibration results. The numerical results of the macroelement models are in good agreement with those of the shell element models, confirming the ability and computational efficiency of the developed macroelement in representing steel shear walls within retrofitted RC frames subjected to cyclic loading.

7.1.2 Optimal seismic retrofitting design procedure

Previous research for the optimal seismic retrofitting design using genetic algorithms has been introduced in Chapter 2. However, most of the previous research focused on dampers, FRP or bracing systems and some studies used single-objective optimisation. Chapter 5 proposes a novel multi-objective optimal seismic retrofitting design procedure using steel shear wall macroelements, which automatically selects the length and thickness of the infill panels. The optimisation objectives are introduced to (i) minimise the gap between seismic demand and capacity, (ii) add the minimum amount of steel material for the wall components and (iii) achieve a uniform distribution of inter-storey drift along the height of the building.

An overview of the proposed optimal design procedure is provided first, which adopts the capacity spectrum method for assessing the seismic performance of the retrofitted systems considering the ease of estimating EVD. The deformation capacity of the bare and retrofitted models is determined by checking chord rotation and shear force limits for each RC beam and column of the original frame at the end of each analysis step. A GA procedure is then developed for the selection of optimal solutions. In the final part of Chapter 5, the characteristic EVD ratio of steel shear wall components is estimated based on the results from virtual tests on steel wall macroelement models with different properties under different drift levels. Then, a nonlinear function for the damping ratio in terms of plate length, height, thickness and drift demand is determined with the aid of nonlinear regression.

The potential of the proposed optimal seismic retrofitting design with steel shear walls is shown in Chapter 6, where it is applied to the retrofitting of a substandard 4-storey RC frame building. Seismic assessment is carried out under nonlinear dynamic simulations by checking local brittle and ductile failure modes. Thanks to the regularity characteristics of the analysed building, the proposed optimal seismic retrofitting design procedure is then performed on the X- and Y-direction frames independently. Optimal solutions are selected from the Pareto front considering relative values of the optimisation objectives, and then applied to the 3D frame model under the selected accelerograms. A significant enhancement of the seismic performance can be observed from the seismic assessment results of the retrofitted structure, showing that

the added steel shear walls can prevent global collapse and local failures in RC beams and columns.

7.2 Future work

As pointed out previously, the developed efficient macroelement formulation for steel shear wall components with calibrated material parameters provides response predictions in a very good agreement with more expensive FE models using shell elements. However, some refinements in the macroelement formulation could be developed in future research:

- The current macroelement considers only material nonlinearity. Thus, geometric nonlinearity effects can be introduced in future work;
- When developing FE models for frames equipped with macroelements representing steel shear walls, link elements available in ADAPTIC are currently added to the boundary nodes of the macroelements for convenient connectivity with the beam-column elements of the frame. Further model enhancements could be carried out to incorporate the link elements within the macroelement formulation to facilitate the connectivity with the frame, and achieve an improved representation of the local interaction between boundary beams and columns and steel plates;
- Only a single macroelement is currently adopted for each steel plate. The effects of mesh refinement considering more macroelements for a single steel plate could be investigated in further research;
- Only one type of structural material (i.e. structural steel with fixed yield strength and Young's modulus) has been considered for the definition of the macroelement model material parameters, where specific regression functions for material properties have been derived assuming variations of panel geometrical characteristics only. Therefore, further studies are needed to determine suitable relationships for model material properties considering structural steel with different yield strengths or different metallic materials like aluminium alloy (Mazzolani, 2008; Formisano et al., 2010) for the retrofitting panels.

Regarding the optimal seismic retrofitting design approach, further work could be carried out focusing on different aspects:

- The use of the N2 method instead of the capacity design spectrum method for seismic assessment could be explored together with the consideration of different load distributions for the pushover nonlinear simulation at the base of the seismic assessment procedure;
- Comparisons could be carried out between the proposed optimal seismic retrofitting design and the conventional retrofitting design method following trial-and-error procedures;
- The application of the design procedure to irregular structures could be developed, where additional design variables related to the location of the steel wall element within a 3D building model could be included in the definition of the optimisation problem for seismic retrofitting design;
- 3D nonlinear simulations for the optimal seismic retrofitting design could be used to improve the accuracy of the optimisation procedure taking into account 3D effects induced by biaxial bending in RC columns;
- Local retrofitting solutions could be considered in combination with the use of steel shear walls to achieve an enhanced seismic retrofitting design;
- The proposed optimal design framework could be adopted for other types of seismic intervention techniques, such as dissipative bracing or damping systems.

Reference

ABOU-ELFATH, H. & GHOBARAH, A. J. C. J. O. C. E. 2000. Behaviour of reinforced concrete frames rehabilitated with concentric steel bracing. *Canadian Journal of Civil Engineering,* 27(3)**,** 433-444.

ABOU-ELFATH, H., RAMADAN, M. & OMAR ALKANAI, F. 2017. Upgrading the seismic capacity of existing RC buildings using buckling restrained braces. *Alexandria Engineering Journal,* 56**,** 251-262.

AISC. 2016. *Seismic provisions for structural steel buildings*, AISC Chicago, IL.

ALMEIDA, A., FERREIRA, R., PROENÇA, J. M. & GAGO, A. S. 2017. Seismic retrofit of RC building structures with Buckling Restrained Braces. *Engineering Structures,* 130**,** 14-22.

ALPAYDIN, E. 2020. *Introduction to machine learning*, MIT press.

AMADIO, C., RINALDIN, G. & FRAGIACOMO, M. 2016. Investigation on the accuracy of the N2 method and the equivalent linearization procedure for different hysteretic models. *Soil Dynamics and Earthquake Engineering,* 83**,** 69-80.

ASCE. 2013. *Seismic evaluation and retrofit of existing buildings*.

ASTANEH-ASL, A. & ZHAO, Q. 2001. Cyclic tests of steel shear walls. *Research project. Berkeley: Dept. of Civil and Env Engineering, Univ of California*.

ATC. 1996. *Seismic Evaluation and Retrofit of Concrete Buildings (Report SSC 96-01 of California Seismic Safety Commission)*, Applied Technology Council, Redwood City, Califonia, USA.

BADOUX, M. & JIRSA, J. O. J. J. O. S. E. 1990. Steel bracing of RC frames for seismic retrofitting. 116**,** 55-74.

BAI, J. & OU, J. 2016. Earthquake-resistant design of buckling-restrained braced RC moment frames using performance-based plastic design method. *Engineering Structures,* 107**,** 66-79.

BAROS, D. K. & DRITSOS, S. E. 2008. A simplified procedure to select a suitable retrofit strategy for existing rc buildings using pushover analysis. *Journal of Earthquake Engineering,* 12**,** 823-848.

BERMAN, J. & BRUNEAU, M. 2003. Plastic analysis and design of steel plate shear walls. *Journal of Structural Engineering,* 129**,** 1448-1456.

BERMAN, J. W. 2011. Seismic behavior of code designed steel plate shear walls. *Engineering Structures,* 33**,** 230-244.

BRUNEAU, M., BERMAN, J. W., LOPEZ-GARCIA, D. & VIAN, D. 2007. A review of steel plate shear wall design requirements and research.

BUSH, T., JONES, E. & JIRSA, J. O. J. J. O. S. E. 1991. Behavior of RC frame strengthened using structural steel bracing. *Journal of Structural Engineering,* 117**,** 1115-1126.

CACCESE, V., ELGAALY, M. & CHEN, R. 1993. Experimental study of thin steel-plate shear walls under cyclic load. *Journal of Structural Engineering,* 119**,** 573-587.

CAN, C. 2001. *CSA-S16-01, Limit states design of steel structures*, Toronto (ON, Canada): Canadian Standards Association.

CASTRO, J. M., ARAÚJO, M., D'ANIELLO, M. & LANDOLFO, R. 2018. Strengthening of RC Buildings with Steel Elements. *Strengthening and Retrofitting of Existing Structures.*

CHA, Y.-J. & AGRAWAL, A. K. 2017. Seismic retrofit of MRF buildings using decentralized semi-active control for multi-target performances. *Earthquake Engineering & Structural Dynamics,* 46**,** 409-424.

CHARMPIS, D. C., KOMODROMOS, P. & PHOCAS, M. C. 2012. Optimized earthquake response of multi-storey buildings with seismic isolation at various elevations. *Earthquake Engineering & Structural Dynamics,* 41(15)**,** 2289-2310.

CHARMPIS, D. C., PHOCAS, M. C. & KOMODROMOS, P. 2015. Optimized retrofit of multi-storey buildings using seismic isolation at various elevations: assessment for several earthquake excitations. *Bulletin of Earthquake Engineering,* 13**,** 2745-2768.

CHISARI, C. & BEDON, C. J. B. D. G. T. E. A. 2017. Performance-based design of FRP retrofitting of existing RC frames by means of multi-objective optimisation. 58.

CHISARI, C., MACORINI, L. & IZZUDDIN, B. 2019. Macroscale model calibration for seismic assessment of brick/block masonry structures. *7th International Conference on Computational Methods in Structural Dynamics and Earthquake Engineering***,** 1356-1367.

CHISARI, C., MACORINI, L. & IZZUDDIN, B. A. 2020. Multiscale model calibration by inverse analysis for nonlinear simulation of masonry structures under earthquake loading. *International Journal for Multiscale Computational Engineering,* 18.

CHOI, I.-R. & PARK, H.-G. 2009. Steel plate shear walls with various infill plate designs. *Journal of Structural Engineering,* 135**,** 785-796.

CHOI, I.-R. & PARK, H.-G. 2010. Hysteresis model of thin infill plate for cyclic nonlinear analysis of steel plate shear walls. *Journal of Structural Engineering,* 136**,** 1423-1434.

CHOI, S. W. 2017. Investigation on the seismic retrofit positions of FRP jackets for RC frames using multi-objective optimization. *Composites Part B: Engineering,* 123**,** 34-44.

CHOI, S. W., KIM, Y. & PARK, H. S. 2014. Multi-objective seismic retrofit method for using FRP jackets in shear-critical reinforced concrete frames. *Composites Part B: Engineering,* 56**,** 207-216.

CHOI, S. W., PARK, S. W. & PARK, H. S. 2017. Multi-objective design model for retrofit of reinforced concrete frames with infilled walls using FRP bracings. *Construction and Building Materials,* 140**,** 454-467.

CHOPRA, A. K. & GOEL, R. K. 1999. Capacity-demand-diagram methods for estimating seismic deformation of inelastic structures: SDF systems. *Report No. PEER1999/02*.

CLAYTON, P. M., BERMAN, J. W. & LOWES, L. N. 2012a. Seismic Design and Performance of Self-Centering Steel Plate Shear Walls. *Journal of Structural Engineering,* 138**,** 22-30.

CLAYTON, P. M., BERMAN, J. W. & LOWES, L. N. 2013. Subassembly testing and modeling of self-centering steel plate shear walls. *Engineering Structures,* 56**,** 1848-1857.

CLAYTON, P. M., BERMAN, J. W. & LOWES, L. N. 2015. Seismic performance of self-centering steel plate shear walls with beam-only-connected web plates. *Journal of Constructional Steel Research,* 106**,** 198-208.

CLAYTON, P. M., DOWDEN, D. M., WINKLEY, T., BERMAN, J. W., BRUNEAU, M. & LOWES, L. N. Experimental investigation of self-centering steel plate shear walls. Structures Congress 2012, 2012b. 1586-1597.

DARWIN, C. 2004. *On the origin of species, 1859*, Routledge.

DE MATTEIS, G., FORMISANO, A. & MAZZOLANI, F. M. 2009. An innovative methodology for seismic retrofitting of existing RC buildings by metal shear panels. *Earthquake Engineering & Structural Dynamics,* 38**,** 61-78.

DEB, K., PRATAP, A., AGARWAL, S. & MEYARIVAN, T. 2002. A fast and elitist multiobjective genetic algorithm: NSGA-II. *IEEE transactions on evolutionary computation,* 6**,** 182-197.

DELLA CORTE, G., D'ANIELLO, M. & LANDOLFO, R. 2015. Field testing of all-steel buckling-restrained braces applied to a damaged reinforced concrete building. *Journal of Structural Engineering,* 141.

DIETTERICH, T. G. 1997. Machine-learning research. *AI magazine,* 18**,** 97-97.

DIETTERICH, T. G. 2003. Machine Learning. *Nature Encyclopedia of Cognitive Science.* London.

DRIVER, R. G., CIVIL, U. O. A. D. O. & ENGINEERING, E. 1997. *Seismic behaviour of steel plate shear walls*, Department of Civil and Environmental Engineering, University of Alberta.

DRIVER, R. G., KULAK, G. L., ELWI, A. E. & KENNEDY, D. L. 1998a. FE and simplified models of steel plate shear wall. *Journal of Structural Engineering,* 124**,** 121-130.

DRIVER, R. G., KULAK, G. L., KENNEDY, D. L. & ELWI, A. E. 1998b. Cyclic test of four-story steel plate shear wall. *Journal of Structural Engineering,* 124**,** 112-120.

DWAIRI, H. M., KOWALSKY, M. J. & NAU, J. M. 2007. Equivalent Damping in Support of Direct Displacement-Based Design. *Journal of Earthquake Engineering,* 11**,** 512-530.

ELGAALY, M., CACCESE, V. & DU, C. 1993. Postbuckling behavior of steel-plate shear walls under cyclic loads. *Journal of Structural Engineering,* 119**,** 588-605.

EN1990. 2002. *Eurocode: Basis of structural design*, BSI London, UK.

EN1993-1-1. 2005. *Eurocode 3. Design of steel structures. General rules and rules for buildings*, BSI London, UK.

EN1993-1-5. 2005. *Eurocode 3. Design of steel structures. General rules. Plated structural elements*, BSI London, UK.

EN1998-1. 2004. *Eurocode 8: Design of structures for earthquake resistance. Part 1: General rules, seismic actions and rules for buildings*, BSI London, UK.

EN1998-3. 2005. *Eurocode 8: Design of structures for earthquake resistance. Part 3: Assessment and retrofitting of buildings*, BSI London, UK.

FAELLA, C., LIMA, C., MARTINELLI, E. & REALFONZO, R. 2014. Steel bracing configurations for seismic retrofitting of a reinforced concrete frame. *Proceedings of the Institution of Civil Engineers - Structures and Buildings,* 167**,** 54-65.

FAJFAR, P. & FISCHINGER, M. N2-A method for non-linear seismic analysis of regular buildings. Proceedings of the ninth world conference in earthquake engineering, 1988. 111-116.

FAJFAR, P. & GAŠPERŠIČ, P. 1996. The N2 method for the seismic damage analysis of RC buildings. *Earthquake Engineering & Structural Dynamics,* 25**,** 31-46.

FALCONE, R. 2018. *Optimal seismic retrofitting of existing RC frames through soft-computing approaches.*

FALCONE, R., CARRABS, F., CERULLI, R., LIMA, C. & MARTINELLI, E. 2019. Seismic retrofitting of existing RC buildings: a rational selection procedure based on Genetic Algorithms. *Structures,* 22**,** 310-326.

FARDIS, M. N. 2009. *Seismic design, assessment and retrofitting of concrete buildings: based on EN-Eurocode 8*, Springer.

FARHAT, F., NAKAMURA, S. & TAKAHASHI, K. 2009. Application of genetic algorithm to optimization of buckling restrained braces for seismic upgrading of existing structures. *Computers & Structures,* 87**,** 110-119.

FEMA. 2000. *Prestandard and commentary for the seismic rehabilitation of buildings*, Washington, DC, FEMA-356, Federal Emergency Management Agency.

FORMISANO, A. 2007. *Seismic upgrading of existing RC buildings by means of metal shear panels: design models and full-scale tests.* Università degli Studi di Napoli Federico II.

FORMISANO, A., DE MATTEIS, G., PANICO, S. & MAZZOLANI, F. J. A. S. C. 2008. Seismic upgrading of existing RC buildings by slender steel shear panels: A full-scale experimental investigation. *Advanced Steel Construction,* 4**,** 26-45.

FORMISANO, A., MATTEIS, G. D. & MAZZOLANI, F. M. 2010. Numerical and experimental behaviour of a full-scale RC structure upgraded with steel and aluminium shear panels. *Computers & Structures,* 88**,** 1348-1360.

FREEMAN, S. A. 2004. Review of the development of the capacity spectrum method. *ISET Journal of Earthquake Technology,* 41**,** 1-13.

GOLBERG, D. E. 1989. Genetic algorithms in search, optimization, and machine learning. *Addion wesley,* 1989**,** 36.

GRANT, D. N., BLANDON, C. & PRIESTLEY, M. 2005. Modelling inelastic response in direct displacement-based design.

GUO, L., JIA, M., LI, R. & ZHANG, S. 2013. Hysteretic analysis of thin steel plate shear walls. *International Journal of Steel Structures,* 13**,** 163-174.

HOLLAND, J. H. 1975. Adaptation in natural and artificial systems: An introductory analysis with applications to biology, control, and artificial intelligence.

IERVOLINO, I., GALASSO, C. & COSENZA, E. 2009. REXEL: computer aided record selection for code-based seismic structural analysis. *Bulletin of Earthquake Engineering,* 8**,** 339-362.

IZZUDDIN, B. A. 1991. *Nonlinear dynamic analysis of framed structures.* Imperial College of Science and Technology (University of London).

IZZUDDIN, B. A. 2005. An enhanced co-rotational approach for large displacement analysis of plates. *International Journal for Numerical Methods in Engineering,* 64**,** 1350-1374.

IZZUDDIN, B. A. 2019. ADAPTIC User Manual, Revision 1.5g. Imperial College London.

IZZUDDIN, B. A. & LIANG, Y. 2017. A hierarchic optimisation approach towards locking-free shell finite elements. *Computers & Structures*.

IZZUDDIN, B. A. & LIANG, Y. 2020. A hierarchic optimisation approach towards locking-free shell finite elements. *Computers & Structures,* 232.

IZZUDDIN, B. A. & LLOYD SMITH, D. 2000. Efficient nonlinear analysis of elasto-plastic 3D R/C frames using adaptive techniques. *Computers and Structures,* 78**,** 549-573.

IZZUDDIN, B. A., MACORINI, L. & RINALDIN, G. Partitioned modelling for nonlinear dynamic analysis of reinforced concrete buildings for earthquake loading. Proceedings of the Fourteenth International Conference on Civil, Structural and Environmental Engineering Computing, 2013.

JALALI, S. A. & BANAZADEH, M. 2016. Development of a new deteriorating hysteresis model for seismic collapse assessment of thin steel plate shear walls. *Thin-Walled Structures,* 106**,** 244-257.

JING, W., RENJIE, L., CHUNLIN, W. & ZHEN, Z. 2011. A Modified Capacity Spectrum Method with Direct Calculation of Seismic Intensity of Points on Capacity Curve. *Journal of Earthquake Engineering,* 15**,** 664-683.

JOKHIO, G. A. & IZZUDDIN, B. A. 2013. Parallelisation of nonlinear structural analysis using dual partition super elements. *Advances in Engineering Software,* 60-61**,** 81-88.

JOKHIO, G. A. & IZZUDDIN, B. A. 2015. A Dual Super-Element Domain Decomposition Approach for Parallel Nonlinear Finite Element Analysis. *International Journal for Computational Methods in Engineering Science and Mechanics,* 16**,** 188-212.

KIM, J. & AN, S. 2016. Optimal distribution of friction dampers for seismic retrofit of a reinforced concrete moment frame. *Advances in Structural Engineering,* 20**,** 1523-1539.

KOZA, J. R. 1994. Genetic programming as a means for programming computers by natural selection. *Statistics and computing,* 4**,** 87-112.

LI, C.-H., WU, A.-C. & TSAI, K.-C. 2015. Experimental investigation on the seismic retrofit of existing reinforced concrete buildings using steel plate shear walls. *Improving the Seismic Performance of Existing Buildings and Other Structures 2015.*

MASJUKI, S. A. 2017. *Assessment and retrofitting of reinforced concrete buildings with shear walls subject to earthquake loading.*

MASRI, A. C. & GOEL, S. C. J. E. S. 1996. Seismic design and testing of an RC slab-column frame strengthened by steel bracing. *Earthquake Spectra,* 12**,** 645-666.

MATHWORKS 2020. MATLAB (2020a). The MathWorks, Inc.

MATHWORKS. 2021. *Nonlinear Regression* [Online]. The MathWorks, Inc. Available: https://uk.mathworks.com/help/stats/nonlinear-regression-1.html [Accessed 06 Dec 2021].

MAZZOLANI, F. M. 2008. Innovative metal systems for seismic upgrading of RC structures. *Journal of Constructional Steel Research,* 64**,** 882-895.

MONTGOMERY, D. C. & RUNGER, G. C. 2010. *Applied statistics and probability for engineers*, John Wiley & Sons.

MPAMPATSIKOS, V., NASCIMBENE, R. & PETRINI, L. 2008. A Critical Review of the R.C. Frame Existing Building Assessment Procedure According to Eurocode 8 and Italian Seismic Code. *Journal of Earthquake Engineering,* 12**,** 52-82.

NTC. 2008. *Normativa Tecnica per Le Costruzionii - DM 14 Gennaio 2008.*

PAN, K.-Y., WU, A.-C., TSAI, K.-C., LI, C.-H. & KHOO, H.-H. 2016. Seismic retrofit of reinforced concrete frames using buckling-restrained braces with bearing block load transfer mechanism. *Earthquake Engineering & Structural Dynamics,* 45**,** 2303-2326.

PARK, H. S., LEE, D. C., OH, B. K., CHOI, S. W. & KIM, Y. 2014. Performance-based multiobjective optimal seismic retrofit method for a steel moment-resisting frame considering the life-cycle cost. *Mathematical Problems in Engineering,* 2014**,** 1-14.

PARK, K., OH, B. K., PARK, H. S. & CHOI, S. W. 2015. GA-based multi-objective optimization for retrofit design on a multi-core PC cluster. *Computer-Aided Civil and Infrastructure Engineering,* 30**,** 965-980.

PENELIS, G. & PENELIS, G. 2019. *Concrete buildings in seismic regions*, CRC Press.

PRIESTLEY, M. N., CALVI, G. M. & KOWALSKY, M. J. 2007. *Displacement based seismic design of structures*, Iuss.

PURBA, R. & BRUNEAU, M. 2009. Finite-element investigation and design recommendations for perforated steel plate shear walls. *Journal of Structural Engineering,* 135**,** 1367-1376.

PURBA, R. & BRUNEAU, M. 2014. Seismic performance of steel plate shear walls considering two different design philosophies of infill plates. I: Deterioration model development. *Journal of Structural Engineering,* 141**,** 04014160.

RAO, S. S. 1983. Optimization theory and applications. *JOHN WILEY & SONS, INC., 605 THIRD AVE., NEW YORK, NY 10158, USA, 1983, 550*.

ROBERTS, T. M. & GHOMI, S. S. 1991. Hysteretic characteristics of unstiffened plate shear panels. *Thin-Walled Structures,* 12**,** 145-162.

SECURITY, U. D. H. & AGENCY, F. E. M. 2013. *Improvement of Nonlinear Static Seismic Analysis Procedures: Fema 440*, Createspace Independent Pub.

SHISHKIN, J. J., DRIVER, R. G. & GRONDIN, G. Y. 2009. Analysis of steel plate shear walls using the modified strip model. *Journal of Structural Engineering,* 135**,** 1357-1366.

SRINIVAS, N. & DEB, K. 1994. Muiltiobjective optimization using nondominated sorting in genetic algorithms. *Evolutionary computation,* 2**,** 221-248.

SUGANO, S. 1996. State-of-the-art in techniques for rehabilitation of buildings. *Proceeding of the 11th World Conference on Earthquake Engineering, Paper No. 2175.* Acapulco, Mexico.

SYMANS, M., CHARNEY, F., WHITTAKER, A., CONSTANTINOU, M., KIRCHER, C., JOHNSON, M. & MCNAMARA, R. J. J. O. S. E. 2008. Energy dissipation systems for seismic applications: current practice and recent developments. *Journal of Structural Engineering,* 134**,** 3-21.

TANIWANGSA, W. 2002. Design Considerations for a Base-Isolated Demonstration Building. *Earthquake Spectra,* 18**,** 761-776.

THE-CRANKSHAFT-PUBLISHING. no date. *FEM for Trusses (Finite Element Method) Part 1* [Online]. Available: http://what-when-how.com/the-finite-element-method/fem-for-trusses-finite-element-method-part-1/ [Accessed 16 April 2021].

THERMOU, G. E. & ELNASHAI, A. S. 2006. Seismic retrofit schemes for RC structures and local-global consequences. *Progress in Structural Engineering and Materials,* 8**,** 1-15.

THORBURN, L. J., MONTGOMERY, C. & KULAK, G. L. 1983. Analysis of steel plate shear walls.

TIAN, W., HAO, J. & FAN, C. 2015. Analysis of thin steel plate shear walls using the three-strip model. *Journal of Structural Engineering,* 142**,** 04015169.

TIMLER, P. A. & KULAK, G. L. 1983. Experimental study of steel plate shear walls.

TSAI, K.-C., LAI, J.-W., HWANG, Y.-C., LIN, S.-L. & WENG, C.-H. Research and application of double-core buckling restrained braces in Taiwan. Proceeding of the 13th World Conference on Earthquake Engineering, Paper, 2004.

UNIDO 1991. Use of natural rubber-based bearings for earthquake protection of small buildings.

WANG, M. & YANG, W. 2018. Equivalent constitutive model of steel plate shear wall structures. *Thin-Walled Structures,* 124**,** 415-429.

WONGPRASERT, N. & SYMANS, M. 2004. Application of a genetic algorithm for optimal damper distribution within the nonlinear seismic benchmark building. *Journal of Engineering Mechanics,* 130**,** 401-406.

YETTRAM, A. L. & HUSAIN, H. M. 1966. Plane-framework methods for plates in extension. *Journal of the Engineering Mechanics Division,* 92**,** 157-168.

Appendix

Seismic assessment results for 3D bare building model

Record 170

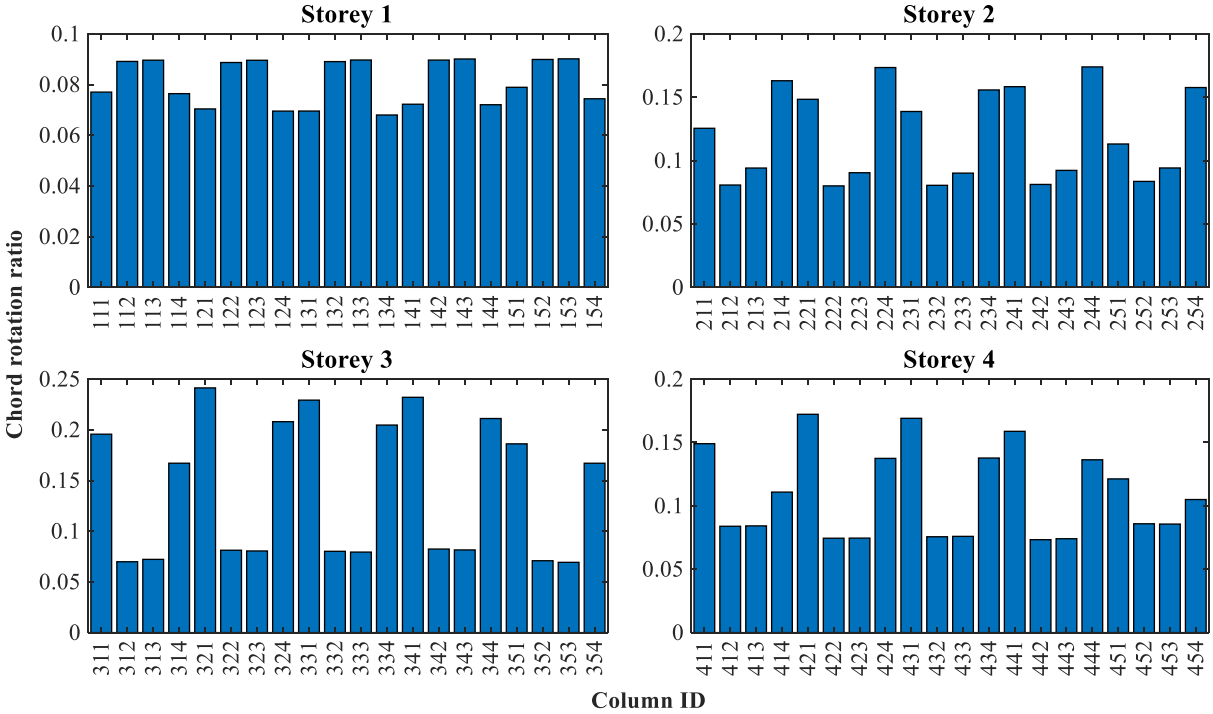

Fig. A. 1. Column chord rotation ratio for 3D bare building model under Record 170

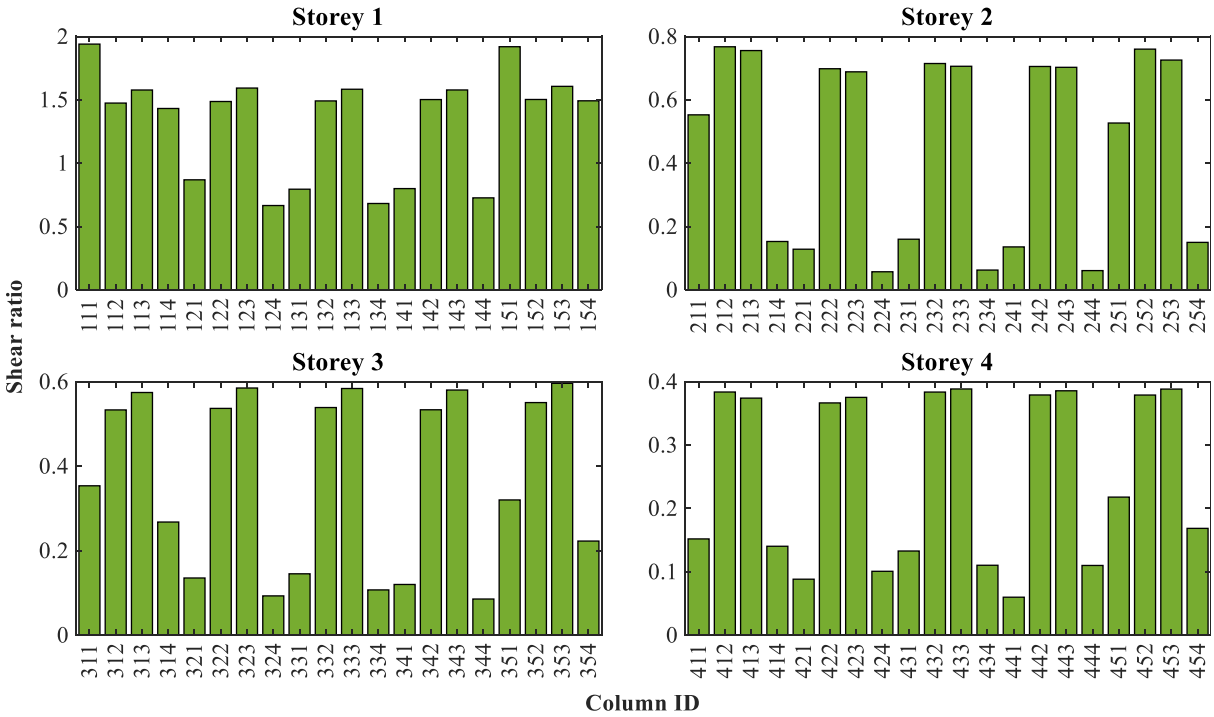

Fig. A. 2. Column shear ratio for 3D bare building model under Record 170

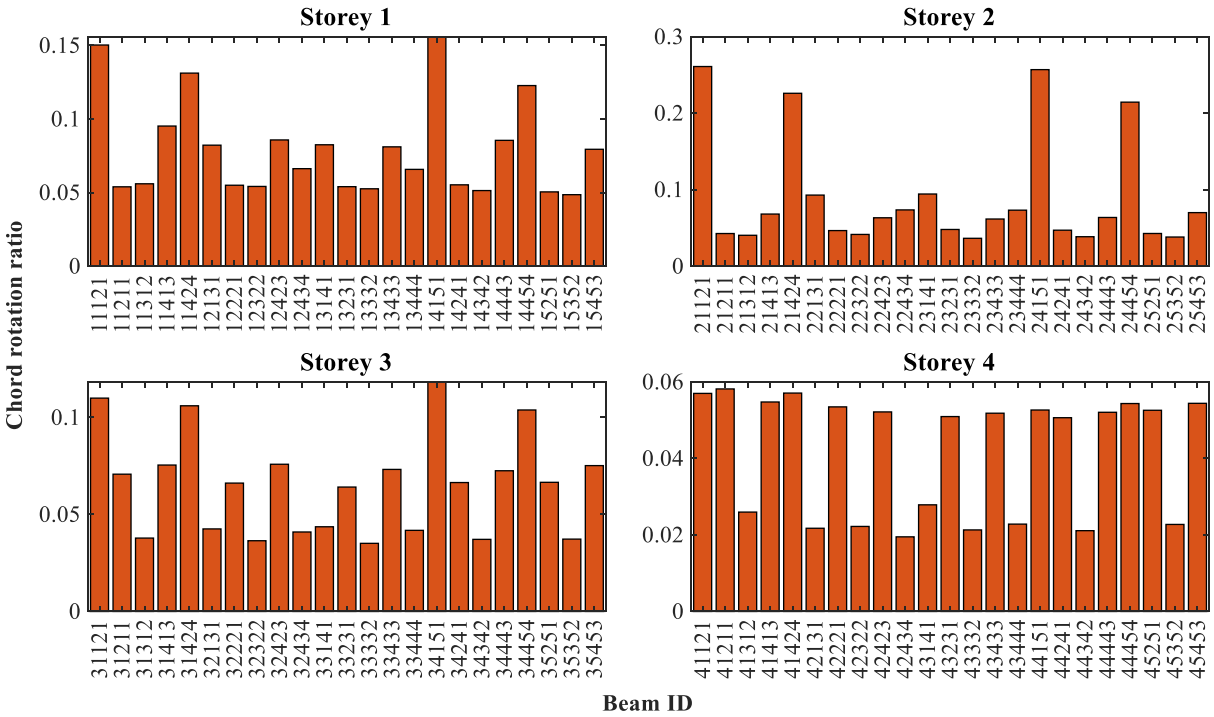

Fig. A. 3. Beam chord rotation ratio for 3D bare building model under Record 170

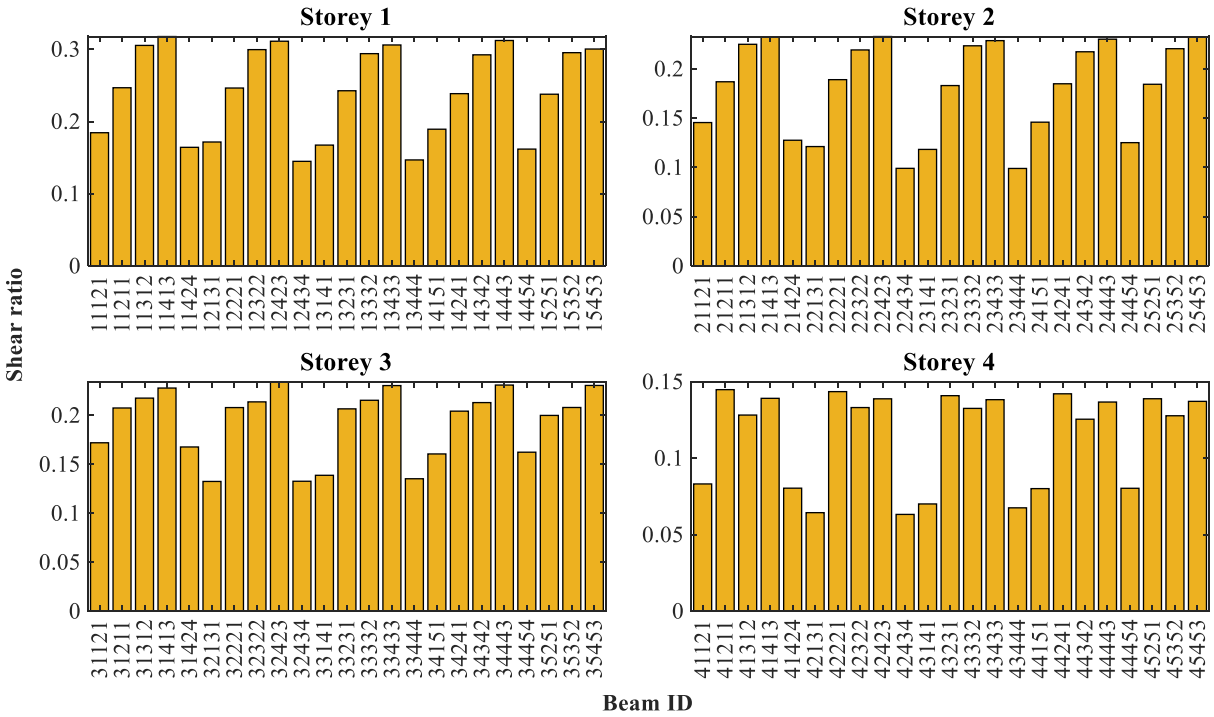

Fig. A. 4. Beam shear ratio for 3D bare building model under Record 170

Record 199

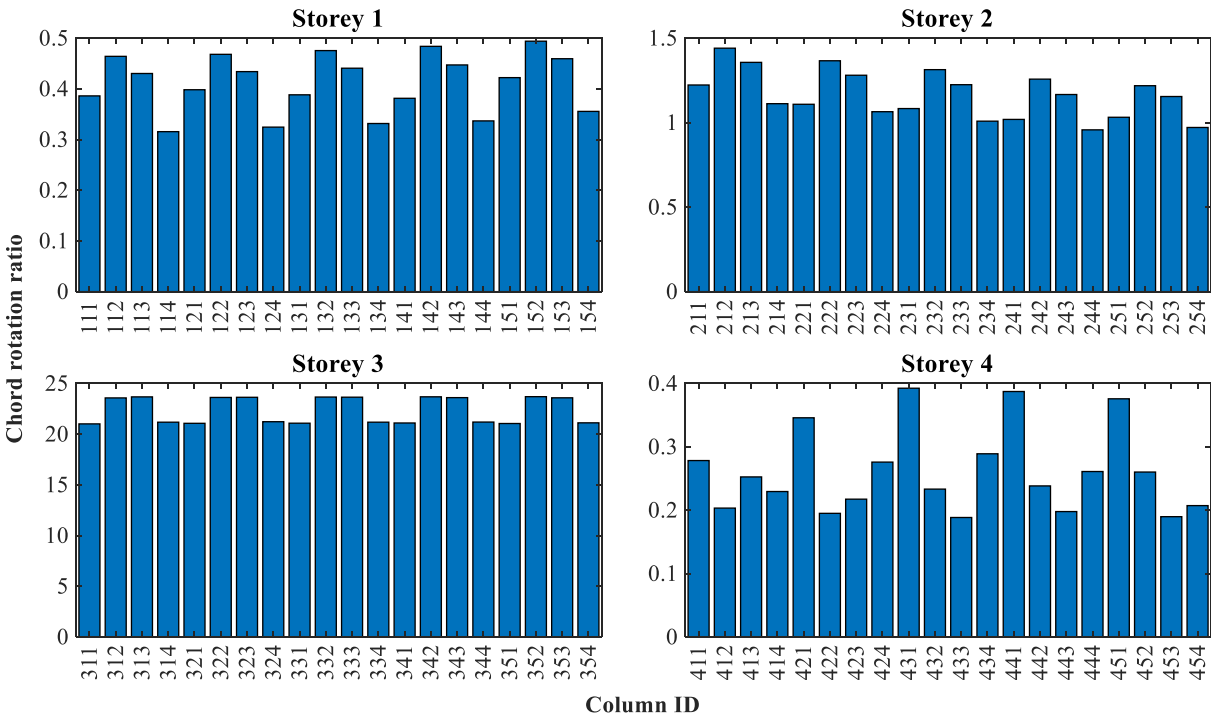

Fig. A. 5. Column chord rotation ratio for 3D bare building model under Record 199

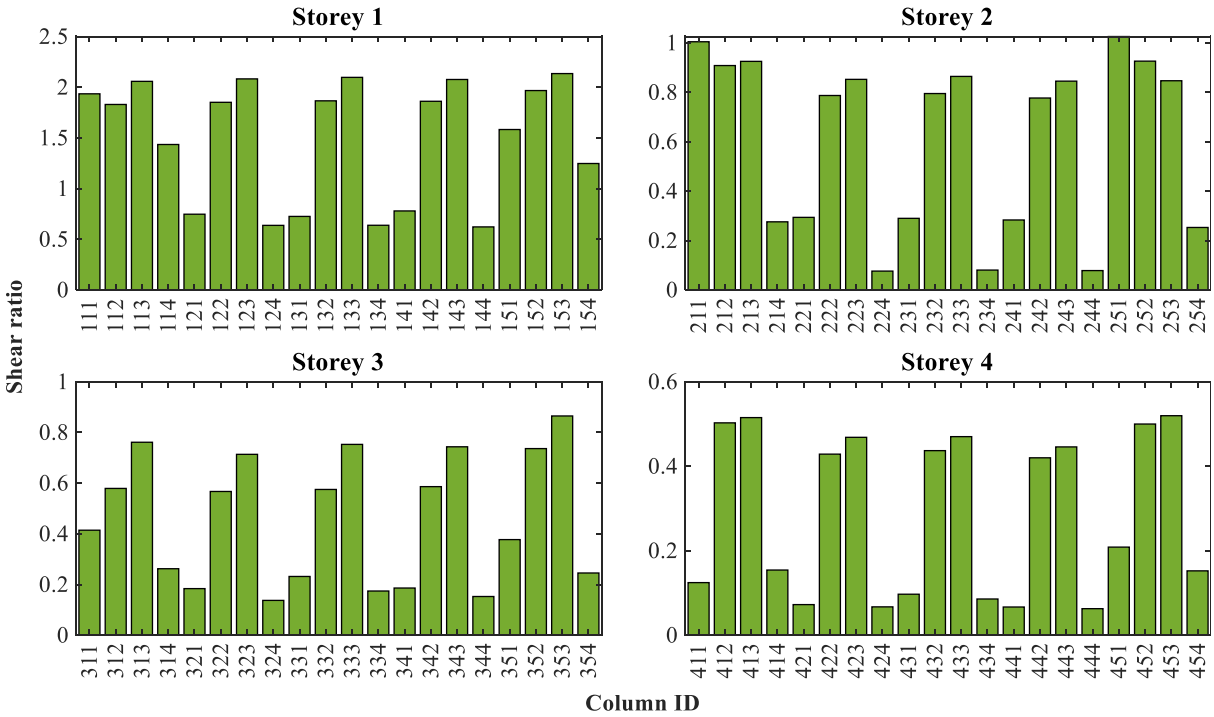

Fig. A. 6. Column shear ratio for 3D bare building model under Record 199

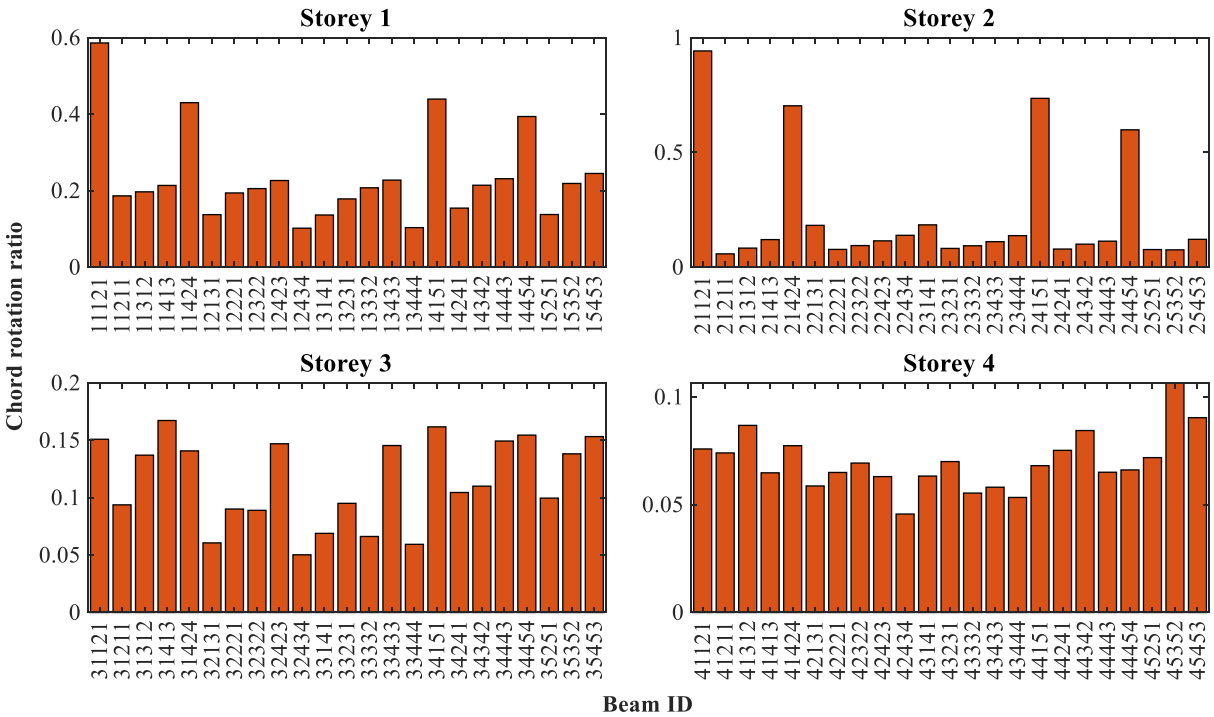

Fig. A. 7. Beam chord rotation ratio for 3D bare building model under Record 199

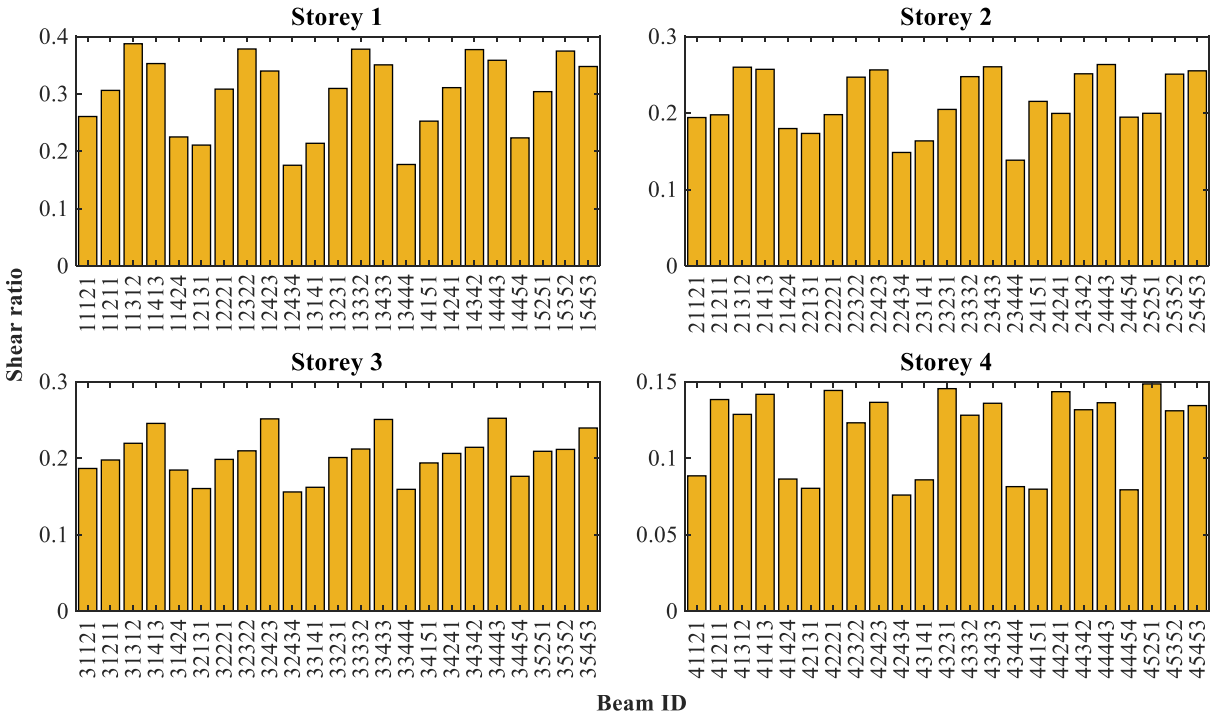

Fig. A. 8. Beam shear ratio for 3D bare building model under Record 199

Record 292

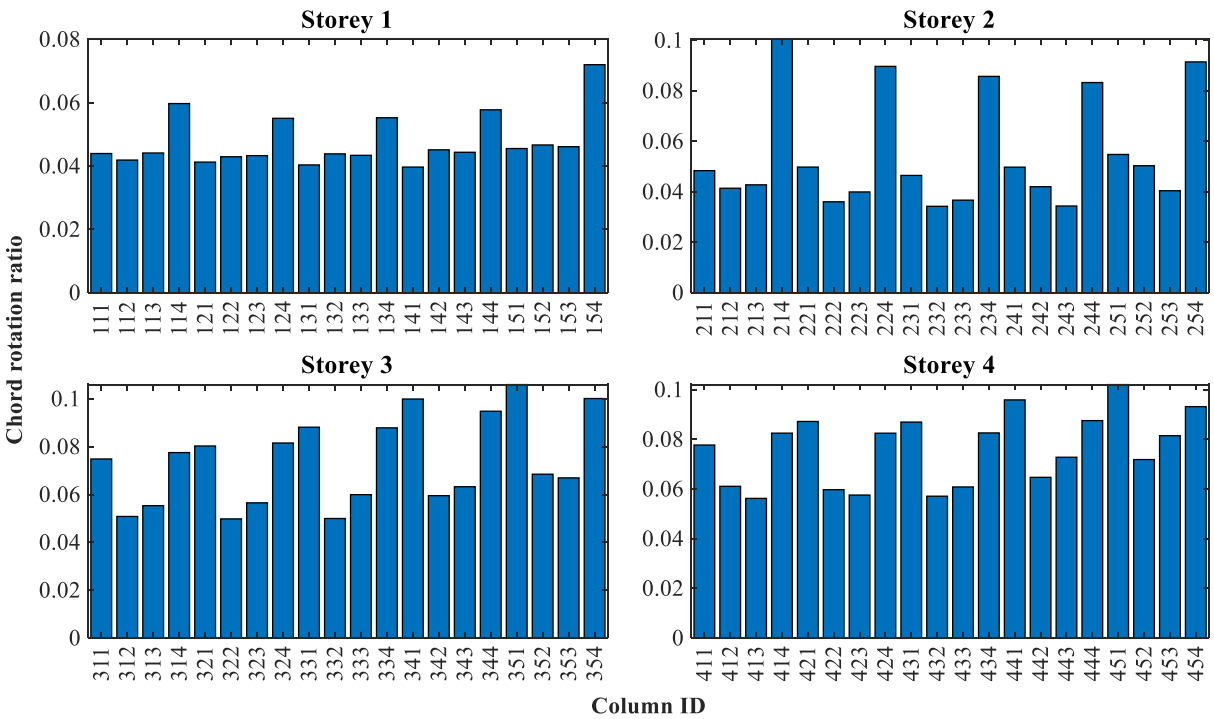

Fig. A. 9. Column chord rotation ratio for 3D bare building model under Record 292

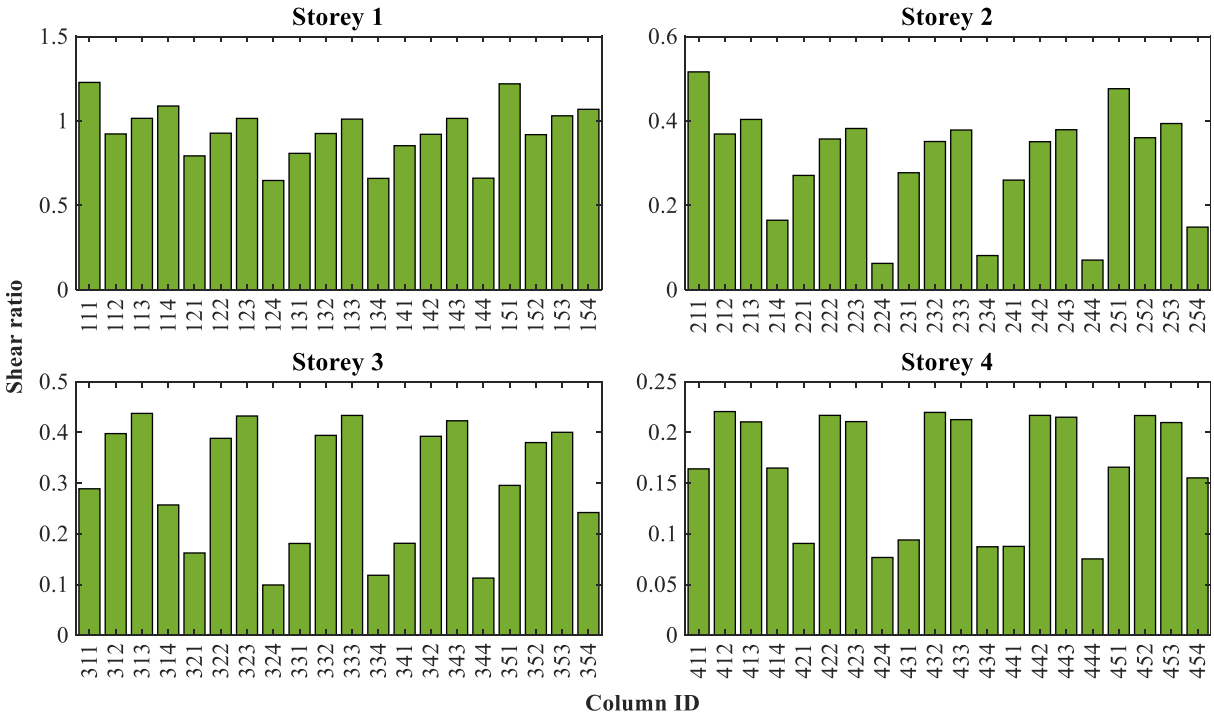

Fig. A. 10. Column shear ratio for 3D bare building model under Record 292

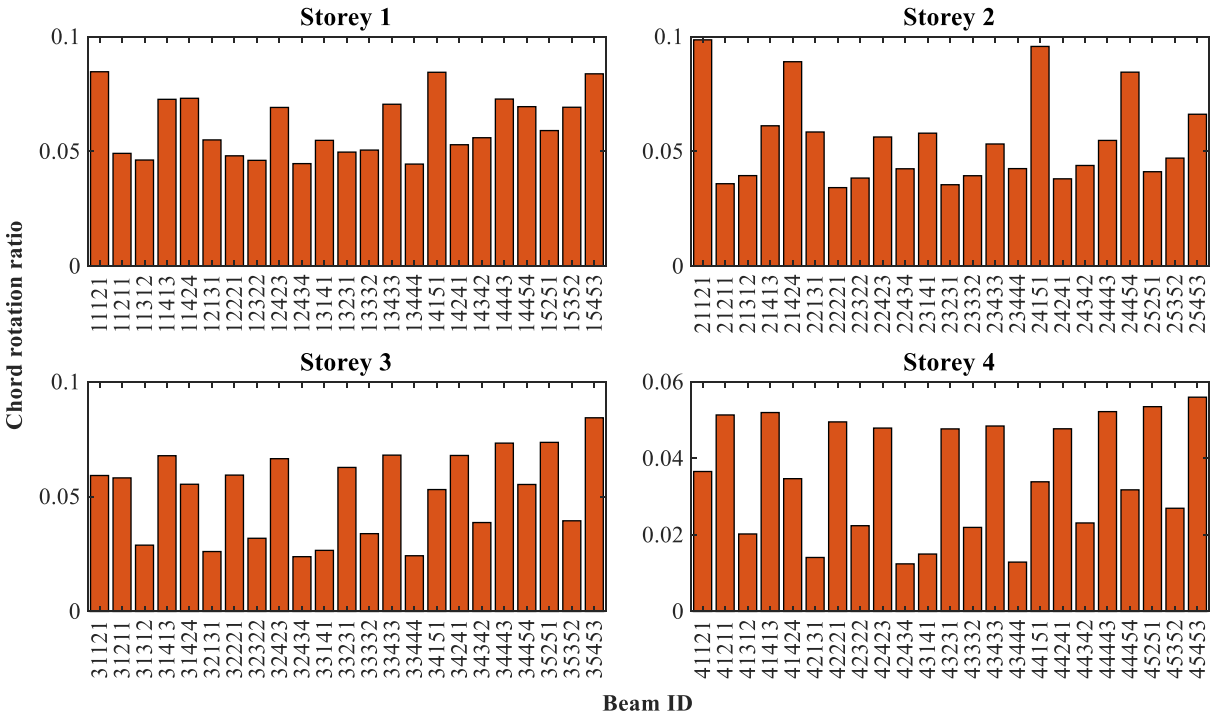

Fig. A. 11. Beam chord rotation ratio for 3D bare building model under Record 292

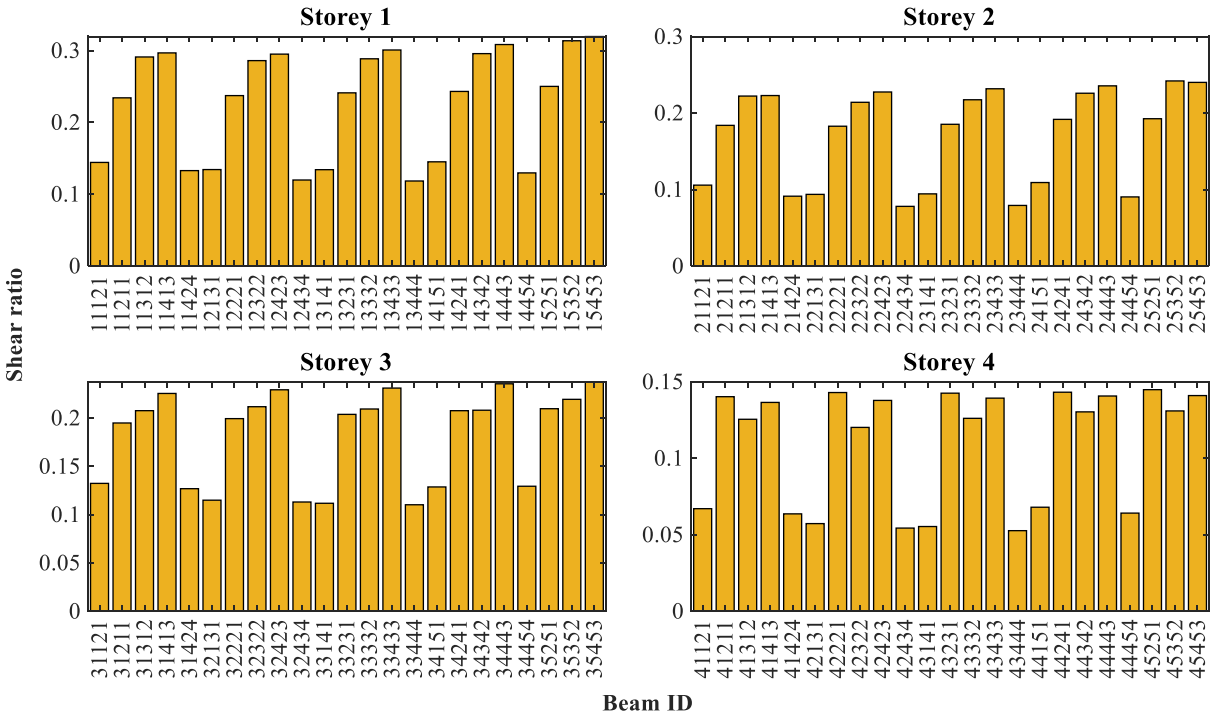

Fig. A. 12. Beam shear ratio for 3D bare building model under Record 292

Record 333

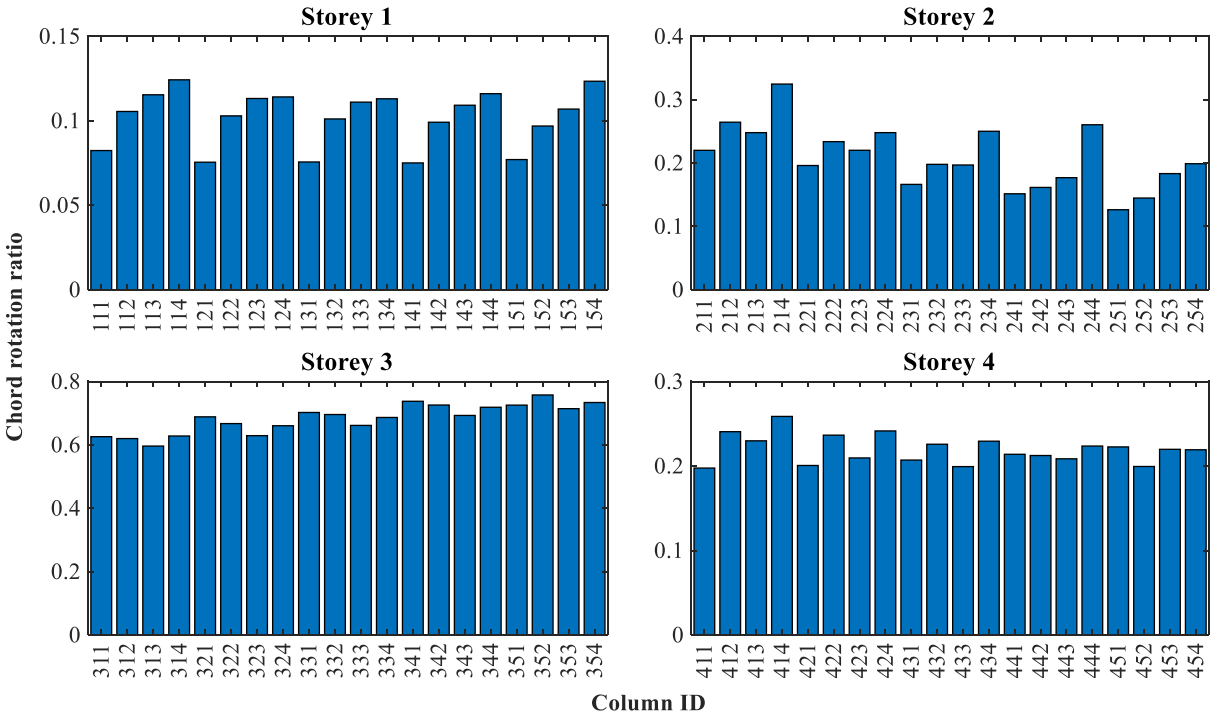

Fig. A. 13. Column chord rotation ratio for 3D bare building model under Record 333

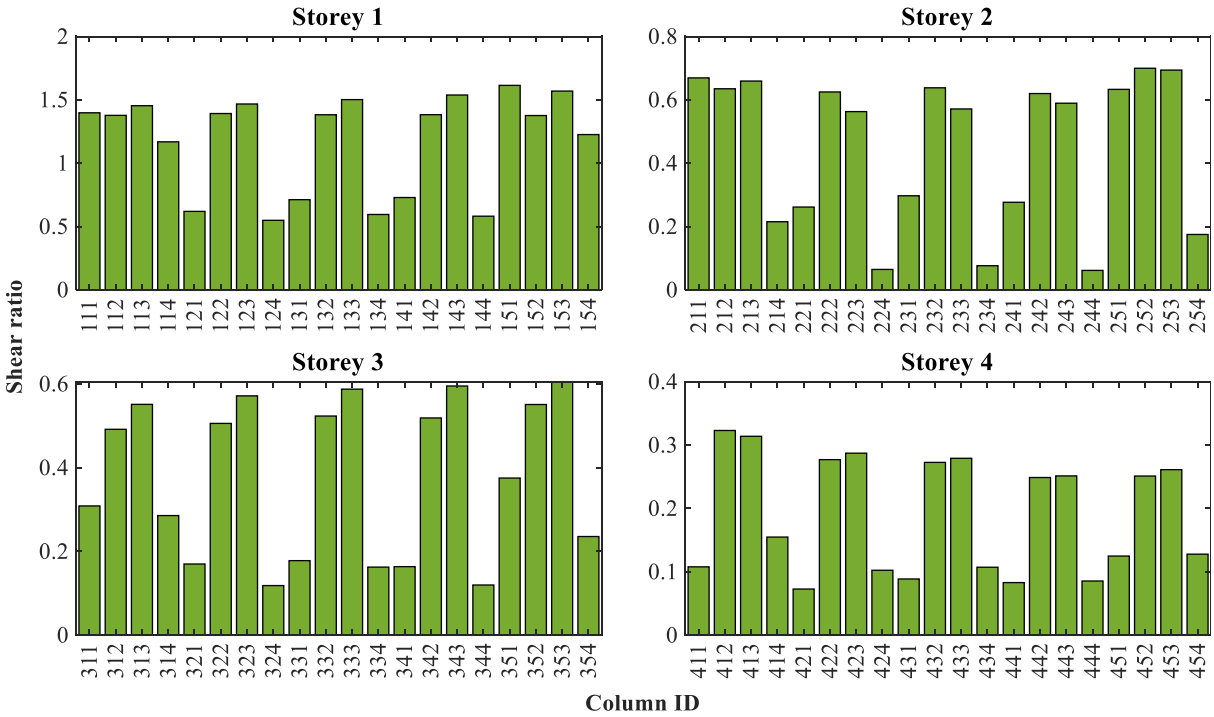

Fig. A. 14. Column shear ratio for 3D bare building model under Record 333

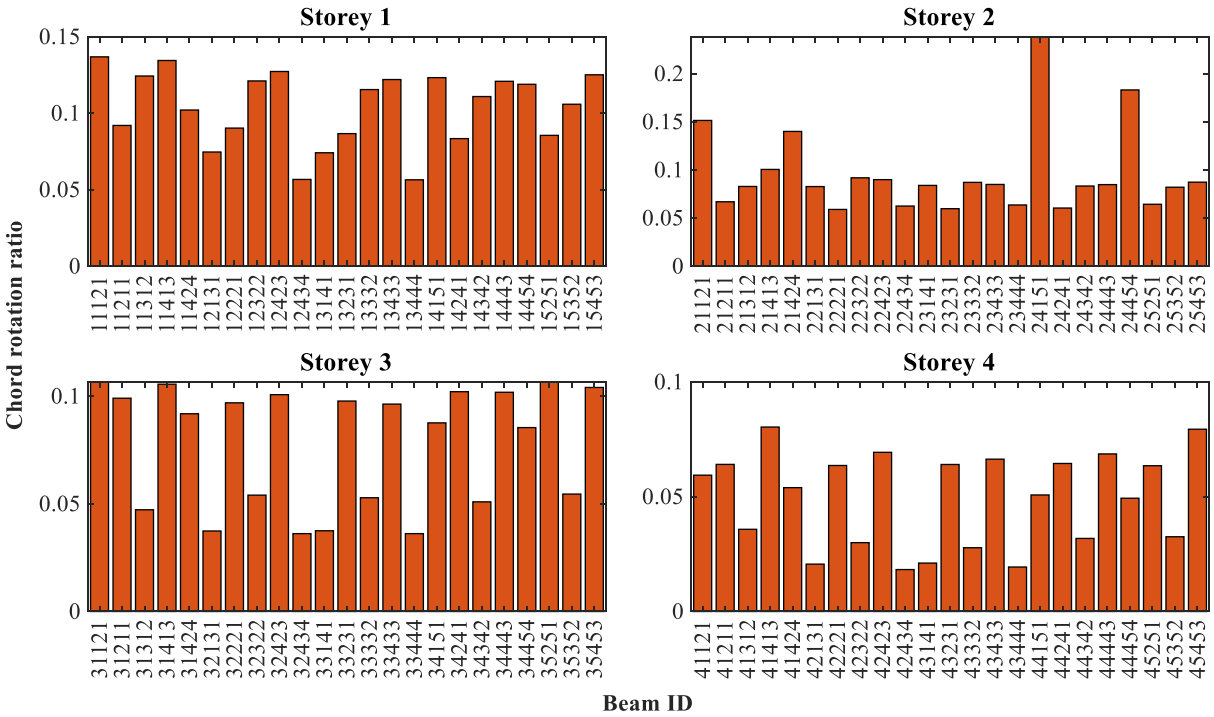

Fig. A. 15. Beam chord rotation ratio for 3D bare building model under Record 333

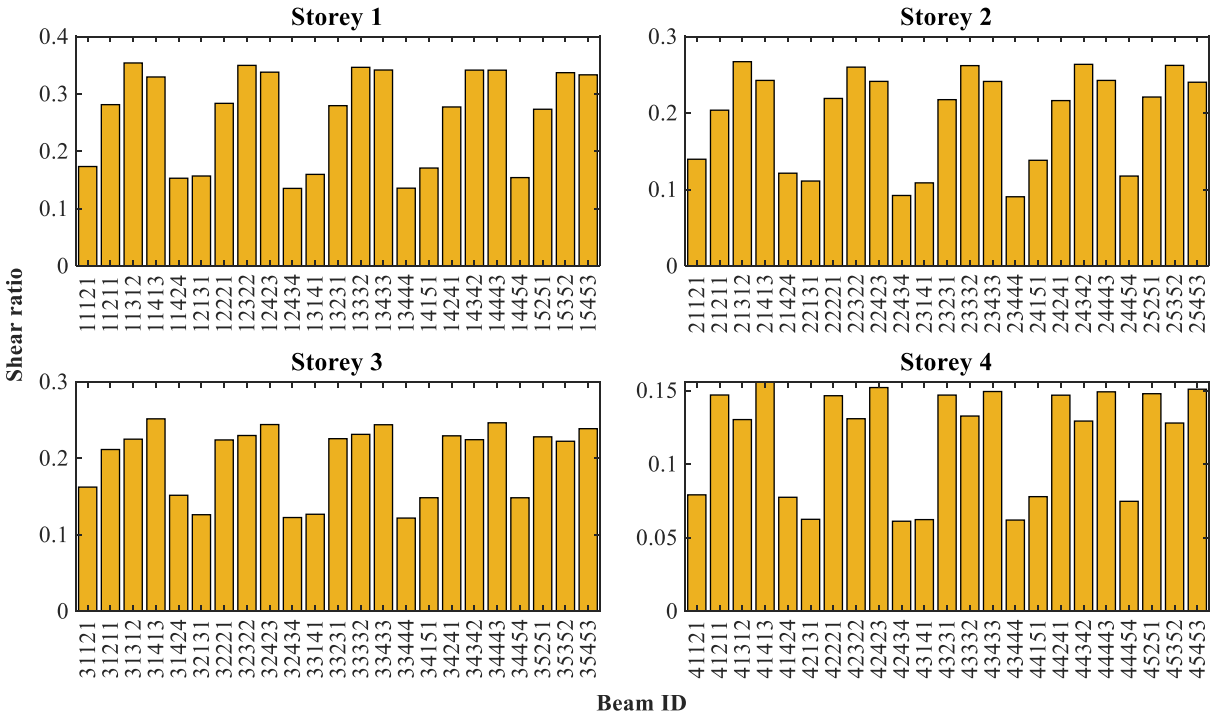

Fig. A. 16. Beam shear ratio for 3D bare building model under Record 333

Record 600

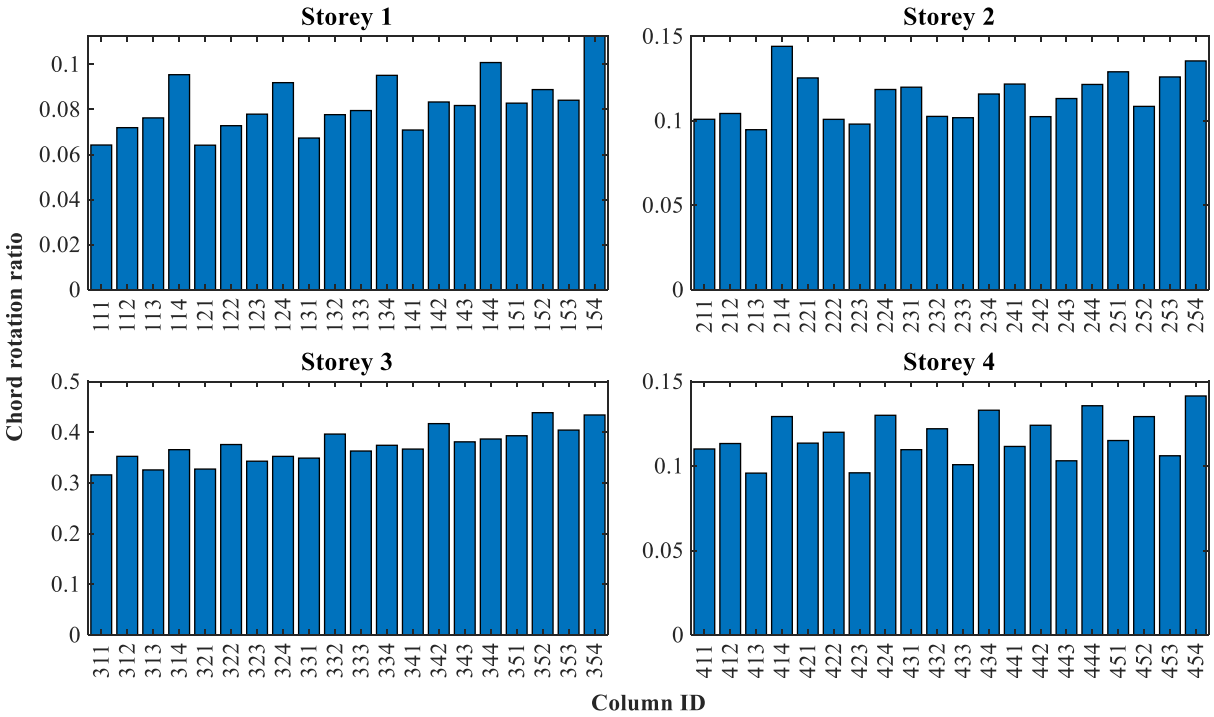

Fig. A. 17. Column chord rotation ratio for 3D bare building model under Record 600

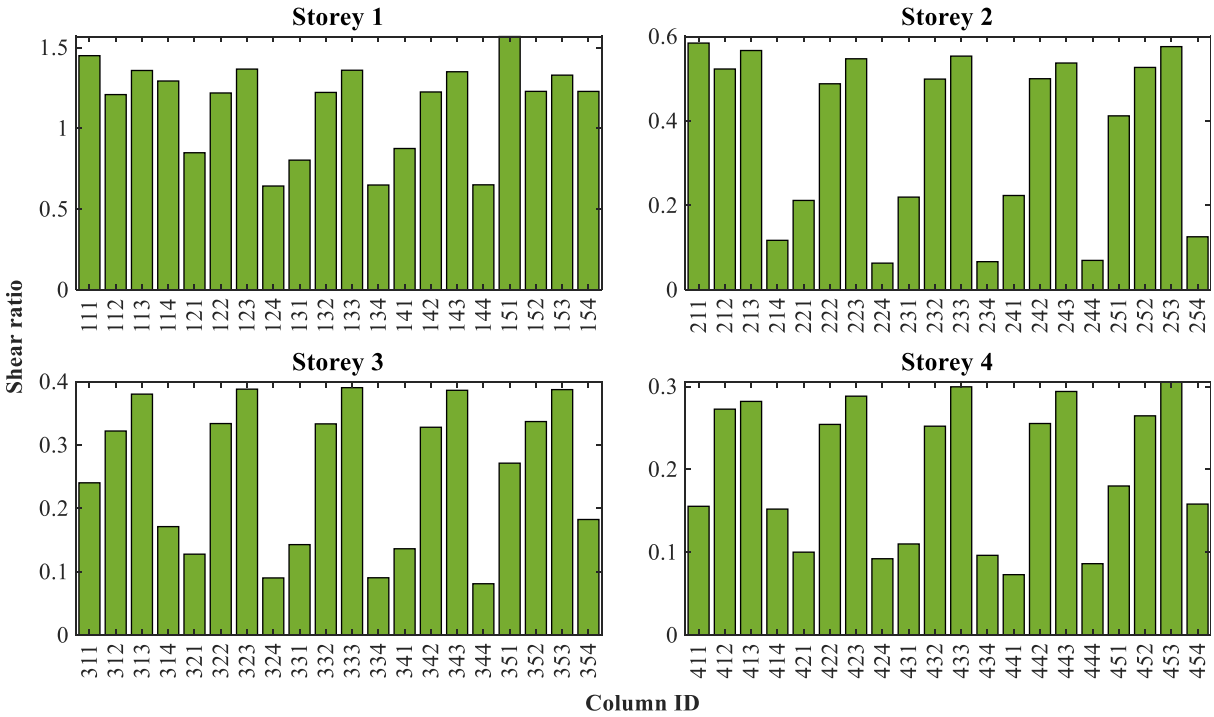

Fig. A. 18. Column shear ratio for 3D bare building model under Record 600

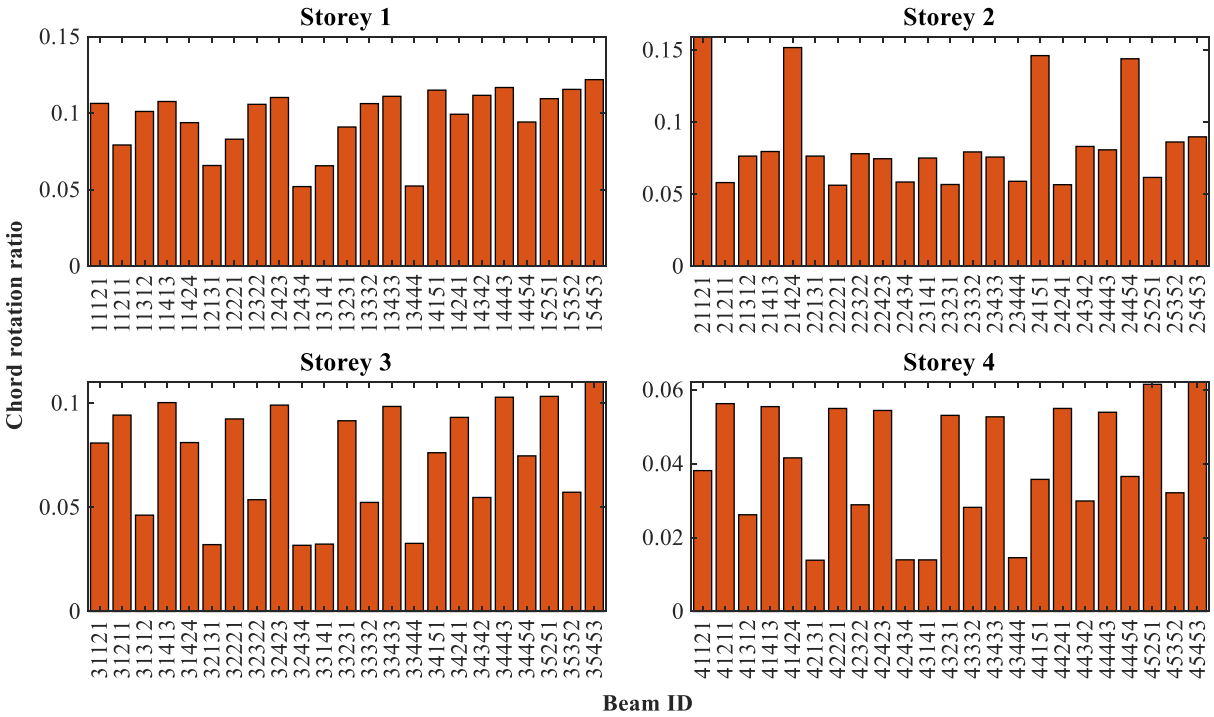

Fig. A. 19. Beam chord rotation ratio for 3D bare building model under Record 600

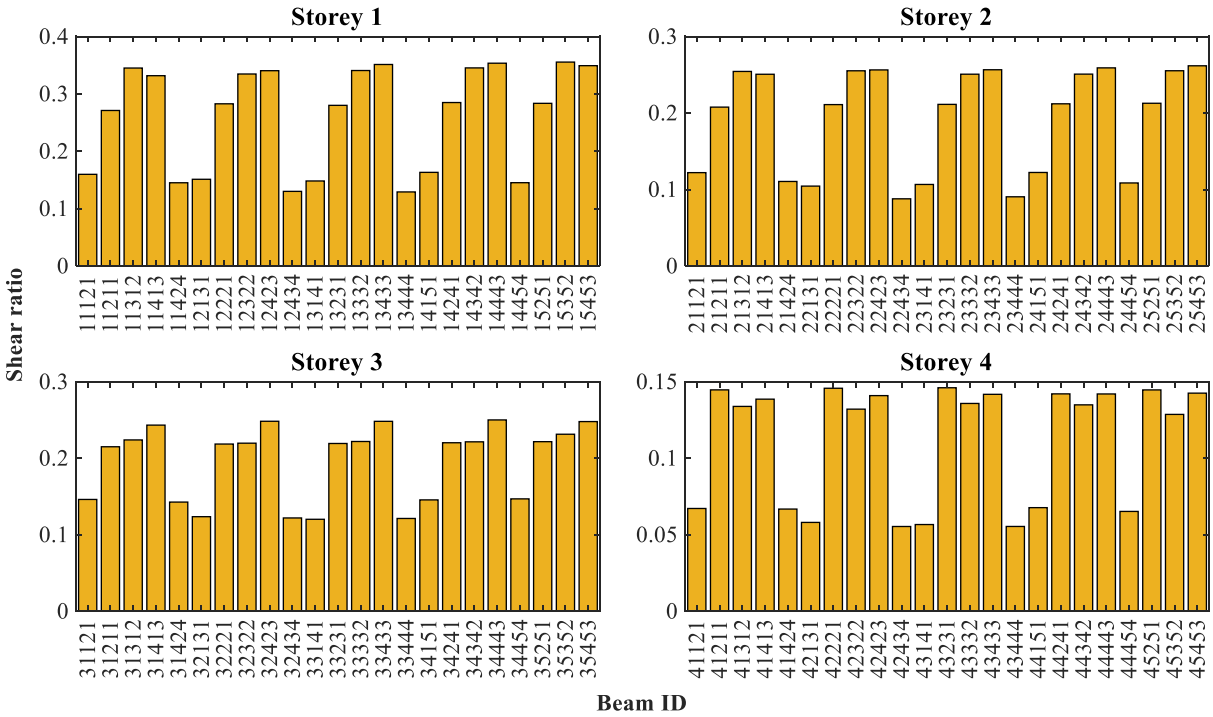

Fig. A. 20. Beam chord rotation ratio for 3D bare building model under Record 600

Record 6331

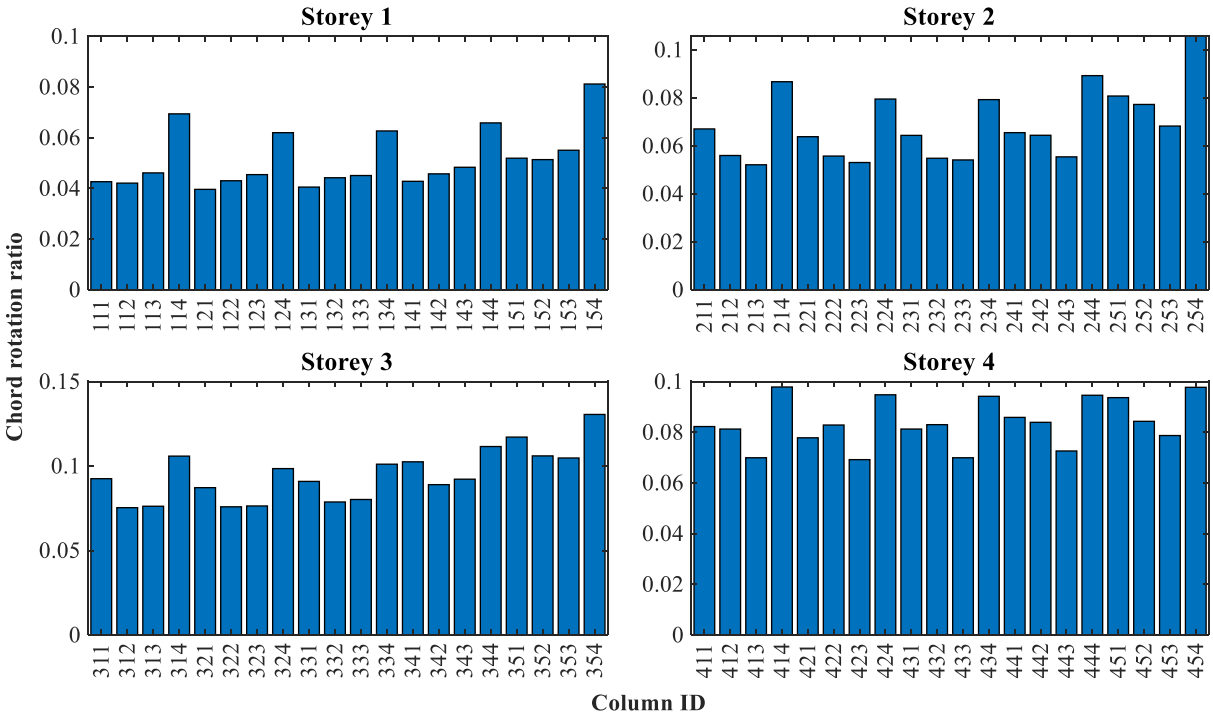

Fig. A. 21. Column chord rotation ratio for 3D bare building model under Record 6331

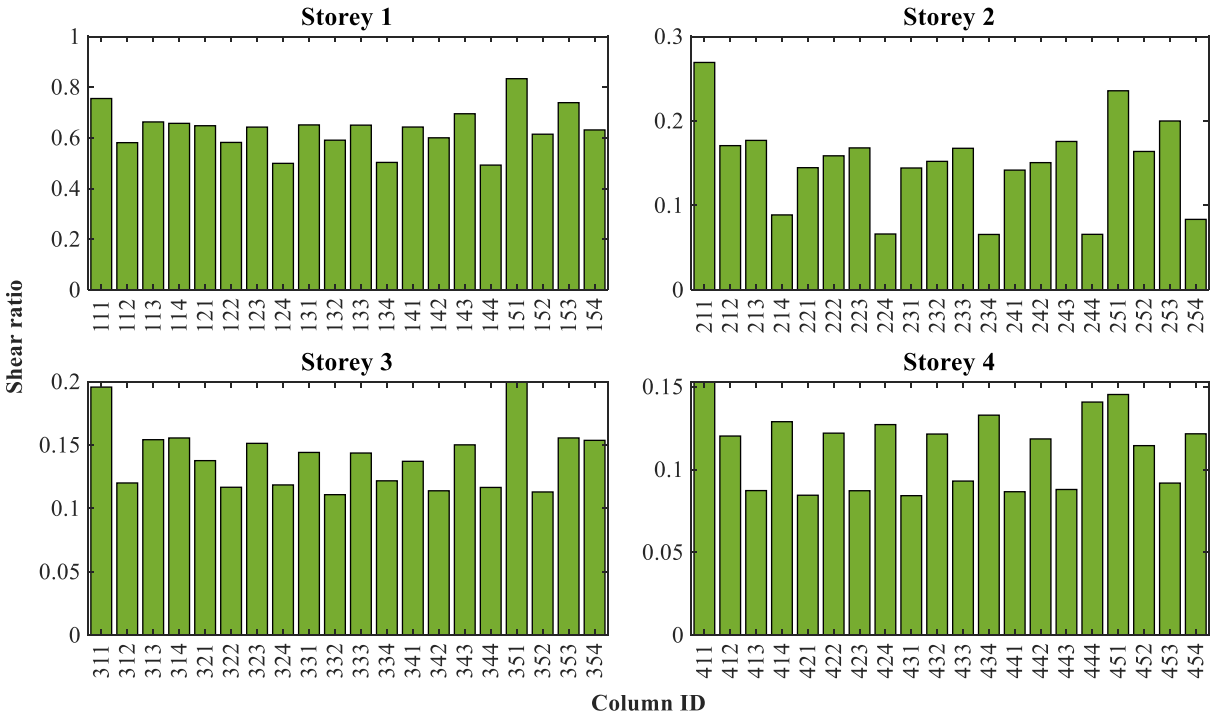

Fig. A. 22. Column shear ratio for 3D bare building model under Record 6331

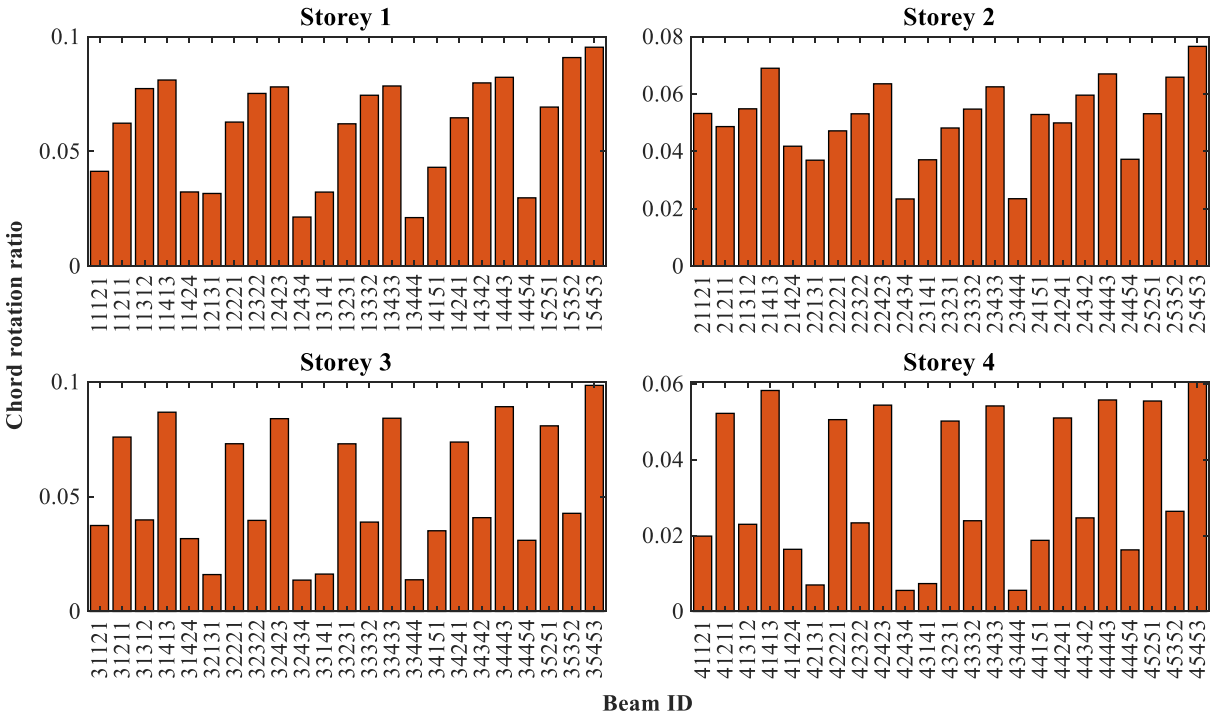

Fig. A. 23. Beam chord rotation ratio for 3D bare building model under Record 6331

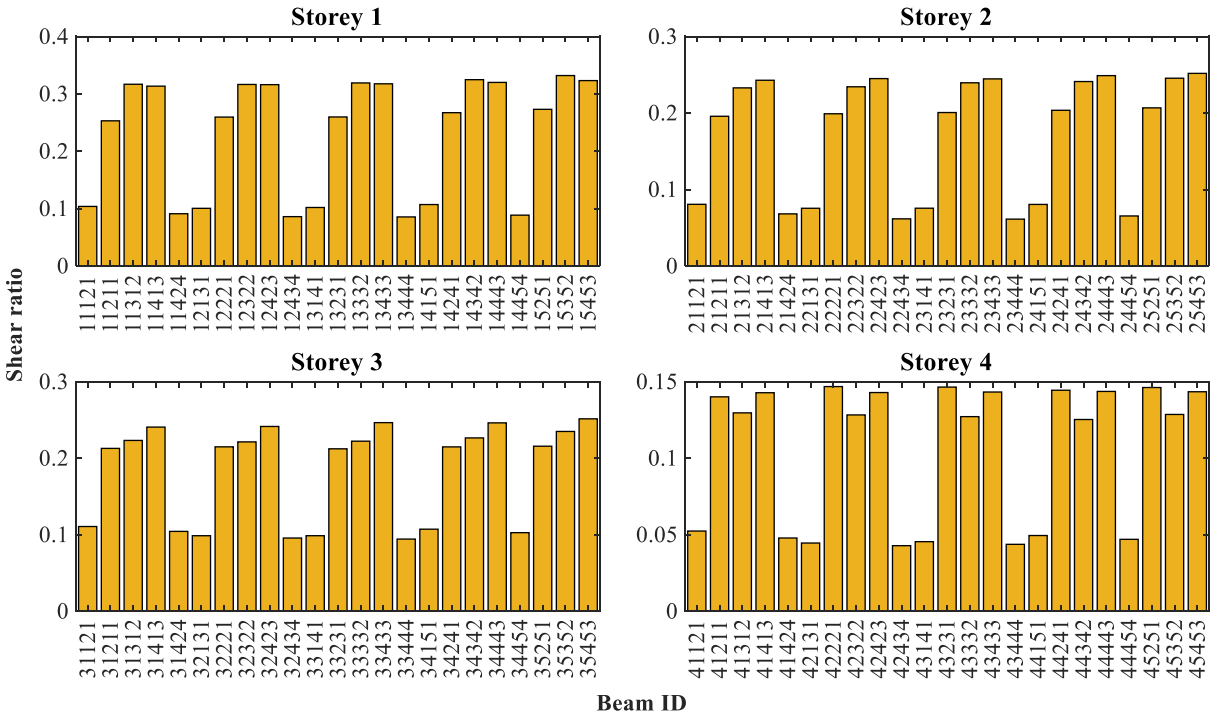

Fig. A. 24. Beam shear ratio for 3D bare building model under Record 6331

Record 6335

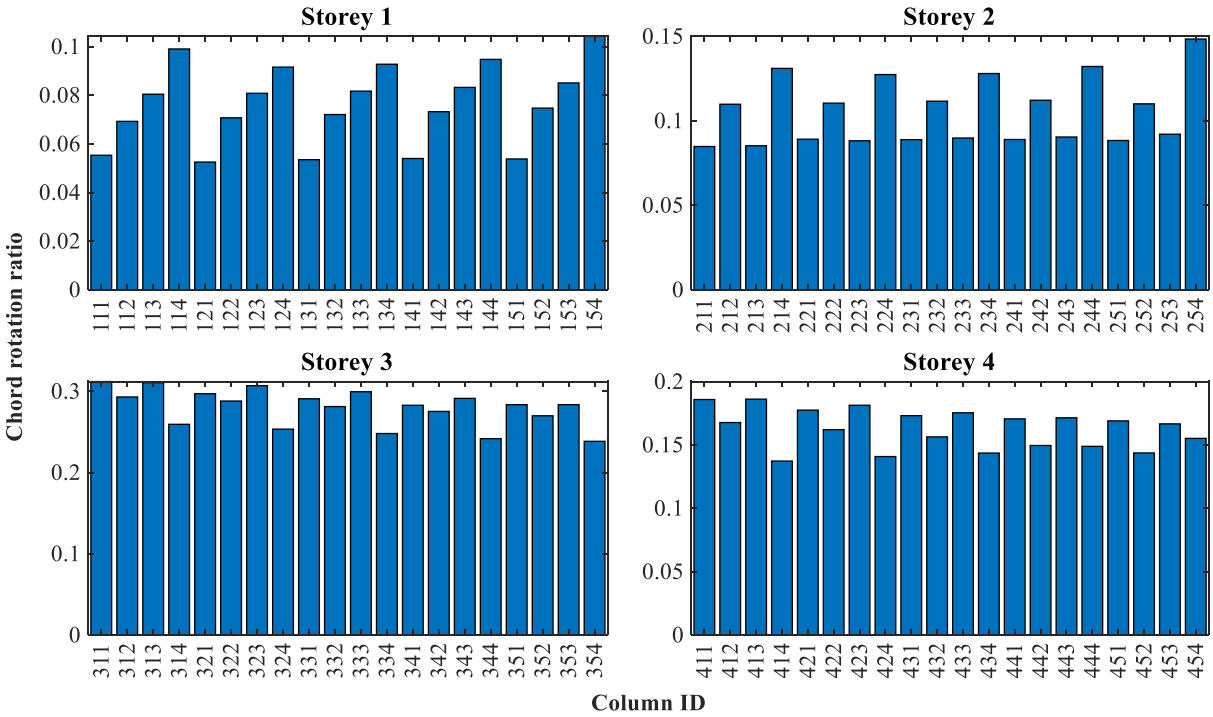

Fig. A. 25. Column chord rotation ratio for 3D bare building model under Record 6335

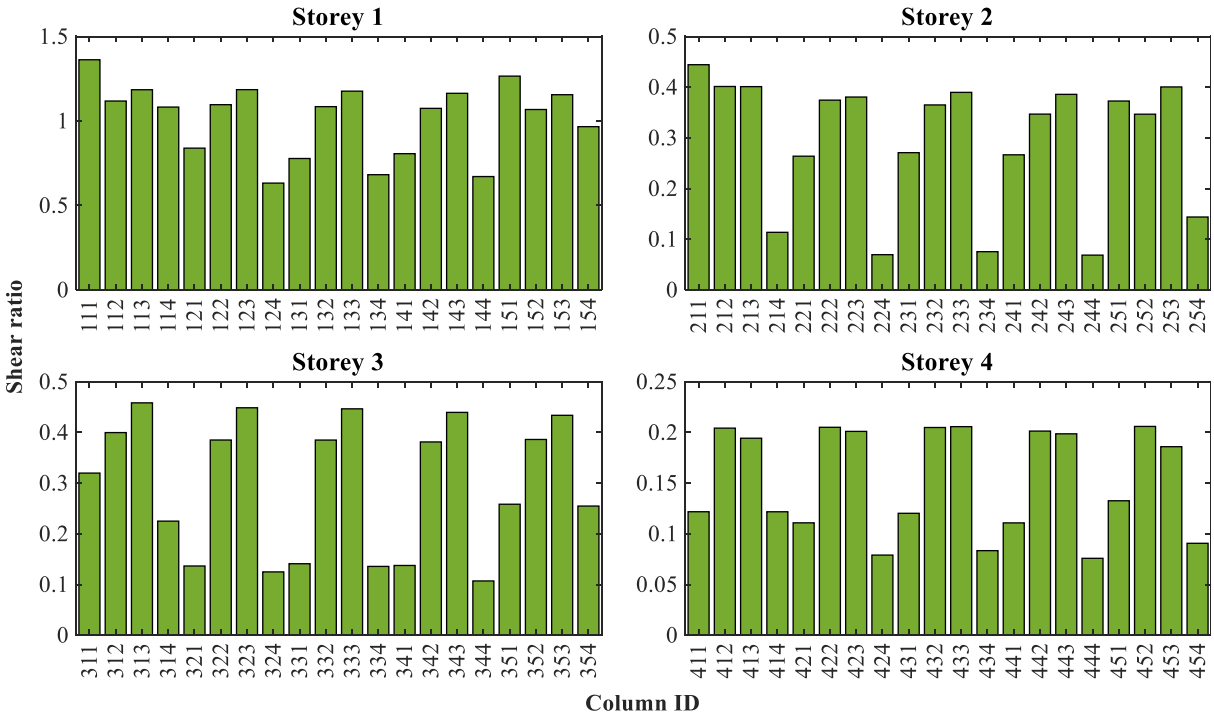

Fig. A. 26. Column shear ratio for 3D bare building model under Record 6335

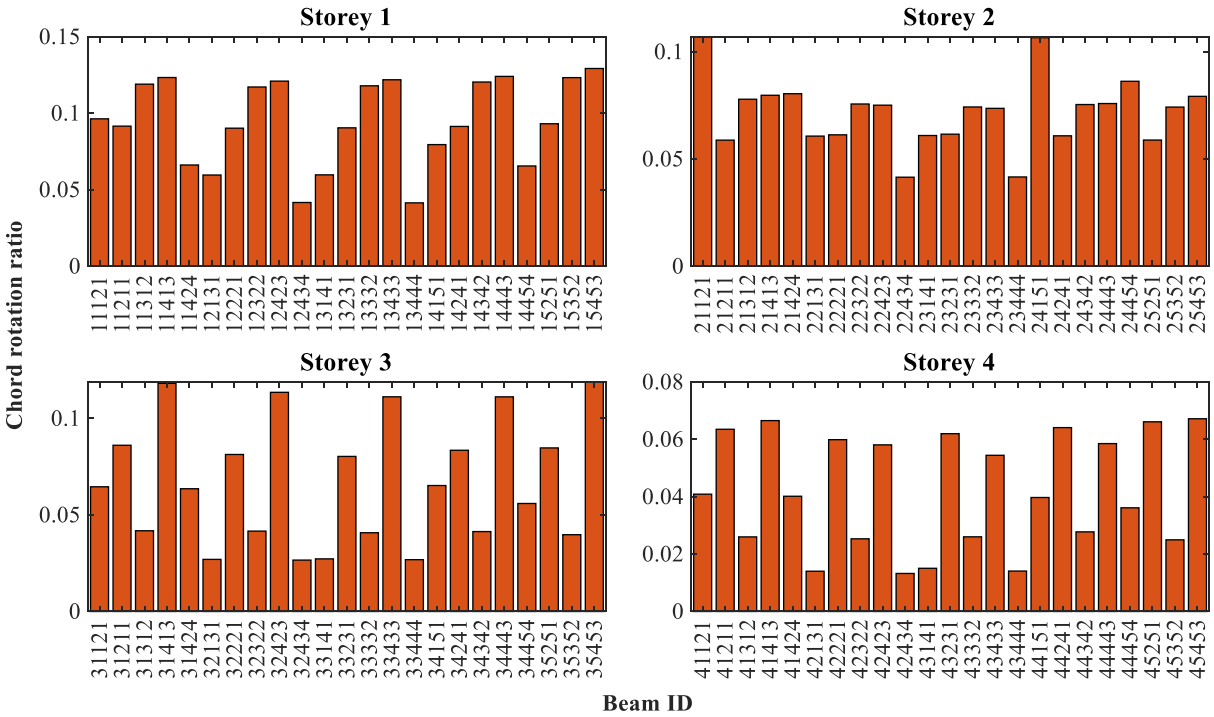

Fig. A. 27. Beam chord rotation ratio for 3D bare building model under Record 6335

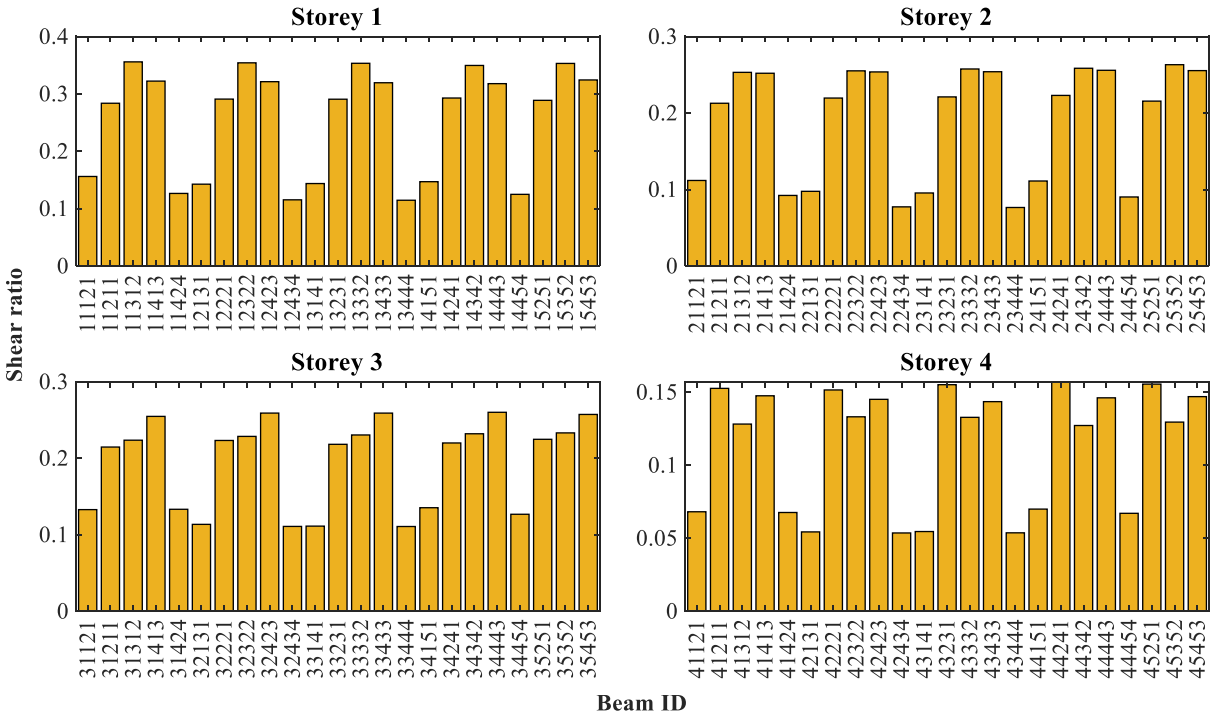

Fig. A. 28. Beam shear ratio for 3D bare building model under Record 6335

Seismic assessment results for 3D retrofitted building model

Record 170

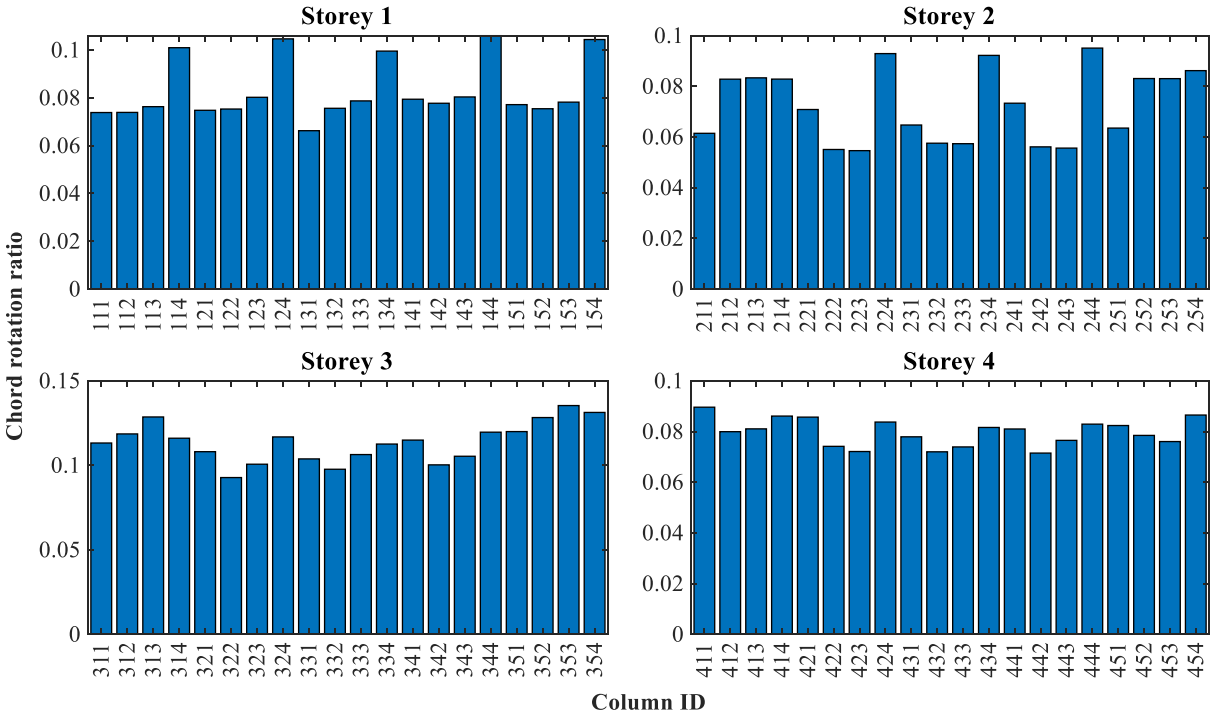

Fig. A. 29. Column chord rotation ratio for 3D retrofitted building model under Record 170

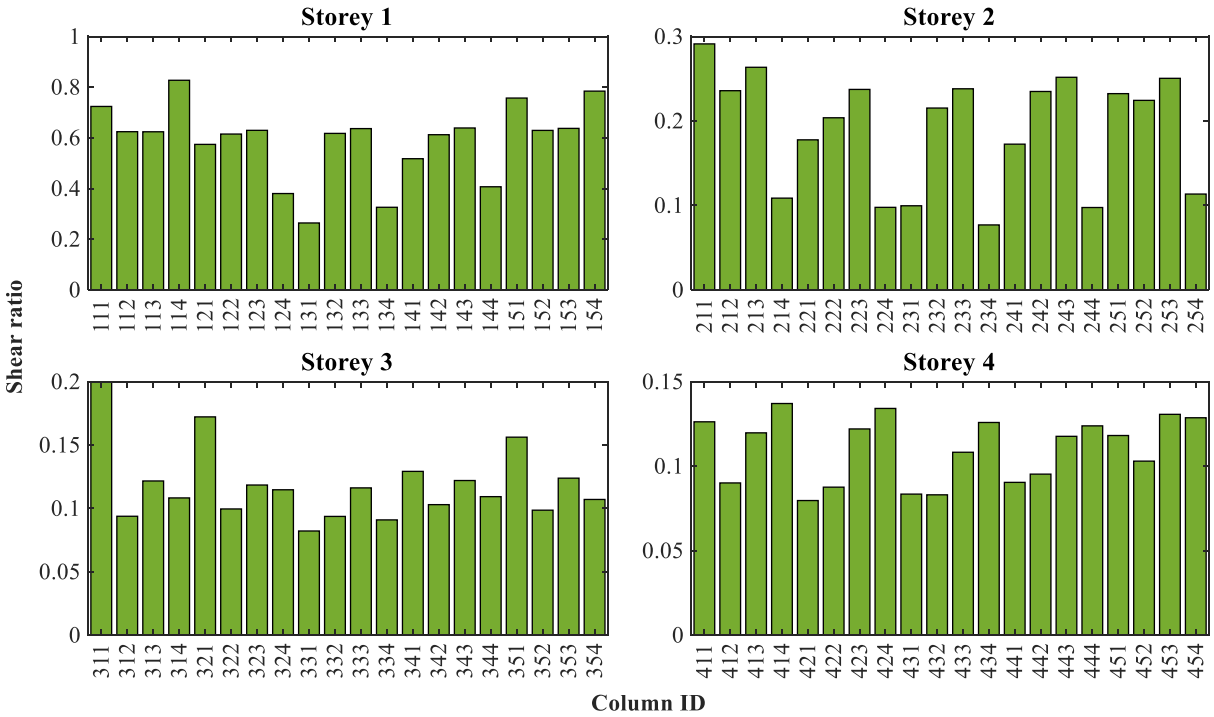

Fig. A. 30. Column shear ratio for 3D retrofitted building model under Record 170

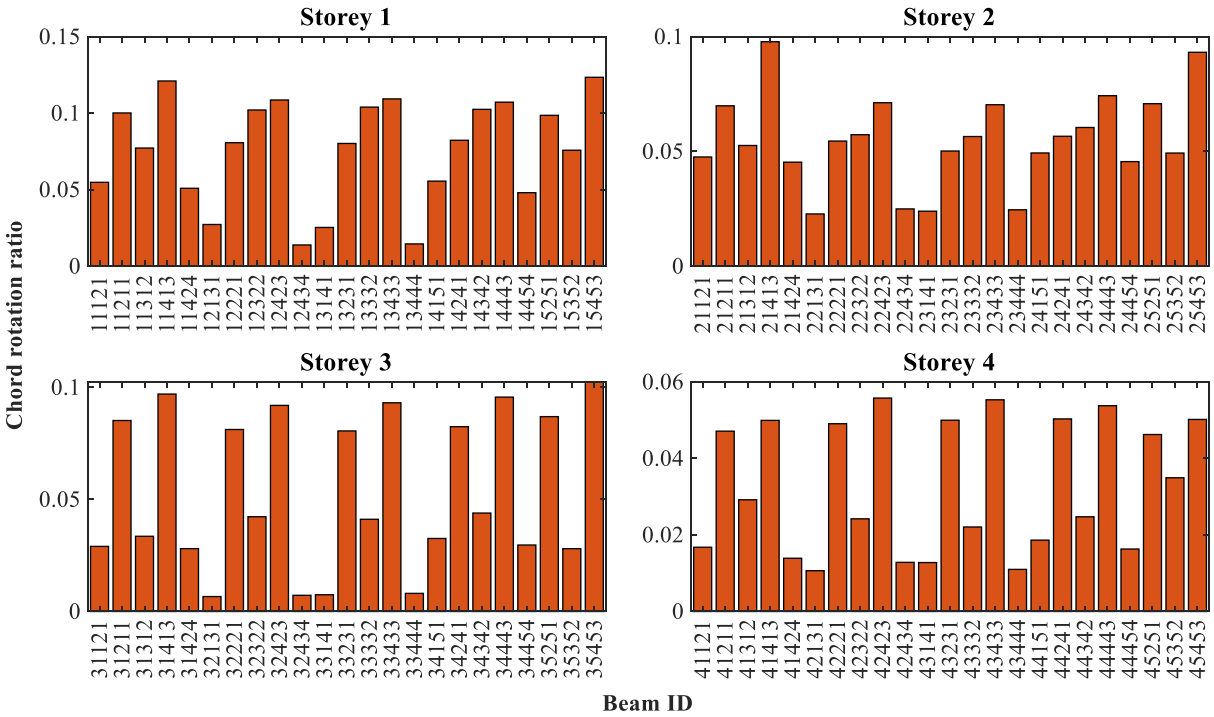

Fig. A. 31. Beam chord rotation ratio for 3D retrofitted building model under Record 170

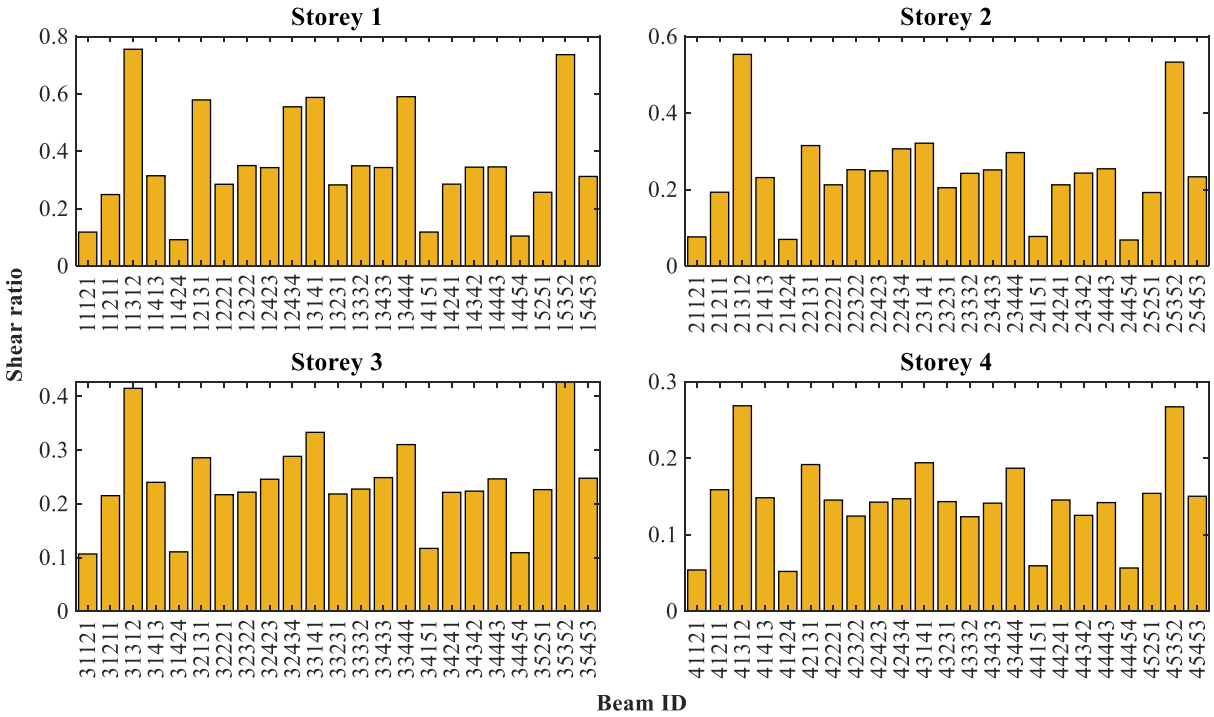

Fig. A. 32. Beam shear ratio for 3D retrofitted building model under Record 170

Record 199

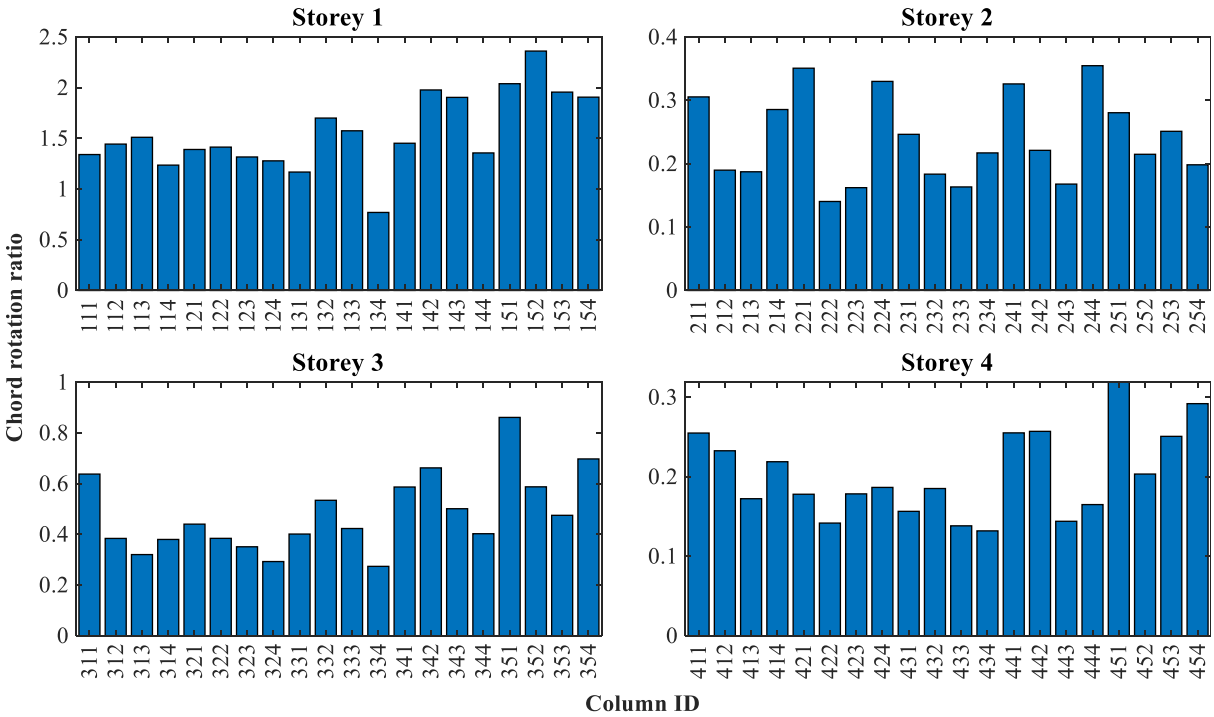

Fig. A. 33. Column chord rotation ratio for 3D retrofitted building model under Record 199

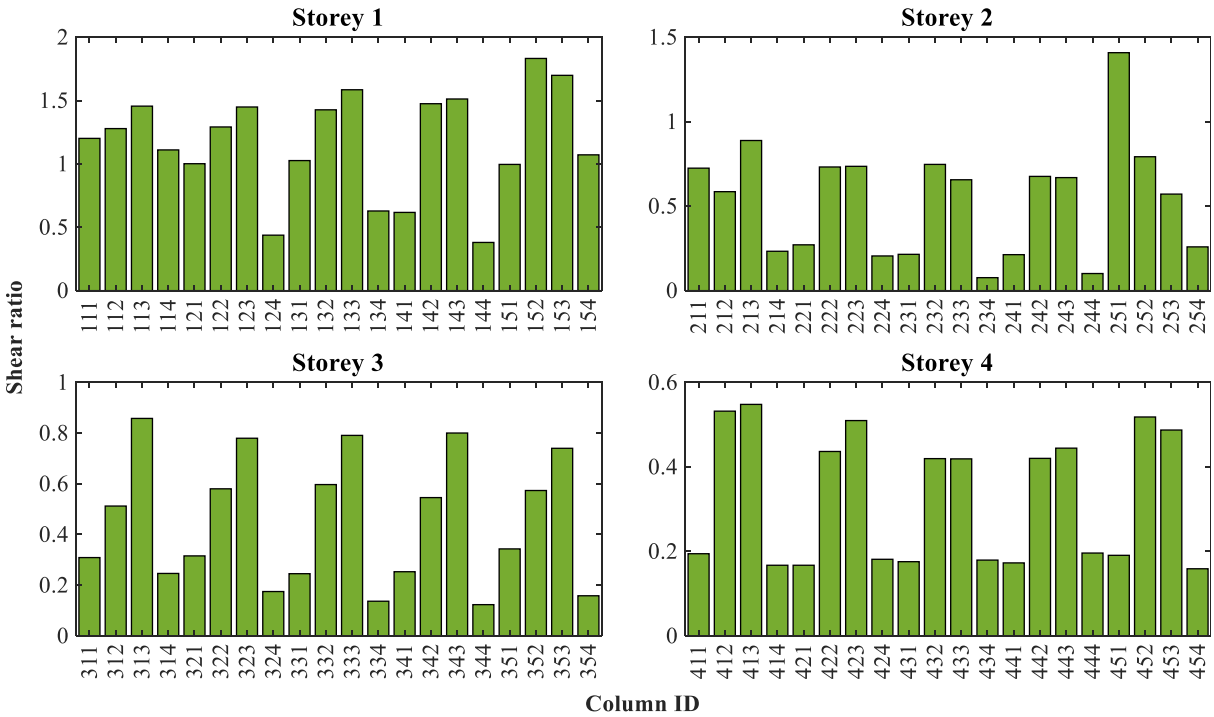

Fig. A. 34. Column shear ratio for 3D retrofitted building model under Record 199

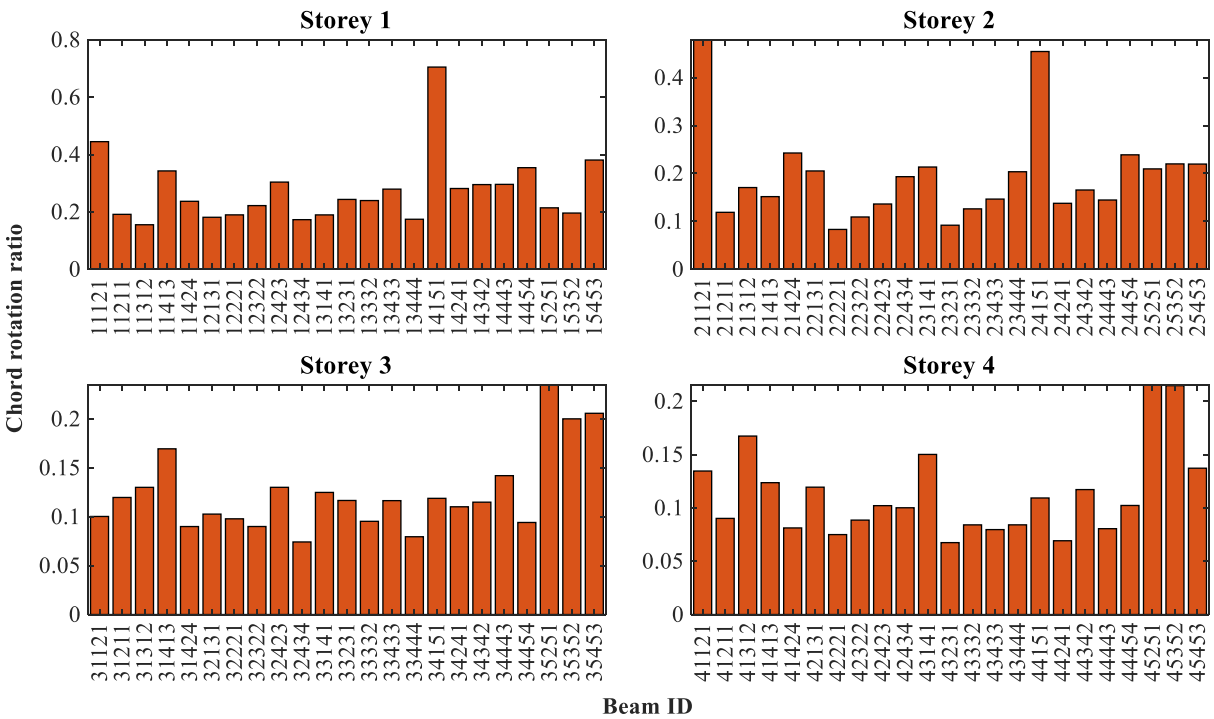

Fig. A. 35. Beam chord rotation ratio for 3D retrofitted building model under Record 199

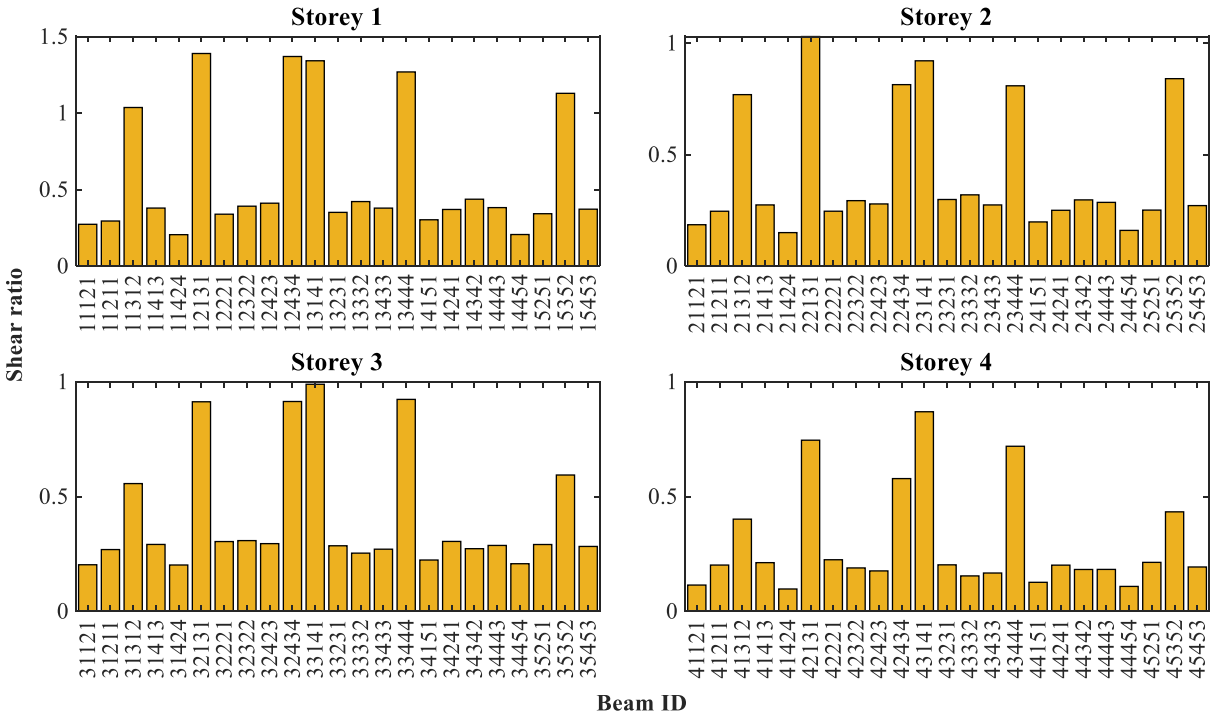

Fig. A. 36. Beam shear ratio for 3D retrofitted building model under Record 199

Record 292

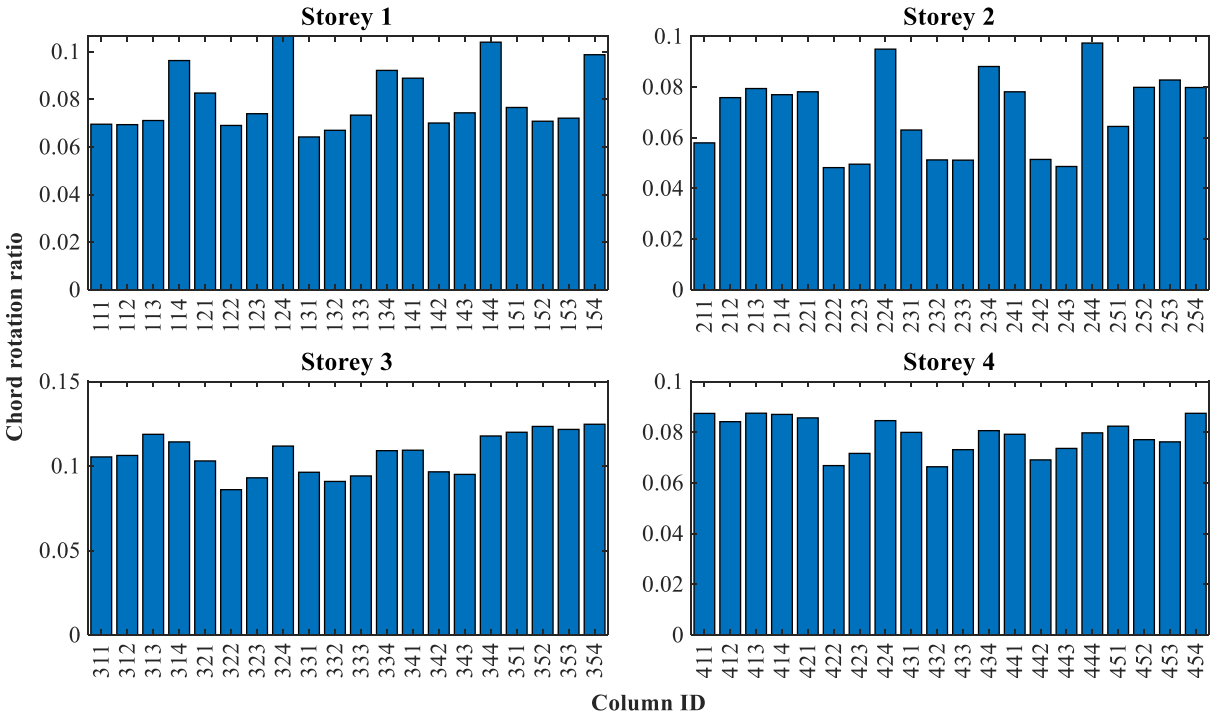

Fig. A. 37. Column chord rotation ratio for 3D retrofitted building model under Record 292

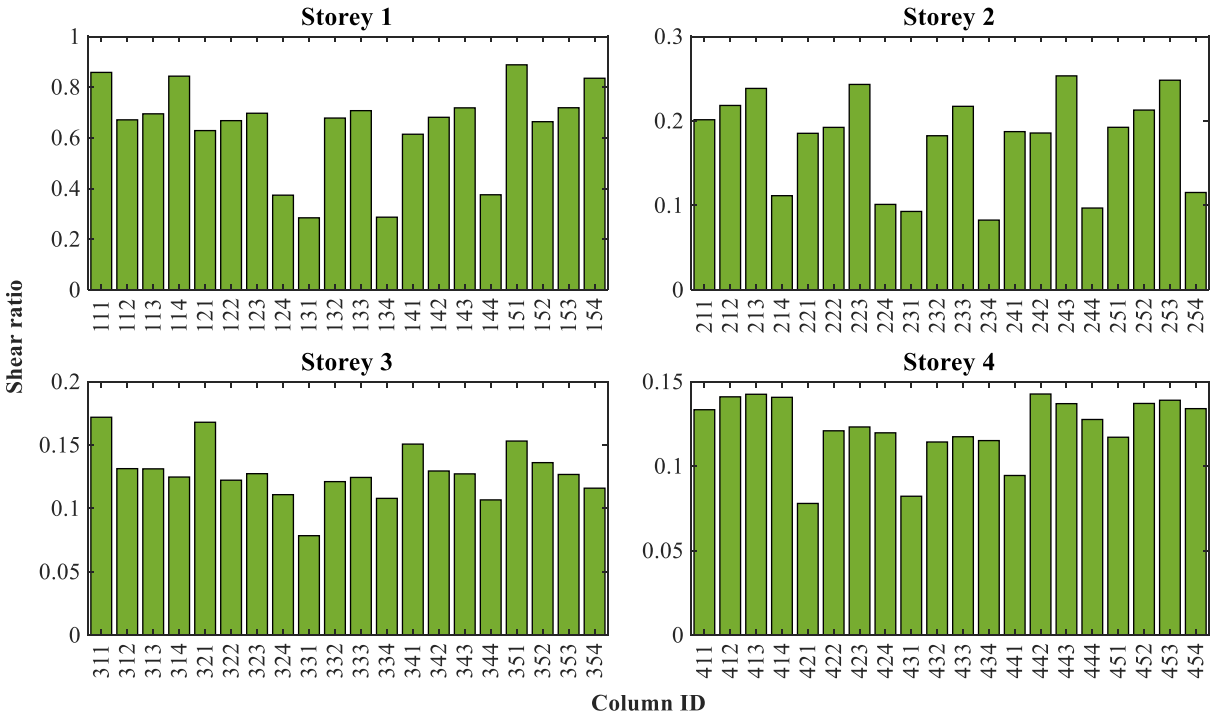

Fig. A. 38. Column shear ratio for 3D retrofitted building model under Record 292

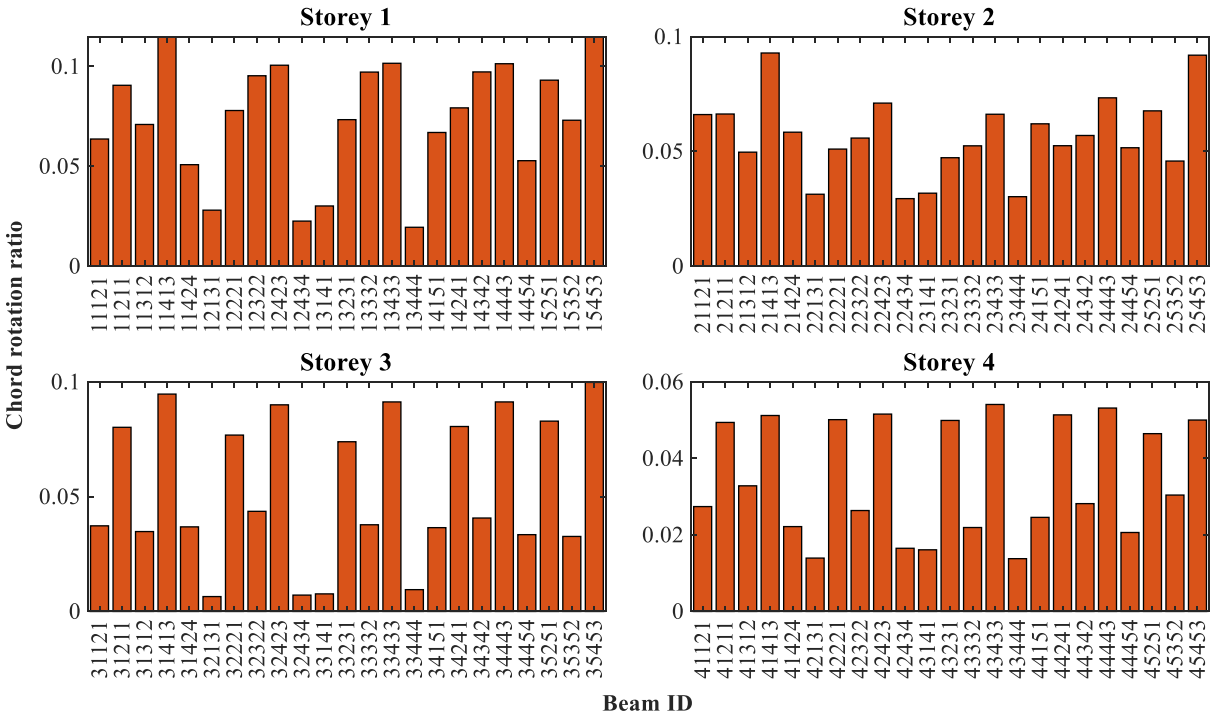

Fig. A. 39. Beam chord rotation ratio for 3D retrofitted building model under Record 292

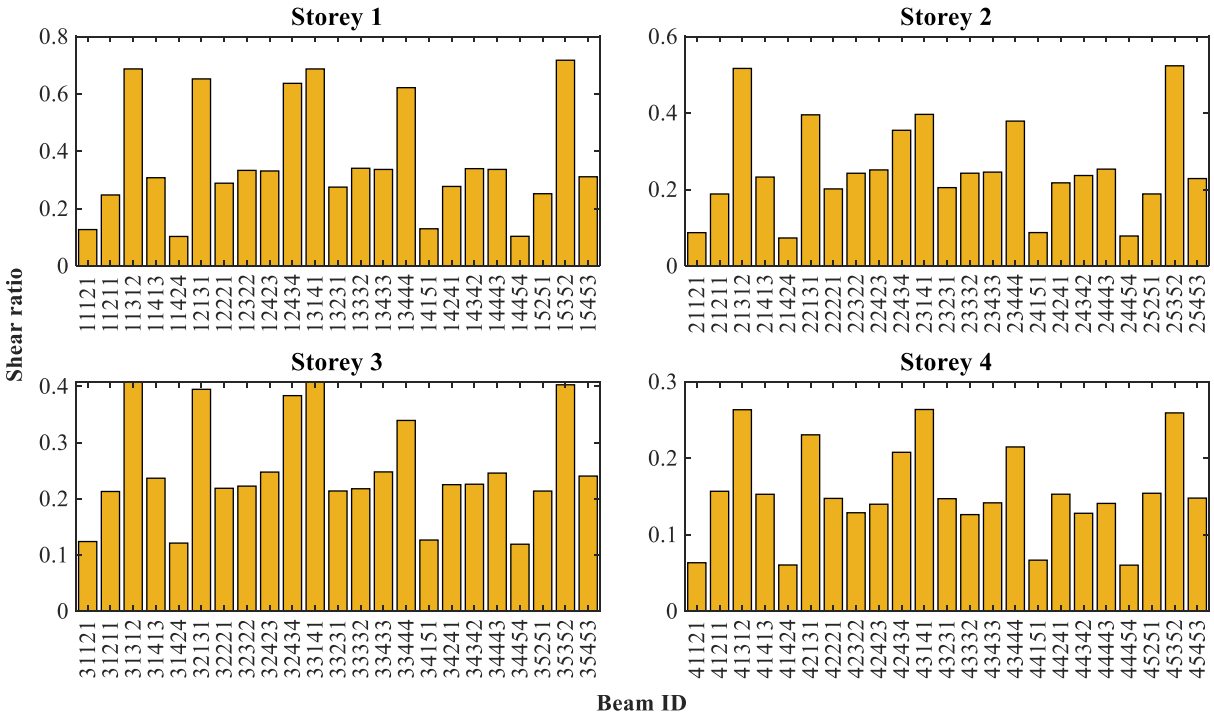

Fig. A. 40. Beam shear ratio for 3D retrofitted building model under Record 292

Record 333

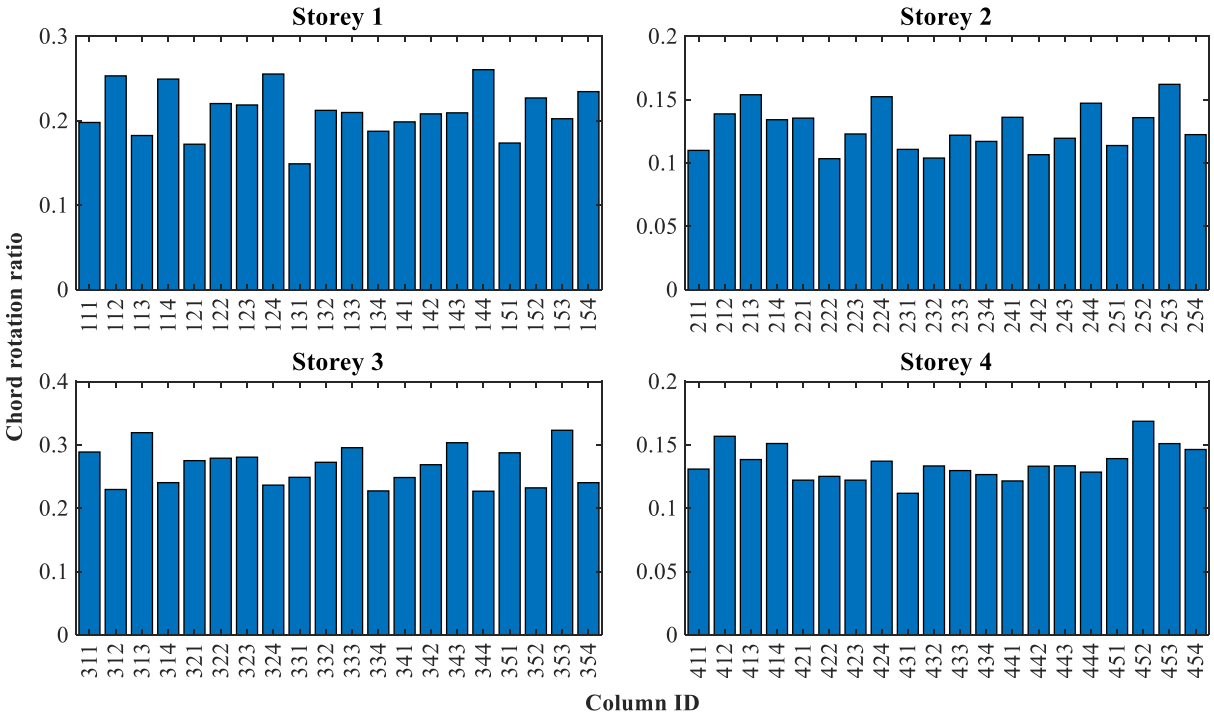

Fig. A. 41. Column chord rotation ratio for 3D retrofitted building model under Record 333

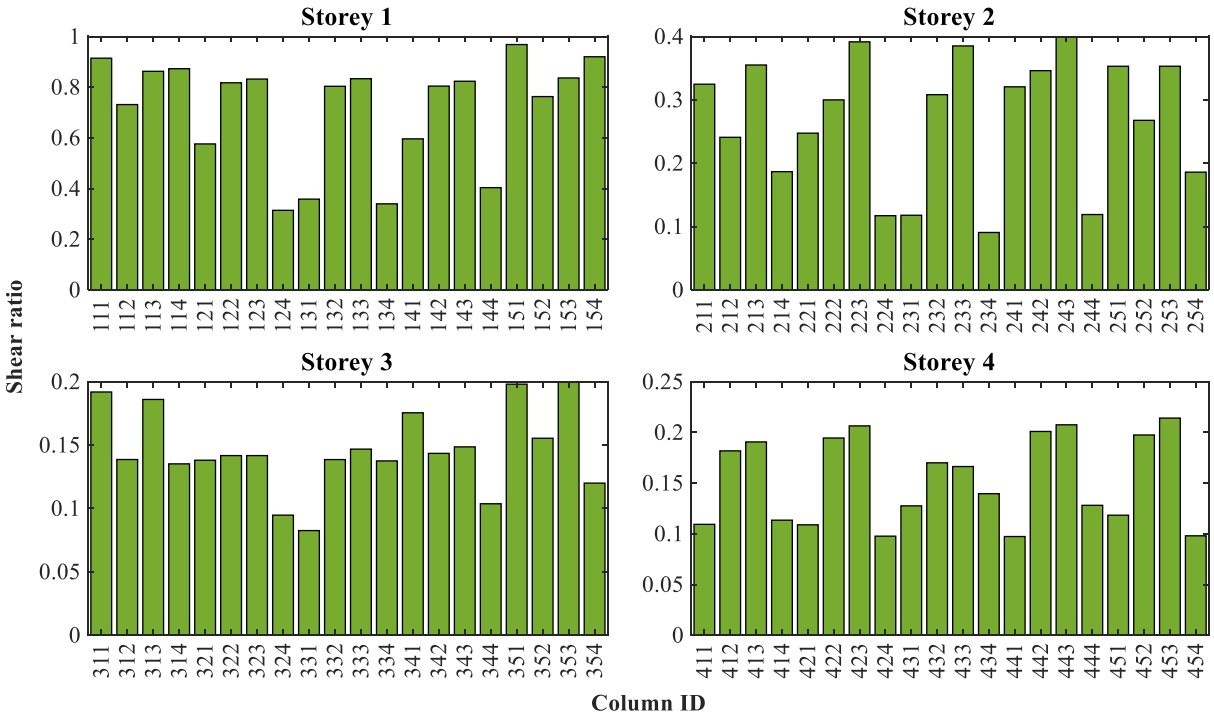

Fig. A. 42. Column shear ratio for 3D retrofitted building model under Record 333

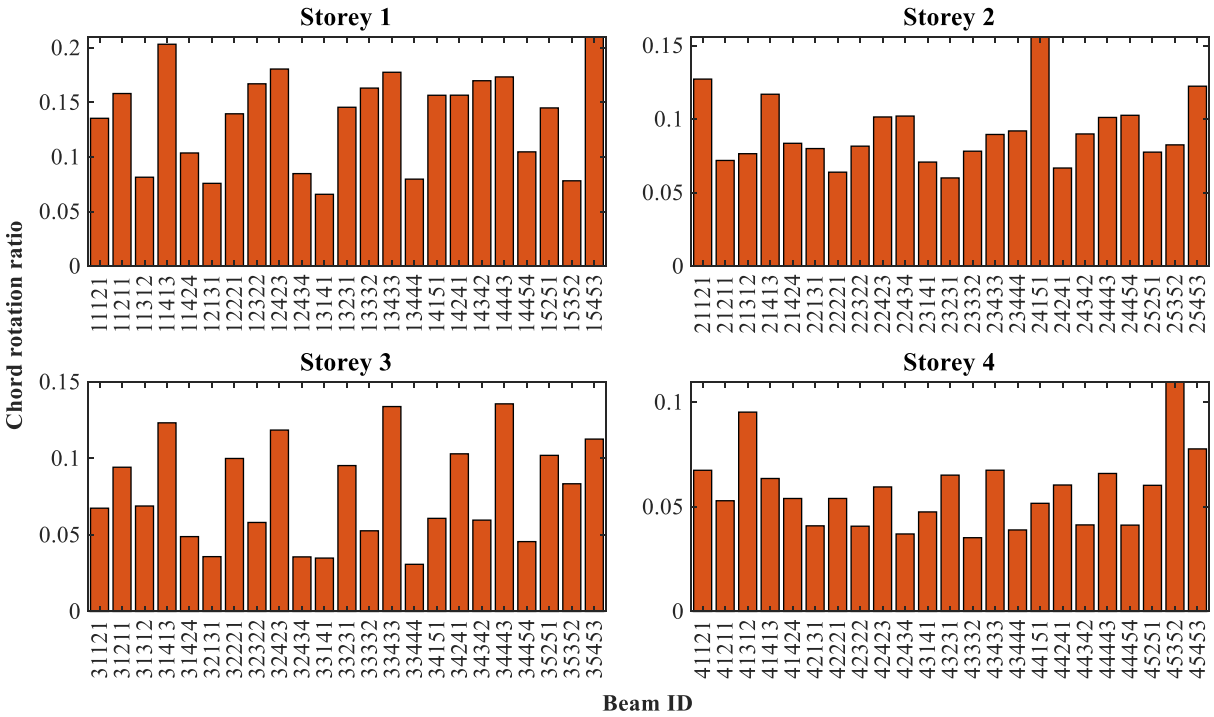

Fig. A. 43. Beam chord rotation ratio for 3D retrofitted building model under Record 333

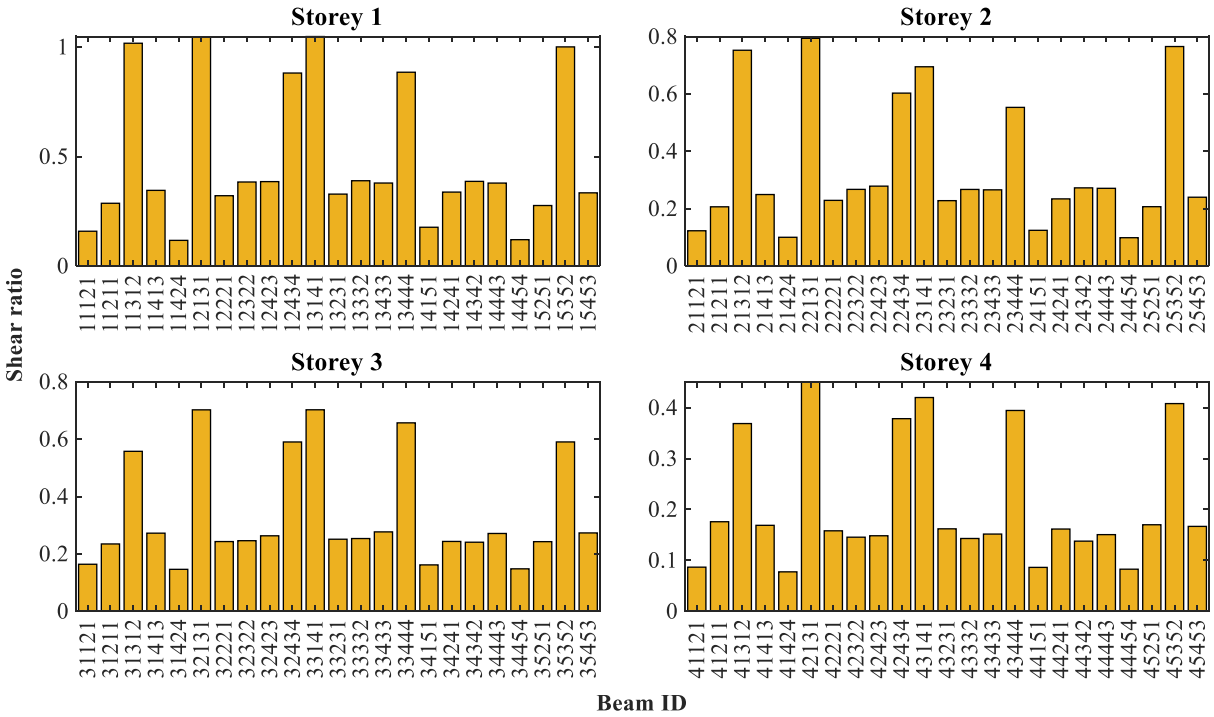

Fig. A. 44. Beam shear ratio for 3D retrofitted building model under Record 333

Record 600

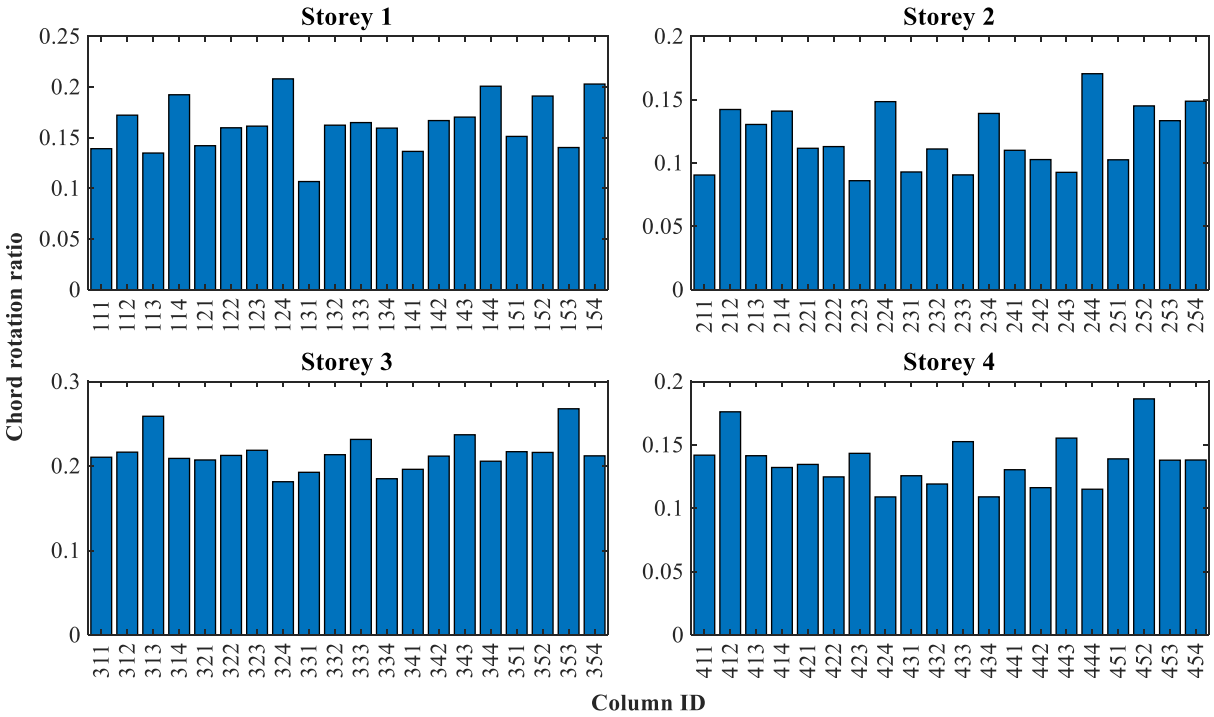

Fig. A. 45. Column chord rotation ratio for 3D retrofitted building model under Record 600

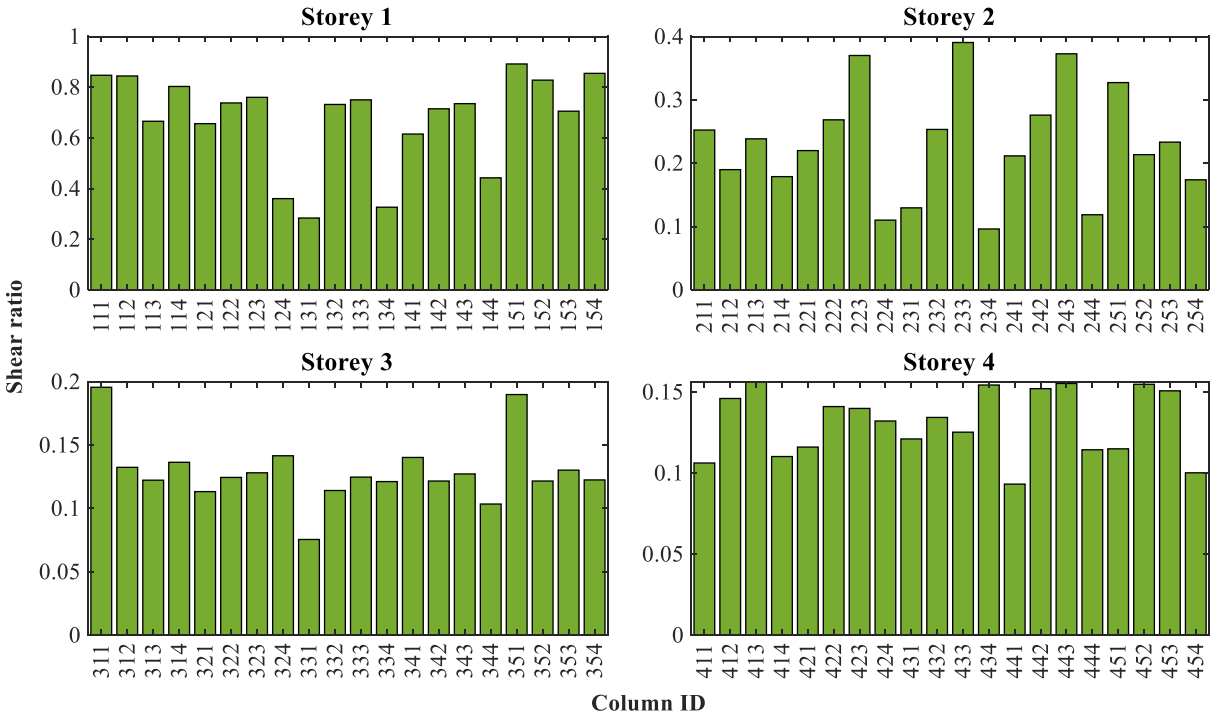

Fig. A. 46. Column shear ratio for 3D retrofitted building model under Record 600

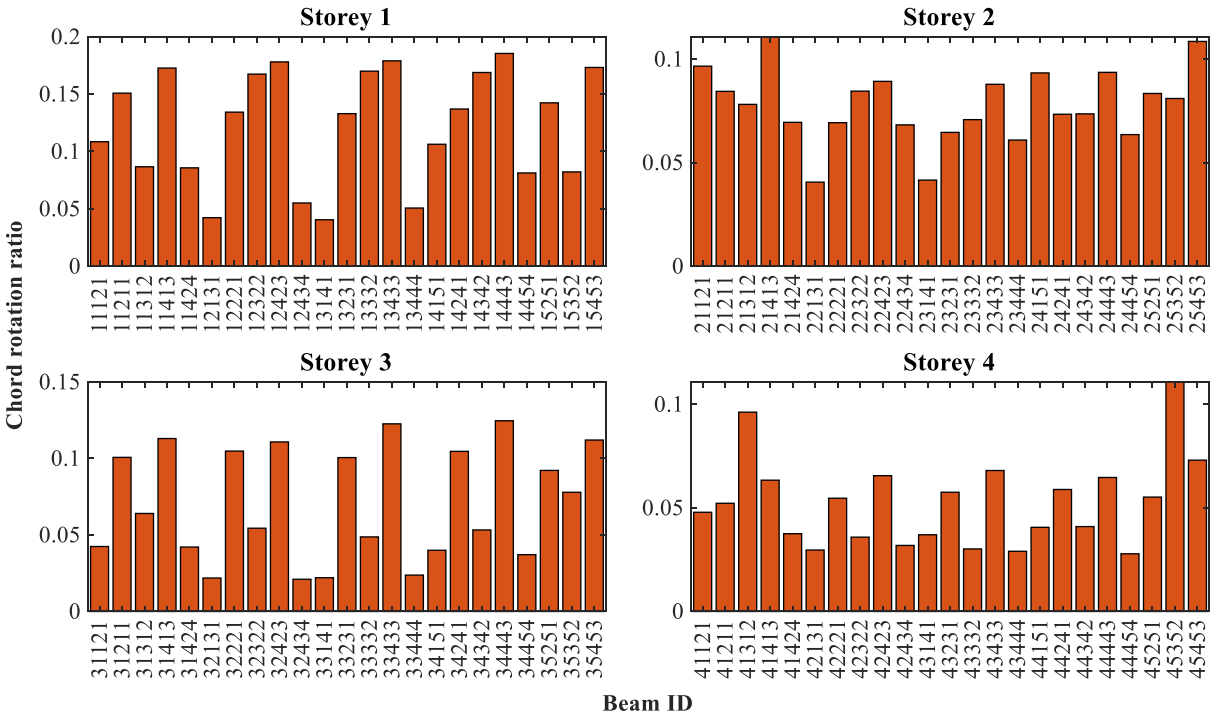

Fig. A. 47. Beam chord rotation ratio for 3D retrofitted building model under Record 600

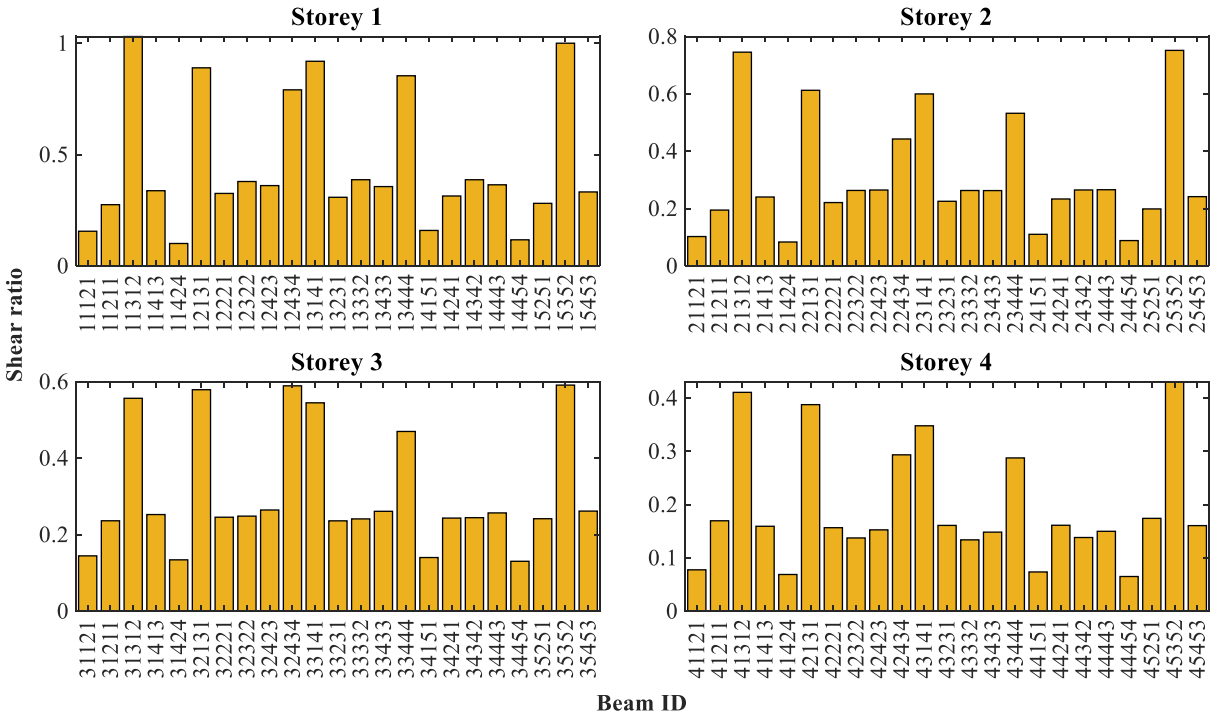

Fig. A. 48. Beam shear ratio for 3D retrofitted building model under Record 600

Record 6331

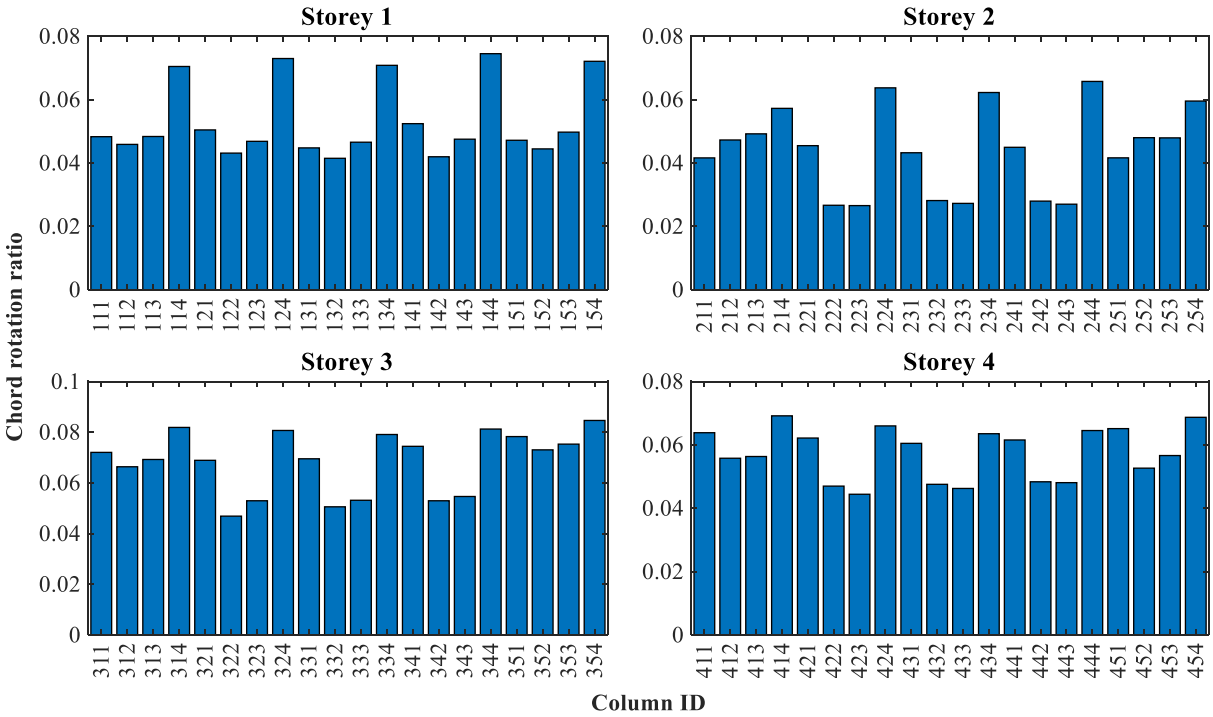

Fig. A. 49. Column chord rotation ratio for 3D retrofitted building model under Record 6331

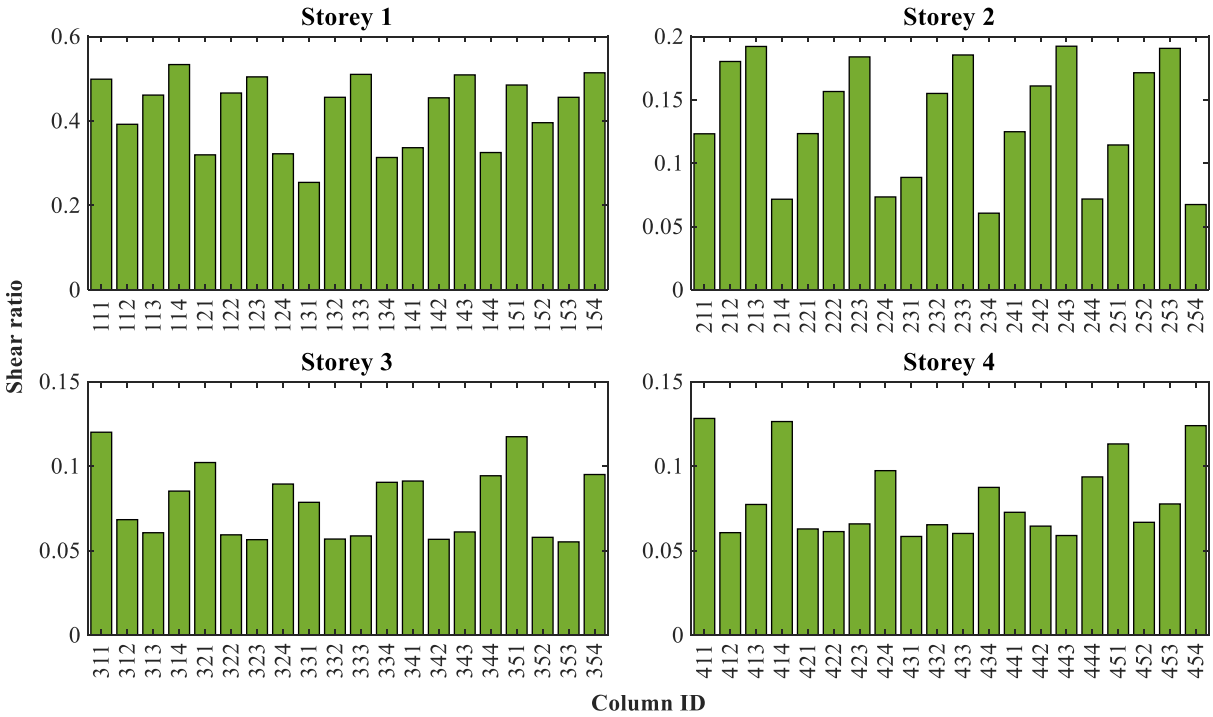

Fig. A. 50. Column shear ratio for 3D retrofitted building model under Record 6331

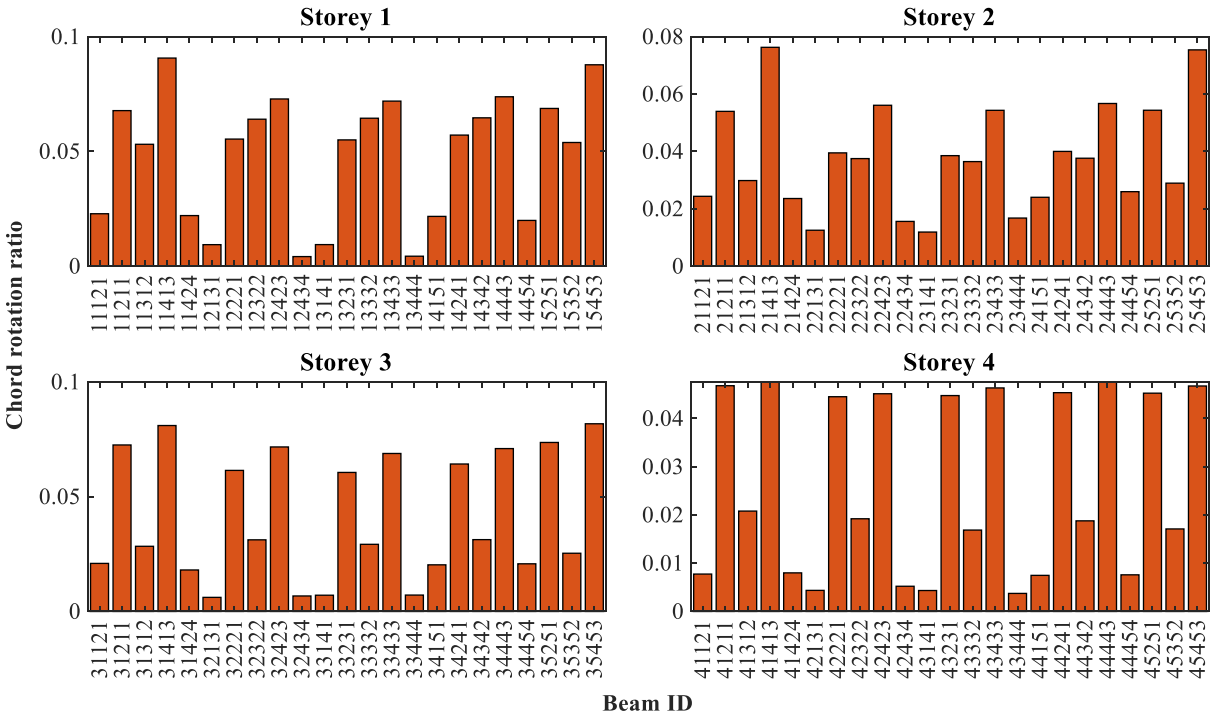

Fig. A. 51. Beam chord rotation ratio for 3D retrofitted building model under Record 6331

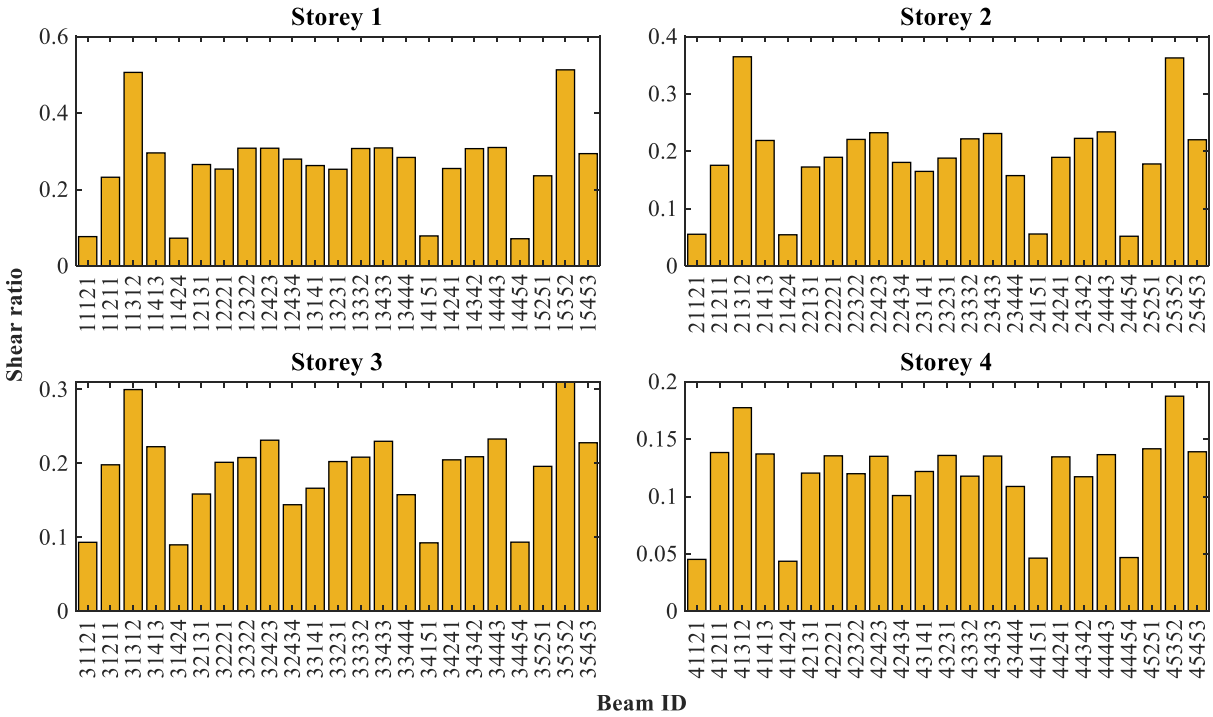

Fig. A. 52. Beam shear ratio for 3D retrofitted building model under Record 6331

Record 6335

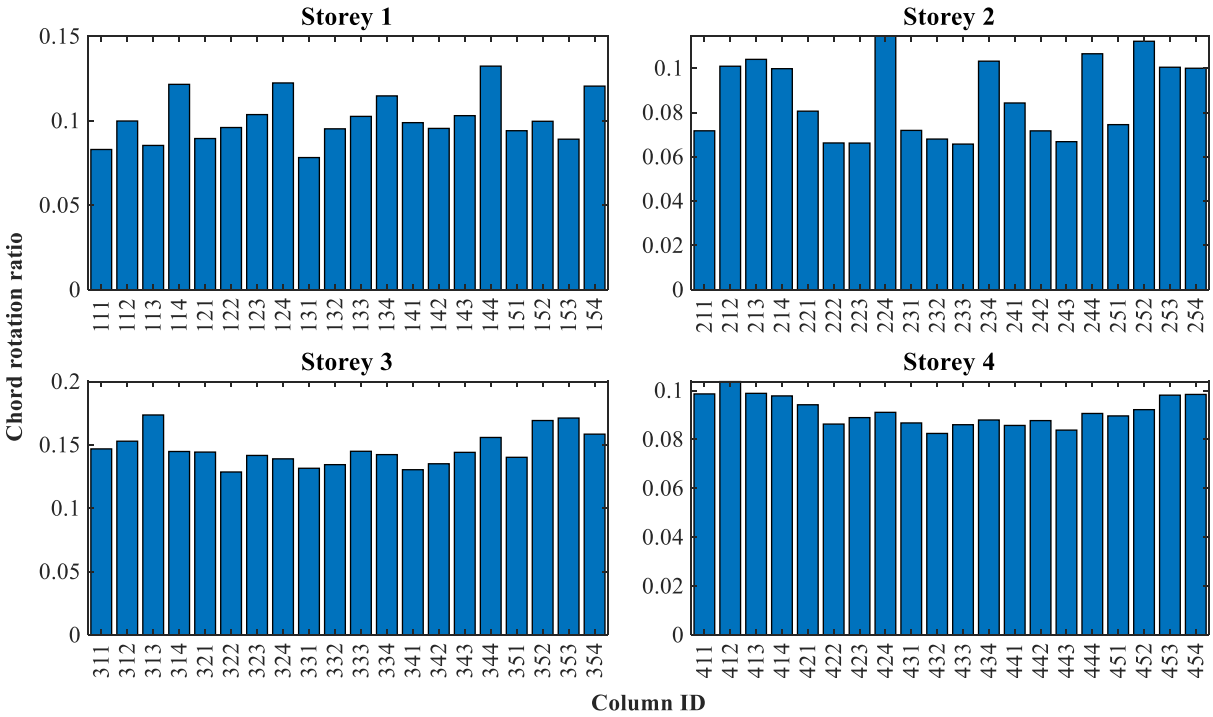

Fig. A. 53. Column chord rotation ratio for 3D retrofitted building model under Record 6335

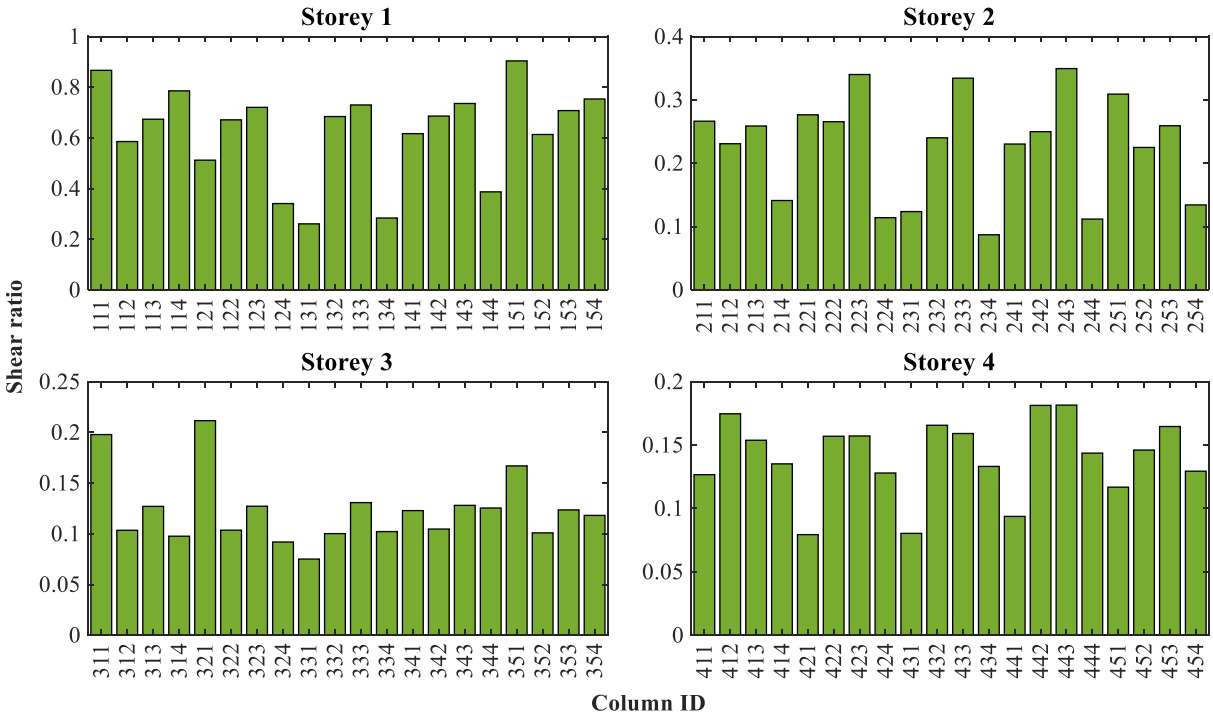

Fig. A. 54. Column shear ratio for 3D retrofitted building model under Record 6335

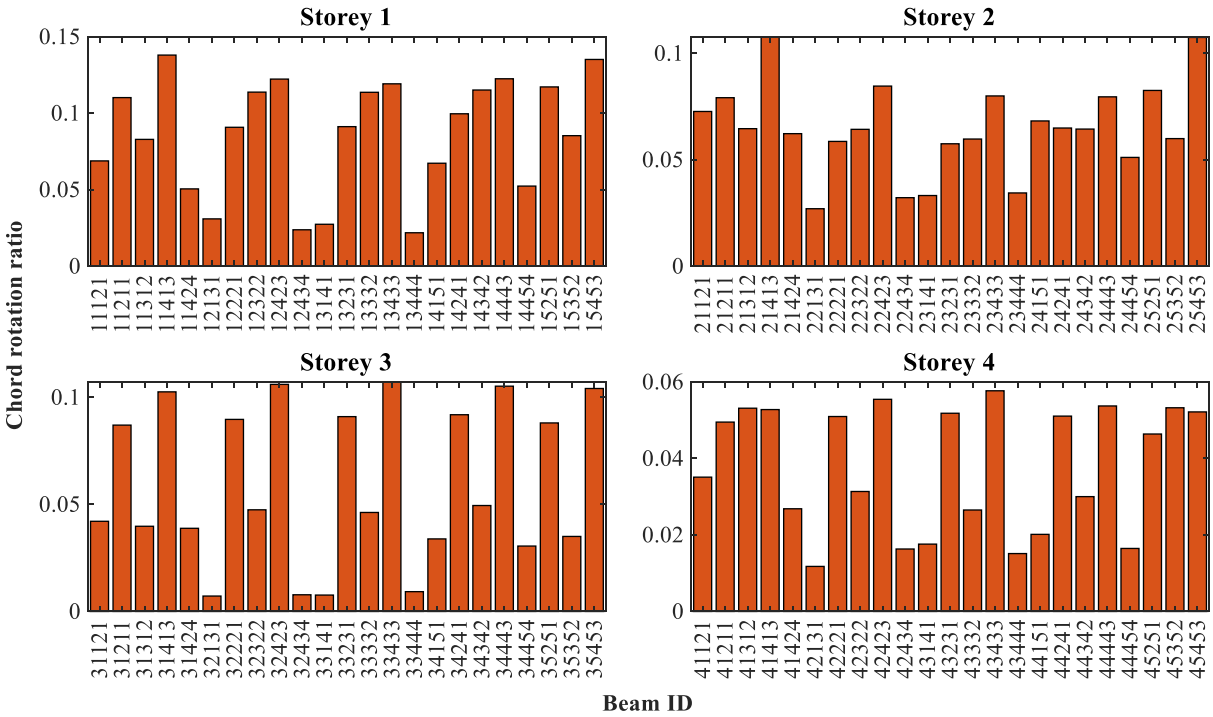

Fig. A. 55. Beam chord rotation ratio for 3D retrofitted building model under Record 6335

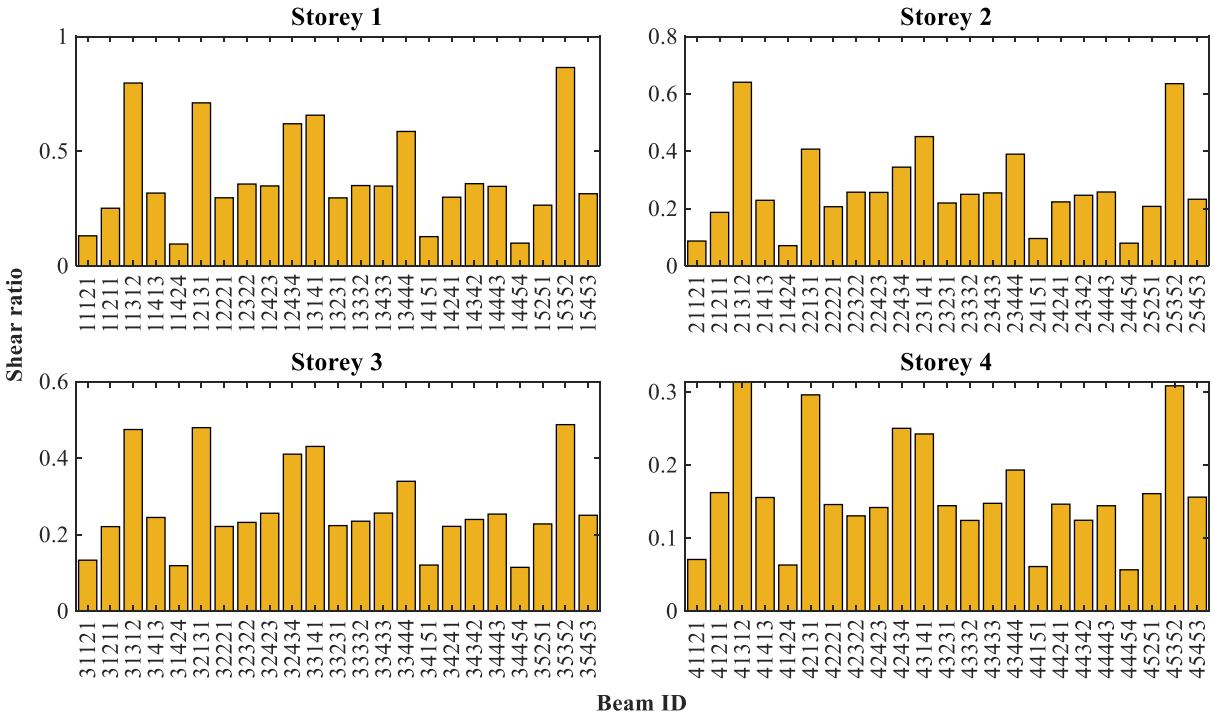

Fig. A. 56. Beam shear ratio for 3D retrofitted building model under Record 6335